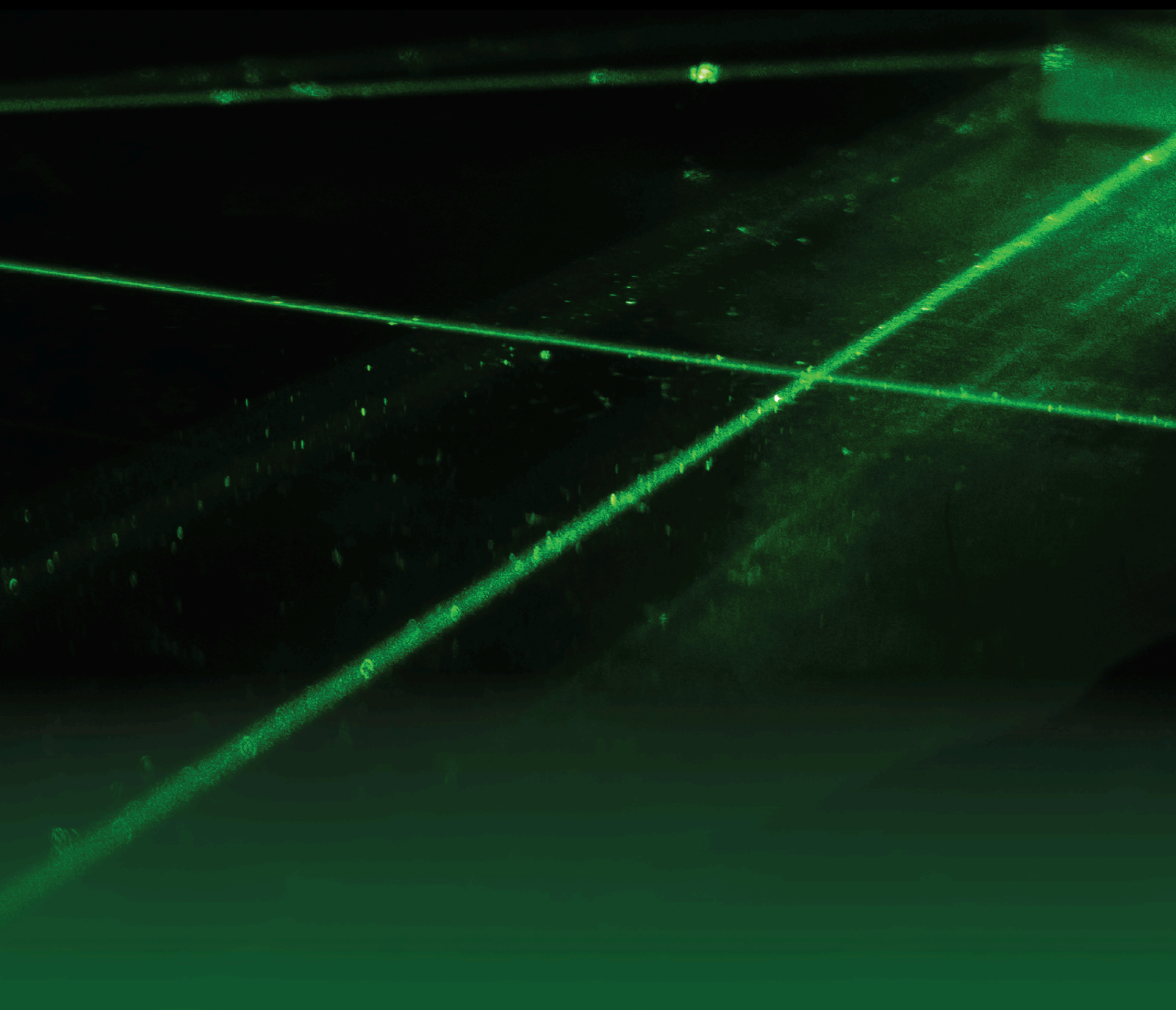


Advances In the Study of Laser-Driven Proton-Boron Fusion

Lead Guest Editor: Dimitri Batani

Guest Editors: Daniele Margarone and Fabio Belloni





Advances In the Study of Laser-Driven Proton-Boron Fusion

Laser and Particle Beams

Advances In the Study of Laser-Driven Proton-Boron Fusion

Lead Guest Editor: Dimitri Batani

Guest Editors: Daniele Margarone and Fabio
Belloni



Copyright © 2023 Hindawi Limited. All rights reserved.

This is a special issue published in "Laser and Particle Beams." All articles are open access articles distributed under the Creative Commons Attribution License, which permits unrestricted use, distribution, and reproduction in any medium, provided the original work is properly cited.


Chief Editor


Katarzyna Batani, Poland

Chief Editor Emeritus

Dieter H. H. Hoffmann, Germany

Academic Editors


Dimitri Batani , France

Yuji Fukuda , Japan

Ahmed Hassanein, USA


Daniele Margarone, United Kingdom

Devki Nandan Gupta , India

Vincenzo Palleschi , Italy


Jose Manuel Perlado, Spain

Sergey Pikuz, Russia

Bhuvanesh Ramakrishna , India

Tao Shao , China

Xinxin Wang , China

Mingsheng Wei , USA



Yongtao Zhao, China

Zongqing Zhao, China

Advisory Board Member(s)

Contents



Advances in the Study of Laser-Driven Proton-Boron Fusion

Dimitri Batani , Daniele Margarone , and Fabio Belloni 

Editorial (3 pages), Article ID 9824024, Volume 2023 (2023)




Univocal Discrimination of α Particles Produced by $^{11}\text{B}(p, \alpha)2\alpha$ Fusions in Laser-Matter Experiments by Advanced Thomson Spectrometry

Martina Salvadori , Massimiliano Scisciò , Giorgio Di Giorgio, Mattia Cipriani , Pier Luigi

Andreoli, Giuseppe Cristofari, Riccardo De Angelis , Danilo Giulietti, and Fabrizio Consoli 




Research Article (12 pages), Article ID 7831712, Volume 2023 (2023)

Photon and Neutron Production as In Situ Diagnostics of Proton-Boron Fusion

B. M. Hegelich, L. Labun , O. Z. Labun , and T. A. Mehlhorn 


Research Article (14 pages), Article ID 6924841, Volume 2023 (2023)

Oscillating Plasmas for Proton- Boron Fusion in Miniature Vacuum Discharge

Yu. K. Kurilenkov , V. P. Tarakanov , A. V. Oginov , S. Yu Gus'kov , and I. S. Samoylov 



Research Article (10 pages), Article ID 9563197, Volume 2023 (2023)

Cross-Section Measurements of the $^{11}\text{B}(p, \alpha)2\alpha$ Reaction near the First Resonant Energy

Shizheng Zhang , Hao Xu, Xing Xu, Wenqing Wei, Jieru Ren, Benzheng Chen, Bubo Ma, Zhongmin Hu,


Fangfang Li, Lirong Liu, Mingzhe Yang, Zeyu Lai, Hongwei Yue, Jie Xiong, Zhongfeng Xu, Yanhong Chen,



Zhao Wang, Zexian Zhou, Lulin Shi, Rui Cheng , Zhigang Deng, Wei Qi, Weimin Zhou, Guanchao

Zhao, Bing Liu, Di Luo, Dieter H. H. Hoffmann , and Yongtao Zhao 

Research Article (6 pages), Article ID 9697329, Volume 2023 (2023)





High-Sensitivity Thomson Spectrometry in Experiments of Laser-Driven Low-Rate NeutronLess Fusion Reactions

M. Scisciò , G. Di Giorgio, P. L. Andreoli, M. Cipriani, G. Cristofari, R. De Angelis, M. Salvadori, G. A. P.

Cirrone, L. Giuffrida, D. Margarone , G. Milluzzo, G. Petringa, and F. Consoli 

Research Article (11 pages), Article ID 3531875, Volume 2023 (2023)

Path to Increasing p-B11 Reactivity via ps and ns Lasers






Thomas A. Mehlhorn , Lance Labun , Bjorn Manuel Hegelich , Daniele Margarone , Ming Feng

Gu , Dimitri Batani , E. Michael Campbell, and S. X. Hu 

Research Article (16 pages), Article ID 2355629, Volume 2022 (2022)

Investigation of Proton Beam-Driven Fusion Reactions Generated by an Ultra-Short Petawatt-Scale Laser Pulse

Marius S. Schollmeier , Vahe Shirvanyan, Christie Capper, Sven Steinke , Adam Higginson , Reed

Hollinger , John T. Morrison, Ryan Nedbailo , Huanyu Song , Shoujun Wang , Jorge J. Rocca ,





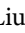
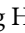



and Georg Korn

Research Article (13 pages), Article ID 2404263, Volume 2022 (2022)


Alpha-Particle Generation from H-¹¹B Fusion Initiated by Laser-Accelerated Boron Ions

Defeng Kong , Shirui Xu, Yinren Shou, Ying Gao, Zhusong Mei, Zhuo Pan, Zhipeng Liu, Zhengxuan Cao, Yulan Liang, Ziyang Peng, Pengjie Wang, Di Luo, Yang Li, Zhi Li, Huasheng Xie, Guoqiang Zhang, Wen Luo, Jiarui Zhao , Shiyou Chen, Yixing Geng, Yanying Zhao, Jianming Xue, Xueqing Yan, and Wenjun Ma 
Research Article (8 pages), Article ID 5733475, Volume 2022 (2022)








Laser-Driven Proton-Boron Fusions: Influences of the Boron State

Xiaochuan Ning , Tianyi Liang , Dong Wu , Shujun Liu , Yangchun Liu , Tianxing Hu , Zhengmao Sheng , Jieru Ren, Bowen Jiang, Yongtao Zhao , Dieter H. H. Hoffmann , and X.T. He
Research Article (7 pages), Article ID 9868807, Volume 2022 (2022)

Multiplication Processes in High-Density H-¹¹B Fusion Fuel

Fabio Belloni 
Review Article (9 pages), Article ID 3952779, Volume 2022 (2022)

Particles Detection System with CR-39 Based on Deep Learning

Gal Amit , Idan Mosseri, Ofir Even-Hen , Nadav Schneider , Elad Fisher , Hanan Datz , Eliahu Cohen , and Noaz Nissim 
Research Article (6 pages), Article ID 3820671, Volume 2022 (2022)

Analysis of the p-¹¹B Fusion Scenario with Compensation of the Transfer of Kinetic Energy of Protons and Alpha Particles to the Gas Medium by the Electric Field

Mikhail L. Shmatov 
Research Article (3 pages), Article ID 7473118, Volume 2022 (2022)



Editorial

Advances in the Study of Laser-Driven Proton-Boron Fusion

Dimitri Batani ^{1,2} **Daniele Margarone** ^{3,4} and **Fabio Belloni** ⁵

¹University of Bordeaux, CNRS, CEA, CELIA (Centre Lasers Intenses et Applications), F-33405 Talence, France

²HB11 Energy Holdings Pty, 11 Wyndora Ave, Freshwater, NSW 2096, Australia

³ELI Beamlines Facility, The Extreme Light Infrastructure ERIC, Dolni Brezany, Czech Republic

⁴Centre for Light-Matter Interactions, School of Mathematics and Physics, Queen's University Belfast, Belfast, UK

⁵School of Electrical Engineering and Telecommunications, Faculty of Engineering, UNSW Sydney, Kensington, Australia

Correspondence should be addressed to Dimitri Batani; dimitri.batani@u-bordeaux.fr

Received 22 April 2023; Accepted 22 April 2023; Published 13 June 2023

Copyright © 2023 Dimitri Batani et al. This is an open access article distributed under the Creative Commons Attribution License, which permits unrestricted use, distribution, and reproduction in any medium, provided the original work is properly cited.

The topic of proton-boron fusion has recently attracted considerable interest in the scientific community, both for its future perspectives for energy production and for nearer-term possibilities to realize high-brightness α -particle sources. Very interesting experimental results have been obtained, in particular in laser-driven experiments but also using other experimental approaches. The goal of this special issue is to collect the most recent developments in experiments, theory, advanced targetry, diagnostics, and numerical simulation codes.

Fusion energy represents the most promising scientific and technology option for a long-term sustainable energy solution for mankind. It will also help meet the decarbonization targets for the second half of the century. The conventional route to fusion for power generation is based on the deuterium-tritium (DT) reaction, which yields one α -particle and one neutron and releases a total energy of 17.6 MeV. Worldwide research focuses on magnetic or inertial confinement of DT fuel. These approaches show the highest potential to demonstrate net energy gain, due also to the fact that DT fuel has the highest thermal reactivity among all possible fusion fuels at relatively low temperatures. Significant progress continues being made in both magnetic and inertial DT fusion. In August 2021, 1.3 MJ of fusion energy was obtained at the National Ignition Facility in the U.S. by irradiating a DT capsule with 1.8 MJ of laser energy, a result very close to breakeven [1–3]. Later, in December 2022, the laser energy was increased to 2.1 MJ allowing to obtain 3 MJ of fusion energy [4]. This corresponds to a gain of 1.5: the first result in history beyond breakeven and the first to demonstrate net energy gain. On the side of magnetic confinement fusion, in December 2021, a total fusion energy of 59 MJ was obtained at the tokamak JET (Joint European Torus) based in Culham, UK, more than doubling JET's 1997 record [5].

While DT fusion appears to be the most scientifically mature approach to build a fusion power plant by mid-century [6], it also faces severe physics and engineering challenges which are very likely to increase costs, complicate regulations, and hinder public acceptance and economic viability. We recall, here, tritium's initial availability (production), breeding, and on-site management, as well as the radiation damage and activation induced by the high-energy neutrons in reactor materials. These challenges motivate the continued pursuit of alternative approaches which may simplify the pathway to commercial fusion energy.

Proton-boron (pB) fusion has long been seen as the holy grail of fusion energy [7]. Indeed, the reaction ($p + {}^{11}\text{B} \rightarrow 3\alpha + 8.7\text{ MeV}$) does not produce neutrons. Although some neutrons are produced by secondary reactions, the total neutron yield remains negligible with respect to future fusion reactors based on DT reaction or to power plants using nuclear fission of uranium. This implies little activation of materials and hence a very low amount of radioactive waste. In addition, the reaction involves only abundant and stable isotopes in the reactants, avoiding breeding, radiation protection, and security issues related to tritium. This makes pB fusion a clean and environmentally acceptable technology. Furthermore, the reaction produces

only charged particles (3α -particles per fusion event), with the potential advantage of allowing direct energy conversion, without passing through a thermodynamic cycle. This might dramatically enhance the efficiency of electricity generation.

However, the hydrogen-boron fusion plasma requires unpractical temperatures to be thermodynamically ignited and sustained in the laboratory, which explains why pB fusion has been left, from a historical perspective, as a future step after the achievement of DT fusion.

Following the discovery of the laser in the 1960s, Heinrich Hora, now Emeritus Professor at the University of New South Wales, pursued an alternative means to realize the proton-boron fusion reaction from the 1970s [8].

Hora's work included computer hydrodynamic simulations applied to plasmas [7] which suggested that the acceleration of a plasma front irradiated by a short-pulse (100 ps) laser pulse could reach extremely high values, potentially enough to achieve energies required for fusion. This finding was practically simultaneous to the discovery of chirped pulse laser amplification and the modern understanding of laser ion acceleration mechanisms. A more complete summary of this history is given in [10].

In the last decade, several experiments demonstrated high yields in α -particle production [11–14], thus reviving the interest in pB fusion amongst many research groups and also bringing to the creation of private companies working on the topic, as it is the case of the company HB11 Energy Holdings (Sydney, Australia) founded by Prof Hora himself [15].

These experiments used high-energy short-pulse lasers and produced up to 10^{11} α -particles per shot [16, 17] and additionally provided the evidence of a few-MeV boost in their kinetic energy, an effect allowed by the kinematics of the fusion reaction [18]. Indeed, these lasers can produce highly energetic protons that can directly transfer part of their energy to the reaction products. This opens the possibility of inducing reactions which are useful, for instance, to produce radioisotopes for medical therapeutics or imaging.

Although interesting, all current results remain far from energy breakeven, which corresponds to about 2×10^{15} α -particles generated per shot per kJ laser energy. Achieving breakeven and gain might rely on the possibility of departing from the thermal equilibrium of classical inertial confinement schemes and initiating a fusion avalanche (or chain) reaction [19].

Following these latest developments, this special issue aims at collating original research and review articles with a focus on the mechanism of pB fusion in laser-produced plasmas, the possible implications for future energy production, and the possibility of developing high-brightness α -particle sources for applications such as the production of

medical radioisotopes. The special issue is composed of a balanced selection of articles, encompassing a broad spectrum of topics, including in particular

- (i) Recent results in laser-driven proton-boron fusion experiments
- (ii) The onset of avalanche processes in H- 11 B fuel and the quest for breakeven
- (iii) Measurements of cross section of the proton-boron fusion reaction
- (iv) Developments in diagnostics for proton-boron fusion experiments
- (v) Hybrid approaches (thermal/nonthermal) to proton-boron fusion for energy production
- (vi) Proton-boron fusion in nonlaser systems (e.g., vacuum discharges)
- (vii) Advanced targetry for laser-driven proton-boron experiments.

It is worth noticing how wide is the geographical distribution of the contributors to this special issue (Europe, US, China, Australia, and Russia), which shows how nowadays pB fusion is an active research topic spreading worldwide.

This special issue was inspired by a series of on-line seminars (2021-2022) [20] promoted by HB11 energy to map the state of the art of pB fusion research. Some of the articles refer to work presented in that series of seminars.

We shall emphasize that the results reported in the special issue and elsewhere in the last two decades are not part of a coordinated research program. Unlike fusion studies based on DT, pB fusion research remains the initiative of single research groups mainly based in university and academia. We hope that our editorial initiative will establish a foundation for the systematic investigation of possible ignition schemes by consolidating research efforts in laser-driven pB fusion to date. We also hope that it will help building and strengthening the cooperation in the field as it evolves.

Looking forward, a European Union COST program has been granted to support the development of the community studying proton-boron fusion: PROBONO (CA21128-proton-boron nuclear fusion: from energy production to medical applications) [21]. This program represents the first attempt to coordinate the research effort across European countries (and several extra-European partners) on pB research. We also call for additional and more systematic support in terms of funding opportunities (both public and private) and policy recognition in order to further develop this research field and the related international cooperation in the near future.

Conflicts of Interest

The authors declare that there are no conflicts of interest.

Acknowledgments

We conclude by warmly thanking all the authors for contributing their work to this special issue and Hb11 Energy for supporting the publication of the issue through a financial contribution to the publication charges. We also acknowledge the contributions from many research groups taking part in the COST Action PROBONO (CA21128-proton-boron nuclear fusion: from energy production to medical applications).

Dimitri Batani
Daniele Margarone
Fabio Belloni

References

- [1] H. Abu-Shawareb, R. Acree, P. Adams et al., “Lawson criterion for ignition exceeded in an inertial fusion experiment,” *Physical Review Letters*, vol. 129, no. 7, Article ID 075001, 2022.
- [2] A. B. Zylstra, A. L. Kritcher, O. A. Hurricane et al., “Experimental achievement and signatures of ignition at the national ignition facility,” *Physical Review E - Statistical Physics, Plasmas, Fluids, and Related Interdisciplinary Topics*, vol. 106, no. 2, Article ID 025202, 2022.
- [3] A. L. Kritcher, A. B. Zylstra, D. A. Callahan et al., “Design of an inertial fusion experiment exceeding the Lawson criterion for ignition,” *Physical Review E - Statistical Physics, Plasmas, Fluids, and Related Interdisciplinary Topics*, vol. 106, no. 2, Article ID 025201, 2022.
- [4] “See for instance “National Ignition Facility demonstrates net fusion energy gain,” 2023, <https://physicsworld.com>.
- [5] Iter, “Jet makes history, again,” 2022, <https://www.iter.org/newsline/-/3722>.
- [6] A. J. Donné, “Roadmap towards fusion electricity (editorial),” *Journal of Fusion Energy*, vol. 38, no. 5-6, pp. 503–505, 2019.
- [7] M. George, J. Herbert Berk, R. McNally Jr., and C. Bogdan, “Discussion of report of the aneutronic fusion committee of the national academy of science’s Air Force Studies Board,” *Nuclear Instruments and Methods in Physics Research Section A*, vol. 271, no. 1, pp. 217–221, 1988.
- [8] H. Hora, “Increased nuclear energy yields from the fast implosion of cold shells driven by nonlinear laser plasma interactions,” *Soviet Journal of Quantum Electronics*, vol. 6, no. 2, pp. 154–159, 1976.
- [9] H. Hora, *The Nonlinear Force of Electrodynamical Laser-Plasma Interaction in Laser Interaction and Related Plasma Phenomena*, H. J. Schwarz and H. Hora, Eds., Springer, Boston, MA, USA, 1977.
- [10] H. Hora, “Fighting Climatic Change by NASEM with Help of Non-thermal Optical Laser Pressure,” *Journal of Energy and Power Engineering*, vol. 15, pp. 163–168, 2021.
- [11] A. Picciotto, D. Margarone, A. Velyhan et al., “Boron-proton nuclear-fusion enhancement induced in boron-doped silicon targets by low-contrast pulsed laser,” *Physical Review X*, vol. 4, no. 3, Article ID 031030, 2014.
- [12] D. Margarone, A. Picciotto, A. Velyhan et al., “Advanced scheme for high-yield laser driven nuclear reactions,” *Plasma Physics and Controlled Fusion*, vol. 57, no. 1, Article ID 014030, 2015.
- [13] C. Labaune, C. Baccou, S. Depierreux et al., “Fusion reactions initiated by laser-accelerated particle beams in a laser-produced plasma,” *Nature Communications*, vol. 4, no. 1, p. 2506, 2013.
- [14] C. Baccou, S. Depierreux, V. Yahia et al., “New scheme to produce aneutronic fusion reactions by laser-accelerated ions,” *Laser and Particle Beams*, vol. 33, no. 1, pp. 117–122, 2015.
- [15] Hb11 Energy, “Clean, safe, reliable and unlimited energy,” 2023, <https://hb11.energy>.
- [16] L. Giuffrida, F. Belloni, D. Margarone et al., “High-current stream of energetic α particles from laser-driven proton-boron fusion,” *Physical Review E*, vol. 101, no. 1, Article ID 013204, 2020.
- [17] D. Margarone, A. Morace, J. Bonvalet et al., “Generation of α -particle beams with a multi-kJ, peta-watt class laser system,” *Frontiers in Physics*, vol. 8, p. 343, 2020.
- [18] J. Bonvalet, P. H. Nicolai, D. Raffestin et al., “Energetic α -particle sources produced through proton-boron reactions by high-energy high-intensity laser beams,” *Physical Review*, vol. 103, no. 5-1, Article ID 053202, 2021.
- [19] F. Belloni, “Multiplication processes in high-density H-11B fusion fuel,” *Laser and Particle Beams*, vol. 2022, Article ID 3952779, 9 pages, 2022.
- [20] Hb11 Energy, “Seminars,” 2022, <https://hb11.energy/seminars/>.
- [21] “TheAction is coordinated by Katarzyna Batani from IPPLM Warsaw (for contacts: katarzyna.batani@ifilm.pl),” 2022, <https://www.cost.eu/actions/CA21128/>.



Research Article

Univocal Discrimination of α Particles Produced by $^{11}\text{B}(p, \alpha)2\alpha$ Fusions in Laser-Matter Experiments by Advanced Thomson Spectrometry

Martina Salvadori ¹, Massimiliano Scisciò ¹, Giorgio Di Giorgio,¹ Mattia Cipriani ¹, Pier Luigi Andreoli,¹ Giuseppe Cristofari,¹ Riccardo De Angelis ¹, Danilo Giulietti,² and Fabrizio Consoli ¹

¹ENEA, Fusion and Technology for Nuclear Safety and Security Department, C.R. Frascati, Rome, Italy

²University of Pisa, Physics Department E. Fermi, Pisa, Italy

Correspondence should be addressed to Martina Salvadori; martina.salvadori90@gmail.com

Received 25 July 2022; Revised 23 December 2022; Accepted 7 April 2023; Published 8 June 2023

Academic Editor: Daniele Margarone

Copyright © 2023 Martina Salvadori et al. This is an open access article distributed under the Creative Commons Attribution License, which permits unrestricted use, distribution, and reproduction in any medium, provided the original work is properly cited.

The energy problem is an open issue becoming increasingly pressing. The possibility to use nuclear fusion as an alternative energy source is thus acquiring progressively more importance and many investors are pushing to achieve the goal of an electric plant based on fusion. The most studied reaction is the deuterium-tritium one, but this poses several technical issues related to the handling of the radioactive fuel and neutron generation. In this frame, the aneutronic $^{11}\text{B}(p, \alpha)2\alpha$ fusion reaction has attracted the interest of many researchers. Despite a fusion reactor based on pB is still a long-term goal, the study of this reaction is important both for astrophysics research and for its possible employment in schemes of high brightness source of α particles for applications, as for instance in medicine. Nevertheless, the univocal identification of the produced alphas is a well-known challenging task when the reaction is triggered by high-intensity lasers. Indeed, due to the multifaceted emission typical of laser-matter interactions, the signal coming from alphas is often superimposed to that generated by protons and by other ions, and in many cases, it is therefore hardly recognizable. In this work, we analysed the possibility of employing a Thomson spectrometer (TS) with an adequate differential filtering system for the exclusion from the α -particle trace, the contribution of all other ionic species. Moreover, for the energy ranges where the filtering method cannot be successfully applied, we investigated the feasibility of integrating in the TS assembly a particle detector for time-of-flight (TOF) measurements.

1. Introduction

The aneutronic fusion reaction based on the synthesis of a proton with a Boron-11 nucleus [1–3] has attracted the interest of both researchers and investors [4, 5]. Indeed, despite the lower cross section, the $^{11}\text{B}(p, \alpha)2\alpha$ fusion reaction presents some non-negligible advantages with respect to the more studied deuterium-tritium one, such as the abundance of the reactant, the use of nonradioactive fuel, and the lack of neutrons as products. Even though fusion reactors based on p+ ^{11}B reaction are still a long-term goal, the study of this process is relevant both for astrophysics

research [6] and for its possible employment as high brightness source of α particles for important applications, such as medicine [7, 8]. To trigger the reaction, two main schemes involving high energy and intensity lasers have been studied: the “in target” scheme [2, 9–13], where a high-intensity laser pulse is focused on an hydrogenated boron target, and the “pitcher-catcher” scheme, where a beam of laser-accelerated protons is directed onto a boron target or a preformed boron plasma [14–18]. Both geometries showed a progressive increment in the yield of p+ ^{11}B fusion reactions along the experiments that were carried out during the last years [2, 10, 11, 14]. Nevertheless, aiming at further

progresses in this field, the understanding of the process needs to be deepened. To pursue this objective, a detailed characterization of the laser-matter interaction and of the fusion products must be achieved. Given the environment in which these experiments are conducted, the latter is anything but a simple task [19]. Indeed, along with the fusion reactions, several other processes are triggered inducing electromagnetic ionizing radiation spanning over a broad spectrum, particle radiation, and radiofrequency-microwave emission [20–22]. Hence, a non-negligible background is produced, hindering the detection of the fusion products characterized by a low yield. Moreover, the emitted electromagnetic pulses (EMPs) in the radiofrequency-microwave regime can lead to the malfunctioning of some of the deployed diagnostic systems, especially when located near the interaction point [21, 23].

The diagnostic techniques commonly used in this field are solid state nuclear track detectors (SSNTDs) [24, 25], time-of-flight method [26] and Thomson spectrometers [27]. Each of these presents some specific advantages and drawbacks for this context [19].

In the SSNTD, the impinging radiation damages the film in localized spots and an etching procedure is used to reveal the tracks. A detailed analysis of the track characteristics allows to infer information on the impinging radiation [18, 28, 29]. However, the background due to the detection of all other emitted radiation produced during the laser-matter interaction hinders the effective discrimination of α particles. Thus, the film is usually covered by a thin plastic or metal foil to cut the contribution of low energy and heavy ions while allowing for α -particle detection. Nevertheless, protons are more penetrant than alphas; hence, the presence of the filter does not cut their contribution from the signal [19].

The time-of-flight technique is an efficient way to obtain information on the energy of the detected particles once their type is known. Its working principle relies on the measurement of the time needed by the particle to travel through a known distance, i.e., from the source to the detector. The arrival time of the particle must be detected together with the reference of the laser-matter interaction time, which is usually retrieved by the detection of the emitted UV and X-rays. The main issue in this kind of diagnostic system is the simultaneous detection of alphas and other ions. As for SSNTD, the contribution coming from low energy and heavier ions can be cut by the employment of filters of proper material and thickness. However, also in this case, the use of filters is not effective in excluding the proton contribution [19].

The discrimination of particles having different mass-to-charge ratios can be achieved by employing Thomson spectrometers. These devices exploit the action of parallel electric and magnetic fields, both orthogonal to the direction of propagation of the incoming charged particles. As a result, particles reaching the detector plane leave different parabolic traces, each associated to a specific mass-over-charge ratio. As shown in Figure 1, ions entering a Thomson spectrometer will first traverse an entrance pinhole, whose dimension determines the energy resolution as well as the capability of

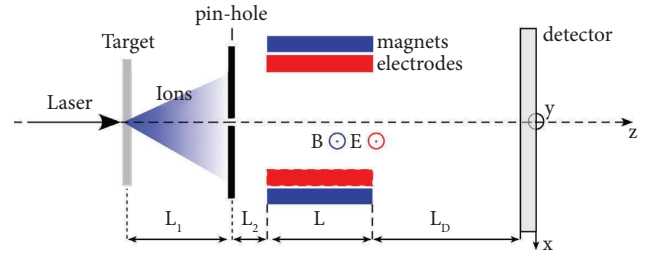


FIGURE 1: A schematic representation of the Thomson spectrometer main components. The entrance pinhole, the magnets, and the electrodes providing the binding fields and eventually the drift space before reaching the detector for the imaging.

discriminating the different ion traces. Then, there is a region where both an electric and magnetic field are applied. Here, the charged particles are deflected and afterwards they travel over a proper drift space, while increasing their mutual separation until they reach the detector site. This could either be a passive detector [30], such as imaging plates [31] and SSNTDs, or an active one to allow on-line measurement [32].

A strong effort has been required to design Thomson spectrometers resistant to the electromagnetic pulses (EMPs) produced during the interaction and being thus capable to work near the interaction point, for enhancing the device sensitivity by the increase of the solid angle covered. This allows to employ a small entrance pinhole while maintaining a high signal-to-noise ratio even for the products of low-rate nuclear fusion reactions. For this purpose, it was necessary to have an optimized shielding for EMPs otherwise they can couple to the spectrometer and cause an unwanted modulation, and thus superimposition, of the traces [11, 33, 34]. An optimal EMP resistance was achieved by keeping the deflector compact, the spectrometer has indeed only one deflecting unit providing both electric and magnetic deflection. This grants that the residual EMPs entering the device act on the particles only for a limited amount of time. The employment of a single deflecting unit also reduces the overall spectrometer dimension allowing to place it near the interaction point without blocking the line of view of other diagnostics.

The main advantage of Thomson spectrometers is that the proton trace is well separated from all the others. Hence, using this diagnostic, the issue related to the superimposition of proton to alpha particle signal is solved, easing the procedure for alphas univocal discrimination. However, the limitations in employing this technique come from the fact that the trace due to α particles is superimposed to those left by all other ion species with the same mass over charge ratio such as C^{6+} , N^{7+} , or O^{8+} , that are routinely detected during laser-matter interaction experiments [19, 20].

One possibility in achieving the univocal characterization of the produced α particles consists in the simultaneous characterization of the interaction by means of several different diagnostics placed in close proximity and providing complementary information [19, 35]. Nevertheless, this is not always a viable solution due to space limitation in the experimental chamber.

In this article, we intend to analyse in detail the possibility of employing a Thomson spectrometer with an adequate differential filtering system [36] to obtain univocal identification of alphas produced by the fusion reaction. We will also investigate the feasibility of using a TOF line coupled to a Thomson spectrometer to discriminate carbon ions from alpha particles for the energy ranges where the differential filtering methods cannot be used.

2. Differential Filtering Method

The motion of a charged particle moving along the z direction with velocity v_z entering a Thomson spectrometer characterized by an electric field $E = |\vec{E}_y|$ and a magnetic field $B = |\vec{B}_y|$ applied for region of length L followed by a drift space of length L_D can be described by the following equations (37):

$$\begin{aligned} x &= \frac{Zq_e [C]}{Am_p [kg]v_z [ms^{-1}]} A_B [Tm^2] \\ &= \frac{Zq_e [C]}{\sqrt{2Am_p [kg]E_k [J]}} A_B [Tm^2], \end{aligned} \quad (1)$$

$$y = \frac{Zq_e [C]}{Am_p [kg]v_z^2 [m^2 s^{-2}]} A_E [Vm] = \frac{Zq_e [C]}{2E_k [J]} A_E [Vm],$$

where Z is the atomic number, q_e is the electronic charge expressed in Coulomb, A is the atomic mass, m_p is the proton mass expressed in kg, and E_k is the ion energy expressed in Joule. A_B and A_E are the integral coefficients of the magnetic and electric field along the longitudinal direction z that includes the nonuniform field. They include both the field integral I_B and I_E [38] as well as all the dependences from the distances as follows:

$$\begin{aligned} A_B &= \int_0^{L_1+L_2+L+L_D} \int_0^z B(z') dz' dz, \\ A_E &= \int_0^{L_1+L_2+L+L_D} \int_0^z E(z') dz' dz, \end{aligned} \quad (2)$$

where L_1 is the distance from the target to the pinhole and L_2 is the distance from the pinhole to the electrodes and magnets, as labelled in Figure 1. A_B and A_E are thus expressed in Tm^2 and Vm , respectively. From these relations, the following equation of the parabolic traces detected by the chosen imaging system can be retrieved:

$$y(x) = \frac{Am_p}{Zq_e} \frac{A_E}{A_B} x^2. \quad (3)$$

These expressions do not consider relativistic effects of the particle motion, assumption which is reasonable for the typical energies of laser-accelerated ions (in the range of a few tens of MeV at most). The equations also assume the case where $(L/R) \ll 1$ (being L the length of the dipole and R the bending radius of the particles travelling through it) condition that is often satisfied given the dimensions of the dipoles implemented in TS devices (usually a few centimetres long). As expected, the traces have a parabolic shape:

each parabola is related to a specific mass over charge ratio and each point on the parabola corresponds to a different ion energy. The capability of resolving different traces and energies is related to the strength of deflection of the magnetic and electric field, as well as to the pinhole projection size [32, 39]. In general terms, to improve both the energy and the charge resolution, small pinhole sizes and large deflecting fields are preferred, according to the specific energy ranges of interest and the expected ion fluxes [39]. Identifying the size of the pinhole projection on the detector plane as s , the energy resolution along a parabolic trace for any A/Z can be expressed as follows [40]:

$$\frac{\Delta E}{E} = \frac{2s}{x(1 - (s/2x)^2)}, \quad (4)$$

where the A and Z appear in the expression of x , from equation (1). The charge resolution is limited by the capability of separating the traces left by ions having different mass over charge ratios on the imaging system. In general, the separation between the different traces decreases as the ion energy increases, i.e., getting closer to the pinhole image projection. For each couple of parabolic traces, it is possible to identify their merging point and the corresponding energy here, it is called merging energy. This is the maximum energy over which ion specie discrimination is no more achievable due to the intersection of the traces. The mentioned merging energy E_m is strongly related to the electric field deflection as well as to the pinhole image size. For a pair of two ion species, it is possible to write the following equation:

$$E_m = \frac{Z_i q_e A_E}{s R_Q}, \quad (5)$$

Where $R_Q = (Q_1 + Q_2)/(Q_1 - Q_2)$ with $Q_1 = (Z_1 q_e / A_1 m_p) > Q_2$, the subscripts "1" and "2" are two generic indexes referring to the two different ionic species considered, and E_m defines the merging energy of the ion with charge $Z_i q_e$ [40].

For instance, taking as reference the parameters of the Thomson spectrometer labelled as "BIG" described in Giorgio et al. [33] and assuming to have $s = 1.5$ mm the superimposition of the alpha trace with the one of protons happens for $E_\alpha \approx 88$ MeV, whereas the superimposition of the alpha trace with the one of C^{5+} happens for $E_\alpha \approx 24$ MeV.

As mentioned in the introduction, the trace of the α particles will be superimposed to those of other fully stripped ions such as carbon, oxygen, and nitrogen, each having $A/Z = 2$. In each point (x, y) of this specific parabolic trace, from equation (1), it results that all ions contributing to the signal have the same velocity, thus the same energy per nucleon. Being E_α the energy of α particles, for each (x, y) point, it is possible to write $E_{C^{6+}} = 3E_\alpha$, $E_{N^{7+}} = 3.5E_\alpha$, and $E_{O^{8+}} = 4E_\alpha$. Because of the higher stopping power of heavier ions, the action of a foil of suitable thickness placed in front of the imaging system can be exploited to cut out the contribution of heavier ions from the trace, while allowing

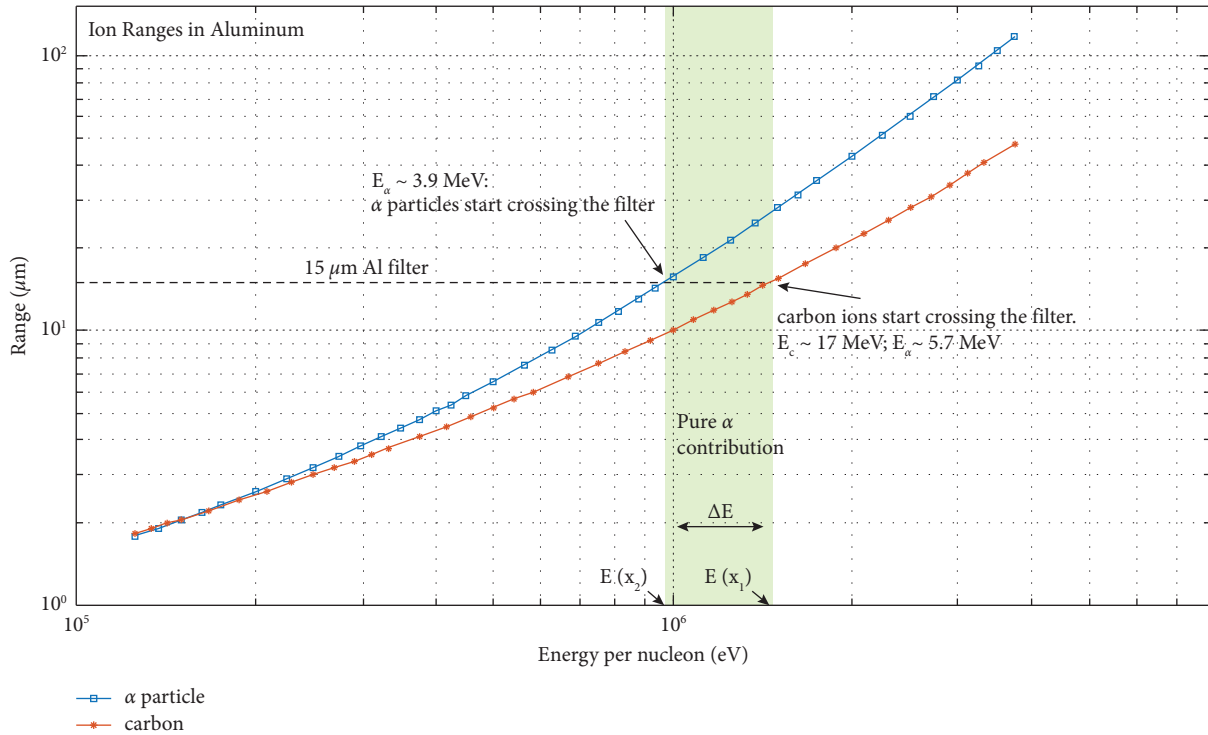


FIGURE 2: The ranges of carbon and alpha particles in aluminium are compared. The horizontal dotted line highlights the 15 μm range and the intercept with the alpha and carbon curves identifies the energy needed by the two types of ions to cross a filter of the mentioned thickness. Since the graph is plotted as a function of energy per nucleon, the ΔE where only alphas can cross the filter will correspond to a certain Δx on the parabola trace where only the alpha particles are contributing to the signal.

alphas to pass through it. Nevertheless, given the expected broad spectrum of the emitted alphas, the employment of a single filter is not suitable to recover a complete information since it would be too thin to cut the contribution coming from heavier ions having higher energies or too thick for the alphas of lower energy. For instance, according to simulations performed with the Montecarlo code SRIM [41], a 15 μm of aluminium foil allows to detect alphas free from any other ion contribution in the energy range (3.9–5.7) MeV. But for $E_\alpha < 3.9 \text{ MeV}$, the filter is too thick, and alphas are not able to cross it, whereas for $E_\alpha > 5.7 \text{ MeV}$, carbon ions of 17.1 MeV start to pass through the filter contributing to the trace generation, as highlighted in Figure 2 where the ranges of alphas and carbon ions are depicted as a function of energy per nucleon.

A similar issue has been discussed and addressed by Alejo et al. [36] for the univocal characterization of deuteron ions emitted during the irradiation of a deuterated plastic. The author suggests the possibility of employing a set of different filters along the energy dispersion axis, tailoring the material and the thickness of each to cut the contributions of all other ions but deuterons. A similar approach can be used for our purpose: for each energy interval, delimited by (x_1, x_2) coordinates, the chosen filter must cut the contribution coming from heavier ions while allowing alphas with energies within the range $(E_\alpha(x_2), E_\alpha(x_1))$ to reach the detector.

In Figures 3(a)–3(d), the ranges of alphas and carbons for different foil materials are reported as a function of the energy per nucleon. The data are obtained from the SRIM [41] tables.

Therefore, it is possible to determine the proper filter thickness to use in each energy region just by comparing the ranges of the ions.

Once the ideal filter material and thickness has been found, it is necessary to translate the energy interval into the corresponding spatial region where the filter has to be placed. This can be performed by exploiting equation (1), which allows to calculate the spatial range (along the horizontal direction x) that corresponds to a given energy range.

The discussed methodology is now applied taking as reference the Thomson spectrometer labelled as “BIG,” described in detail in Giorgio et al. [33]. The mentioned spectrometer was expressly designed to detect low-rate fusion reaction products. It is supplied with a double entrance pinhole drilled in lead with the smaller one having a 0.35 mm diameter. The spectrometer works with magnetic field $B \sim 4 \text{ kG}$ and electrostatic potential $V = 7 \text{ kV}$. The length of the electrodes and magnets is of 25 mm. The gap between the magnets is 5 mm and the drift space before reaching the imaging system (either an imaging plate or a CR-39) is 197 mm long.

The values reported in Table 1 have been retrieved according to the ion ranges provided by the SRIM tables and depicted in Figure 3 by applying equation (1). The value of A_B was evaluated from both measurements and numerical simulations of the magnetic field of our Thomson spectrometer. Except for α energies below 3 MeV, the set of aluminium filters of 10, 15, and 30 microns would allow to cover the whole alpha spectrum expected from $p+^{11}\text{B}$ reaction when triggered at the energy of the maximum cross

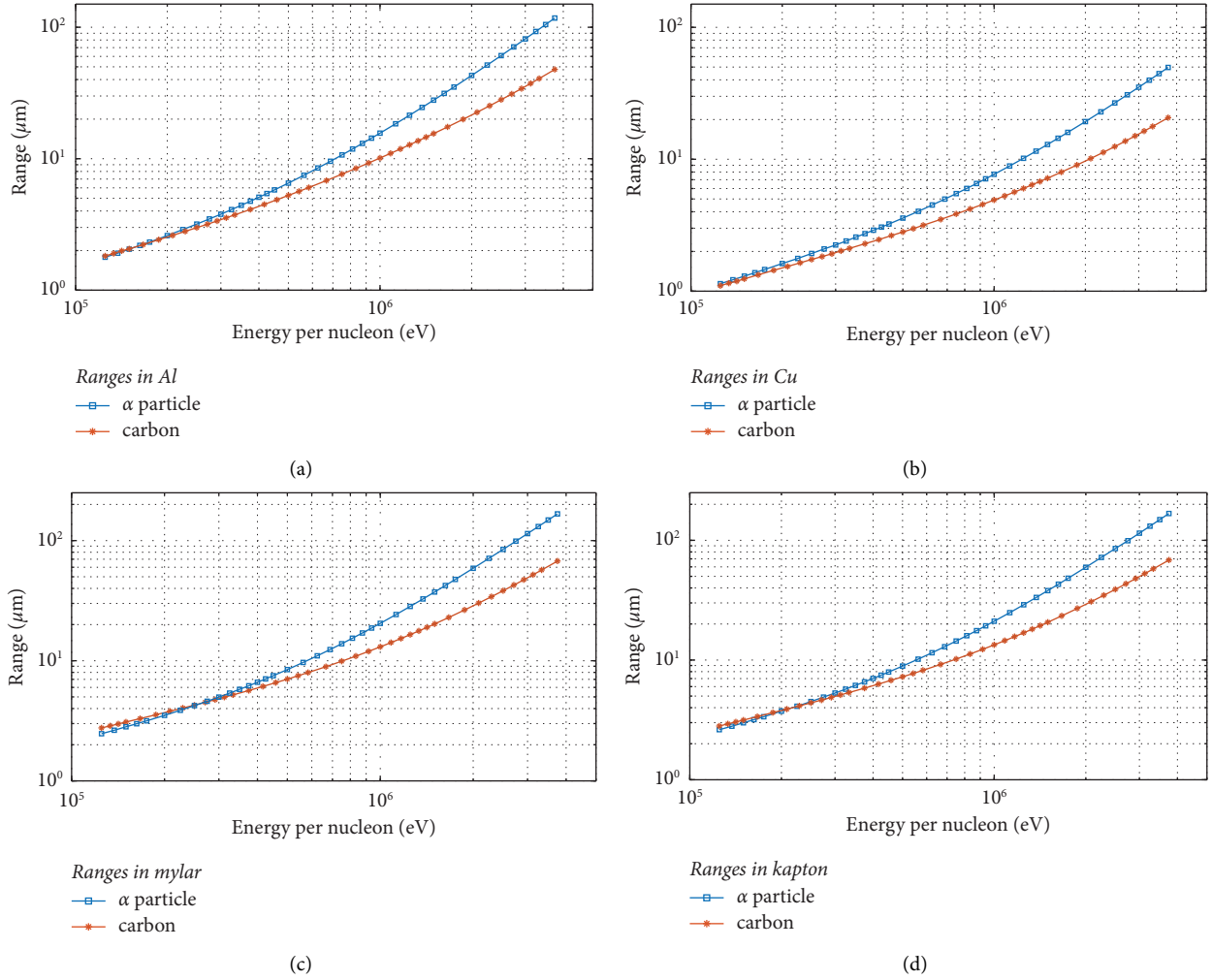


FIGURE 3: The ranges of carbon ions and alpha particles are depicted as a function of the energy per nucleon in different materials: (a) aluminium, (b) copper, (c) mylar, and (d) kapton.

TABLE 1: For each aluminium filter thickness, the energy range where only the contribution of alphas is visible, is reported together with the spatial extension on the parabola trace.

Filter material	Filter thickness (μm)	E_α (MeV)	x_1 (mm)	x_2 (mm)	$\Delta x = x_2 - x_1$ (mm)
Al	10	2.9–3.9	9.5	11.0	1.5
Al	15	3.9–5.76	7.8	9.5	1.7
Al	18	4.4–6.8	7.2	8.9	1.7
Al	20	4.75–7.4	6.9	8.6	1.7
Al	30	6.4–10.5	5.8	7.4	1.6

x_1 and x_2 are the coordinates on the detector plane corresponding to the maximum and minimum alpha energy able to cross the filter ($x = 0$ corresponds to the pinhole image position).

section, as reported in Kimura et al. [42], and also to investigate if alphas of slightly higher energies are detected.

From Table 1, the Δx values for the specific configuration of the TS in use appear to be rather small. To guarantee the stability and precision in mounting such thin stripes of few μm thick filters avoiding issues related to their disruption as well as to their jagged sides (originated by the cutting procedure), an ad hoc holding structure made of stainless steel was designed and it is here shown in Figure 4. The

physical dimension of the holder although, does not allow to use the set of the three mentioned filters, since the width of the structure will be covering a portion of the imaging system. The set of filters is thus reduced to two and we found convenient the employment of the $10\ \mu\text{m}$ and $30\ \mu\text{m}$ one. These will allow to investigate the energy region where the maximum alphas yield is expected and to explore what happens for energies higher than $6.4\ \text{MeV}$, beyond the current alpha energy cut-off.

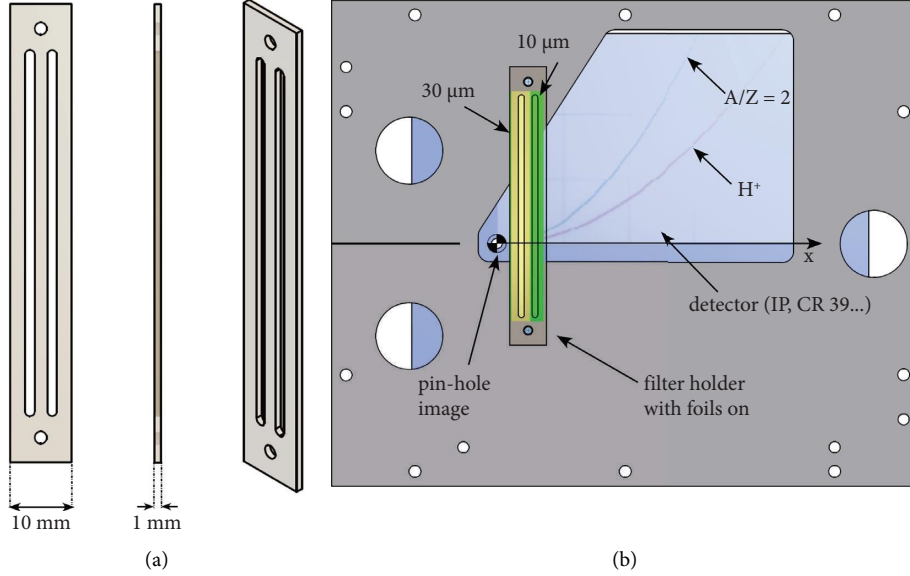


FIGURE 4: (a) The mounting of the filters with the two openings for the chosen filters. (b) The holder with the filters placed in front of the imaging system where it is possible to see a raw sketch of the expected parabolic traces.

2.1. Thomson Spectrometer Integrated with Time-Resolved Detector. As it is possible to see from the graphs in Figure 2, the differential filter method cannot be used for low energy particles. Indeed, for energies/nucleon lower than ~ 300 keV (i.e., $E_\alpha \sim 1.2$ MeV), the spatial extension of the energetic region free from ions contribution would either be too small or cannot be defined. For this energy region, we need to find some other method. We here investigate the possibility of integrating a time-of-flight (ToF) methodology in the Thomson spectrometer assembly. The general idea is to discriminate the different species according to their different time of arrival by placing a time-resolved detector after the region where the particles are subjected to the electric and magnetic field of the Thomson spectrometer. The detector will be placed along the trajectory of the particles having an $A/Z = 2$, so to exclude the contribution of protons and other ions to the signal generation. Since the ions contributing to each (x, y) point in this parabola trace have the same velocity, the simple TOF technique does not work for particle discrimination. Nevertheless, if a thin metal or plastic foil is placed in the particle path, the different species may undergo to a different energy attenuation and thus to a different variation of their velocities, according to the different stopping range of the various species for the used material. Then, if a time-resolved detector is placed at a proper distance, it would be possible to recognize the contribution of the various populations, as schematically shown in Figures 5(a) and 5(b). The method would be applied by punching one hole in the imaging system used for the parabolic traces detection, allowing for ions to pass through it and reach the time-resolved detector. This would allow to simultaneously obtain information on the alphas from the Thomson spectrometer (for higher energies) and the ToF methodology (for lower energies).

As discussed, in each position of the $A/Z = 2$ trace, only particles with a certain energy per nucleon will be detected. For a generic position in this trace, we now consider a simplified model of a δ -like Dirac distribution of the energies. In the basic scheme shown in Figure 5(b), particles with energy and velocity E_{in} and v_{in} , respectively, will pass through a foil filter and those with enough energy will emerge on the other side with E_{out} and v_{out} . In particular, it will be $E_{out} = k_i(E_{in}, f) E_{in}$ [43] with $k_i(E_{in}, f)$ the attenuation coefficient depending on the type of the incoming particle, its energy, and the filter characteristics (material and thickness, here labelled as f). This attenuation can be determined by SRIM [41] simulations. The time of detection t_i of each ion can be determined by knowing at which distance from the filter the time-resolved detector is placed (d_{TOF}), the type of filter used, and the energy of the incoming particle ($E_{in,i}$), as follows:

$$t_i = \frac{d_{TOF}}{v_{i,out}} = d_{TOF} \sqrt{\frac{m_i}{k_i(E_{in,i}, f) E_{in,i}}}, \quad (6)$$

where $v_{i,out}$ is the velocity of the ion after crossing the filter and m_i is the ion mass. The temporal interval between the detection of an alpha particle and a carbon ion can be written as follows:

$$\Delta t = t_c - t_\alpha = d_{TOF} \sqrt{\frac{m_p + m_n}{E_{in,\alpha}}} \left(\frac{\sqrt{k_\alpha(E_{in,\alpha})} - \sqrt{k_C(E_{in,C})}}{\sqrt{k_\alpha(E_{in,\alpha})} k_C(E_{in,C})} \right), \quad (7)$$

where m_p and m_n are the proton and neutron mass, respectively, and the relation $E_{C^{5+}} = 3E_\alpha$ was exploited. For a fixed energy, determined by the positioning of the ToF detector behind a certain (x, y) point of the imaging plane, and a given d_{TOF} , the delay would depend only on the

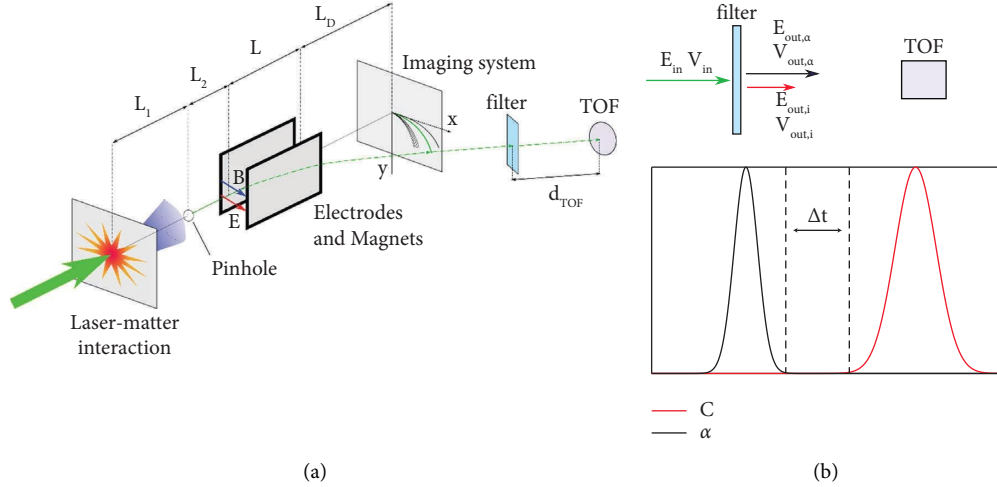


FIGURE 5: (a) Thomson spectrometer assembly integrated with the time-of-flight detector. (b) A simplified scheme of the working principle of the diagnostic.

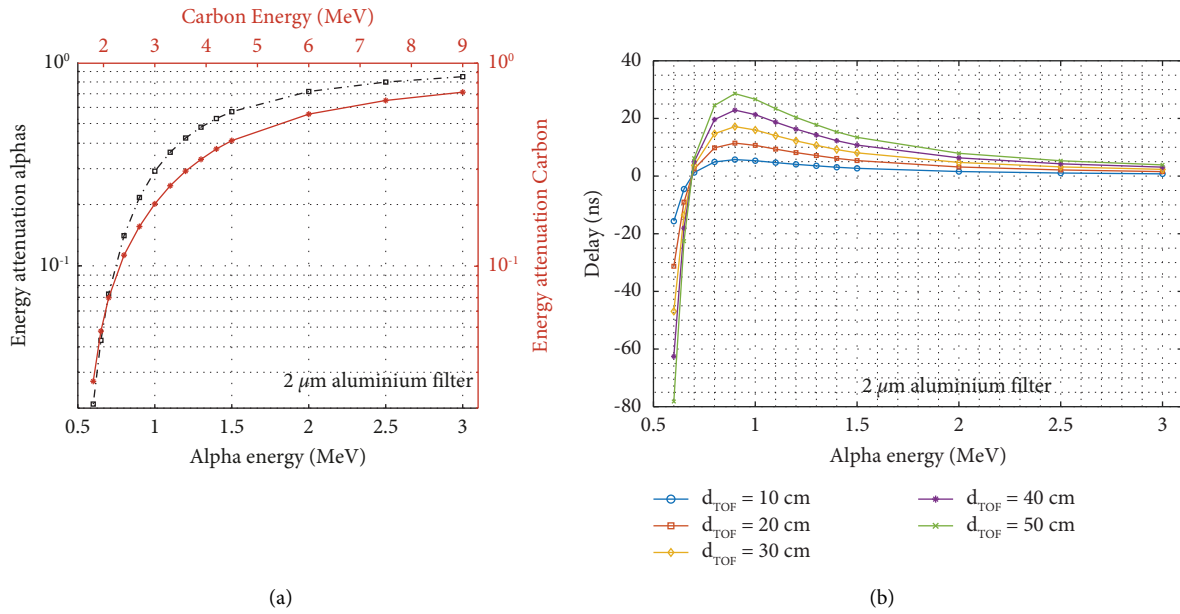


FIGURE 6: (a) The attenuation coefficients for alphas and carbon ions crossing 2 μm aluminium. (b) The delays $\Delta t = t_c - t_\alpha$ obtained for different length of the time-of-flight line applying equation (5).

material and thickness of the filter, represented by the attenuation coefficient $k_i(E_{in}, f)$ and can thus be used to discriminate the ion species by comparing the arrival times.

Equation (7) was applied to compute the delays, supposing to use a 2 μm aluminium foil as filter along the particle path. The attenuation coefficients for alphas and carbon ions, depicted in Figure 6(a), were computed by means of SRIM simulations [41] in the energy range of interest ($0.6 \text{ MeV} < E_{\text{alpha}} < 3 \text{ MeV}$). In Figure 6(b), the delays for different TOF line lengths are reported.

It is possible to see that two different regimes exist. For alphas energies lower than $\approx 0.7 \text{ MeV}$, the computed delays result to be lower than zero. Since, from equation (6), the temporal distance is defined as $\Delta t = t_c - t_\alpha$, this means that

$t_c < t_\alpha$, hence carbon ions would reach the detector before alphas. For higher energies, on the other hand, alphas arrive first on the detector and, for a TOF line length of 50 cm, delays up to several tens of nanoseconds are obtained, which are well in the range of efficient ToF detection by fast diamond detectors [44].

Nevertheless, some remarks are necessary. Even in case of an ideal δ -like distribution, the alignment of a diagnostic based on this scheme is not trivial since a displacement of a few millimetres of the ToF line can lead to the blinding of the diagnostic. Moreover, for many of the energies shown in Figure 6, the obtained delays are of a few nanoseconds. Therefore, a detector with high temporal resolution is needed. In the case of chemical-vapor-deposition diamond

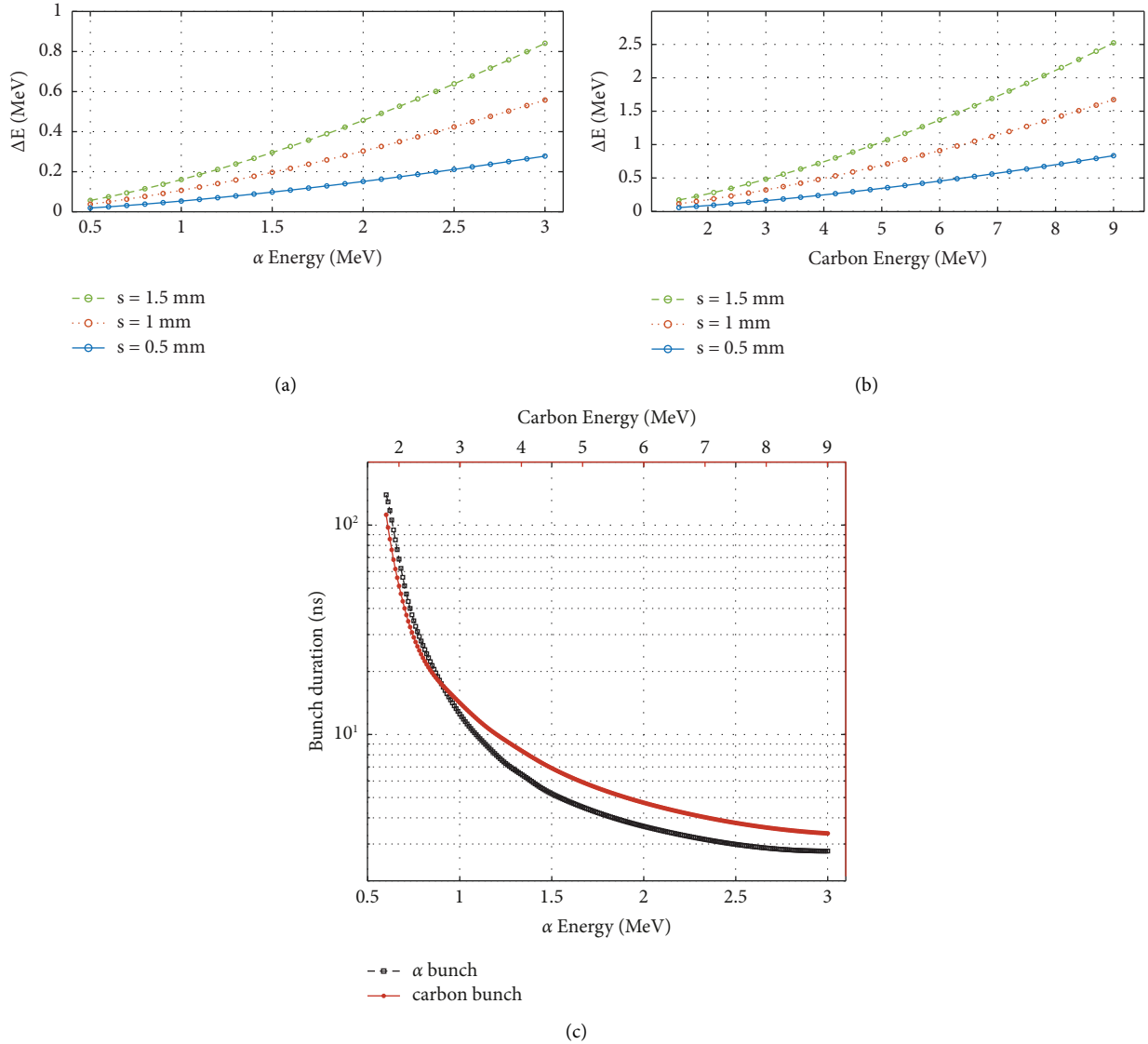


FIGURE 7: The ΔE computed for different size of the pinhole image according to equation (6) for (a) alpha particles and (b) carbon ions. (c) The bunch duration of alphas and carbon ions at the detector site for $s = 0.5$ mm and $d_{\text{TOF}} = 0.5$ m.

detectors, often used in time-of-flight measurements [43, 45], this is usually achieved by single crystal structures, having temporal resolution better than ~ 0.8 ns and high charge collection efficiency. On the other hand, this kind of structures can be grown up to a surface of a few square millimetres resulting in a small solid angle covered worsening the alignment issue.

Moreover, in a realistic scenario, the energy distribution for each detected ion species is not a δ -like distribution but will have a certain width. Hence, each point of the parabolic trace will correspond to an energy span and not to a single energy value. The amplitude of the energy span to consider in each point can be related to the size of the pinhole image on the detector plane [19, 40]. The latter defines the energy resolution of the spectrometers along the parabola trace, and this will correspond to the FWHM of the Gaussian distribution of the energies to be considered in our computations. As a result, instead of a single time of arrival for each species,

there will be a temporal window where α particles will be detected and a temporal window where carbon and other ions will arrive (see Figure 5(b)). To be still able to use the ToF technique to discriminate the various contributions, it is thus necessary for the fastest carbon ion to be slower than the slowest alpha particle. Alternatively, if this condition is not satisfied, it is possible to compute the time interval where the two populations overlap and define the portion of the alpha time window free from other ions, here in after labelled Δt^* .

Taking into account the energy distribution due to the finite pinhole extension, the requirements for the energy resolution become even more strict. Indeed, by applying equation (4) with the parameters of the considered Thomson spectrometer and assuming a pinhole image size ranging from 0.5 mm to 1.5 mm, the obtained ΔE for alphas and carbon ions is reported in Figures 7(a) and 7(b), respectively. Assuming a ToF line length of 0.5 m and a pinhole image size of 0.5 mm, the temporal duration of the α and carbon

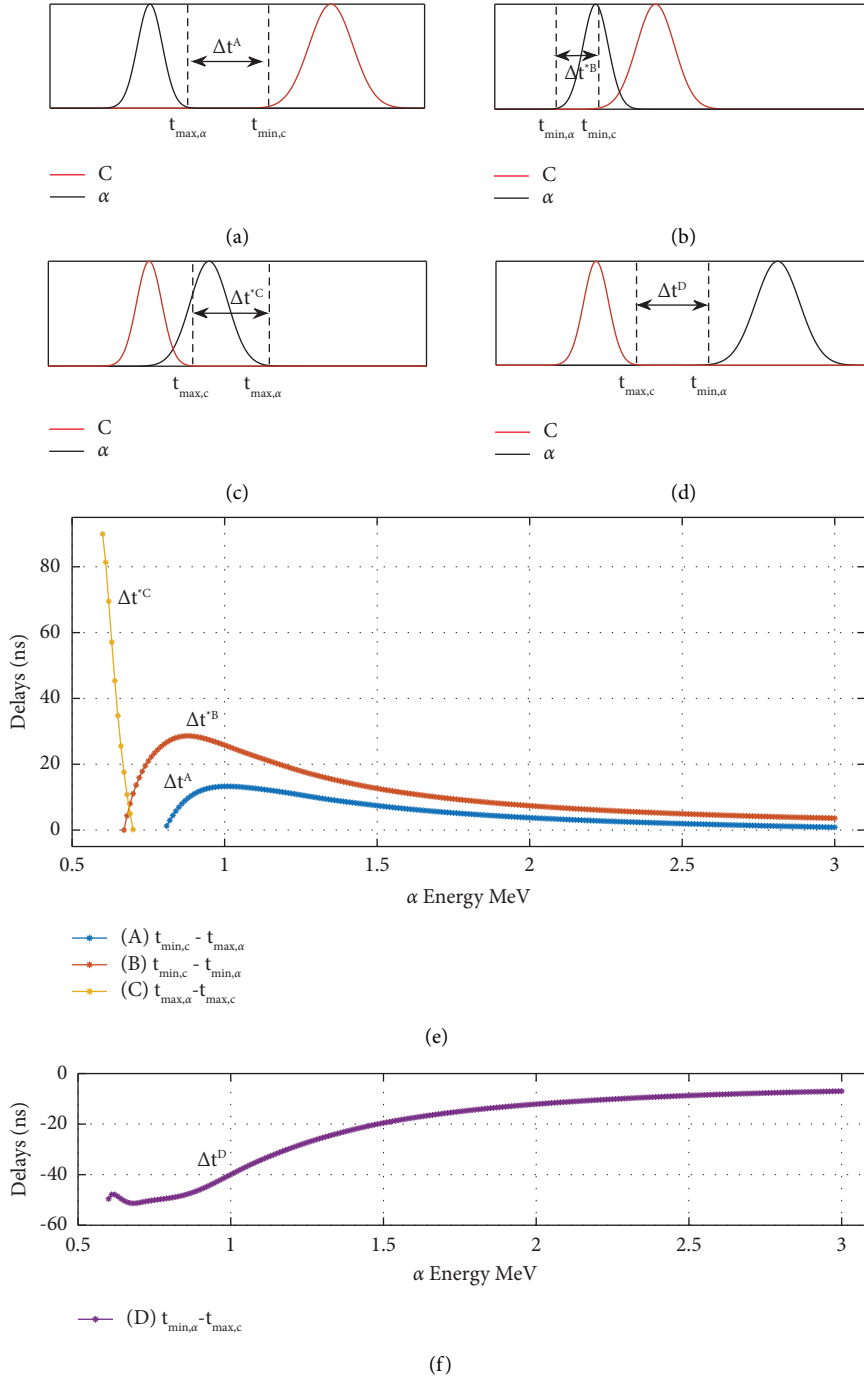


FIGURE 8: (a)–(d) Schematic representation of the possible reciprocal positions of carbon ions and alphas arriving on the ToF detector. The Δt highlights the temporal separation between the signal generated by the alphas and carbon ions, Δt^* points out the interval where the signal is generated by the contribution of alphas only when partial superimposition occurs. (e) The amplitude of Δt and Δt^* intervals for different energies and $d_{TOF} = 0.5$ m each curve corresponds to one of the situations depicted in (A)–(C). (f) The amplitude of Δt corresponding to case (D) and the negative amplitude points out that this particular situation never occurs for our conditions.

bunches has been also computed and is reported in Figure 7(c).

Taking these values as the width of the energy distribution to consider for each particle energy, it is possible to compute the temporal interval Δt where the signal generated by the alphas is free from the carbon ions contribution (see

Figures 8(a)–8(d)). We then chose the favourable case of a pinhole image of 0.5 mm size, and the resulting Δt and Δt^* are reported in Figures 8(e) and 8(f) for a TOF line of 50 cm length. Notice that in Figure 8(e), for each of the depicted cases, only positive values of Δt and Δt^* are considered because when the delay becomes negative, it means that the

examined energy falls into one of the other cases. This also clarifies Figure 8(f), where only negative delays are present, indeed the situation depicted in Figure 8(d) never occurs for the parameters examined here and, for each energy, the behaviour of the two bunches is described by one of the cases a–c.

It is possible to see that, even considering a broad energy distribution, an appreciable Δt can still be defined. In this case, it is useful to consider not only the whole separation of the traces but also their partial overlapping, defining Δt^* the temporal interval where only alphas are detected. By doing so, the methodology can still be applied. Nevertheless, for bigger pinhole sizes, the width of the energy distribution increases causing a decrement in Δt , issue that can be partially solved by extending the TOF line length.

In this scheme, it is also necessary to assess the effect of the filter on the particle motion. It is indeed well known that particles traversing a material undergo a modification of their trajectory. This effect is more severe for particles energies in a range comparable with the thickness of the material used as filter. In these conditions a broadening of the energy distribution is also experienced. The latter will, in turn, cause a broadening of the temporal interval interested by a certain energy during TOF measurements. Namely, alpha particles having energies ≈ 600 keV can be detected at a certain time $t_{\text{TOF}} \pm \Delta t_{\text{broad}}$. SRIM simulations were performed to quantitatively estimate this effect for the scheme considered here i.e., alphas with energies ≥ 600 keV up to 3 MeV impinging on $2 \mu\text{m}$ thick aluminium. The range covered by the energy distribution of the alphas entering in the filter with 600 keV is ≈ 25 keV, within the ΔE already considered due to the spectrometer energy resolution (see Figure 7(a)). The trajectories of the particles, though, are strongly affected by the presence of the filter and the beam outcoming from it is strongly divergent. Nevertheless, this effect rapidly decreases for increasing particle energies.

Another effect to consider is the one given by the electrostatic-magnetostatic deflector which also produces a clear increase on the tangential (both horizontal and vertical) components of the particle velocity, due to the effect of both magnetic and electric fields. This increases the beam radius and makes it dependent on the distance from the deflector. Therefore, the beam section on the detector plane will be much larger than that on the filter plane, according to the filter-detector distance. So, on one side, larger distances ease the separation of the particle bunches. On the other side, the requirement for large-area detectors increases, and on the other hand, large area detectors mean low temporal resolution. Therefore, for a specific alpha energy, an optimum value for the ToF line length has to be found.

A way to deal with this issue may be the employment of suitable electric-magnetic lenses, capable to correct the beam divergence given by the spectrometer, and to keep the detector diameter small also at large flight distances. However, this is of course at the expenses of the detector complexity.

3. Conclusions

The differential filter method seems to be a viable solution for the univocal detection of α -particles in low-rate fusion reactions. An optimal implementation of this methodology, able to give characterization of a wide portion of the broad alpha spectrum, requires the spectrometer to be designed trying to obtain a large spatial dispersion of incoming particles, so large fields, and large drift distances are needed. This would ease the optimal filter placement along the whole parabola trace, but gives problems in case compact spectrometers are needed, as required for high sensitivity devices useful for diagnostics of proton-11B fusion reactions [19]. The prototype presented in this article is planned to be used soon in tailored p-11B experimental campaigns.

The discussed methodology of differential filtering can be applied not only in the context of the proton-boron fusion reactions but also to monitor the alphas produced during the deuterium-deuterium fusion reaction and the deuterium-tritium one. In this case, the parabolic trace of the fully stripped alpha particles is not useful since the deuterium will also contribute to the signal on the very same $A/Z=2$ trace and, being more penetrant with respect to alpha particles, the differential filtering method is not capable of excluding its contribution. Nevertheless, if we consider the parabolic trace having $A/Z=4$, the deuterium will not contribute to the signal whereas the ${}^4\text{He}^+$ may be detected instead. On this trace, an approach similar to what discussed earlier can thus be applied for their characterization.

The methodology that foresees the integration of a time-resolved detector in the Thomson spectrometer could, in principle, provide very interesting results for the univocal discrimination of low energy alpha particles. Nevertheless, the technique presents some significant technical issues concerning the TP-TOF assembly alignment, and the need for high temporal resolution, high sensitivity, and large area detectors. All this points need to be faced and assessed for the technique to be successfully applied in a real-case scenario. The use of an electric-magnetic lens to correct the beam divergence can be very useful to highly improve the detector requirements, but at the expenses of the whole device complexity.

The methodologies here shown are of primary interest for the univocal identification of alpha products in experiments of laser-generated fusion reactions. Especially in cases of low yields, the simultaneous presence of a large number of laser-accelerated ions different from fusion products very often makes their actual characterization technically impossible by common diagnostic methodologies [19].

Data Availability

The data used in this study are available from the author upon reasonable request.

Disclosure

Views and opinions expressed are however those of the authors only and do not necessarily reflect those of the European Union or the European Commission. Neither the European Union nor the European Commission can be held responsible for them. The involved teams have operated within the framework of the Enabling Research Project: ENR-IFE.01.CEA “Advancing shock ignition for direct-drive inertial fusion.”

Conflicts of Interest

The authors declare that they have no conflicts of interest.

Acknowledgments

This work has been carried out within the framework of the EUROfusion Consortium, funded by the European Union via the Euratom Research and Training Programme (Grant Agreement no. 101052200—EUROfusion).

References

- [1] M. Oliphant and E. Rutherford, “Experiments on the transmutation of elements by protons,” *Proceedings of the Royal Society of London A*, vol. 141, p. 259, 1933.
- [2] V. S. Belyaev, A. P. Matafonov, V. I. Vinogradov et al., “Observation of neutronless fusion reactions in picosecond laser plasmas,” *Physical Review E - Statistical Physics, Plasmas, Fluids, and Related Interdisciplinary Topics*, vol. 72, Article ID 026406, 2005.
- [3] V. S. Belyaev, V. P. Krainov, A. P. Matafonov, and B. V. Zagreev, “The new possibility of the fusion $p + {}^{11}\text{B}$ chain reaction being induced by intense laser pulses,” *Laser Physics Letters*, vol. 12, no. 9, Article ID 096001, 2015.
- [4] HB11 Energy, *New Laser Hydrogen-Boron Fusion Energy*, HB11 Energy, Sydney, Australia, 2022.
- [5] Marvel Fusion, *Marvel Fusion -The Ultimate Clean Energy Solution*, Marvel Fusion, Bayern, Germany, 2022.
- [6] D. D. Clayton, *Principles of Stellar Evolution and Nucleosynthesis: With a New Preface*, University of Chicago Press, Chicago, IL, USA, 1983.
- [7] G. A. P. Cirrone, L. Manti, D. Margarone et al., “First experimental proof of Proton Boron Capture Therapy (PBCT) to enhance protontherapy effectiveness,” *Scientific Reports*, vol. 8, no. 1, p. 1141, 2018.
- [8] L. Giuffrida, D. Margarone, G. A. P. Cirrone, A. Picciotto, G. Cuttone, and G. Korn, “Prompt gamma ray diagnostics and enhanced hadron-therapy using neutron-free nuclear reactions,” *AIP Advances*, vol. 6, no. 10, Article ID 105204, 2016.
- [9] D. Margarone, J. Bonvalet, L. Giuffrida et al., “In-target proton–boron nuclear fusion using a PW-class laser,” *Applied Sciences*, vol. 12, no. 3, p. 1444, 2022.
- [10] A. Picciotto, D. Margarone, A. Velyhan et al., “Boron-proton nuclear-fusion enhancement induced in boron-doped silicon targets by low-contrast pulsed laser,” *Physical Review X*, vol. 4, no. 3, Article ID 031030, 2014.
- [11] L. Giuffrida, F. Belloni, D. Margarone et al., “High-current stream of energetic α particles from laser-driven proton-boron fusion,” *Physical Review E - Statistical Physics, Plasmas, Fluids, and Related Interdisciplinary Topics*, vol. 101, no. 1, Article ID 013204, 2020.
- [12] D. Margarone, A. Picciotto, A. Velyhan et al., “Advanced scheme for high-yield laser driven nuclear reactions,” *Plasma Physics and Controlled Fusion*, vol. 57, no. 1, Article ID 014030, 2015.
- [13] A. Bonasera, A. Caruso, C. Strangio et al. “Measuring the astrophysical S-factor in plasmas,” in *Fission and Properties of Neutron-Rich Nuclei*, World Scientific, Sanibel Island, SI, USA, 2008.
- [14] C. Labaune, C. Baccou, S. Depierreux et al., “Fusion reactions initiated by laser-accelerated particle beams in a laser-produced plasma,” *Nature Communications*, vol. 4, no. 1, p. 2506, 2013.
- [15] D. Margarone, A. Morace, J. Bonvalet et al., “Generation of α -particle beams with a multi-kJ, peta-watt class laser system,” *Frontiers in Physics*, vol. 8, p. 343, 2020.
- [16] C. Baccou, S. Depierreux, V. Yahia et al., “New scheme to produce aneutronic fusion reactions by laser-accelerated ions,” *Laser and Particle Beams*, vol. 33, no. 1, pp. 117–122, 2015.
- [17] D. Giulietti, P. Andreoli, D. Batani et al., “Laser-plasma energetic particle production for aneutronic nuclear fusion experiments,” *Nuclear Instruments and Methods in Physics Research Section B: Beam Interactions with Materials and Atoms*, vol. 402, pp. 373–375, 2017.
- [18] F. Ingenito, P. Andreoli, D. Batani et al., “Directional track selection technique in cr39 ssntd for lowyield reaction experiments,” in *EPJ Web Of Conferences*, L. Torrisi and M. Cutroneo, Eds., vol. 167, Article ID 05006, 2018.
- [19] F. Consoli, R. De Angelis, P. Andreoli et al., “Diagnostic methodologies of laser-initiated $11\text{B}(p,\alpha)2\alpha$ fusion reactions,” *Frontiers in Physics*, vol. 8, Article ID 561492, 2020.
- [20] H. Daido, M. Nishiuchi, and A. S. Pirozhkov, “Review of laser-driven ion sources and their applications,” *Reports on Progress in Physics*, vol. 75, no. 5, Article ID 056401, 2012.
- [21] F. Consoli, V. T. Tikhonchuk, M. Bardon et al., “Laser produced electromagnetic pulses: generation, detection and mitigation,” *High Pow Laser Sci Eng*, vol. 8, p. e22, 2020.
- [22] K. Nelissen, M. Liszi, M. D. Marco et al., “Characterisation and modelling of ultrashort laser-driven electromagnetic pulses,” *Scientific Reports*, vol. 10, no. 1, p. 3108, 2020.
- [23] M. De Marco, L. Volpe, G. Gatti et al., “Propagation of laser-driven electromagnetic pulses in laser target areas,” in *Proceedings of the 2019 International Symposium on Electromagnetic Compatibility - EMC EUROPE, IEEE, Barcelona, Spain, June 2019*.
- [24] A. Szydłowski, J. Badziak, J. Fuchs et al., “Application of solid-state nuclear track detectors of the CR-39/PM-355 type for measurements of energetic protons emitted from plasma produced by an ultra-intense laser,” *Radiation Measurements*, vol. 44, no. 9-10, pp. 881–884, 2009.
- [25] C. Baccou, V. Yahia, S. Depierreux et al., “CR-39 track detector calibration for H, He, and C ions from 0.1–0.5 MeV up to 5 MeV for laser-induced nuclear fusion product identification,” *Review of Scientific Instruments*, vol. 86, no. 8, Article ID 083307, 2015.
- [26] A. E. Cameron and D. F. Eggers, “An ion Velocitron,” *Review of Scientific Instruments*, vol. 19, no. 9, pp. 605–607, 1948.
- [27] J. Thomson, “Rays of positive electricity,” *Proceedings of the Royal Society of London A*, vol. 89, p. 1, 1913.
- [28] F. H. Séguin, J. A. Frenje, C. K. Li et al., “Spectrometry of charged particles from inertial-confinement-fusion plasmas,” *Review of Scientific Instruments*, vol. 74, no. 2, pp. 975–995, 2003.

- [29] A. P. Fews and D. L. Henshaw, "High resolution alpha particle spectroscopy using CR-39 plastic track detector," *Nuclear Instruments and Methods in Physics Research*, vol. 197, no. 2-3, pp. 517–529, 1982.
- [30] C. G. Freeman, G. Fiksel, C. Stoeckl et al., "Calibration of a Thomson parabola ion spectrometer and Fujifilm imaging plate detectors for protons, deuterons, and alpha particles," *Review of Scientific Instruments*, vol. 7, 2014.
- [31] J. Miyahara, "Imaging Plate," in *Computed Radiography*, Y. Tateno, T. Iinuma, and M. Takano, Eds., Springer, Berlin, Germany, 1987.
- [32] K. Harres, M. Schollmeier, E. Brambrink et al., "Development and calibration of a Thomson parabola with microchannel plate for the detection of laser-accelerated MeV ions," *Review of Scientific Instruments*, vol. 79, no. 9, Article ID 093306, 2008.
- [33] G. D. Giorgio, F. Consoli, R. D. Angelis et al., "Development of advanced Thomson spectrometers for nuclear fusion experiments initiated by laser," *Journal of the Instrumentation*, vol. 15, no. 10, Article ID C10013, 2020.
- [34] M. Scisciò, F. Consoli, M. Salvadori et al., "High sensitivity Thomson spectrometry: analysis of measurements in high power picosecond laser experiments," *Journal of the Instrumentation*, vol. 17, no. 01, Article ID C01055, 2022.
- [35] J. Bonvalet, P. Nicolai, D. Raffestin et al., "Energetic α -particle sources produced through proton-boron reactions by high-energy high-intensity laser beams," *Physical Review E - Statistical Physics, Plasmas, Fluids, and Related Interdisciplinary Topics*, vol. 103, no. 5, Article ID 053202, 2021.
- [36] A. Alejo, S. Kar, H. Ahmed et al., "Characterisation of deuterium spectra from laser driven multi-species sources by employing differentially filtered image plate detectors in Thomson spectrometers," *Review of Scientific Instruments*, vol. 85, no. 9, Article ID 093303, 2014.
- [37] F. Consoli, R. D. Angelis, A. Bonasera et al., "Study on a compact and adaptable thomson spectrometer for laser-initiated $^{11}\text{B}(p, \alpha)^8\text{Be}$ reactions and low-medium energy particle detection," *Journal of the Instrumentation*, vol. 11, no. 05, Article ID C05010, 2016.
- [38] J.-E. Ducret, D. Batani, G. Boutoux et al., "Calibration of the low-energy channel Thomson parabola of the LMJ-PETAL diagnostic SEPAGE with protons and carbon ions," *Review of Scientific Instruments*, vol. 89, no. 2, Article ID 023304, 2018.
- [39] R. F. Schneider, C. M. Luo, and M. J. Rhee, "Resolution of the Thomson spectrometer," *Journal of Applied Physics*, vol. 57, pp. 1–5, 1985.
- [40] D. Jung, R. Hörlein, D. Kiefer et al., "Development of a high resolution and high dispersion Thomson parabola," *Review of Scientific Instruments*, vol. 82, no. 1, Article ID 013306, 2011.
- [41] J. F. Ziegler, M. D. Ziegler, and J. P. Biersack, "Srim – the stopping and range of ions in matter," *Nuclear Instruments and Methods in Physics Research Section B: Beam Interactions with Materials and Atoms*, vol. 268, no. 11-12, pp. 1818–1823, 2010.
- [42] S. Kimura, A. Anzalone, and A. Bonasera, "Comment on "observation of neutronless fusion reactions in picosecond laser plasmas,"" *Physical Review E - Statistical Physics, Plasmas, Fluids, and Related Interdisciplinary Topics*, vol. 79, no. 3, Article ID 038401, 2009.
- [43] M. Salvadori, F. Consoli, C. Verona et al., "Accurate spectra for high energy ions by advanced time-of-flight diamond-detector schemes in experiments with high energy and intensity lasers," *Scientific Reports*, vol. 11, no. 1, p. 3071, 2021.
- [44] R. S. Sussmann, *CVD Diamond for Electronic Devices and Sensors*, J. Wiley, Chichester, UK, 2009.
- [45] V. Scuderi, G. Milluzzo, D. Doria et al., "TOF diagnosis of laser accelerated, high-energy protons," *Nuclear Instruments and Methods in Physics Research Section A: Accelerators, Spectrometers, Detectors and Associated Equipment*, vol. 978, Article ID 164364, 2020.



Research Article

Photon and Neutron Production as In Situ Diagnostics of Proton-Boron Fusion

B. M. Hegelich,¹ L. Labun¹,¹ O. Z. Labun¹,¹ and T. A. Mehlhorn^{2,3}

¹Department of Physics, The University of Texas, Austin 78712, USA

²Mehlhorn Engineering Consulting Services, Beaverton, OR, USA

³HB11 Energy Holdings Pty, 11 Wyndora Ave, Freshwater, NSW 2096, Australia

Correspondence should be addressed to L. Labun; labun@utexas.edu

Received 26 July 2022; Revised 17 November 2022; Accepted 4 April 2023; Published 8 May 2023

Academic Editor: Dimitri Batani

Copyright © 2023 B. M. Hegelich et al. This is an open access article distributed under the Creative Commons Attribution License, which permits unrestricted use, distribution, and reproduction in any medium, provided the original work is properly cited.

Short-pulse, ultrahigh-intensity lasers have opened new regimes for studying fusion plasmas and creating novel ultrashort ion beams and neutron sources. Diagnosing the plasma in these experiments is important for optimizing the fusion yield but difficult due to the picosecond time scales, 10 s of micron-cubed volumes, and high densities. We propose to use the yields of photons and neutrons produced by parallel reactions involving the same reactants to diagnose the plasma conditions and predict the yields of specific reactions of interest. In this work, we focus on verifying the yield of the high-interest aneutronic proton-boron fusion reaction $^{11}\text{B}(p, 2\alpha)^4\text{He}$, which is difficult to measure directly due to the short stopping range of the produced α s in most materials. We identify promising photon-producing reactions for this purpose and compute the ratios of the photon yield to the α yield as a function of plasma parameters. In beam-fusion experiments, the ^{11}C yield is an easily-measurable observable to verify the α yield. In light of our results, improving and extending measurements of the cross-sections for these parallel reactions are important steps to gain greater control over these laser-driven fusion plasmas.

1. Introduction

Short-pulse lasers offer new experimental approaches to create and study fusion plasmas. In contrast to long-pulse lasers which have been a primary tool in inertial-confinement fusion (ICF), short-pulse lasers have pulse durations < 1 ps and use small focal spots to obtain peak intensities up to 10^{23} W/cm² in a single pulse. Short-pulse lasers deliver their energy to the plasma in a time much shorter than the typical expansion timescale, and both electrons and ions achieve much higher momenta. These plasma conditions are far from the quasi-thermal equilibrium of ICF, where burn has recently been achieved [1], and the question is open whether or not the dynamics admit a pathway to net energy gain [2]. Short-pulse lasers have successfully driven high-yield beam-fusion experiments [3, 4], which can in turn be translated into novel high-flux, ultrashort-pulse ions [5–7], and neutron sources [8–11].

Short-pulse lasers can drive fusion in two ways: direct irradiation of a target containing the fusion reactants or laser-ion acceleration creating an ion beam that is dumped into a catcher/target. To our knowledge, no experiment can claim to have optimized the fusion yield, and the efficiencies of these two methods for different candidate fusion reactions remain a topic of research. Naively, one expects direct irradiation to convert laser energy more efficiently into fusion yield, in part because fusion can occur both in the neighbourhood of the focus where all ion species are heated and in the colder bulk of the target by ions accelerated out of the focal region. Anecdotally, recent experiments support this hypothesis [2].

Proper optimization will require greatly improved understanding and control of experimental outcomes compared to current capabilities. However, the same laser properties, namely, ultrashort-pulse and typically small $\sim (10\mu\text{m})^3$ focal volume make the plasma difficult to diagnose. Most interpretation is based on inference from the

measured particle yields and spectra, sometimes supported by Monte Carlo or numerically-expensive kinetic laser-plasma simulations. Improving experimental diagnostics of laser-driven nuclear reactions has, thus, become a significant topic of discussion [12]. Our goal in this work is to identify new diagnostics providing information on the plasma conditions and nuclear reaction dynamics.

Out of the reactions studied with short-pulse lasers, we focus on the proton-boron-11 fusion reaction $^{11}\text{B}(p, 2\alpha)^4\text{He}$, which is of particular interest because it releases ≈ 8 MeV into kinetic energy of the 3 α particles and no neutrons. The α particles themselves provide the most direct measure of the fusion yield, but because they deposit their kinetic energy into the surrounding medium very efficiently, only a small fraction of those produced escape the target. This problem is especially acute in direct-irradiation experiments [5, 13–18], where the mean kinetic energy and density of the medium vary by orders of magnitude in different regions of the target, precluding a systematic analytic correction for α stopping.

Since direct diagnostics of plasma conditions, such as probe laser pulses or atomic spectroscopy, remains an enormous technical challenge, we investigate other nuclear reactions for products whose yield or spectrum can be measured more reliably. Photons and neutrons are the best candidates, but not all reactions will yield enough photons or neutrons that can be identified as coming from a specific reaction. We introduce the yield ratio as a phenomenological tool to relate an easily-measured yield to the yield of interest. Yield ratios have an established history in diagnosing the ICF plasma, where they can determine several of the important ρR parameters [19]. We have previously used the ratio between α and ^{11}C yields to determine the $^{11}\text{B}(p, 2\alpha)^4\text{He}$ reaction yield more accurately in beam-target experiments [20], and here, we demonstrate its utility in direct-irradiation experiments as well. The yield ratio eliminates normalization unknowns such as the local density of reactants, effective reaction volume, and time and takes as input a few model parameters, such as the mean ion kinetic energy, that can be determined from particle diagnostics. We conclude by identifying the two best candidate reactions for proxy measurements of the $^{11}\text{B}(p, 2\alpha)^4\text{He}$ yield in direct-irradiation experiments and confirm ^{11}C as the best proxy in beam-target experiments.

2. Accessible Reactions

The goal is to predict the outcomes and analyse the data from experiments on the aneutronic proton-boron fusion reaction $^{11}\text{B}(p, 2\alpha)\alpha$. The $^{11}\text{B}(p, 2\alpha)$ cross-section reaches ~ 1 b around 650 keV center-of-mass (CM) energy, significantly higher than DD or DT fusion reactions because of the higher charge of boron. In fact, most other proton-boron reactions require even higher CM energy before the cross-section approaches 100 mb, and the high cross-section of $^{11}\text{B}(p, 2\alpha)\alpha$ in the $E < 1$ MeV range is due to two identified resonances, related to above-threshold excited states of ^{12}C [21]. Recent work has resolved apparent normalization discrepancies in the measured

cross-section [22], resulting in reevaluation of the process as a candidate for fusion energy.

With its cross-section reaching ~ 1 b already at 650 keV CM energy, lower than the thresholds of many other proton-initiated reactions on boron, $^{11}\text{B}(p, 2\alpha)\alpha$ is expected to have the highest yield in the laser-driven beam-fusion experiments. With higher laser intensities $I \geq 10^{20}$ W/cm² though, the proton beam in the experiment can provide energies upto ~ 50 MeV [20], allowing many additional reactions that are naturally grouped as “primary” or “secondary.” Primary reactions are initiated by the protons scattering on ^{11}B , ^{10}B , or ^{14}N as present in typical boron or boron-nitride solid targets. These are listed in Table 1 with peak cross-section, the corresponding CM energy at which the peak cross-section is found, and the range of CM energy over which data is available. Secondary reactions are rescattering of the α particles on the boron and nitrogen nuclei most prevalent in the environment. These are listed in Table 2, similarly to the primary reactions. The databases contain additional processes, such as $^{14}\text{N}(p, n + p)^{13}\text{N}$ and $^{14}\text{N}(p, n + ^3\text{He})^{11}\text{C}$, but the data are too sparse, and the larger number of fragments generally makes the Q values for such reactions negative and large in magnitude. Consequently, their cross-sections should have somewhat higher thresholds suppressing their contributions to the yields.

The corresponding cross-sections are plotted in Figure 1. The global sets from EXFOR [24] frequently include inconsistent measurements, as, for example, the recently resolved normalization in the $^{11}\text{B}(p, 2\alpha)^4\text{He}$ cross-section [22]. Cross-section data are one significant source of uncertainty in our yield predictions. We have plotted the global data sets for each cross-section without distinguishing their sources and in our calculations, and we will use fits to these global data with a few exceptions described in the captions of Tables 1 and 2. We do not attempt to model the cross-sections outside the range of available data. Instead, for numerical integrations, we implement best fit curves that are forced rapidly to zero outside the range of experimental data. This choice almost certainly underestimates the yield for several processes. Notably, the cross-sections of $^{11}\text{B}(p, \alpha)^8\text{Be}$, $^{10}\text{B}(p, \gamma)^{11}\text{C}$, and all secondary reactions for which data are available and seem likely to continue to increase with CM energy. However, the lack of information precludes quantifying the uncertainty in any attempted modeling of the cross-section.

Among these primary and secondary reactions, we identify promising candidates to be diagnostics. As mentioned above, the difficulty in verifying the $^{11}\text{B}(p, 2\alpha)^4\text{He}$ yield is greater in direct-irradiation type of experiments. For these, we need a reaction occurring in parallel with a product that escapes the plasma unperturbed, such as neutrons and photons.

To strengthen the identification of the originating reaction, a neutron or photon produced with definite energy is preferable. Exothermic reactions ($Q > 0$) are, therefore, better candidates, since we can expect the neutron or photon spectrum to peak at nonzero kinetic energy. Of the primary reactions Table 1, only two satisfy these conditions, $^{11}\text{B}(p, \gamma)^{12}\text{C}$ and $^{10}\text{B}(p, \gamma)^{11}\text{C}$, both emitting photons. The

TABLE 1: Primary reactions in the range of proton energies. The range of CoM energy for which data are available as well as the maximum cross-section and its CoM energy are given for numerical comparison. All data retried from sources in the EXFOR and JANIS databases, with the exception of $^{11}\text{B}(p, 2\alpha)^4\text{He}$ for which we use the concordant normalization of Reference [22].

Reaction	Q (MeV)	σ_{max} (b)	$E_{\text{cm}}^{(\text{max}\sigma)}$ (MeV)	Data range (MeV)
$^{11}\text{B}(p, 2\alpha)^4\text{He}$	8.59, 5.65, 8.68	0.8	0.6	$0.03 < E_{\text{cm}} < 19$
$^{11}\text{B}(p, \alpha)^8\text{Be}$	8.1*	0.01	1.0	$0.03 < E_{\text{cm}} < 1$
$^{11}\text{B}(p, n)^{11}\text{C}$	-2.765	0.4	7	$2.5 < E_{\text{cm}} < 15$
$^{11}\text{B}(p, \gamma)^{12}\text{C}$	15.9	3×10^{-6}	14	$7 < E_{\text{cm}} < 25$
$^{10}\text{B}(p, \alpha)^7\text{Be}$	1.147	0.5	5.0	$0.07 < E_{\text{cm}} < 11.15$
$^{10}\text{B}(p, n)^{10}\text{C}$	-4.94*	0.004 ^a	8	$4 < E_{\text{cm}} < 16$
$^{10}\text{B}(p, \gamma)^{11}\text{C}$	8.69	0.0003	6	$1.8 < E_{\text{cm}} < 6$
$^{14}\text{N}(p, \alpha)^{11}\text{C}$	-2.92	0.29	7	$3.78 < E_{\text{cm}} < 22$
$^{14}\text{N}(p, n)^{14}\text{O}$	-6.44*	0.01 ^b	9.5	$6.3 < E_{\text{cm}} < 30$

Q values marked with an * are computed from the mass difference of the initial and final states. Others are from the literature. ^a A recent measurement [23] finds $\sim 5\times$ larger cross-section than several previous measurements. To be conservative, we quote the older but more consistent results here. ^b There appear two distinct groups of cross-sections measurements; two experiments find the cross-section roughly $10\times$ larger than the majority of others.

TABLE 2: Secondary reactions in the range of α particle energies. The range of CoM energy for which data are available as well as the maximum cross-section and its CoM energy are given for numerical comparison.

Reaction	Q (MeV)	σ_{\max} (b)	$E_{cm}^{(\max \sigma)}$ (MeV)	Data available
$^{11}\text{B}(\alpha, p)^{14}\text{C}$	1.3*	0.04	3.6	$0.6 < E_{cm} < 36$ MeV
$^{11}\text{B}(\alpha, n)^{14}\text{N}$	0.16*	4×10^{-4}	1.5	$0.4 < E_{cm} < 1.76$ MeV
$^{10}\text{B}(\alpha, p)^{13}\text{C}$	3.85	—	—	No data
$^{10}\text{B}(\alpha, n)^{13}\text{N}$	1,3.51	0.1	4.6	$2.55 < E_{cm} < 4.7$ MeV
$^{14}\text{N}(\alpha, n)^{17}\text{F}$	-4.74*	0.12	9.2	$6.3 < E_{cm} < 20$ MeV
$^{14}\text{N}(\alpha, \gamma)^{18}\text{F}$	4.42	—	—	No data

Q values marked with an * are computed from the mass difference of the initial and final states. Others are from the literature.

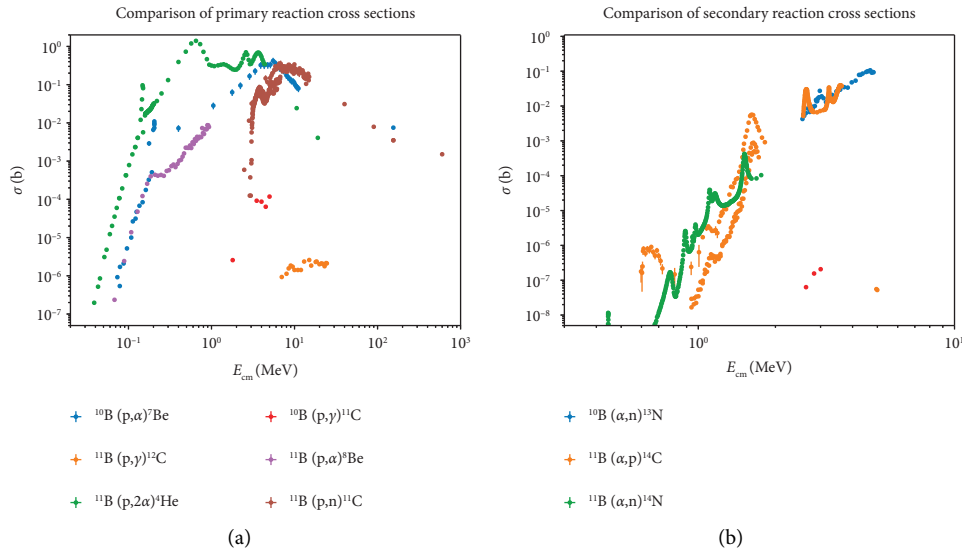


FIGURE 1: Cross-sections of primary reactions (a) and secondary reactions (b) Data from EXFOR with all sources combined. The scales are logarithmic, and the extent of the energy range is different on each.

cross-section data for both reactions are very limited. For the $^{10}\text{B}(p, \gamma)^{11}\text{C}$ reaction especially, the trend in the available data suggests our calculations here may significantly underestimate the photon yield. Of the secondary reactions, three satisfy these conditions, $^{11}\text{B}(\alpha, n)^{14}\text{N}$, $^{10}\text{B}(\alpha, n)^{13}\text{N}$, and $^{14}\text{N}(\alpha, \gamma)^{18}\text{F}$.

As several of the candidate reactions have limited cross-section data available and even more limited data on the spectrum of the outgoing neutron or photon, it would be a reasonable first step to verify yields with beam-target type of experiments. Since the target remains intact, we can measure a wider variety of reaction products, in particular unstable nuclides with half-lives much greater than the experiment duration. Several of the reactions selected by the previous approach also yield unstable nuclei, specifically ^{11}C , ^{13}N , and ^{18}F with half-lives on the order of 10^3 s. Other unstable nuclides produced are listed in Table 3. The significantly differing half-lives make identification by reactivity straightforward with a Geiger counter placed near the target, though ^{14}C probably has too long a half-life and ^{10}C too has short a half-life for reliable identification. ^7Be is undetectable by this means but arises from a reaction without particular interest in this study.

TABLE 3: Half-lives and decay modes of unstable nuclei produced by reactions in Tables 1 and 2.

Nuclide	Half-life (s)	Decay mode
^7Be	4.60×10^6	ϵ
^{10}C	19.3	β^+
^{11}C	1.22×10^3	β^+
^{13}N	598	β^+
^{14}C	1.81×10^{11}	β^-
^{14}O	70.6	β^+
^{17}F	64.5	β^+
^{18}F	6.59×10^3	β^+

Now, synthesizing and narrowing the list of promising reactions, two of the photon- and neutron-producing reactions stand out in utility. First, $^{11}\text{B}(p, \gamma)^{12}\text{C}$ is promising to directly correlate with the reaction $^{11}\text{B}(p, 2\alpha)^4\text{He}$, because it has the same initial state and produces a photon with energy significantly above most other products. The $\sim 100\times$ larger cross-section for $^{10}\text{B}(p, \gamma)^{11}\text{C}$ makes it a practical proxy in the near term, though it has a different initial state, which introduces additional uncertainty. Ultimately, the yields of these two reactions will determine which is more useful in the experiment.

The second $^{10}\text{B}(\alpha, n)^{13}\text{N}$ could help verify the α yield. Since this reaction is the isospin partner of $^{10}\text{B}(\alpha, p)^{13}\text{C}$, the cross-sections are very similar in magnitude and energy dependence, and its measurement would verify the role of proton-recycling from secondary reactions and propose as an important mechanism in enhancing $^{11}\text{B}(p, 2\alpha)^4\text{He}$ yields in some experiments [25]. Moreover, ^{13}N is unstable, and its yield can be measured independently in beam-target experiments. A small drawback to this reaction is that the cross-section decreases sharply below CM energy of 3 MeV. The majority of α s produced by $^{11}\text{B}(p, 2\alpha)^4\text{He}$ should have energy above this threshold, but α s also lose energy quickly in a cold medium, and the yield is expected to be small.

Of the remaining two, (a) there is unfortunately no cross-section data for $^{14}\text{N}(\alpha, \gamma)^{18}\text{F}$, though it should produce a peak in the photon spectrum, and (b) the neutron produced in $^{11}\text{B}(\alpha, n)^{14}\text{N}$ is likely have very little kinetic energy, making detection difficult.

Of the radioactive nuclides, ^{11}C has already proven its utility in beam-target experiments providing a significantly higher-confidence estimate of the α yield than a direct measurement of the α s by CR-39 [20]. ^{18}F has been detected [20, 25] but the absence of a cross-section for its production limits the information gained. More surprisingly, ^{13}N has not been detected, probably due to a combination of shorter half-life and low yield making it difficult to distinguish from the ^{11}C signal. Since better data exist for the ^{13}N production cross-section and it is generated almost entirely by α scattering, we consider it the most important candidate for future experiments as a means to help verify the α yield. ^{14}O and ^{17}F are of little interest in both production processes, $Q < 0$ so the neutron released is not a potential diagnostic in direct-irradiation experiments.

3. Yield Equations

Having winnowed the set of interesting reactions based on general criteria for good diagnostics of the fusion dynamics, we now evaluate the yields of the various products.

The challenge in deriving analytic expressions for the yield expression is two-fold. First, the ion momentum distribution function generally varies from shot to shot due to variations in the laser. Therefore, the ion distribution should be measured on each shot as well as possible and used in predictions. We address modeling related to incomplete measurement in Section 4

Second, the ion momentum distribution is heterogeneous, with two or more distinguishable populations. Short-pulse, high-intensity lasers deposit energy into a region of 10–100 μm in radius from the focal spot, which we call the directly-irradiated (DI) volume. In this volume, electrons gain many MeV of energy, and ions are likely to have more isotropic momentum distributions. Fast electrons pushed through and out of this volume, largely in the laser beam direction, can create large magnitude electrostatic fields that accelerate ions out of the DI volume. The precise ion acceleration mechanism and shape of the resulting ion spectrum depend on the thickness of the target. To maximize fusion yields, we assume the target is thick, that is, greater

than the stopping range of these high-energy ions, so that the probability of undergoing fusion is saturated. The fast ions are more likely to collide with at-rest ions much deeper in the bulk of the target, and the reaction kinematics are essentially those of beam fusion. We model the yield from each of these regions and ion populations separately, addressing reactions in the DI volume first and the beam-fusion reactions second.

The dichotomy between the DI volume and the beam-fusion region is artificial, and the plasma will certainly contain some transitional regions. Given the dynamics described so far, these transitional regions are likely to contain electrons of intermediate kinetic energy $1\text{eV} \ll \langle E_e \rangle \ll 1\text{MeV}$, both low energy ions and some beam ions and particle number densities similar to the initial state. In this region, ion stopping is reduced compared to the cold limit, and the fusion probability is similar to the beam-fusion limit. Thus, the contribution to the yield can be thought of as a correction to the beam-fusion yield since the length of such transitional regions is much less than the stopping range of the fast ions passing through.

The starting point to derive the yield is a classical expression for the total number of particles of type A produced in a 2-body collision:

$$Y_A = \int f_1(\vec{x}, \vec{p}_1, t) f_2(\vec{x}, \vec{p}_2, t) |\vec{v}_1 - \vec{v}_2| \sigma_A d^3x dt \frac{d^3p_1 d^3p_2}{(2\pi)^3 (2\pi)^3}. \quad (1)$$

Here, $f_i(\vec{x}, \vec{p}_i, t)$ is the distribution function describing the probability of finding particle $i = 1, 2$ with momentum $\vec{p} + d\vec{p}$ in the volume element $\vec{x} + d\vec{x}$ at time t , σ is the cross-section, and $|\vec{v}_1 - \vec{v}_2|$ is the relative speed of the incident particles. We integrate over all initial particle momenta, all final states, and all space and time for the reaction to occur. For the reactions of interest here, sufficiently complete cross-sections differential in a solid angle are generally not available, and cross-sections for the process exhibit resonances of nuclei with different quantum numbers, suggesting that the angular dependence will have a strong energy dependence, which we will not attempt to model here. We can focus on the total yield as the most relevant observable for both applications and practically available measurements from recent experiments.

We consider two models for our yield calculations, corresponding to the direct-irradiation and beam-target experiments.

3.1. Direct Irradiation. The laser deposits a large amount of energy in the fusion target, and reactions occur within the 10s of picosecond timescale that the ions are heated but before the target expands and its density drops. Although neither the electron nor the ion population can equilibrate in this short time, experimental ion spectra are frequently fit by the Maxwellian distribution, $dN/dE \propto e^{-\beta E}$. The parameter β is an inverse energy scale that characterizes the mean

kinetic energy per particle of the distribution $\langle E \rangle / N = \beta^{-1}$. We stress that local thermal equilibrium is certainly not achieved, and we do not assume equilibrium distributions. The Maxwellian fit to experimental spectra is a phenomenological choice, enabling simple quantitative comparison between shots and facilities.

Maxwellian ion distributions are a strong simplifying approximation: kinetic simulations of short-pulse laser-target interaction have found that the ion distributions can have significantly higher numbers of high-energy ions $E_i > \beta^{-1}$ than expected from the Maxwellian distribution. To account for the excess of high-energy $E > \beta^{-1}$ ions, the single Maxwellian model can be improved by introducing a second Maxwellian distribution of smaller β . This second population often corresponds to the beam population that has significant directionality and is less likely to react with the larger β population, being accelerated out of the DI region by plasma fields on its boundary. Even so, the contribution is computed easily since the yield is linear in the distribution function, and the yield in the double Maxwellian case can be derived by summing four yields corresponding to the four

combinations of the two ion species' two β values. Therefore, for simplicity and clarity here, we use the single Maxwellian.

Since the electrons have MeV-scale kinetic energy in the DI region, their stopping power is significantly reduced. While the high-intensity laser can drive large, short-lived, local increases in the electron density, the ion density varies from the initial value by a factor much less than 1, at least until the target expands significantly on the 10s of pico-second timescale. Consequently, the proton and α stopping ranges ($> 100\mu\text{m}$) are certainly larger than the radius of the DI region ($\leq 100\mu\text{m}$), and we consider that the ion energy losses are negligible for the duration in the DI region.

Given these conditions, the yield of a given process is straightforwardly derived from equation (1). The reaction volume is a few times larger than the focal volume but is generally not known precisely. Reactions will continue as long as the plasma remains relatively dense upto several picoseconds, though this plasma "confinement time" as it is sometimes known is not well-determined either. We, therefore, consider the yield per unit volume per unit time for a $2 \rightarrow A + X$ reaction for nonrelativistic ions with Maxwellian distributions:

$$\frac{dY_A}{d^3xdt} = \frac{n_1 n_2}{\pi} \left(\frac{2\beta_1 m_1 \beta_2 m_2}{m_1 \beta_1 + m_2 \beta_2} \right)^{3/2} \frac{1}{\beta_r m_r} \int_0^\infty \mathcal{Y}(m_r, \beta_r, \mu, \nu; \nu) \sigma_A \left(\frac{m_r \nu^2}{2} \right) \nu d\nu \quad (2)$$

$$\mathcal{Y}(m_r, \beta_r, \mu, \nu; \nu) = e^{-\mu \nu^2} \left(e^{y_\nu^2} (2y_\nu^2 + 1) \frac{\sqrt{\pi}}{2} \text{Erf}(y_\nu) + y_\nu \right), \quad y_\nu = \frac{\beta_r m_r \nu}{\sqrt{2\nu}}$$

where the parameters $n_i, m_i,$ and β_i for $i = 1, 2$ are the number densities, masses, and inverse mean kinetic energy of the two ion species. The remaining parameters are the reduced mass m_r , difference of inverse mean kinetic energy, and combinations thereof:

$$\begin{aligned} m_r &= \frac{m_1 m_2}{m_1 + m_2}, \quad \beta_r = \beta_1 - \beta_2, \quad \nu = \beta_1 m_1 + \beta_2 m_2, \mu \\ &= \frac{m_r^2}{2} \left(\frac{\beta_1}{m_1} + \frac{\beta_2}{m_2} \right). \end{aligned} \quad (3)$$

The result is even in β_r as it must be since the choice of labels is arbitrary and the yield should always be positive. The integration variable corresponds to the magnitude of the relative velocity of the two ions. The integration will be performed numerically to use experimental data for the cross-section $\sigma_A(E_{cm})$, which is a function of the CM energy. $\text{Erf}(z)$ is the usual error function with the normalization defined by

$$\text{Erf}(z) = \frac{2}{\sqrt{\pi}} \int_0^z e^{-u^2} du. \quad (4)$$

The limit of equal mean kinetic energies simplifies the result considerably to

$$\frac{dY_A}{d^3xdt} = \frac{2n_1 n_2}{\pi \sqrt{\beta(m_1 + m_2)}} \int_0^\infty dy e^{-y^2/2} y^2 \sigma_A \left(\frac{y}{2\beta} \right). \quad (5)$$

Considering our interest in particular reactions as *in situ* diagnostics of the $^{11}\text{B}(p, 2\alpha)^4\text{He}$ reaction, we introduce ratios of yields to eliminate experimental unknowns. For reactions with the same initial state, e.g., $p\text{-}^{11}\text{B}$ scattering, all the prefactors in equation (2) cancel. For example, to use the $^{11}\text{B}(p, \gamma)^{12}\text{C}$ reaction as a diagnostic on $^{11}\text{B}(p, 2\alpha)^4\text{He}$, we might consider the ratio

$$\frac{dY_\gamma}{dY_\alpha} = \frac{\int_0^\infty d\nu \mathcal{Y}(m_r, \beta_r, \mu, \nu; \nu) \nu \sigma_{pB \rightarrow ^{12}\text{C}\gamma} \left(\frac{m_r \nu^2}{2} \right)}{3 \int_0^\infty d\nu \mathcal{Y}(m_r, \beta_r, \mu, \nu; \nu) \nu \sigma_{pB \rightarrow 3\alpha} \left(\frac{m_r \nu^2}{2} \right)}, \quad (6)$$

in which all the mass- and β -dependent parameters are identical in the numerator and denominator. Only the cross-sections differ. For $2 \rightarrow 2$ reactions such as considered here, the spectra of produced neutrons and photons have been computed semianalytically showing that their widths and small shifts in the peak depend on the momentum distribution of scattering ions [26]. This allows the (approximate) β parameters of the ions to be retrieved by fitting spectra of the measured neutron or photon. Since the reactions have exactly the same initial state, potentially large scaling factors such as volume and time must be the same. Thus, this yield ratio depends only on the mean kinetic

energies of the two ion species. Considered as a function of these two energy scales, the ratio manifests the difference in the energy dependence of the cross-sections, though less so than the beam-target experiments described below. In equation (6), the factor 3 has been included in the numerator to count the total number of α s produced for each $^{11}\text{B}(p, 2\alpha)^4\text{He}$ reaction. With this yield ratio, the number of

$^{11}\text{B}(p, 2\alpha)^4\text{He}$ reactions is recovered by multiplying by the measured yield of photons identified as arising from this reaction.

Another reaction of interest for diagnostics is $^{10}\text{B}(p, \gamma)^{11}\text{C}$, which differs from $^{11}\text{B}(p, 2\alpha)^4\text{He}$ in the isotope of boron in the initial state. As a consequence, some prefactors remain in the yield ratio:

$$\frac{dY_\gamma}{dY_\alpha} = \frac{n_{10}}{n_{11}} \left(\frac{1 + (m_p/m_{11})(T_{11}/T_p)}{1 + (m_p/m_{10})(T_{10}/T_p)} \right)^{3/2} \frac{T_{r10}}{T_{r11}} \frac{m_{r11}}{m_{r10}} \frac{\int_0^\infty dv \mathcal{Y}(m_{r11}, T_{r11}, \mu_{11}, \nu_{11}; \nu) \nu \sigma_{pB \rightarrow {}^{11}\text{C}\gamma} \left((m_r/2)v^2 \right)}{3 \int_0^\infty dv \mathcal{Y}(m_{r10}, T_{r10}, \mu_{10}, \nu_{10}; \nu) \nu \sigma_{pB \rightarrow 3\alpha} \left((m_r/2)v^2 \right)}. \quad (7)$$

The subscripts for boron parameters have been shortened to the isotope number for clarity. The measured constants in the prefactor, such as masses, are no trouble, but for this ratio to be useful we must argue that the ratio of densities remains nearly constant during the relevant period of plasma evolution. Since the charge is the same and the masses differ only by 10%, we suppose significant separation of isotopes from the initially uniform mixture can only develop slowly, on the same time scale (or longer) that the plasma expands and diffuses into free space. Note that dynamically, we expect the mean kinetic energy of the boron ions and protons to be similar, making the prefactor in parentheses close to 1. The remaining ratio of reduced kinetic energies is expected to be near unity for the same reason.

Another useful yield ratio could be $^{10}\text{B}(\alpha, p)^{13}\text{C}$ relative to $^{10}\text{B}(\alpha, n)^{13}\text{N}$. The ratio would cancel dynamical unknowns such as the density of α s. The other proton-producing secondary reaction $^{11}\text{B}(\alpha, p)^{14}\text{C}$ could be added to the ratio to completely determine the secondary proton production, though the same remarks as above would apply to the prefactor. A measurement of the neutrons produced from $^{10}\text{B}(\alpha, n)^{13}\text{N}$ constrains the number of protons able to be recycled into the $^{11}\text{B}(p, 2\alpha)^4\text{He}$ reaction. In this case, the input is the α spectrum derived from all primary reactions, is a complicated function of energy, and is expected to vary significantly as a function of mean ion kinetic energy. We consider its derivation beyond the scope of this study.

3.2. Beam-Target. The beam-target experiment involves simpler kinematics. In the frame with the target material at rest, the center-of-mass energy is

$$E_{cm} = \frac{m_r}{2} v_b^2 = \frac{m_r}{m_b} E_b, \quad (8)$$

with the reduced mass given above by equation (3). The b subscript indicates a particle from the beam, and the t subscript indicates a particle in the target. For pB scattering, $m_r/m_b \approx 1.1$. The momentum integral then only runs over the proton distribution. The target particle distribution is nonzero only in the spatial region of the target material, and integrating over the beam axis and time convolves the projectile beam with the target distribution.

In standard beam-target experiments in order to maximize exposure, the target is placed on or adjacent to the anticipated axis of the ion beam. In the TPW experiment of particular interest, we were able to verify that the target material contained the cone of the highest ion flux, which subtended an opening angle $\theta \leq 0.3$. We, therefore, assume that the transverse momentum of the beam is small relative to longitudinal momentum. These together imply that we can reduce the beam momentum integral to the longitudinal momentum only and integrate the transverse position dependence into a 1-dimensional beam distribution function:

$$\begin{aligned} Y_A &\approx \int_{V_t} d^3x \int_{-\infty}^{\infty} dt \int \frac{dp_z}{2\pi} f_b(\vec{x}, p_z, t) n_t(\vec{x}) |\vec{v}_b| \sigma_A(E_{cm}) \\ &= n_t \int_0^L dz \int_{-\infty}^{\infty} dt \int_0^\infty \frac{dp_z}{2\pi} v_z \sigma_A(E_{cm}) f_b(z, p_z, t), \end{aligned} \quad (9)$$

where V_t signifies the volume of the target. In this expression, the longitudinal coordinate can also be considered as parameterizing the distance along the on-average straight-line trajectory; trajectories diverging from the beam axis would make a small geometric correction due to exiting through the side of the target rather than the opposite end. The constant density of the target has been taken outside the integral and the target length defined as L .

Due to energy loss in the target, the beam distribution evolves as it propagates through the target. First, as a limiting model, we compute the yield neglecting the beam energy loss. This case also clarifies the dynamics in the subsequent derivation that includes stopping. The beam distribution function remains constant in the absence of stopping, so the convolution yields the length of the target times the spatial length scale of the beam divided by the longitudinal velocity, i.e., the length of the beam multiplying the traverse time and a numerical factor depending on the longitudinal profile of the beam. Then, the yield can be written simply

$$Y_A^\emptyset \approx n_t L \int \frac{dE_b}{2\pi} \frac{dN_b}{dE_b} \sigma_A \left(\frac{m_r}{m_b} E_b \right). \quad (10)$$

The beam distribution function f_b has been reduced to its energy dependence dN_b/dE .

The importance of stopping is seen by comparing the stopping range to the target dimensions. The stopping range is defined as

$$z_s = \int_0^{E_0} \left(\frac{dE}{dx}(E') \right)^{-1} dE', \quad (11)$$

where E_0 is the initial energy of the ion before interacting with the target, dE/dx from data is conventionally positive, and the expected minus sign is compensated by the flipping the limits on the integral. Note that dE/dx is frequently given in units of energy/(mass density) or energy/(number density) so that one multiplies by the density of the medium to obtain the energy loss in units of energy/length.

The target temperature is more difficult to estimate in direct-irradiation experiments. As the laser energy is absorbed within the first few 10s of microns of the target (at most), the bulk is only heated by ions and electrons accelerated out of the laser-heated region. Ions dominate the energy transfer to the bulk; electrons have very low (a few-MeV cm²/g) stopping power in the few-MeV energy range compared to ions. With similar estimates for the total energy of laser-accelerated ions as in the preceding paragraph, the average energy transferred is 10–100 eV per electron, orders of magnitude higher because the volume into which it is deposited is orders of magnitude smaller $\sim (0.1\text{mm})^3$. The temperature-dependent correction to ion stopping would be non-negligible in this case. For this reason, in yield calculations below, we compare zero-temperature stopping to finite-temperature stopping.

For a zero-temperature boron target and ion energies representative of the higher end of the expected distributions, SRIM predicts the stopping range of a 20 MeV proton as 2 mm and 8 MeV α as 38 micron. However, target can be heated by both the ion beam and the even higher energy electrons that are accelerated out of the ion source by the laser driver. Using the fact that the stopping range is less than the target length even for the highest energy ions, the total energy deposited is just the total energy of the beam that enters the target. Even for the relatively high-energy ions obtained from the Texas Petawatt, the total ion beam energy transferred to the target is at most $\sim 10\%$ of the laser energy. For the upper limit on the Texas Petawatt, 10 J deposited into a hemisphere of radius equal to the 2 mm stopping range, the specific heats of boron and boron-nitride imply a temperature change $\Delta T \approx 280\text{ K} \approx 2.4\text{--}2.6 \times 10^{-2}\text{ eV}$. Without direct measurements of the electron spectrum emitted by the ion source, we resort to an estimate. While experiments and simulations of ion acceleration suggest that electrons absorb a similar amount of energy from the laser-plasma interaction as the ions, the electrons are less efficient at depositing energy in the target. Therefore, an estimated upper bound on the deposition of energy in the target by electrons is 10 J. Carbon and other heavy ions that may come from the ion sources carry equal or less energy than the protons and in any case arrive later. Thus, our best estimate for the temperature of the target remains $\Delta T \leq 5 \times 10^{-2}\text{ eV}$. This estimate, much less than the work function ($\sim\text{eV}$) of the target material, is consistent with the target's survival of the interaction.

Nevertheless, for reference and comparison, Figure 2 shows the stopping power and stopping range equation (11) for both cold and high-temperature ($T = 1\text{ keV}$) boron and boron-nitride. This unphysically high target temperature is chosen to exhibit its negligible impact on the yields for the processes of interest. The stopping power data are obtained from calculations using the enhanced RPA-LDA (eRPA-LDA) model of Mehlhorn [27, 28]. Stopping ranges for lower energy ions are shorter, and ranges are generally less than the typical length ($\leq\text{cm}$) of the targets. The highest energy protons ($E_p \leq 20\text{ MeV}$) have stopping ranges equal to or greater than the target length, but their number and hence contribution are smaller by an order of magnitude or more. Neglecting this not-quite-stopped component, therefore, amounts to an error of $\sim 10\%$ or less, smaller than the error propagated from the cross-section and certainly smaller than the error due to the limited energy range of the cross-section data. Therefore, to our working accuracy, the target can be considered “thick” in that almost all particles in the beam will be stopped.

The conventional definition of the “thick-target yield” for a monoenergetic input is

$$I_A(E_0) = \int_0^{E_0} \left(\frac{dE}{dx}(E') \right)^{-1} \sigma_A \left(\frac{m_r E'}{m_b} \right) dE', \quad (12)$$

where dE/dx from data is conventionally positive, and the expected minus sign is compensated by the flipping the limits on the integral. The density factor in converting tabulated dE/dx data into energy loss per unit length cancels with the density of target nuclei in the yield. Note that the integration can effectively be restricted to the energy range where the cross-section is non-negligible. Since most of the cross-sections have thresholds of order 1 MeV, Figure 2 shows that finite-temperature corrections to stopping matter only for $T \geq 1\text{ keV}$. Raising the target temperature increases the projectile energy at which dE/dx achieves its maximum, but 1 keV is a much higher temperature than can be dynamically achieved in a typical beam-target experiment without external heating.

Thick target yields for all of the primary reactions in Figure 3 show these properties. $^{11}\text{B}(p, 2\alpha)^4\text{He}$ and $^{11}\text{B}(p, \alpha)^8\text{Be}$ display the greatest sensitivity to the target temperature because $^{11}\text{B}(p, 2\alpha)^4\text{He}$ cross-section is largest, and the cross-section for $^{11}\text{B}(p, \alpha)^8\text{Be}$ is only available for CM energy $\leq 1\text{ MeV}$, where the dE/dx curves differ the most.

The total yield of the product nucleus A is obtained by integrating the thick target yield over the beam, weighted by the beam energy distribution dN/dE_b :

$$Y_A^{\text{tt}} = \int_0^\infty \frac{dN}{dE_b} I(E_b) dE_b. \quad (13)$$

Yield ratios in the beam-fusion geometry, as in direct-irradiation experiments, analytically eliminate dependence on geometric factors in the yield, such as target length and density. Less obviously, the overall normalization of the beam energy distribution also cancels in the ratio, since one could easily write $dN/dE = N_b f(E)$ where N_b is the total number of particles (that interact with the target) and $f(E)$

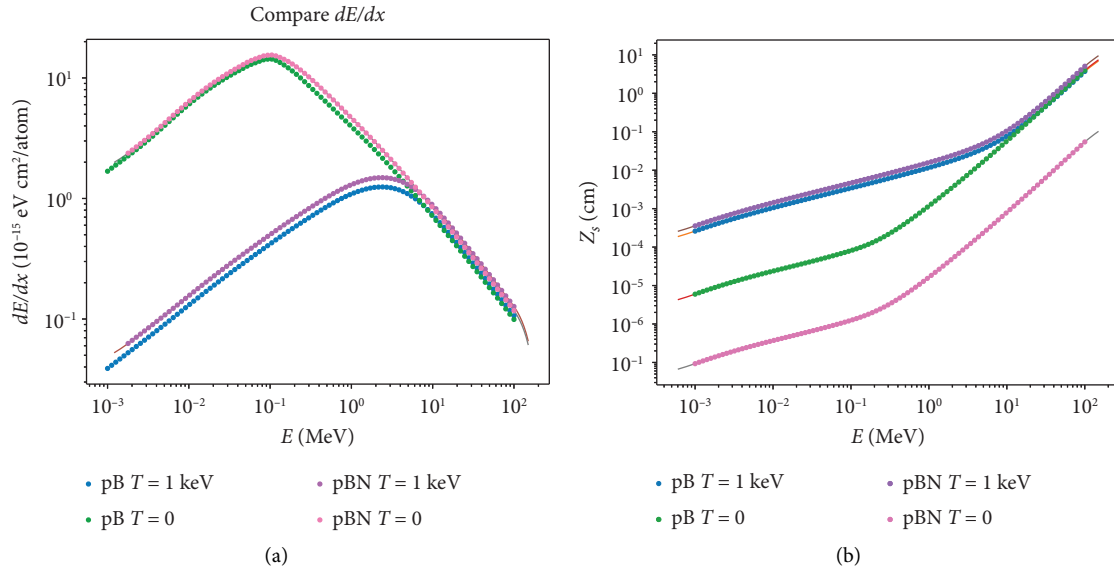


FIGURE 2: (a) Stopping power, dE/dx , for protons in pure boron and boron-nitride, cold and warm $T = 1 \text{ keV}$ thick targets. (b) Resulting range z_s equation (11).

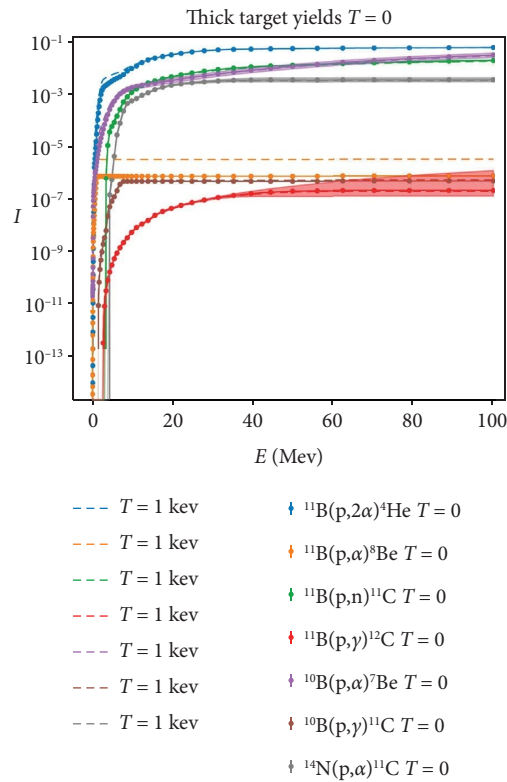


FIGURE 3: Thick target yields for the reactions in Table 1. Solid bands show the error propagated from the cross-section. Error bars, where visible, present the numerical error.

is a normalized probability distribution for the ion energy. For example, the ratio of γ s from $^{11}\text{B}(p, \gamma)^{12}\text{C}$ to α s from $^{11}\text{B}(p, 2\alpha)^4\text{He}$ is

$$\frac{Y_\gamma}{Y_\alpha} = \frac{\int_0^\infty f(E_b) \int_0^{E_b} \left((dE/dx)(E') \right)^{-1} \sigma_{pB \rightarrow ^{12}\text{C}\gamma} \left((m_r/m_b)E' \right) dE' dE_b}{\int_0^\infty f(E_b) \int_0^{E_b} \left((dE/dx)(E') \right)^{-1} \sigma_{pB \rightarrow 3\alpha} \left((m_r/m_b)E' \right) dE' dE_b}, \quad (14)$$

with the same stopping power dE/dx and normalized proton spectrum. Removing this dependence on the total number in the beam significantly reduces uncertainty in practice given the available on-shot beam measurements.

The yield ratio retains important information of the beam energy distribution. As seen in Figure 1, different reactions have different thresholds and collision energies where the cross-section approaches its maximum usually in the 0.1–1 b range. The yield ratio is greatly enhanced in case the beam energy distribution reaches the threshold of one reaction but not the other. Since laser-driven ion beams generally have a broad and decreasing energy distribution at low energy, the typical case is that a beam may contain ions of sufficient energy for a reaction with a low threshold but not for a reaction with a higher threshold. Thus, for example, the $^{11}\text{B}(p, 2\alpha)^4\text{He}$ has a peak cross-section around 650 keV whereas the $^{11}\text{B}(p, n)^{11}\text{C}$ has a peak around 7 MeV, so that the Maxwellian distribution with $\beta^{-1} \approx 0.5\text{--}5$ MeV would yield significant α particles but not ^{11}C . This effect is demonstrated in Figure 4.

4. Modeling and Results

Some modeling and assumptions have already been established in setting up expressions for the yield. We, now, discuss the details and quantitative inputs to the models.

As seen in Tables 1 and 2 and Figure 1, data for the cross-sections of interest are available only for limited ranges of CM energy. The available data and comparison with analogous reactions suggest that the cross-sections may have similar values across a wider range of CM energies. However, to avoid undue speculation and modeling, we assume the cross-section vanishes quickly outside the available data range. Considering also the ion mean kinetic energy not likely exceeding ~ 10 MeV, the numerical results for the yields are likely under estimates by a factor of a few, but not more than ten.

4.1. Direct Irradiation. The yield ratio eliminates dependence on local, dynamic quantities, including effective reaction volume, confinement time, and the densities. We need both the absolute kinetic energy scale and the relative kinetic energies of the two ion species. The absolute energy scale is determined by how efficiently laser energy is transferred the plasma, which in turn generally depends on laser properties, such as total pulse energy, pulse length (if it is greater than ps-scale), and contrast. For comparison

between facilities, we scan the absolute kinetic energy scale, using the proton mean kinetic energy as the reference. For intensities upto 10^{22} W/cm², we expect ion kinetic energies inside the target to be MeV-scale as the typical momentum obtained from a cycle of the laser field and so also from plasma-generated electrostatic fields.

The relative kinetic energy can be estimated from kinematics. For the same field strength and duration of interaction, the relative work done on ions of charge Z_1, Z_2 and mass m_1, m_2 is $W_1/W_2 = (Z_1)^2 m_2 / (Z_2)^2 m_1$. This suggests the typical energy of protons should be smaller than that of (fully-ionized) boron by factor of 2.5 (i.e., $T_p \approx 0.4T_B$). Good experimental measurements of ion kinetic energy distributions inside the laser-heated target are difficult to come by. Fortunately, we find that the yield is mostly sensitive to the absolute kinetic energy scale, controlling how much of the ion distribution is above the threshold CM energy determined by the cross-section. Once the threshold CM energy is achieved by a majority of the distribution, the yield becomes less sensitive to further increases in kinetic energy. At next order, the yield equation (2) is more sensitive to the kinetic energy of the heavier ion, due to the residual exponential dependence on ν . Note, however, that these yields are likely to increase somewhat for higher kinetic energy range if cross-section data across a wider range of CM energy were available. These results are exhibited in Figure 5.

The relative insensitivity of $^{10}\text{B}(p, \gamma)^{11}\text{C}$ to ion mean kinetic energy is probably an artifact of the limited data range available for the cross-section, which causes the thick target yield to plateau rapidly above ~ 8 MeV. The greater sensitivity of $^{11}\text{B}(p, \gamma)^{12}\text{C}$ to the mean kinetic energy could allow the yield ratio to be used in a more conventional manner: measuring both yields in the ratio determines the mean ion kinetic energy in the target to high accuracy. This method is in fact how yield ratios are commonly used in heavy-ion collisions [29]. In particular, if photons from both processes $^{11}\text{B}(p, \gamma)^{12}\text{C}$ and $^{10}\text{B}(p, \gamma)^{11}\text{C}$ can be detected, the ratio of these photon yields alone could probe the mean kinetic energy of ions in the target. We expect the sensitivity of the photon ratio can only be established with more cross-section data.

4.2. Beam Target. More experimental information is available on the inputs for the beam-target setup. With a $\sim 1/2$ reduction to the total yield, experiments can measure the laser-produced ion beam on-shot. For example, the target can cover roughly half the solid angle of the beam, so that the

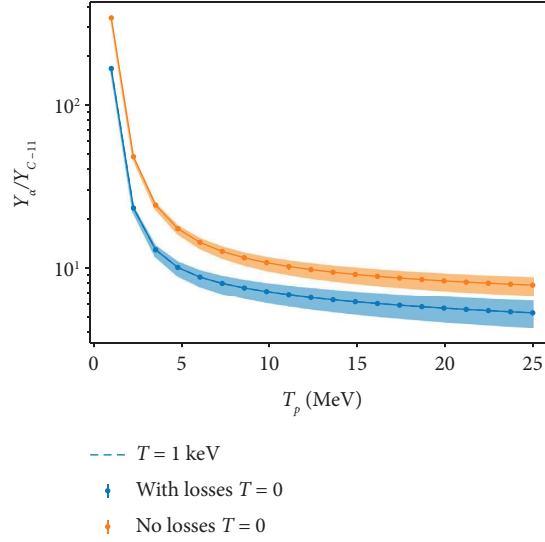


FIGURE 4: Yield ratio of α to ^{11}C for a normalized Maxwellian input proton spectrum in boron, comparing the yield with and without beam energy losses in the target. Target temperature makes a negligible difference to the energy loss for proton energies in this regime, and the $T = 1$ keV curve lies on top of the $T = 0$. Solid bands show the error propagated from the cross-section. Error bars, where visible, present the numerical error.

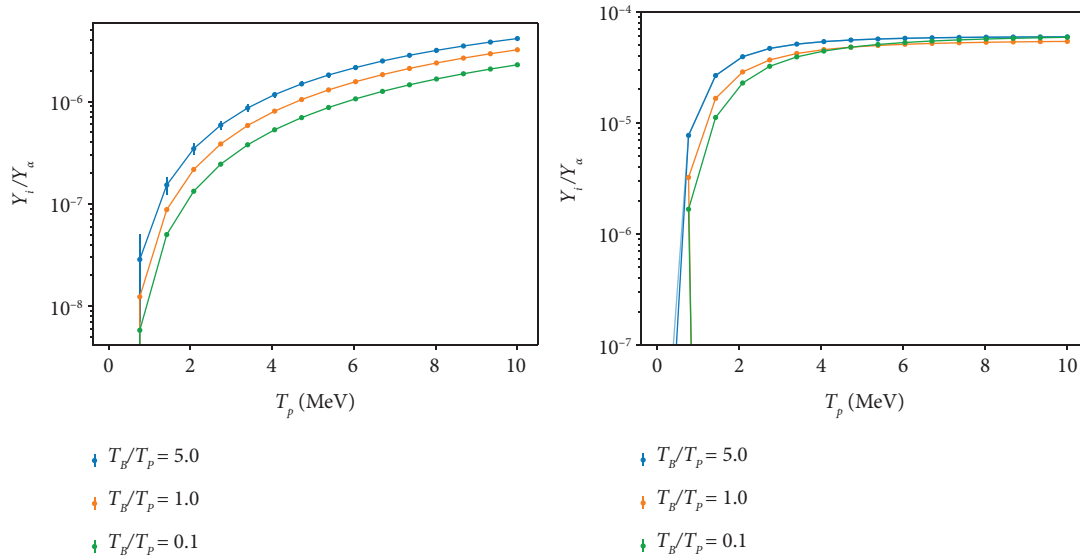


FIGURE 5: Ratio of photon (γ) yield to α yield in a quasi-thermal plasma as a function of proton mean kinetic energy. At left for the $^{11}\text{B}(p, \gamma)^{12}\text{C}$ reaction and at right for the $^{10}\text{B}(p, \gamma)^{11}\text{C}$ reaction. The yield increases rapidly as the mean kinetic energy nears the CM energy corresponding to the threshold for the cross-section (of Figure 1) and then plateaus. Different curves correspond to different boron to proton kinetic energy, showing that the yield is only sensitive to the relative kinetic energy if the boron mean kinetic energy is much less than the proton mean kinetic energy. Error bars, where visible, present the numerical error.

other half the beam propagates unperturbed into a diagnostic. Since ion acceleration mechanisms are azimuthally symmetric or at most display a dipole azimuthal mode (for example, in BOA [30]), we can infer the distribution in the unmeasured half by mirroring the measured half. Experiments on the TPW and else frequently show single or double Maxwellian ion spectra. For simplicity and clarity, we consider a single Maxwellian distribution describing the beam, though with much smaller β parameter than in the

DI-region ion distributions. The yield for a double Maxwellian is a suitably weighted superposition of the yield for single Maxwellians, and the effect on the yield ratios can be naturally deduced from this.

We first compare the total α yield to the ^{11}C yield in boron and boron-nitride targets. As shown in Figure 4, for the cross-sections and expected temperature of the target, beam energy losses are well-approximated by the cold limit, which we use here. In boron targets, $^{11}\text{B}(p, 2\alpha)^4\text{He}$ is the

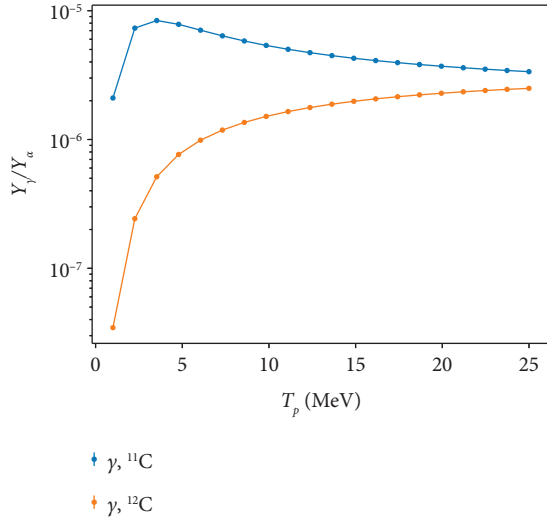


FIGURE 6: Yield ratios: number of photons per $^{11}\text{B}(p, 2\alpha)^4\text{He}$ reaction for $^{11}\text{B}(p, \gamma)^{12}\text{C}$ and $^{10}\text{B}(p, \gamma)^{11}\text{C}$ processes.

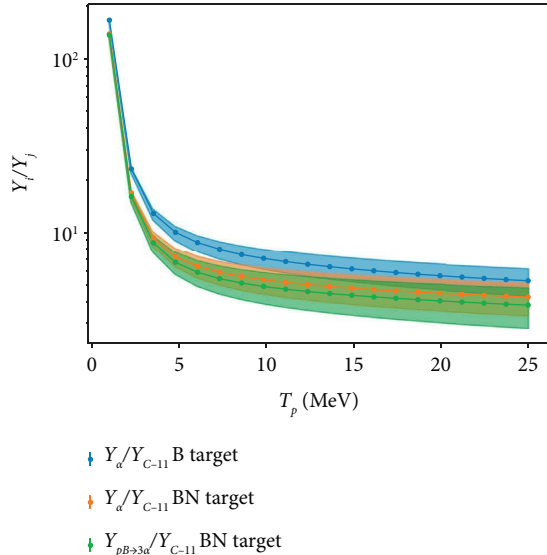


FIGURE 7: Yield ratios: measured total α and $^{11}\text{B}(p, 2\alpha)^4\text{He}$ yield relative to measured ^{11}C for boron and boron-nitride targets. Beam energy losses are included with a cold target.

dominant source of α particles, while in boron-nitride targets, the $^{14}\text{N}(p, \alpha)^{11}\text{C}$ process can contribute a similar number. Therefore, for BN targets, we show both the total α to ^{11}C ratio and the $^{11}\text{B}(p, 2\alpha)^4\text{He}$ yield relative to the (total) ^{11}C yield, so that the measured ^{11}C number can be both compared to the measured α yield (e.g., in CR-39) and used to estimate the number of $^{11}\text{B}(p, 2\alpha)^4\text{He}$ reactions occurring.

Photons are also produced by $^{11}\text{B}(p, \gamma)^{12}\text{C}$ and $^{10}\text{B}(p, \gamma)^{11}\text{C}$ processes in the beam-target geometry. Detection of the photons in the beam-target experiment is a natural proof-of-principle/validation step before using the photon measurement to diagnose the direct-irradiation experiments. As shown in Figure 6, the photon yields are 5 to 6 orders of magnitude smaller than the α yield and display different dependence on the beam β parameter in

beam-target experiments compared to the quasi-thermal plasma of direct irradiation. The yield of $^{10}\text{B}(p, \gamma)^{11}\text{C}$ peaks around 3 MeV due to the narrow range of energies for which cross-section data are available; this peak may disappear with more complete cross-section data.

5. Conclusion

We have, thus, arrived at a list of reactions and their products with diagnostic potential:

- (1) ^{11}C is produced by three reactions in Table 1 with cross-sections of several hundred millibarns in 5–20 MeV center-of-mass energy range. The third channel, $^{10}\text{B}(p, \gamma)^{11}\text{C}$, generally contributes less than 10^{-4} to the total yield. Although it requires higher proton energy, in experiments on an ultrahigh-intensity laser, 1 ^{11}C is produced for every 10–100 α particles from the $^{11}\text{B}(p, 2\alpha)^4\text{He}$ reaction (see Figure 7). Modulo some uncertainty in modeling the proton beam, the ^{11}C yield thus offers a strong, easily-measured signal to corroborate or substitute more direct measurements of the α yield [20].
- (2) $^{11}\text{B}(p, \gamma)^{12}\text{C}$ has the same initial state as the $^{11}\text{B}(p, 2\alpha)^4\text{He}$, so that in both direct-irradiation and beam-target experiments, macroscopic factors such as density, volume, and time as well as physical constant prefactors cancel in the yield ratio. The drawback to this process is its low cross-section and higher threshold: only 1 photon per million $^{11}\text{B}(p, 2\alpha)^4\text{He}$ reactions is expected, according to Figure 5. That suggests $\sim 10^3 - 10^4$ such photons were produced in recent experiments such as References [5, 7, 20]. Pending a direct measurement though the photon should be easily distinguishable at an energy ≥ 10 MeV.
- (3) $^{10}\text{B}(p, \gamma)^{11}\text{C}$ involves boron-10, generally leaving nontrivial prefactors in the yield ratio. While these prefactors are expected to be order 1, due to the similar dynamics of boron-10 versus boron-11 in a laser-heated target, they introduce additional uncertainty, which also grows with the duration of the fusion. The yield ratio Figure 5 predicts 1 photon per 100,000 $^{11}\text{B}(p, 2\alpha)^4\text{He}$, implying roughly 10^5 such photons in recent experiments. The photon energy is lower, but still likely high enough in the several MeV range to be distinguishable from other plasma sources.
- (4) $^{10}\text{B}(\alpha, n)^{13}\text{N}$ has not been evaluated here but is an excellent candidate for corroborating the α yield if the neutron number can be measured. This reaction could also determine the importance of p recycling by virtue of its probably near-unity yield ratio to the isospin partner reaction $^{10}\text{B}(\alpha, p)^{13}\text{C}$. A rough estimate of the thick target yield for a 4 MeV α suggests that $\sim 10^{-5}$ of the α s produced may be converted to neutrons by this process. The neutron is slow enough

to be easily identified by time-of-flight spectrometers.

One other reaction could be a good proxy for α yield if its cross-section was independently measured in conventional nuclear scattering experiments: $^{14}\text{N}(\alpha, \gamma)^{18}\text{F}$. This reaction has the benefit of producing an unstable nuclide so that its yield can be first checked in beam-target experiments. We have also noted that the ratio between the two photon-producing processes, $^{11}\text{B}(p, \gamma)^{12}\text{C}$ and $^{10}\text{B}(p, \gamma)^{11}\text{C}$, could provide a measurement sensitive to the mean kinetic energy of the ions in the plasma. However, its accuracy is currently severely limited by the little cross-section data available for $^{10}\text{B}(p, \gamma)^{11}\text{C}$.

Considering the experimental interest and potential applications of the $^{11}\text{B}(p, 2\alpha)^4\text{He}$ reaction and other laser-driven fusion reactions, we strongly recommend increasing engagement with the accelerator-nuclear physics community to improve cross-section measurements and add photon and neutron diagnostics. Particle yields and yield ratios can become a powerful tool to determine laser-driven fusion plasma conditions in the same way, they have been thoroughly developed for probing nuclear-matter plasmas.

Data Availability

Nuclear cross-sections are freely available from the EXFOR database. Energy loss predictions and tabulated results of numerical integrations are available from the authors upon request.

Conflicts of Interest

The authors declare that they have no conflicts of interest.

Acknowledgments

The work performed under the auspices of the University of Texas at Austin was supported in part by the National Science Foundation under grant no. 2108921 and the Air Force Office of Scientific Research under grant nos. FA9550-14-1-0045. This work and a related experiment at the University of Texas, Austin were also supported in part by HB11 Energy PTY, LTD. Experiment time at Texas Petawatt was supplied by LaserNetUS.

References

- [1] A. Zylstra, O. Hurricane, D. Callahan et al., “Burning plasma achieved in inertial fusion,” *Nature*, vol. 601, no. 7894, p. 542, 2022.
- [2] T. A. Mehlhorn, L. Labun, B. M. Hegelich, D. Margarone, and M. F. Gu, “Path to increasing p-B11 reactivity via ps and ns lasers,” *Laser and Particle Beams*, vol. 2022, 2022.
- [3] C. Labaune, C. Baccou, S. Depierreux et al., “Fusion reactions initiated by laser-accelerated particle beams in a laser-produced plasma,” *Nature Communications*, vol. 4, p. 1, 2013.
- [4] C. Baccou, S. Depierreux, V. Yahia et al., “New scheme to produce aneutronic fusion reactions by laser-accelerated ions,” *Laser and Particle Beams*, vol. 33, no. 1, pp. 117–122, 2015.
- [5] L. Giuffrida, F. Belloni, D. Margarone et al., “High-current stream of energetic α particles from laser-driven proton-boron fusion,” *Physical Review E*, vol. 101, no. 1, Article ID 013204, 2020.
- [6] D. Margarone, A. Morace, J. Bonvalet et al., “Generation of α -particle beams with a multi-kJ, peta-watt class laser system,” *Frontiers in Physics*, vol. 343, 2020.
- [7] J. Bonvalet, P. Nicolai, D. Raffestin et al., “Energetic α -particle sources produced through proton-boron reactions by high-energy high-intensity laser beams,” *Physical Review E*, vol. 103, no. 5, Article ID 053202, 2021.
- [8] P. Norreys, A. Fews, F. Beg et al., “Neutron production from picosecond laser irradiation of deuterated targets at intensities of,” *Plasma Physics and Controlled Fusion*, vol. 40, no. 2, pp. 175–182, 1998.
- [9] W. Bang, M. Barbui, A. Bonasera et al., “Temperature measurements of fusion plasmas produced by petawatt-laser-irradiated D2–He3 or CD4–He3 clustering gases,” *Physical Review Letters*, vol. 111, Article ID 055002, 2013.
- [10] I. Pomerantz, E. McCary, A. R. Meadows et al., “Ultrashort pulsed neutron source,” *Physical Review Letters*, vol. 113, no. 18, Article ID 184801, 2014.
- [11] X. Jiao, J. Shaw, T. Wang et al., “A tabletop, ultrashort pulse photoneutron source driven by electrons from laser wakefield acceleration,” *Matter and Radiation at Extremes*, vol. 2, no. 6, pp. 296–302, 2017.
- [12] Agenda, “In 2nd international workshop on proton-boron fusion,” 2022, <https://agenda.infn.it/event/30291/program>.
- [13] V. Belyaev, V. Vinogradov, A. Kurilov et al., “Neutron production in a picosecond laser plasma at a radiation intensity of $3 \times 10^{17} \text{W/cm}^2$,” *Journal of Experimental and Theoretical Physics*, vol. 98, no. 6, pp. 1133–1137, 2004.
- [14] V. Belyaev, A. Matafonov, V. Vinogradov et al., “Observation of neutronless fusion reactions in picosecond laser plasmas,” *Physical Review E*, vol. 72, no. 2, Article ID 026406, 2005.
- [15] D. Margarone, A. Picciotto, A. Velyhan et al., “Advanced scheme for high-yield laser driven nuclear reactions,” *Plasma Physics and Controlled Fusion*, vol. 57, no. 1, Article ID 014030, 2014.
- [16] A. Picciotto, D. Margarone, A. Velyhan et al., “Boron-proton nuclear-fusion enhancement induced in boron-doped silicon targets by low-contrast pulsed laser,” *Physical Review X*, vol. 4, no. 3, Article ID 031030, 2014.
- [17] D. Kong, S. Xu, Y. Shou et al., “Alpha-particle generation from H-11 B fusion initiated by laser-accelerated boron ions,” *Laser and Particle Beams*, 2022.
- [18] D. Margarone, J. Bonvalet, L. Giuffrida et al., “In-target proton–boron nuclear fusion using a PW-class laser,” *Applied Sciences*, vol. 12, no. 3, p. 1444, 2022.
- [19] J. Frenje, “Nuclear diagnostics for inertial confinement fusion (ICF) plasmas,” *Plasma Physics and Controlled Fusion*, vol. 62, no. 2, Article ID 023001, 2020.
- [20] E. McCary, O. Z. Labun, L. Labun, and B. M. Hegelich, “In preparation,” 2022.
- [21] F. Ajzenberg-Selove, “Energy levels of light nuclei $A = 11–12$,” *Nuclear Physics A 506*, pp. 1–158, 1990.
- [22] M. Sikora and H. Weller, “A New Evaluation of the $^{11}\text{B}(p, \alpha)\alpha$ Reaction Rates,” *Journal of Fusion Energy*, vol. 35, no. 3, pp. 538–543, 2016.
- [23] F. Alves, M. Jensen, H. Jensen, R. Nickles, and S. Holm, “Determination of the excitation function for the $^{10}\text{B}(p, n)^{10}\text{C}$ reaction with implications for the production of ^{10}C carbon dioxide for use as a PET tracer,” *Applied Radiation and Isotopes*, vol. 52, no. 4, pp. 899–903, 2000.

- [24] V. Zerkin and B. Pritychenko, "The experimental nuclear reaction data (EXFOR): e," *Nuclear Instruments and Methods in Physics Research Section A: Accelerators, Spectrometers, Detectors and Associated Equipment*, vol. 888, pp. 31–43, 2018.
- [25] C. Labaune, C. Baccou, V. Yahia, C. Neuville, and J. Rafelski, "Laser-initiated primary and secondary nuclear reactions in boron-nitride," *Scientific Reports*, vol. 6, pp. 1–8, 2016.
- [26] B. Appelbe and J. Chittenden, "The production spectrum in fusion plasmas," *Plasma Physics and Controlled Fusion*, vol. 53, no. 4, Article ID 045002, 2011.
- [27] T. A. Mehlhorn, "A finite material temperature model for ion energy deposition in ion-driven inertial confinement fusion targets," *Journal of Applied Physics*, vol. 52, no. 11, pp. 6522–6532, 1981.
- [28] M. F. Gu, T. A. Mehlhorn, and I. Golovkin, "In preparation," 2022.
- [29] J. Letessier and J. Rafelski, *Hadrons and Quark - Gluon Plasma*, Cambridge University Press, Cambridge, UK, 2002.
- [30] L. Yin, B. Albright, K. Bowers, D. Jung, J. Fernández, and B. Hegelich, "Three-dimensional dynamics of breakout afterburner ion acceleration using high-contrast short-pulse laser and nanoscale targets," *Physical Review Letters*, vol. 107, no. 4, Article ID 045003, 2011.



Research Article

Oscillating Plasmas for Proton- Boron Fusion in Miniature Vacuum Discharge

Yu. K. Kurilenkov ^{1,2}, V. P. Tarakanov ¹, A. V. Oginov ², S. Yu Gus'kov ²
and I. S. Samoylov ¹

¹Joint Institute for High Temperatures, Russian Academy of Sciences, Bd. 2, 13 Izhorskaya st, Moscow 125412, Russia

²P.N. Lebedev Physical Institute, Russian Academy of Sciences, 53 Leninskii Prospect, Moscow 119991, Russia

Correspondence should be addressed to Yu. K. Kurilenkov; yu.kurilenkov@lebedev.ru

Received 14 June 2022; Revised 12 October 2022; Accepted 23 January 2023; Published 4 March 2023

Academic Editor: Dimitri Batani

Copyright © 2023 Yu. K. Kurilenkov et al. This is an open access article distributed under the Creative Commons Attribution License, which permits unrestricted use, distribution, and reproduction in any medium, provided the original work is properly cited.

Earlier, the experiments on the aneutronic proton-boron (pB) fusion in a miniature nanosecond vacuum discharge (NVD) with oscillatory plasma confinement and correspondent α particles yield were presented. In this work, we consider some specific features of oscillatory confinement as a relatively new type of plasma confinement for fusion. Particle-in-cell (PiC) simulations of pB fusion processes have shown that the plasma in NVD, and especially on the discharge axis, is in a state close to a quasineutral one, which is rather different from the conditions in the well-known scheme of periodically oscillating plasma spheres (POPSs) suggested earlier for fusion. Apparently, small-scale oscillations in NVD are a mechanism of resonant ion heating, unlike coherent compressions in the original POPS scheme. Nevertheless, the favorable scaling of the fusion power in NVD turns out to be close to the POPS fusion but differs significantly both in the compression ratio and in the values of the parameter of quasineutrality. In addition, unlike the POPS scheme, PiC simulation reveals that the distribution functions of protons and boron ions in NVD are non-Maxwellian. Therefore, we have an aneutronic pB synthesis in a nonequilibrium plasma remaining “nonignited” on the discharge axis.

1. Introduction

The proton-boron aneutronic reaction ($p + {}^{11}\text{B} \rightarrow \alpha + {}^8\text{Be}^* \rightarrow 3\alpha + 8.7 \text{ MeV}$) [1, 2] has the largest cross section $\sigma \approx 1.2 \text{ b}$ as compared to other neutron-less reactions at the nuclei relative motion energy of about 675 keV [3]. The proton-boron (pB) reaction cross section is smaller and the energy when it occurs is much larger in comparison with the same values for the reaction between deuterium and tritium –6 b and 60 keV. For this reason, the energetically profitable pB reaction requires significantly more extreme plasma states than for the fusion between hydrogen isotopes on the base of traditional schemes with magnetic or inertial confinement [4–6]. In the long term, advanced proton-boron fuel is very promising, like related almost aneutronic “clean” energy [7–9]. To date, the pB reaction and effects related have proved to be in demand in medicine [10, 11]. The laser

initiation of the pB reaction has been demonstrated at the beginning of this century [12]. In recent years, great progress was achieved in laser-driven pB fusion experiments and the growth of α particles yield (sf [13–19] and ref. therein). At the same time, another approach like plasma confinement under extreme conditions in a single device for pB fusion without any external influences is also still of great interest [20]. Overall, the inertial electrostatic confinement (IEC) [21–28] is one of the very few in which ions can quite easily reach the energies required for the beginning of the pB reaction.

Earlier, on the basis of IEC, an oscillating plasma was proposed as a possible thermonuclear fusion scheme [29, 30]. The confinement and acceleration of ions in the IEC scheme take place in the field of a virtual cathode (VC), i.e., in a deep electrostatic potential well (PW) [21]. However, the “beam”-like ion energy distribution is essentially eroded by

Coulomb collisions before the synthesis is substantially realized in traditional IEC schemes [22]. This problem could be avoided if the ionic component of the plasma would be in the local thermodynamic equilibrium (LTE) state, as suggested in [29, 30]. In this scheme, the head-on ion collisions are replaced by the periodically oscillating plasma spheres (POPSs) in the harmonic oscillator potential arranged due to a homogeneous electronic background. At the moment of compression, the high plasma densities and temperatures necessary for nuclear fusion could be achieved. In the process of oscillations, the ions in the POPS scheme have to be in the LTE [29, 30]. An important advantage of the POPS-based device is the obtained scaling of the fusion power, which increases with the inverse of the VC radius [29, 31]. This feature could reduce in size and cost of each subsequent device of this type [31, 32]. Looking forward, if breakeven could be achieved on one small POPS module, this could lead to the creation of a multimodule plant for energy production in the future [29, 31, 33]. Initially, it was assumed that POPS plasma is essentially non-neutral, and there would be enough electrons so that the volume charge would neutralize the plasma sphere at the moments of its collapse [29, 30]. Afterwards, it was shown that there are important limitations on the compression ratio that could be achieved in the original POPS scheme while maintaining the parabolic potential background and the neutralization of the spatial charge [34]. As a result, despite the potentially high efficiency of fusion of the POPS in theory [29, 30] and demonstration of the POPS in the initial experiment [31, 32], in further work, it was not possible to implement the original POPS scheme in nuclear fusion experiments [22, 34].

The study and development of compact IEC devices with ion oscillations is stimulated, in particular, by favorable scaling of fusion power derived for POPS [29, 30], which invites towards the miniaturization of devices. An IEC scheme with reverse polarity [21] based on a miniature nanosecond vacuum discharge (NVD) [35–37], in which ion oscillations occur quite naturally [38], has a direct relation to this. The NVD experiments and related PiC simulations began at the turn of the century, and over time, it became clear that some hopes associated with the potential advantages of nuclear fusion in the POPS scheme can be realized partially in a miniature NVD [38–41]. The yield of DD neutrons was observed previously and studied in detail in this device [35–41], and an aneutronic proton-boron synthesis was demonstrated also recently [20]. Interestingly, the field of the virtual cathode confines the oscillating ions in the NVD, and at the same time, the inertia of the oscillating ions partially holds the electrons of VC by electric fields. So we have called this type of confinement an electrodynamic or oscillatory one (OSCO) [20, 41].

This paper discusses and compares the features and capabilities of oscillating plasmas for nuclear fusion both in the POPS scheme [29, 31, 34] and the OSCO regime based on NVD [20, 35–41]. The study of a fundamental issue for IEC devices with electron injection as neutralization of the spatial charge started for NVD recently [42] and is developing further. Some prehistory and specifics of DD and pB nuclear synthesis study based on NVD are given in Section 2. The degree of quasineutrality of proton-boron

plasma in the OSCO scheme is investigated numerically in Section 3. An improved scaling of the DD fusion power has been determined for OSCO and compared with POPS in Section 4, and the energy distribution functions of protons and boron ions under pB fusion in the OSCO scheme, which are qualitatively different from the Maxwellian ones in the POPS scheme, are presented also. Section 5 discusses the evolution of the IEC reverse polarity scheme over the past half century and draws some conclusions for the future.

2. On DD and pB Nuclear Synthesis in Miniature Nanosecond Vacuum Discharge (NVD)

Experiments on X-ray generation and DD synthesis in NVD were started at the end of the last century [43], and both single and pulsating yields of DD neutrons were soon registered [35, 44]. However, for some time, the nature of DD neutrons was still unclear. Just subsequent 2D PiC modeling of the processes leading to DD synthesis in NVD [36], based on the full electrodynamic code KARAT [45] revealed the fundamental role of the formation of a virtual cathode (VC) and its corresponding deep potential well (PW) [37, 38], which accelerates and confines deuterons. In fact, the OSCO is based on an IEC scheme with reverse polarity [20, 21, 36, 37] and makes it possible to operate in a vacuum, where beams of auto-electrons from the cathode will be formed when the high voltage is applied. The auto-electrons, interacting with the deuterium-loaded Pd anode tubes, at first, will create erosive plasma [38, 46] near the anode with deuterons and deuterium-containing clusters. Secondly, the electron beams, while flying into the anode space (through the “mesh” of thin Pd tubes) are slowing down as they approach the discharge axis, and then change the direction of movement, thereby forming a VC and the PW corresponding thereto. Thus, the OSCO scheme based on miniature NVD, unlike the rather complex POPS experiment, includes the natural injection of auto-electrons into the anode space, the formation of a very small VC with a radius of $r_{VC} \sim 0.1$ cm, and a corresponding PW with a depth of $\varphi_{PW} \sim 50\text{--}100$ kV [20, 41]. Head-on collisions of deuterons accelerated in PW up to ~ 100 keV are accompanied by the release of DD neutrons. Deuterons can oscillate in the PW, and at the moments of their collapses at the PW bottom, the main DD synthesis takes place [38]. As a result, periodic oscillations of deuterons in PW are leading to the pulsating output of DD neutrons [35, 41, 47]. At the same time, the PW permanently holds the oscillating deuterons, since the energy they gain in the VC field is always insufficient to leave the well.

Earlier, in the POPS scheme, the scaling of the oscillation frequency f_{POPS} by the ion mass and the depth of the potential well was obtained [31, 32]. There was a good agreement between the observed resonant frequency for some test ions [31] and theoretical predictions for $f_{POPS} \approx (2e\varphi_{PW}/r_{VC}^2 m_i)^{1/2}/2\pi$ [32] (m_i -deuteron mass and e -electrostatic charge). In a more general case, a similar dependence of the ion oscillation frequency can be estimated from the inverse time of the ion flight by the radius of anode space to the discharge axis (Figure 1(a)) and back $f_{OSCO} \sim u_i/r_{VC}$, where $u_i \approx (Ze\varphi_{PW}/2m_i)^{1/2}$ -the average velocity of an ion with a charge Z . Remarkably, the theoretical POPS

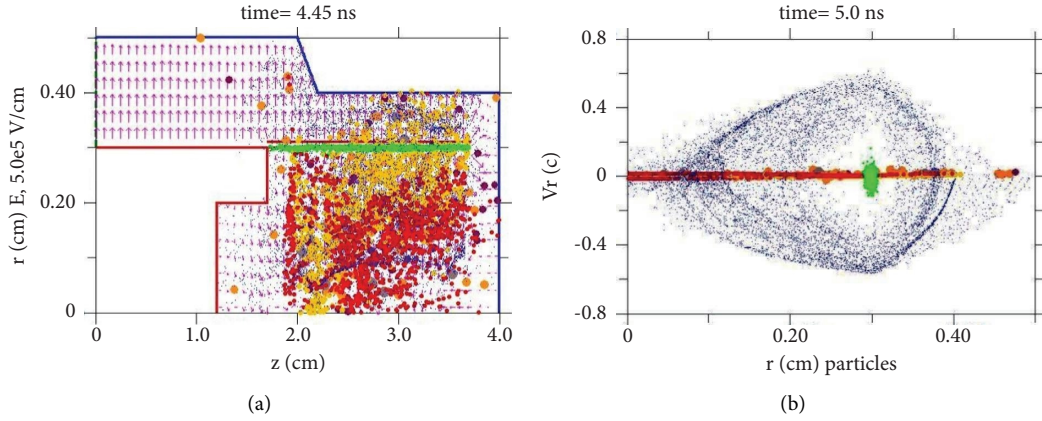


FIGURE 1: (a) Geometry of electrodes in nanosecond vacuum discharge (NVD) under PiC simulations of pB syntheses for $U=100$ kV and front $\Delta t_f=1$ ns (anode-red, cathode-blue, and green area-“anode plasma” with protons and boron ions). Electrons (blue dots), protons (red), and boron ions ($Z_B=+3$, yellow), and residues of pB reaction products are shown in the anode space at the simulation moment $t=4.45$ ns (circles of larger diameter, gray: $^8\text{Be}^*$, purple: primary α particles, dark orange: secondary α particles [20]). (b) The velocity of electrons on radius, $Vr/c < 0$, accelerated to an energy of ≈ 100 keV when passing in simulations through “the anode Pd tubes” (green area) at $t=5$ ns (c -velocity of light). The electrons are inhibited in the anode space close to the discharge axis, form a virtual cathode, $r_{VC} \approx 0.1$ cm and are reflected further ($Vr/c > 0$) by oncoming electron flows in the opposite direction (VC along axis Z is also visible in Figure 1(a)). Protons, boron ions, and pB reaction products are represented partially here also in the vicinity of $Vr/c \approx 0$.

scheme has some analogue of the oscillating deuterons in NVD which are manifesting through pulsating neutron yield observed [35, 41]. In fact, at the NVD experiment with deuterated Pd anode we have PW depth $\varphi \approx 50\text{--}60$ kV, namely, for deuterons (φ_{PW} is about 80% of the voltage applied), and the frequency of pulsating neutron yield registered comes to about ≈ 80 MHz [35, 36, 47]. A close value can be evaluated by extrapolation of expressions f_{POPS} or f_{OSC} presented above to the parameters of the NVD experiment and A-C geometry. Further definite similarities and differences of the POPS physics and some oscillating ions regimes at nanosecond vacuum discharge are discussed in Section 4.

It should be noted the great progress made in recent years in the study of laser-driven pB fusion and increasing α particles yields in the experiments related [13–19]. In addition to laser-driven fusion schemes, the implementation of pB fusion in one very compact device without the external influence of lasers or proton beams is also of fundamental and applied interest. In general, the scenario of DD synthesis in NVD with a virtual cathode remains valid for the pB reaction. By analogy with DD synthesis, PiC simulation showed that the proton-boron aneutronic reaction can also be achieved by accelerating and confining protons and boron ions by the field of the virtual cathode in NVD [48]. In the process of their oscillations in PW, head-on collisions of a part of protons and boron ions with energies of $\sim 100\text{--}500$ keV lead to a proton-boron reaction. The specifics of an OSCO at pB syntheses are that the oscillations periods of boron ions and protons are different due to the difference in their masses and charges. Nevertheless, under certain conditions, which are realized both in PiC simulations [48, 49] and in the testing experiments [20], these ions and protons can collide in the vicinity of the discharge axis and with a certain probability reaction pB takes place. The results of the first experiments on the pB fusion in miniature NVD

with plasma oscillatory confinement were presented recently [20]. The device is based on a low energy (≈ 1 J) NVD with a virtual cathode also. The field of VC accelerates protons and boron ions to the energy thresholds required for notable pB synthesis under the collapse of ions in the vicinity of the PW “bottom.” On average, the yield of α particles registered was about 250 α particles per one shot (≈ 1 J, voltage pulse $U \approx 100$ kV, duration $\tau \approx 20$ ns) in a given series of demonstration experiments [20]. As noted [20], the geometry of the old Pd anode used earlier in DD synthesis was sub-optimal, but it was very convenient for filling with boron nanoparticles due to the developed surface microrelief (Figure 3 in [20]). For the case of a larger number of well-defined oscillations of ions in a better geometry of electrodes (Figures 1(a) and 2(b)), we have to obtain at least $\sim 10^3/4\pi$ α particles per one J. This is still significantly less than what is observed in the modern laser-driven pB fusion experiments (where the yield of α particles can reach $\sim 10^7$ sr/J), from the outlet [16, 19]), but obtaining in a single miniature device without external influence of lasers or proton beams [20].

Let us note that the energies of protons (≤ 100 keV) and boron ions (≤ 500 keV) in the NVD are relatively small, for example, in comparison with those in the laser-driven proton-boron fusion [16]. As a result, the efficiency $Q = E_{\text{output}}/E_{\text{input}}$ in the first experiments on pB synthesis in a single miniature device for proton-boron plasma confinement also is still very low $\sim 10^{-9}$. If the voltage is increased to $U=150$ kV or higher, we can get closer to the main resonance peak of the pB reaction at 675 keV. Looking forward to an α particles source based on NVD, if we use a pulse periodic high voltage generator and solve the problem of heat dissipation, the α particles yield in NVD will be proportional to the frequency of the voltage applied, for example, at ~ 100 kHz it would be about 10^8 α particles/s. Again, it is not so much as for laser-driven α particles sources, but a practical niche as a simple and cheap compact

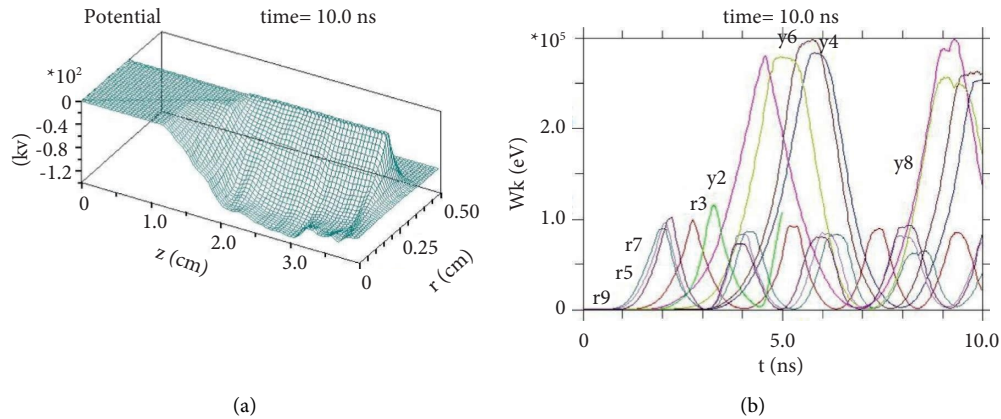


FIGURE 2: (a) The field of virtual cathode (or potential well) for $U = 100$ kV with a front $\Delta t_f = 1$ ns and (b) the energy of the isolated groups of boron ions ($Z_B = +3$, index (y)) and protons (index (r)) during their oscillations in the potential well on time (for $U_{\text{exp}} \approx 100$ kV with $\Delta t_f \approx 2$ ns).

α particle source is not excluded. Last but not least, further studies are to show the prospects for the creation of a practical miniature reactor for pB synthesis based on oscillatory confinement in NVD. In the very long term, if reasonable values $Q > 1$ would be achieved in a single miniature device (Chapter 13 in [22]), the possible route for energy production could be associated with a multimodule ($\sim 10^7$) arrays for a power plant which were suggested for fusion in a POPS scheme [31, 33].

3. Space Charge Neutralization and Degree of Quasineutrality in NVD

Neutralization of the space charge is an important issue under electron injection in devices like IEC [22, 29, 31]. In this section, we will consider the degree of plasma quasineutrality in the OSCO scheme at cylindrical geometry using the example of PiC modeling of pB synthesis. As earlier [20, 48], we will also use the code KARAT [45] for this purpose. It is a versatile FDTD relativistic, fully electromagnetic code based on the PIC method. The code is designed to solve nonstationary problems of electrodynamics having complex geometry and including plasma, electron, and ion beams. For current research [20], modeling of binary interaction has been added. It is based on PiC simulation of particle collisions and the subsequent generation of secondary particles with a probability corresponding to the velocity of the primary particles and theoretical or experimental cross-section. When modeling the processes leading to the synthesis of pB in NVD, we will derive the concentrations of all charged particles at different parts of the anode space (Figure 1(a)) on time. It will allow estimating the degree of plasma quasineutrality in anode space by radius. The 2D PiC simulations presented below were carried out for two cases: at the voltage applied of $U = 100$ kV with a voltage front $\Delta t_f = 1$ ns, and for the experimental values $U_{\text{exp}} \approx 100$ kV, $\Delta t_f \approx 2$ ns used for demonstration of the pB fusion in NVD [20] (VA characteristics of the voltage pulse-periodical generator are given in Figure 2(b) in [20]). There were 50 grid points by radius r

and 300 ones by Z axis under PiC simulations. The total number of macro particles was up to 10^6 .

In Figure 1(a) the cylindrical geometry of the electrodes is shown, with the anode-cathode (A-C) space 0.1 cm. In 2D simulations, a thin anode “plateau” inside the cathode corresponds to the real anode from cylindrical Pd tubes attached to the end of the anode along its perimeter [38]. On the left, a TEM wave from a high-voltage generator is launched into the coaxial along the axis Z .

In Figure 1(a), it shows the creation of an electric field between anode and cathode, providing auto-electronic emission. In this field, the electrons are accelerated by radius to the discharge center (blue dots are shown in the figures), and cross the anode (green area at $r \approx 0.3$ cm) with an energy of ≈ 100 keV ($Vr/c < 0$, Figure 1(b)). Irradiation of the anode by electron beams produces the “emission” of boron ions and protons. Penetrating further into the anode space, electrons are inhibited and reflected by oncoming flows and form a VC with a radius of ≈ 0.1 cm in a result (Figure 1; [20] for details and PiC simulations movie). Inside the anode the external pulse electric field is absent; however, the negative electric charge of electrons creates PW in the vicinity of the axis. It provides acceleration of protons and boron ions along the radius to the discharge axis Z ($r = 0$). Here, the latter’s velocity reaches its maximum value, as well as its density.

The potential well corresponding to the VC of the electron cloud inside the anode space is presented in Figure 2(a) (at the 10th ns of simulation). The PW depth is about ≈ 100 kV. In the pB fusion experiment, the anode Pd tubes were filled with hydrogen, and a tube surface with a microrelief developed is covered by boron nanoparticles [20]. The protons and boron ions will appear at the edge of the PW under irradiating Pd anode tubes by energetic electrons. In PiC modeling, the anode “tube” (Figure 1(a)) was also “fulfilled” by protons and boron ions (with a charge just of +3). Radial acceleration of protons and boron ions in the field of VC were followed by their oscillations in the deep PW, which will confine them also during oscillations.

The specifics of OSCO are illustrated in Figure 2(b), where the energies of randomly chosen isolated groups of protons (index r) and boron ions (index y) in PW on time are given. For this purpose, at five Z coordinates (in the range of 2–3 cm), the locations of protons and boron ions were randomly selected at $r = 0.3$ cm (distance to the anode, Figure 1(a)). The particles closest to these points were selected from the cloud of “anode plasma” at the initial moment of time. Furthermore, the histories of all particle parameters (coordinates, velocities, and energies) in time, as well as the electric fields acting on them, were traced. PiC modeling recognizes the oscillatory nature of confinement of protons and boron ions in PW; in fact, the maximum energy of the charges corresponds to the moment when they are passing through the discharge axis, and a minimum of kinetic energy corresponds to the full deceleration of ions in PW and a downward turn at its upper edge. Note that, fast boron ions appear for the voltage front $\Delta t_f \approx 2$ ns only in the time interval 4–5 ns (Figure 2(b)), while for the voltage front $\Delta t_f = 1$ ns they will appear already at 2–3 ns (not shown here), and also earlier than for $\Delta t_f \approx 2$ ns the first α particles will appear here (Section 4). For a voltage front $\Delta t_f = 5$ ns, fast boron ions and α particles will appear as in the first case at interval 4–5 ns (the results of 2D PiC simulations for the case of slower voltage rise $\Delta t_f = 5$ are presented in [42]).

The frequencies of oscillation for protons and boron ions are different (Figure 2(b)) since there is a difference in mass and charge (Section 2). This circumstance does not contribute properly to the efficiency of synthesis. Nevertheless, head-on collisions of protons and boron ions at the discharge axis and in its vicinity with sufficient energies lead to a pB reaction, and related α particles were registered in the first pB fusion NVD experiments [20]. Thus, Figures 1 and 2 illustrate the key role of formation VC and the deep PW related in the sequence of the main events leading to pB fusion in NVD.

Earlier, for the POPS model, there was a question on the amount of compression that can be achieved by oscillating plasmas while simultaneously maintaining parabolic background potential and space charge neutralization [31, 34]. Let us proceed to the analysis of the latter and the degree of quasineutrality of the pB plasma in the OSCO regime in NVD. For illustration, the rather typical concentration ratio of all charges at selected point $r = 0.2$ cm of the anode space on time is given in Figure 3. We see that, in general, the number of electrons slightly exceeds the total number of ions (curves in Figure 3 are calculated by the average over an area of ± 0.05 cm adjacent to the chosen point $r = 0.2$ cm). The concentration of protons fluctuates periodically on the electronic background, which corresponds to the arrival of protons in this area; meanwhile, the density of boron ions represents at this area of anode space something like a positively charged plateau. Underline, the concentration ratio of ions and electrons presented in NVD under simulations even far from the discharge axis (Figure 3) is different qualitatively and quantitatively from the ratio $n_i/n_e \sim 0.1$ accepted widely under the study and analysis of the POPS fusion scheme [29–33].

Let us consider in more detail the range which is closer to discharge axis under the short voltage front $\Delta t_f = 1$ ns. Figures 4(a) and 4(b) show the concentrations of

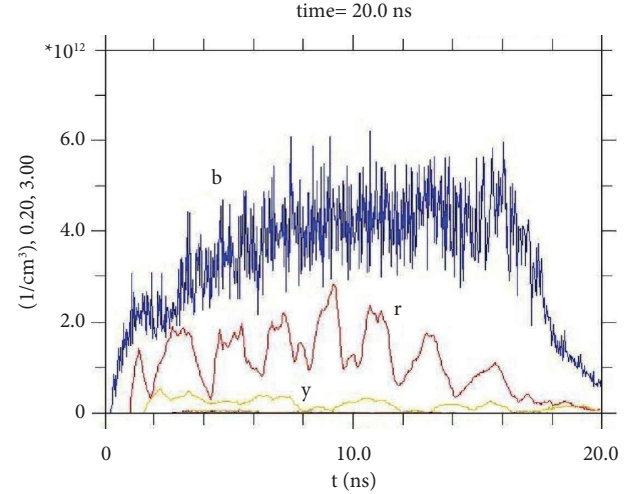


FIGURE 3: Density of electrons (b), protons (r), and boron ions (y) (with a charge of $Z_B = +3$) on time at the selected point by radius $r = 0.2$ cm of the anode space and the axis point $Z = 3$ cm Figure 1(a) for $U_{\text{exp}} \approx 100$ kV with a front $\Delta t_f \approx 2$ ns.

electrons, protons, and boron ions on time for two fixed points $r = 0.0$ cm and 0.1 cm by discharge radius at chosen $Z = 2.5$ cm on the discharge axis. The data in Figure 4(a) corresponds to a point $r = 0.1$ cm which is rather close to the axis (Figure 1(a)). The electron density is given by curve b , and curves r and y represent the densities of protons and boron ions, respectively. The first protons are coming to this area at $t \approx 2$ ns, and boron ions are appearing later due to the larger mass. We see that there are more electrons than ions in the entire time interval presented since $r \approx r_{\text{VC}} \approx 0.1$ cm. Meanwhile, on the axis of discharge (Figure 4(b), $r = 0.0$ cm), where n_e is several times higher than for the case of $r = 0.1$ cm, the electron density curve practically corresponds in magnitude to the total density of protons and boron ions (the latter have to be multiplied by their charge $Z_b = +3$) on time. Let us introduce the function $\mu(t) = -n_e(t) + n_p(t) + Z_B n_B(t)$ for a qualitative assessment of the degree of quasineutrality using the obtained graphs of electrons and ions concentrations (Figures 4(a) and 4(d)). Functions $\mu(t)$ are shown for both cases at Figure 4(c) ($r = 0.1$ cm) and Figure 4(d) ($r = 0.0$ cm), correspondingly. So we see that the plasma in the close vicinity of the discharge axis is almost a quasineutral one $n_i(t) \approx n_e(t)$ not only at individual moments of time but also during almost the entire time of simulation $t = 20$ ns (Figure 4(d)). Similar quasineutrality is available also for slower voltage rise $\Delta t_f = 5$ ns [42]. Remark, in the region of the anode space $r \approx 0.1$ cm, electrons, decelerating and unfolding, form a VC with a large electron density (Figure 1), and the deviation from quasineutrality there naturally should be maximal (Figure 4(c)).

At $t > 15$ ns, the “fuel” for pB nuclear fusion embedded in the “anode plasma” (Figure 1(a)) under simulation runs out (Figure 4).

To describe the degree of quasineutrality of the plasma, by analogy with [34], we introduce the parameter $\eta = n_{i0}/n_{e0}$, where n_{i0} is the initial ion density, $n_{e0} = n_e - n_i$ is the electron

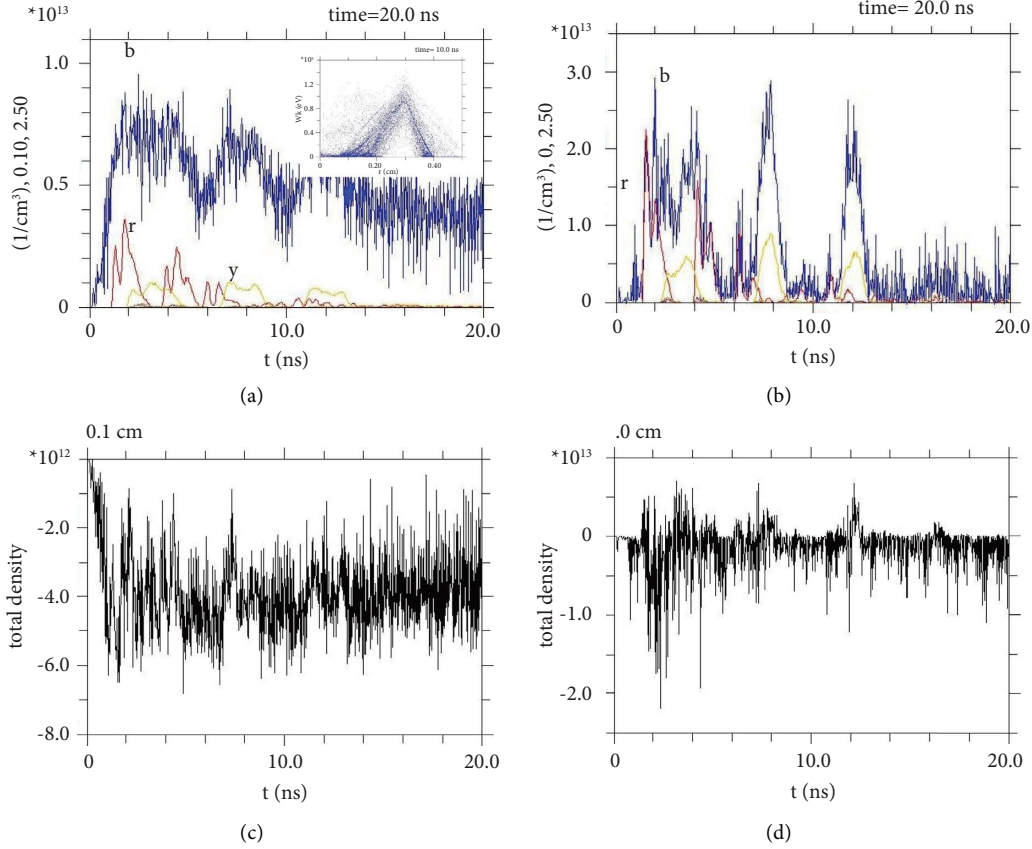


FIGURE 4: Concentrations of charges at selected points of the anode space on time at $Z=2.5$ cm (PiC simulations for an applied voltage $U=100$ kV with a front $\Delta t_f=1$ ns): (a) $r=0.1$ cm and (b) $r=0.0$ cm. The blue curves are electrons (b), the red ones are protons (r), and the yellow ones are boron ions (y) with a charge of $Z_B=+3$. The related values of total density of charges, or function $\mu(t)=-n_e(t)+n_p(t)+Z_B n_B(t)$, are given at (c) and (d) for radial points $r=0.1$ cm and $r=0.0$ cm, correspondingly (see text). The energy of electrons as a function of their position along the discharge radius is shown in the Figure 4(a) inset ($r_{VC}\approx 0.1$ cm, see Figure 1(a) also).

density which is forming a virtual cathode of homogeneous density (n_e and n_i are concentrations of electrons and ions, respectively, depending generally on coordinates and time). In a quasineutral limit, we have $n_{e0}\rightarrow 0$ and get $\eta\rightarrow\infty$ formally [34]. Based on the simulations presented above, we may conclude that in a certain area around the axis of discharge ($r=0$ cm) during the oscillations of ions in PW, the parameter of quasineutrality η can reach the local values of the order of 10–100 (after the first 3–4 ns, function $\mu(t)\approx 0$ fluctuates around zero, and almost does not change over time, as shown in Figure 4(d)).

4. Small-Scale Oscillations at the Quasineutral Limit in Vacuum Discharge. The Advantages and Limitations of a POPS Fusion Scheme

The advanced concept of POPS [29–33] gave a new strong pulse to the study of the IEC scheme with reverse polarity, especially in theory. It was shown that the total power of thermonuclear fusion in POPS is scaled as $P\sim\varphi_{PW}^2\eta^2\theta^2/r_{VC}$, where $\eta\approx n_i/n_e\sim 0.1$, $r_{VC}\sim a$ —anode space radius, and θ is the compression ratio [29, 31] (in the original POPS scheme, the value θ should be $\sim 10^3$). Thus, a critical advantage for

a POPS-like device for fusion is favorable fusion power scaling, which increases with the inverse of VC radius [29]. Each next POPS device generation has to be more efficient and smaller compared to the previous one [31], and it also might lead to a modular and high mass power density economical device (see Table I in [31] for potential applications of POPS fusion devices). Looking forward, it was remarked also that a multimodule power plant or advanced space propulsion [31, 33] could be considered if breakeven would be achieved.

Furthermore, the POPS scheme was demonstrated experimentally for H_2^+ , He^+ и Ne^+ ions for IEC with grids [31], where the ions exhibit resonant behavior in the field of VC when moving at the frequencies of POPS. The scaling of the oscillation frequency f_{POPS} by the ion mass and the depth of the potential well was obtained, and it was in good agreement with the predictions of the theory [32]. The PW depths estimated for the experiment did not exceed 300 V, and the ion oscillation frequencies did not exceed 700 kHz. Thus, the values of the applied voltage U were rather small there, and so far it was not about DD nuclear fusion. Nevertheless, the experiment on the demonstration of POPS was successful [31–33], but some factors such as a separate injection of electrons and setting external resonant pulses with

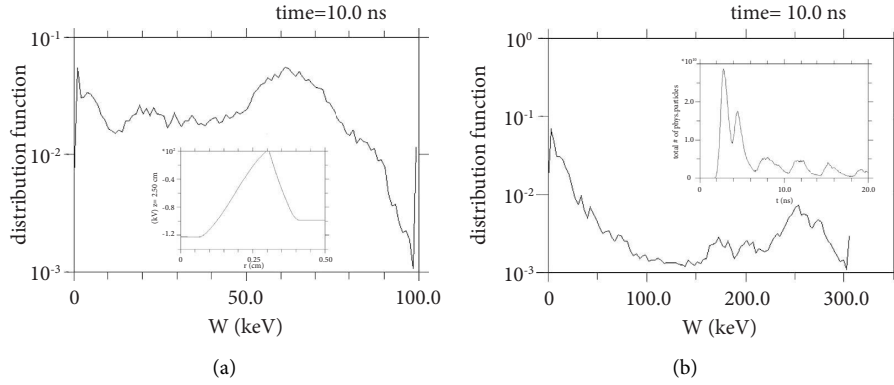


FIGURE 5: Energy distribution functions in NVD for (a) protons and (b) boron ions with charge $Z_B = +3$ for $U_{\text{exp}} \approx 100$ kV with a front $\Delta t_f \approx 2$ ns. The potential along the radius is shown at the inset in Figure 5(a) for $t = 10$ ns (it is cross section at $Z = 2.5$ cm for the PW presented in Figure 2(a)). The output of secondary α particles from pB reaction on time for $U = 100$ kV and $\Delta t_f = 1$ ns (see Figure 4(b) also) is shown at the inset in Figure 5(b).

a frequency of POPS made it quite complicated. Besides, a subsequent more detailed analysis by the authors of the POPS have shown [34] that there are some critical limitations on the degree of compression that can be achieved by an oscillating plasma while maintaining the neutralization of the spatial charge and the parabolic background potential. These conditions make operation in the POPS regime impractical [34].

At the same time, the work [34] has also suggested the use of small compressions as another option in the quasineutral limit $\eta \rightarrow \infty$ [34]. It was noted that this leads to a device different from the one originally envisioned for POPS. For the new device, POPS-type oscillations are primarily a mechanism of resonant ion heating, rather than coherent compression. Since the compression ratios are small there, a high ion temperature is required when the plasma is expanded [34]. Unlike the initial scenario with POPS, in these devices, it is possible to work with a mixture of deuterium and tritium also. Note that, a similar device was originally studied theoretically by Elmore et al. [21]. Apparently, small compressions, very small r_{VC} values, and plasma in the quasineutral limit are options which have been realized in experiments with miniature NVD independently [35, 36, 44]. This was preceded namely by a broad experimental search for the possibility of DD synthesis in a miniature NVD scheme [43, 44], partially stimulated at that time by the exciting results on DD fusion from explosions of femtosecond laser-heated deuterium clusters [50, 51].

In fact, oscillatory confinement in NVD also uses small POPS-type oscillations to heat the plasma [20, 41]. Present PiC simulations (as well as preliminary ones [42]) are showing that the oscillating plasma in the NVD near and on the discharge axis represents a rather quasineutral mode (Figure 4(d)), where the value of the parameter η can reach ~ 100 . Also, we can estimate the compression ratio value as just $\theta < 10$ if comparing charge densities on the discharge axis (Figure 4(b)) and far from the axis (Figure 3). The aneutronic pB synthesis demonstrated recently [20], where the working fuel mixture was of different masses, indirectly confirms also [34] that the plasma regime in NVD is

a quasineutral one. Note that, the experiment on DD synthesis in NVD [35, 44] with a small-scale deuteron oscillation (via neutron yield which is pulsating, Figure 4 in [35]) have appeared slightly earlier than small POPS-like oscillations were suggested to heat the plasma (Section 5 in [34]).

The physics of POPS and small-scale oscillations in NVD are different, nevertheless, favorable scaling of DD fusion power for POPS is also preserved for an OSCO. For the cylindrical geometry of NVD, we can get $P \sim \varphi_{PW}^2 \eta^2 \theta l / \pi e^2 r_{VC}^2$ (l is cylinder length and e is the electron charge). At the same time, the values of the parameters included in the expression for P will themselves vary greatly. For POPS we have $\eta \sim 0.1$ and $\theta \sim 10^3$ [29, 31], while for an OSCO we get $\eta \sim 100$ and $\theta \leq 10$ as well as the typical values $r_{VC} \sim 0.1$ cm and $\varphi_{PW} \sim 100$ kV, which are necessary especially for high fusion power [41] at miniature NVD.

The α particles yield in time, with the maxima at $t \approx 2.7$ ns and at $t \approx 4.2$ ns, shown at inset in Figure 5(b) (small maxima can be barely discerned in Figure 4(b) also, near the horizontal axis, where the densities of protons and boron ions are overlapped, and their energies are sufficient for pB synthesis). The energy of the accelerated protons under OSCO is close to the energy of the electrons injecting radially in the NVD scheme, which ensures its certain stability [21, 34]. However, the ion energy distribution functions remain non-Maxwellian ones [36, 49]. As an illustration, Figure 5 shows the distribution functions (DF) of protons and boron ions obtained in PiC simulations by averaging over the entire anode space (averaging only near the axis leads to a well-defined beam-like DF [22]). Underline, in the experiments with NVD available today, the ions flight time of the entire anode space volume turns out to be less than the time needed for ion-ion relaxation under ions converging to the discharge center [40]. As a result, we do not have the microvolumes of thermonuclear plasma in NVD (such as those predicted earlier [21] in similar, but spherical geometry), while DD [35–41] and aneutronic pB synthesis [20] are observed certainly in the nonequilibrium plasmas (Figure 5) remaining nonignited on the discharge axis [36, 49, 52] (remark, the role of nanoparticles in the

processes of X-ray generation and nuclear synthesis in NVD requires separate consideration, for example, [20, 46, 53, 54]). At the same time, it should be noted that obtaining the desired type of ion distribution functions between two opposite limits like “beam-Maxwellian” ones [22] is a challenging but promising future task. In particular, the type of DF and the specifics of the oscillations and confinement of boron ions are affected, for example, by the rate Δt_f in increase of the high voltage applied. In fact, with a slower voltage increase such as $\Delta t_f = 5$ ns [42], it is possible to obtain a “more Maxwellian” type of DF and a more stable acceleration and confinement of ions during their oscillations in potential well (Figure 2(b) in [42]) in comparison with the case $\Delta t_f = 1$ ns (not shown here), where the part of boron ions can leave rather deep PW (Figure 2(a)) along the axis Z .

5. Concluding Remarks

The concept of IEC was first suggested to try to solve the problem of controlled fusion by Lavrent'ev in 1950 (see [22–25, 28] and refs therein). The first theoretical paper on IEC appeared only in 1959 and was devoted to the IEC with reverse polarity [21]. A device with a nonparabolic potential well has been proposed for the plasma confinement at thermonuclear temperatures. The projection of electrons radially through the surface of a transparent spherical anode was considered. Electrons will be stopped by their mutual repulsion near the center and reflected back, which forms a negative electrostatic potential in the anode interior. Such a PW could ensure the convergence of radial ion flows to the center, where a high ion density can be achieved in the focus itself (we see that this even in detail resembles the physical processes presented in Figures 1 and 2 discussed above for almost parabolic PW at cylindrical geometry). The authors concluded that this scheme is unlikely to be realized as a real thermonuclear reactor, but “it may be suitable for obtaining small volumes of thermonuclear plasma for research” [21]. Despite the relative simplicity of IEC devices with reverse polarity, their evolution is progressing quite slowly. The advanced IEC scheme with POPS proposed only 40 years later [29, 30] has promised in theory the efficiency necessary even for the generation of fusion energy. Unfortunately, it was not possible to move further in the POPS experiments with thermal ions in modified Penning traps [29, 55, 56] and realize the predicted favorable scaling of the fusion power [22, 31, 34].

In order to continue the studies of the IEC with reverse polarity, and relying on the PiC simulations using the electromagnetic code [36, 37, 41], over the past two decades we have been able to implement experimentally both DD synthesis [35, 38, 39, 41, 47] and aneutronic pB synthesis [20, 48, 49] in a miniature NVD with oscillatory confinement. The OSCO, like the POPS scheme, has a very advantageous scaling of nuclear fusion power, and, together with a very small VC radius ($r_{VC} \sim 0.1$ cm, Figure 1) and deep PW (~ 100 kV, Figure 2(a)), it provides high fusion power density in NVD [41, 47]. As shown by the PiC simulations presented above, the neutralization of the spatial charge is

not a problem for an OSCO in cylindrical geometry (Figures 3 and 4), unlike the POPS scheme in the spherical one [34]. The NVD plasma turns out to be quasineutral in the anode space with an accuracy up to a factor of ~ 2 , while in the vicinity and on the discharge axis, where pB synthesis is most likely, it is practically a neutral one (the latter is illustrated also by the view of potential well ϕ_{PW} at $r \leq 0.1$ cm, where the field strength ≈ 0 , Figure 5(a) inset). Nevertheless, the features of scaling of DD fusion power, and especially the specifics of pB fusion power in NVD under oscillatory confinement discussed above, require further more detailed analysis, including the analogue of Lawson criterion [22] for pB fusion.

Overall, it is clear also that the key problem for further work is finding ways to improve the efficiency of available an OSCO scheme. At the present stage of the pB fusion experiment [20], the optimization of geometry and parameters of the discharge can contribute to this goal, which can move closer in ions energies to the maximum of pB reaction cross-section, provide well-defined ions oscillations in the PW at higher energies, shift the DF view towards the Maxwellian type, etc. Apparently, at the next stage of the work, it will be necessary to add a magnetic field in the experiment to confine better the electrons of the virtual cathode, for example, on the basis of the small-scale Polywell-like [22, 57, 58] configuration. It might increase VC lifetime which would provide periodical pB synthesis near the discharge axis (Figures 4(b) and 5(b) inset) without additional injection of electrons and get the higher efficiency. Then, the hypothetical breakeven for pB fusion will be achieved by summation of very small gains over the entire periodic very short times of “nonthermonuclear” pB burning during the whole time [47] of oscillatory confinement needed to get $Q > 1$.

Data Availability

The data used to support the findings of this study are included within the article.

Conflicts of Interest

The authors declare that there are no conflicts of interest.

Acknowledgments

The authors would like to thank V. E. Ostashev, V. A. Zeigarnik, and A. Yu Varaksin for stimulating discussions and support of the work. The authors would like to thank also the company HB11 Energy Pty Ltd for the support of APC for the publication of this paper.

References

- [1] M. L. E. Oliphant and E. Rutherford, “Experiments on the transmutation of elements by protons,” *Proceedings of the Royal Society of London - Series A: Containing Papers of a Mathematical and Physical Character*, vol. 141, p. 259, 1933.
- [2] P. I. Dee and C. Gilbert, “The disintegration of boron into three α -particles,” *Proceedings of the Royal Society of London*,

- Series A: Mathematical and Physical Sciences*, vol. 154, p. 279, 1936.
- [3] S. Atzeni and J. Meyer-ter Vehn, *The Physics of Inertial Fusion: Beam-Plasma Interaction, Hydrodynamics, Hot Dense Matter*, Oxford University Press, Oxford, UK, 2004.
 - [4] E. Teller, Ed., *Fusion. Hardcover*, Academic Press, Cambridge, Massachusetts, 1981.
 - [5] W. J. Hogan, Ed., *Energy from Inertial Fusion*, International Atomic Energy Agency Vienna, Vienna, Austria, 1995.
 - [6] B. Yu. Sharkov, Ed., *Nuclear Syntheses with Inertial Confinement*, FIZMATLIT, Moscow, 2005.
 - [7] D. C. Moreau, "Potentiality of the proton-boron fuel for controlled thermonuclear fusion," *Nuclear Fusion*, vol. 17, no. 1, pp. 13–20, 1977.
 - [8] N. Rostoker, A. Qerushi, and M. Binderbauer, "Colliding beam fusion reactors," *Journal of Fusion Energy*, vol. 22, no. 2, pp. 83–92, 2003.
 - [9] H. Hora, S. Eliezer, G. J. Kirchhoff et al., "Road map to clean energy using laser beam ignition of boron-hydrogen fusion," *Laser and Particle Beams*, vol. 35, no. 4, pp. 730–740, 2017.
 - [10] G. A. P. Cirrone, L. Manti, D. Margarone et al., "First experimental proof of Proton Boron Capture Therapy (PBCT) to enhance protontherapy effectiveness," *Scientific Reports*, vol. 8, no. 1, p. 1141, 2018.
 - [11] S. M. Qaim, I. Spahn, B. Scholten, and B. Neumaier, "Uses of alpha particles, especially in nuclear reaction studies and medical radionuclide production," *Radiochimica Acta*, vol. 104, no. 9, pp. 601–624, 2016.
 - [12] V. S. Belyaev, A. P. Matafonov, V. I. Vinogradov et al., "Observation of neutronless fusion reactions in picosecond laser plasmas," *Physical Review E - Statistical Physics, Plasmas, Fluids, and Related Interdisciplinary Topics*, vol. 72, no. 2, Article ID 026406, 2005.
 - [13] C. Labaune, C. Baccou, S. Depierreux et al., "Fusion reactions initiated by laser-accelerated particle beams in a laser-produced plasma," *Nature Communications*, vol. 4, no. 1, p. 2506, 2013.
 - [14] A. Picciotto, D. Margarone, A. Velyhan et al., "Boron-protonnuclear-fusion enhancement induced in boron-doped silicon targets by low-contrast pulsed laser," *Physics Reviews X*, vol. 4, no. 3, Article ID 031030, 2014.
 - [15] C. Baccou, S. Depierreux, V. Yahia et al., "New scheme to produce aneutronic fusion reactions by laser-accelerated ions," *Laser and Particle Beams*, vol. 33, no. 1, pp. 117–122, 2015.
 - [16] L. Giuffrida, F. Belloni, D. Margarone et al., "High-current stream of energetic α particles from laser-driven proton-boron fusion," *Physical Review*, vol. 101, no. 1, Article ID 013204, 2020.
 - [17] V. S. Belyaev, A. P. Matafonov, V. P. Krainov et al., "Simultaneous investigation of the nuclear reactions B and BC as a new tool for determining the absolute yield of alpha particles in picosecond plasmas," *Physics of Atomic Nuclei*, vol. 83, no. 5, pp. 641–650, 2020.
 - [18] J. Bonvalet, Ph. Nicolai, D. Raffestin et al., "Energetic α -particle sources produced through proton-boron reactions by high-energy-high-intensity laser beams," *Physical Review*, vol. 103, no. 5, Article ID 053202, 2021.
 - [19] D. Margarone, J. Bonvalet, L. Giuffrida et al., "In-target proton-boron nuclear fusion using a PW-class laser," *Applied Sciences*, vol. 12, no. 3, Article ID 12031444, 2022.
 - [20] Yu. K. Kurilenkov, A. V. Oginov, V. P. Tarakanov, S. Yu. Gus'kov, and I. S. Samoylov, "Proton-boron fusion in a compact scheme of plasma oscillatory confinement," *Physical Review*, vol. 103, no. 4, Article ID 043208, 2021.
 - [21] W. C. Elmore, J. L. Tuck, and K. M. Watson, "On the inertial-electrostatic confinement of a plasma," *Physics of Fluids*, vol. 2, no. 3, p. 239, 1959.
 - [22] G. H. Miley and S. K. Murali, *Inertial Electrostatic Confinement (IEC) Fusion Fundamentals and Applications*, Springer, Berlin/Heidelberg, Germany, 2014.
 - [23] O. Lavrent'ev, L. Ovcharenko, B. Safronov, V. Sidorkin, and B. Nemashkalo, "Jenergiya i plotnost' ionov v jelek-tromagnitnoj lovushke," *Ukrainian Journal of Physics*, vol. 8, pp. 440–445, 1963.
 - [24] O. A. Lavrent'ev, "Electrostatic and electromagnetic high-temperature plasma traps," *Annals of the New York Academy of Sciences*, vol. 251, no. 1, pp. 152–178, 1975.
 - [25] B. D. Bondarenko, "Role played by O A Lavrent'ev in the formulation of the problem and the initiation of research into controlled nuclear fusion in the USSR," *Physics-Uspekhi*, vol. 44, no. 8, p. 886, 2001.
 - [26] P. T. Farnsworth, *Electric Discharge Device for Producing Interactions between Nuclei*, United States Patent, Alexandria, Virginia, 1966.
 - [27] R. L. Hirsch, "Inertial-electrostatic confinement of ionized fusion gases," *Journal of Applied Physics*, vol. 38, no. 11, pp. 4522–4534, 1967.
 - [28] T. J. Dolan, "Magnetic electrostatic plasma confinement," *Plasma Physics and Controlled Fusion*, vol. 36, no. 10, pp. 1539–1593, 1994.
 - [29] R. A. Nebel and D. C. Barnes, "The periodically oscillating plasma sphere," *Fusion Technology*, vol. 34, no. 1, pp. 28–45, 1998.
 - [30] D. C. Barnes and R. A. Nebel, "Stable, thermal equilibrium, large-amplitude, spherical plasma oscillations in electrostatic confinement devices," *Physics of Plasmas*, vol. 5, no. 7, pp. 2498–2503, 1998.
 - [31] J. Park, R. A. Nebel, S. Stange, and S. K. Murali, "Periodically oscillating plasma sphere," *Physics of Plasmas*, vol. 12, no. 5, Article ID 056315, 2005.
 - [32] J. Park, R. A. Nebel, S. Stange, and S. K. Murali, "Experimental observation of a periodically oscillating plasma sphere in a gridded inertial electrostatic confinement device," *Physical Review Letters*, vol. 95, no. 1, Article ID 015003, 2005.
 - [33] J. Park, R. A. Nebel, R. Aragona, M. R. Kostora, and E. G. Evstatiev, "high voltage operation of inertial electrostatic confinement (IEC) device for neutron generation and periodically oscillating plasma sphere (POPS)," in *Proceedings of the Innovative Confinement Concepts Workshop*, Texas, Austin USA, February, 2006, <https://icc2006.ph.utexas.edu/proceedings.php>.
 - [34] E. G. Evstatiev, R. A. Nebel, L. Chacon, J. Park, and G. Lapenta, "Space charge neutralization in inertial electrostatic confinement plasmas," *Physics of Plasmas*, vol. 14, no. 4, Article ID 042701, 2007.
 - [35] Y. K. Kurilenkov, M. Skowronek, and J. Dufty, "Multiple DD fusion events at interelectrode media of nanosecond vacuum discharge," *Journal of Physics A: Mathematical and General*, vol. 39, no. 17, pp. 4375–4386, 2006.
 - [36] Y. K. Kurilenkov, V. P. Tarakanov, M. Skowronek, S. Yu. Guskov, and J. Dufty, "Inertial electrostatic confinement and DD fusion at interelectrode media of nanosecond vacuum discharge. PIC simulations and experiment," *Journal of Physics A: Mathematical and Theoretical*, vol. 42, no. 21, Article ID 214041, 2009.

- [37] Y. K. Kurilenkov, V. P. Tarakanov, and S. Y. Gus'kov, "Inertial electrostatic confinement and nuclear fusion in the interelectrode plasma of a nanosecond vacuum discharge," II: particle-in-cell simulations," *Plasma Physics Reports*, vol. 36, no. 13, pp. 1227–1234, 2010.
- [38] Y. K. Kurilenkov, V. P. Tarakanov, S. Y. Gus'kov, V. T. Karpukhin, and V. E. Valyano, "Warm dense matter generation and dd synthesis at vacuum discharge with deuterium-loaded pd anode," *Contributions to Plasma Physics*, vol. 51, no. 5, pp. 427–443, 2011.
- [39] Y. K. Kurilenkov, V. P. Tarakanov, V. T. Karpukhin, S. Y. Gus'kov, and A. V. Oginov, "Nuclear burning in a compact scheme of inertial electrostatic confinement as imitation of stellar nucleosynthesis. Experiment and PIC modeling," *Journal of Physics: Conference Series*, vol. 653, Article ID 012025, 2015.
- [40] S. Y. Gus'kov and Y. K. Kurilenkov, "Neutron yield and Lawson criterion for plasma with inertial electrostatic confinement," *Journal of Physics: Conference Series*, vol. 774, Article ID 012132, 2016.
- [41] Y. K. Kurilenkov, V. P. Tarakanov, S. Y. Gus'kov, A. Oginov, and V. Karpukhin, "Oscillating ions under Inertial Electrostatic Confinement (IEC) based on nanosecond vacuum discharge," *Contributions to Plasma Physics*, vol. 58, no. 10, pp. 952–960, 2018.
- [42] Y. K. Kurilenkov, V. P. Tarakanov, A. V. Oginov, S. Yu. Gus'kov, and I. S. Samoylov, "On the plasma quasi-neutrality under oscillatory confinement based on a nanosecond vacuum discharge," *Applied Physics*, vol. 6, pp. 14–23, 2021.
- [43] Y. K. Kurilenkov, M. Skowronek, G. Louvet, A. A. Rukhadze, and J. Dufty, "Suprathermal hard X-rays and energetic particles from plasmas "dust,"" *Journal de Physique IV*, vol. 10, no. PR5, pp. 409–415, 2000.
- [44] Y. K. Kurilenkov and M. Skowronek, "Hard X-ray bursts and DD microfusion neutrons from complex plasmas of vacuum discharge," *Pramana - Journal of Physics*, vol. 61, no. 6, pp. 1187–1196, 2003.
- [45] V. P. Tarakanov, "Code KARAT in simulations of power microwave sources including Cherenkov plasma devices, vircators, orotron, E-field sensor, calorimeter etc," *European physical journal web of conferences*, vol. 149, Article ID 04024, 2017.
- [46] A. Y. Varaksin, "Effect of macro-micro-and nanoparticles on turbulence in a carrier gas," *Doklady Physics*, vol. 66, no. 3, pp. 72–75, 2021.
- [47] Y. K. Kurilenkov, V. P. Tarakanov, S. Y. Gus'kov, A. V. Oginov, and I. S. Samoylov, "On pulsating DD neutron yield under inertial electrostatic confinement of complex plasma at miniature vacuum discharge," *Journal of Physics: Conf. Ser.*, vol. 1147, Article ID 012103, 2019.
- [48] Y. K. Kurilenkov, V. P. Tarakanov, and S. Y. Gus'kov, "Simulation of proton–boron nuclear burning in the potential well of virtual cathode at nanosecond vacuum discharge," *Journal of Physics: Conference Series*, vol. 774, Article ID 012133, 2016.
- [49] Y. K. Kurilenkov, V. P. Tarakanov, S. Y. Gus'kov, I. S. Samoylov, and V. E. Ostashev, "On the features of bursts of neutrons, hard x-rays and alpha-particles in the pulse vacuum discharge with a virtual cathode and self-organization," *Journal of Physics: Conference Series*, vol. 653, Article ID 012026, 2015.
- [50] T. Ditmire, J. Zweiback, V. P. Yanovsky, T. E. Cowan, G. Hays, and K. B Wharton, "Nuclear fusion from explosions of femtosecond laser-heated deuterium clusters," *Nature (London)*, vol. 398, no. 6727, pp. 489–492, 1999.
- [51] J. Zweiback, R. A. Smith, T. E. Cowan et al., "Nuclear fusion driven by Coulomb explosions of large deuterium clusters," *Physical Review Letters*, vol. 84, no. 12, pp. 2634–2637, 2000.
- [52] R. L. Hirsch, "Where to look for practical fusion power," in *Proceedings of the 14th U.S.-Japan IECF Workshop*, Maryland USA, October, 2012, <https://archive.nytimes.com/dotearth.blogs.nytimes.com/2012/10/19/a-veteran-of-fusion-science-proposes-narrowing-the-field>.
- [53] I. V. Smetanin, Y. K. Kurilenkov, A. V. Oginov, V. P. Tarakanov, and I. S. Samoylov, "Polydisperse inter-electrode plasma of Pd nanoclusters as a random cavity for x-ray spontaneous emission bursts," *Plasma Res. Express*, vol. 3, no. 1, Article ID 015003, 2021.
- [54] A. Y. Varaksin, "Two-phase boundary layer of gas with solid particles," *High Temperature*, vol. 58, no. 5, pp. 716–732, 2020.
- [55] D. C. Barnes, † M. M. Schauer, K. R. Umstadter, L. Chacon, and G. Miley, "Electron equilibrium and confinement in a modified Penning trap and its application to Penning fusion," *Physics of Plasmas*, vol. 7, no. 5, pp. 1693–1701, 2000.
- [56] D. C. Barnes, "Penning traps as neutron sources," in *Proceedings of the 16th US-Japan Workshop on Fusion Neutron Sources for Nuclear Assay and Applications*, Madison, Wisconsin USA, October 2014.
- [57] R. W. Bussard, "The advent of clean nuclear fusion: super-performance space power and propulsion," in *Proceedings of the 57th International Astronautical Congress (IAC)*, Valencia, Spain, October 2006.
- [58] J. F. Santarius, "Polywell physics modeling considerations," in *Proceedings of the 16th US-Japan Workshop Madison*, Wisconsin USA, October 2014.



Research Article

Cross-Section Measurements of the $^{11}\text{B}(p,\alpha)2\alpha$ Reaction near the First Resonant Energy

Shizheng Zhang ¹, Hao Xu,¹ Xing Xu,² Wenqing Wei,¹ Jieru Ren,¹ Benzhen Chen,¹ Bubo Ma,¹ Zhongmin Hu,¹ Fangfang Li,¹ Lirong Liu,¹ Mingzhe Yang,¹ Zeyu Lai,¹ Hongwei Yue,¹ Jie Xiong,¹ Zhongfeng Xu,¹ Yanhong Chen,² Zhao Wang,² Zexian Zhou,² Lulin Shi,² Rui Cheng ², Zhigang Deng,³ Wei Qi,³ Weimin Zhou,³ Guanchao Zhao,^{4,5} Bing Liu,^{4,5} Di Luo,^{4,5} Dieter H. H. Hoffmann ¹, and Yongtao Zhao ¹

¹MOE Key Laboratory for Nonequilibrium Synthesis and Modulation of Condensed Matter, School of Physics, Xi'an Jiaotong University, Xi'an 710049, China

²Institute of Modern Physics, Chinese Academy of Sciences, Lanzhou 730070, China

³Science and Technology on Plasma Physics Laboratory, Laser Fusion Research Center, China Academy of Engineering Physics, Mianyang 621900, China

⁴Hebei Key Laboratory of Compact Fusion, Langfang 065001, China

⁵ENN Science and Technology Development Co., Ltd., Langfang 065001, China

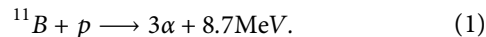
Correspondence should be addressed to Yongtao Zhao; zhaoyongtao@xjtu.edu.cn

Received 2 September 2022; Revised 26 October 2022; Accepted 25 November 2022; Published 14 February 2023

Academic Editor: Dimitri Batani

Copyright © 2023 Shizheng Zhang et al. This is an open access article distributed under the Creative Commons Attribution License, which permits unrestricted use, distribution, and reproduction in any medium, provided the original work is properly cited.

In preparation for an experiment with a laser-generated intense proton beam at the Laser Fusion Research Center at Mianyang to investigate the $^{11}\text{B}(p,\alpha)2\alpha$ reaction, we performed a measurement at very low proton energy between 140 keV and 172 keV using the high-voltage platform at the Institute of Modern Physics, Lanzhou. The aim of the experiment was to test the ability to use CR-39 track detectors for cross-section measurements and to remeasure the cross-section of this reaction close to the first resonance using the thick target approach. We obtained the cross-section $\sigma = 45.6 \pm 12.5$ mb near 156 keV. Our result confirms the feasibility of CR-39 type track detector for nuclear reaction measurement also in low-energy regions.



1. Introduction

The $^{11}\text{B}(p,\alpha)2\alpha$ fusion reaction shows great prospects in many fields. For example, $p^{11}\text{B}$ fusion is regarded as a neutron-free nuclear reaction and is a favorable candidate for fusion energy [1, 2]. The cross section of the $^{11}\text{B}(p,3\alpha)$ provides a direct probe for structures in ^{12}C [3]. The study of the reaction can also give useful information to explain the astrophysical abundances of elements Li, Be, and B in young main-sequence *F* and *G* stars [4]. Besides, the $^{11}\text{B}(p,\alpha)2\alpha$ reaction provides a new method of cancer treatment [5].

The $^{11}\text{B}(p,\alpha)2\alpha$ nuclear fusion reaction was first studied in the 1930s by Oliphant and Rutherford [6]:

Shortly after, Dee and Gilbert [7] observed the breakdown of B into three particles with cloud track photographs. Then, the reaction has been studied numerous times to measure its cross-section [8–10]. Based on these experimental data, the empirical formula for the cross-sections is given by Nevins and Swain [11]. In 2005, Belyaev et al. [12] experimentally achieved the $p^{11}\text{B}$ fusion reaction by using an intense ps laser beam for the first time. Recently, experiments using laser-driven proton beams to initiate the $p^{11}\text{B}$ fusion reaction have demonstrated increasing α yields [13, 14], which has led

to renewed interest in the scientific community for possible fusion energy applications.

In the laser-driven $p^{11}\text{B}$ fusion experiments, CR-39 type track detectors are used instead of silicon detectors like in usual nuclear physics experiments to detect ionizing particles [12–14]. CR-39 type track detectors are polyallyldiglycol-carbonate (PADC) films composed of $\text{C}_{12}\text{H}_{18}\text{O}_7$. The CR-39 type track detectors measure the absolute number of ions and are not sensitive to low fluxes of electrons and photons [15]. In preparation for an experiment with a laser-generated intense proton beam at the Laser Fusion Research Center at Mianyang to investigate the $^{11}\text{B}(p,\alpha)2\alpha$ reaction, we performed an experiment to test the applicability of CR-39 type track detectors for cross-section measurement. We remeasured the cross-section of $^{11}\text{B}(p,\alpha)2\alpha$ close to its first resonance and compared it to previous results.

Here, we report a measurement of the cross-section with a thick target and CR-39 type track detectors in the proton energy range of 140 keV–172 keV.

2. Experiment

The experiment was carried out at the 320 kV high-voltage platform at the Institute of Modern Physics in Lanzhou, mapping the energy region of the resonance at keV of proton energy $E_p = 163$. As shown in Figure 1(a), the proton beam passed through the magnetic quadrupole lens and the Faraday cup. It was then focused on the target with a focal spot diameter of about 1 mm. As shown in Figure 1(b), the incident energy of the proton beam was varied from 140 keV to 172 keV in steps of 4 keV, and the accuracy of the energy is $\Delta E/E = \pm 2 \times 10^{-4}$. We used a thick target of natural boron, and the irradiation was carried out to irradiate the target from top to bottom, leaving a gap of 4 mm between each irradiation spot. The beam current was kept to about $1 \mu\text{A}$. We aimed to have a total proton number on target 10^{15} and used a Faraday for monitoring. The arrangement was such that the proton beam was perpendicular to the target and parallel to the CR-39 track detector. The target is natural boron with a density of $2.35 \pm 0.02 \text{ g/cm}^3$, composed of 80.1% ^{11}B and 19.9% ^{10}B . The target has a thickness of $5.0 \pm 0.1 \text{ mm}$ with dimensions of $40 \pm 1 \text{ mm} \times 44 \pm 1 \text{ mm}$.

The CR-39 type track detector, with a size of $50 \pm 1 \text{ mm} \times 50 \pm 1 \text{ mm} \times 1 \pm 0.1 \text{ mm}$, was placed at 90° perpendicular to the target surface at a distance of 3 mm from the incident beam spot (Figure 1(b)). After irradiation, the CR-39 type track detector was chemically etched in a 6.0 mol/L NaOH solution and kept at a constant temperature of $80.0 \pm 0.5^\circ\text{C}$ for 1 h. Then the CR-39 type track detector was processed by washing, soaking, and drying to eliminate the interference of water droplets, stains, dust, etc. After this appropriate treatment, the tracks of α particles and protons with their respective diameters on the CR-39 type track detector were imaged and measured by an automatic track image analyzer. The measurement error of the track diameter does not exceed 0.05 μm .

3. Results and Discussion

Both, α particles and scattered protons reach the CR-39 type track detector, therefore, it is necessary to tell them apart using the track diameters as a distinguishing feature. We measured α particle tracks on a CR-39 type track detector using a standard ^{241}Am source emitting α particles at an energy of 5.49 MeV, as shown in Figure 2(a). The track diameters of α particles are near to $10 \mu\text{m}$, which is consistent with the results of Hicks [16], who etched the CR-39 type track detector with a solution of the same concentration and temperature as we did. According to Hicks' result, the proton track diameters are smaller than α particle track diameters. Combining our results with Hicks', we believe that there is a great difference in track diameter between protons and α particles, from Figure 2(b) it is obvious to distinguish the tracks with different diameters. Here, the elliptical tracks of protons are caused by the large angle of backscattering. As shown in Figure 1(b), the collected particles on the CR-39 type track detector arise from nine different incident spots. Therefore, particles directed to incident spots far away will have a large incident angle, which leads to the elliptical tracks.

Figure 3 shows the number of detected particle tracks as a function of the track diameter with different etching times. The red line in the figure represents a double-gauss-curve fitting. For both etching times of 1 hour and 3 hours, there are two Gaussian peaks. The first peak is due to protons, and the second peak is caused by α particles.

Figure 2(b) and Figure 2(d) display the tracks without Al film and with $5 \mu\text{m}$ Al film after 3 h etching, respectively. We find that the number of tracks on a CR-39 type track detector with Al film is much less than that without Al film because most of the particles are protons and low-energy protons are filtered out by Al film, which is consistent with the results shown in Figure 3.

In addition, Figure 3 shows that when the etching time is 1 h, the proton track diameter and α track diameter overlap considerably; when the etching time is 3 h, the overlap area of the two tracks is small. This is due to the fact that the etching rates of proton and α particle tracks are different. As the etching time increases, the gap in track diameter will gradually increase. Therefore, it is more convincing to distinguish the two particle species with an etching time of more than 3 h.

However, there still remains some ambiguity because some particle tracks have a large range of mutual masking after an etching time of 3 hours. Therefore, we decided to calculate the yield based on an etching time of 1 hour.

As shown in Figure 3(a), because the proton track diameter and α track diameter overlap considerably, we finally choose the intersection of two Gaussian curves to distinguish two particle species. Thus, tracks with a diameter of more than $2.7 \mu\text{m}$ are considered to be due to α particles. With this assumption, the relative systematic error is 7%.

As shown in Figure 1(b), for any region (for example, the red circle on the detector), on a CR-39 type track detector, the collected particles are the contribution of nine incident proton beams. We select nine regions on a CR-39 type track

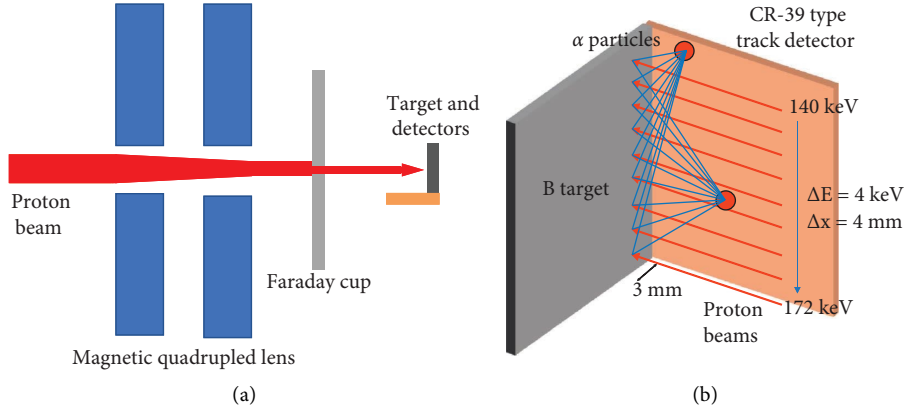


FIGURE 1: Experimental setup. (a) The proton beam passed through the magnetic quadrupled lens and the Faraday cup and then was focused onto (b) the target (grey) and CR-39 type track detector (orange-yellow). The proton energy scan was performed from 140 keV to 172 keV in steps of 4 keV near the $E_p = 163 \text{ keV}$ resonance, forming 9 spots with 4 mm intervals. The irradiation time for each energy is approximately 200 s, with a beam current of about $1 \mu\text{A}$. The particles collected by any region (for example, the red circle) of the CR-39 track detector are the contribution of all nine incident proton beams.

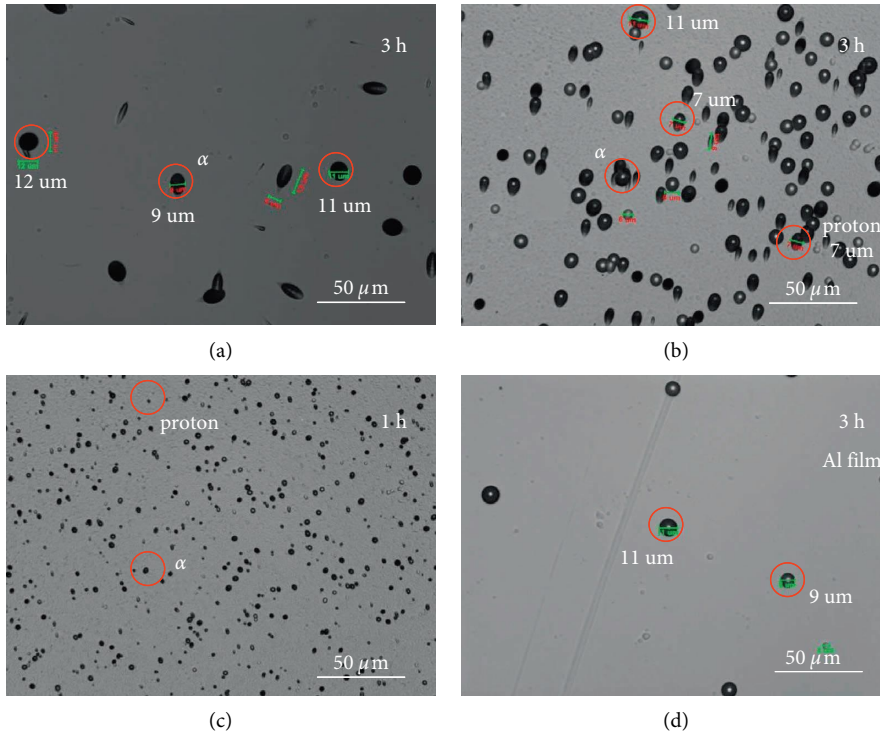


FIGURE 2: Tracks on a CR-39 type track detector. (a) 5.49 MeV α particle tracks from a ^{241}Am radioactive source after 3 h of etching. (b) Experimental particle tracks after 3 h of etching. (c) Experimental particle tracks after 1 h of etching. (d) Experimental particle tracks with the 5 μm Al after 3 h of etching.

detector with uniform brightness and fewer bubbles near each spot, and then the equations are constructed as follows:

$$\sum_{j=1}^9 \frac{\Omega_{i,j}}{4\pi} \rho_{i,j} N_{\alpha,j} = N_{\text{CR39}}(i), i = 1, 2, \dots, 9, \quad (2)$$

where $N_{\alpha,j}$ is the α particle yield corresponding to the j_{th} incident beam, $N_{\text{CR39}}(i)$ is the number of α particles detected on the i_{th} CR-39 type track detector region, Ω_{ij} is the solid angle of the j_{th} proton beam to the i_{th} CR-39 type track detector region. ρ_{ij} represents the ratio of α particles that can

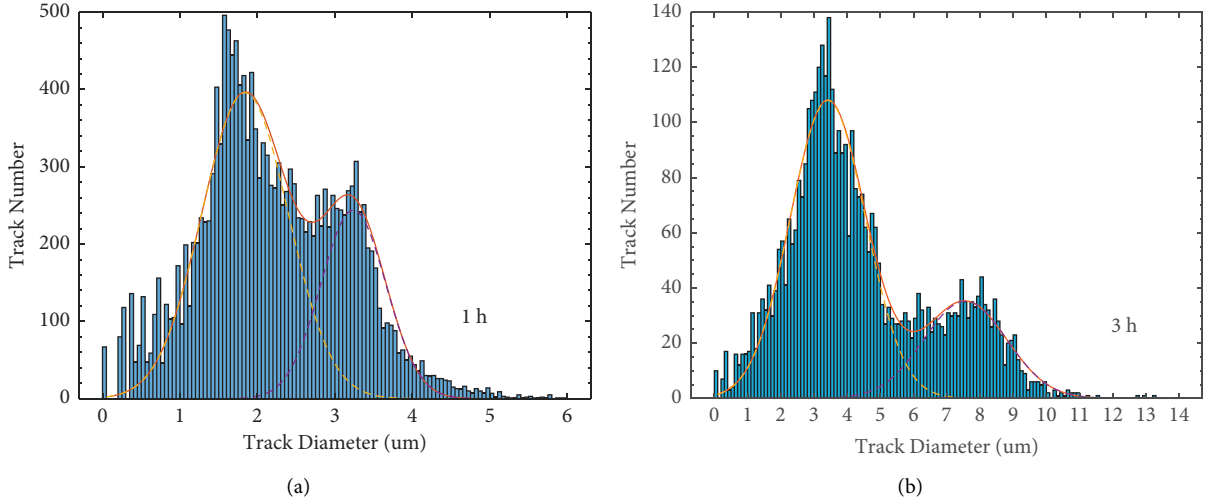


FIGURE 3: Statistical histogram of particle tracks after different etching times. (a) Particle tracks after 1 h of etching. (b) Particle tracks after 3 h of etching. The red line in the figure is the double-gauss-curve fitting for the track number as a function of its diameter.

escape from the target to the total amount of α particles that are produced.

In the thick target case, the change of reaction cross-section caused by proton energy deposition inside the target must be considered. The total reaction cross-section with the thick target is as follows [17]:

$$\sigma = \frac{1}{3} \left[\frac{1}{n} \frac{dN(E)}{dE} \frac{dE}{dR} + \frac{\mu \cos \theta}{n \cos \varphi} N(E) \right], \quad (3)$$

where n is the atomic density of the target, $N(E)$ is the α particle yield per proton with the proton energy E , μ is the absorption coefficient of the target nucleus, θ is the angle between the normal direction of the target plane and the direction of the incident particle, φ is the angle between the normal direction of the target plane and the detector. The factor $1/3$ corrects for the fact that for each reaction, three α particles are created.

In our experiment, the proton energy is 140 keV–172 keV, and the penetration depth into the boron target is about 1 μm . The energy of α particles produced by $p^{11}\text{B}$ reaction is around 1 MeV and 4 MeV. According to the SRIM code and the α spectrum with the incident proton energy of 165 keV [10], we can safely assume that almost all α particles pass through 1 μm thick boron and reach the CR-39 type track detector. Thus, the second term in formula (3) can be ignored.

Figure 4(a) shows the α yield per proton for different energies of the incident proton beams, where the red line is the curve fitting the experimental data with a standard deviation of 24%. Figure 4(b) shows the cross section of $p^{11}\text{B}$ fusion, where the present data are obtained based on the formula (3) and the error of the cross-section was 28%. We can find that the resonance appears near 156 keV, and the measured resonance cross-section is 45.6 ± 12.5 mb. The position of the peak is slightly shifted to the left from the recognized resonance energy of 163 keV [6], and the value of the cross-section is consistent with the previous works [8–10, 18].

The main errors are due to: (1) the fitting error of 24% in Figure 4(a); (2) the statistical error of 12% caused by particles counting on the CR-39 type track detector; and (3) the systematic error of 7%.

The higher values of the first four cross-sections result from proton backscattering. As shown in Figure 3(a), the proton track overlaps with the α particle track in a large range, so some protons will be mistaken for α particles during particle counting. In addition, the first proton beam may not be perpendicular to the target but at an angle to the target plane, which will cause large backscattering and a high particle count.

The shift of the resonance peak is mainly due to the very limited data near the resonance peak and the use of a thick target. According to Munch [18], the resonance width in the lab system of 163 keV is 5.76 keV, while the energy interval of proton beams in our experiments is 4 keV, which means that there are too few energy points measured near the resonance peak. Therefore, this causes a large error in the fitting of the peak position, thus leading to the shift of the peak.

When comparing all these cross-sections, we notice all values deviate significantly from the measurement of Becker et al. [10]. We suspect that this is due to the normalization problem. Becker believes that a correction factor of 2 should be used when calculating the cross-section because two out of three α particles can be detected for one fusion reaction with detectors covering a large solid angle, while others divide the total α particle yields by a factor of 3. Considering our experiment, we have chosen several regions in the CR-39 type track detector to count the α particles. For the image shown in Figure 2, its size is $238.9 \mu\text{m} \times 183.77 \mu\text{m}$, and the solid angle of the image relative to the closest incident point is $\Delta\Omega \approx 10^{-4}$ rad. It is suggested that the α particles produced by $p^{11}\text{B}$ reaction are isotropically in the center of mass system [10], if the total α number produced in reaction is N_{total} , then the α number that can be collected in a region with a solid angle $\Delta\Omega$ should be $N_{\text{total}} \times \Delta\Omega/4\pi$. Considering that one reaction will produce three α particles, therefore, a

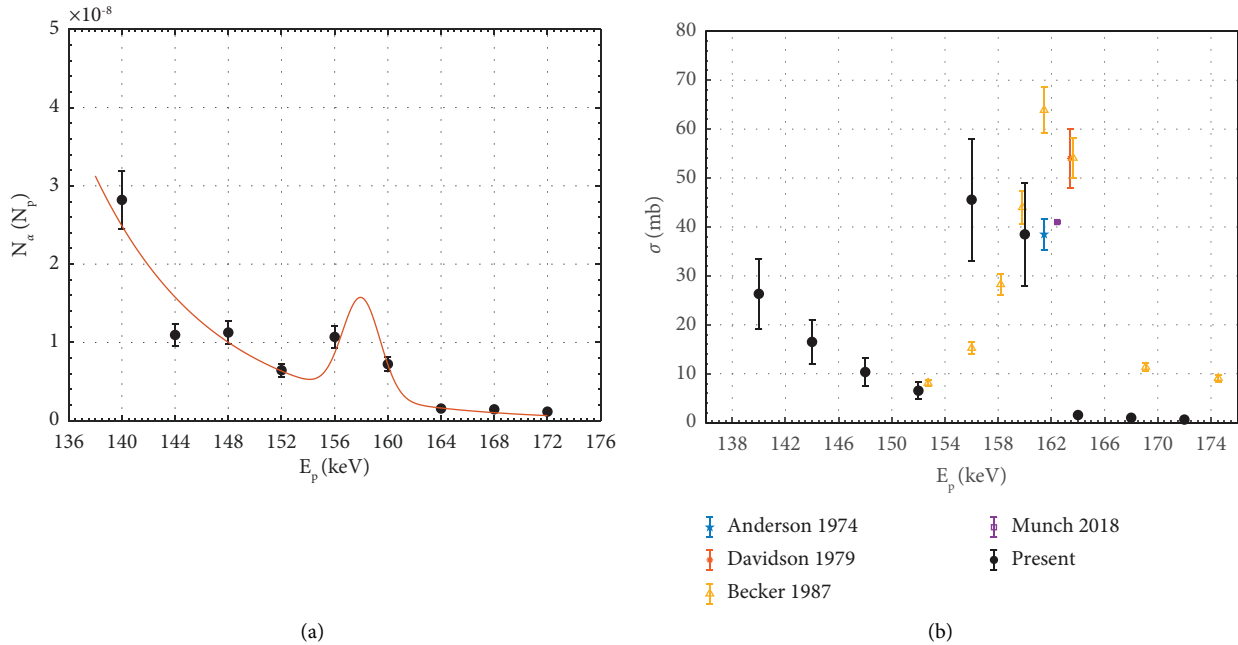


FIGURE 4: (a) The α yield per proton. The red line is the curve fitting. (b) $p^{11}\text{B}$ cross-section (the data are from References [8–10, 18]). Here, we have corrected Becker's value by multiplying a factor of 2/3.

factor of 3 should be divided when calculating the cross-section. In Figure 3(b) we have corrected Becker's value by multiplying a factor 2/3.

4. Conclusion

In this experiment, the cross-section of the hydrogen-boron nuclear reaction at low energy is studied. The experiment was carried out on the 320 kV high-voltage platform, and the CR-39 type track detectors with high sensitivity to charged particles were used to record the particle yield. We can distinguish the protons and α particles clearly in CR-39 type track detector according to their track diameters, after etched in a 6.0 mol/L NaOH solution at a constant temperature of $80.0 \pm 0.5^\circ\text{C}$ for 3 hours. It is more effective to distinguish two particle species with an etching time of more than 3 h. For the nine incident proton beams, the particle yield is obtained by constructing 9-element equations. Based on the integral formula for thick target yield and the α particle energy spectrum, we obtain the peak value of the cross-section $\sigma = 45.6 \pm 12.5$ mb near 156 keV. The peak value is consistent with previous results [8–10, 18], and the position of the resonance is slightly shifted to the left. The shift of the resonance peak is mainly due to the very limited data near the resonance peak and the use of a thick target. Our results show the feasibility of measuring the reaction cross-section with CR-39 type track detectors in low-energy regions.

Data Availability

The data that support the findings of this study are available from the corresponding author upon reasonable request.

Conflicts of Interest

The authors declare that they have no conflicts of interest.

Authors' Contributions

Yongtao Zhao initiated and organized the experiments. Shizheng Zhang, Xing Xu, Yanhong Chen, Zhao Wang, Zexian Zhou, Lulin Shi, and Rui Cheng carried out the experiments together. Shizheng Zhang, Hao Xu, Zhigang Deng, Wei Qi, and Weimin Zhou etched and scanned CR-39 type track detectors. Wenqing Wei, Jieru Ren, Benzheng Chen, Bubo Ma, Zhongmin Hu, Fangfang Li, Lirong Liu, Mingzhe Yang, Zeyu Lai, Hongwei Yue, Jie Xiong, Zhongfeng Xu, Guanchao Zhao, Bing Liu, Di Luo, Yongtao Zhao, and Dieter H. H. Hoffmann contributed in the physical interpretation of experimental data. Shizheng Zhang, Wenqing Wei, Jieru Ren, Yongtao Zhao, and Dieter Hoffmann drafted the paper and all the coauthors revised the manuscript critically. All the authors approved the final version to be published and agreed to be accountable for all aspects of the work in ensuring that questions related to the accuracy or integrity of any part of the work are appropriately investigated and resolved.

Acknowledgments

This experiment was performed at 320 kV high-voltage platform in Lanzhou. The authors are grateful to the staff of the Institute of Modern Physics. The work was supported by National Key R & D Program of China (No. 2019YFA0404900), Chinese Science Challenge Project no. TZ2016005, National Natural Science Foundation of China (Nos. U2030104, 12120101005, 12175174, and 11975174), China Postdoctoral Science Foundation (No.

2017M623145), State Key Laboratory Foundation of Laser Interaction with Matter (Nos. SKLLIM1807 and SKLLIM2106), and the Fundamental Research Funds for the Central Universities.




References

- [1] N. Rostoker, M. W. Binderbauer, and H. J. Monkhorst, "Colliding beam fusion reactor," *Science*, vol. 278, no. 5342, pp. 1419–1422, 1997.
- [2] G. L. Kulcinski and J. F. Santarius, "Advanced fuels under debate," *Nature*, vol. 396, no. 6713, pp. 724–725, 1998.
- [3] R. E. Segel, S. S. Hanna, and R. G. Allas, "States in ^{12}C Between 16.4 and 19.6 MeV," *Physical Review*, vol. 139, no. 4, pp. B818–B830, 1965.
- [4] A. M. Boesgaard, C. P. Deliyannis, and A. Steinhauer, "Boron depletion in F and G dwarf stars and the beryllium-boron correlation," *The Astrophysical Journal*, vol. 621, no. 2, pp. 991–998, 2005.
- [5] G. A. P. Cirrone, L. Manti, D. Margarone et al., "First experimental proof of Proton Boron Capture Therapy (PBCT) to enhance proton therapy effectiveness," *Scientific Reports*, vol. 8, no. 1, pp. 1141–1148, 2018.
- [6] M. L. E. Oliphant and E. Rutherford, "Experiments on the transmutation of elements by protons," *Proceedings of the Royal Society of London - Series A: Containing Papers of a Mathematical and Physical Character*, vol. 141, pp. 259–281, 1933.
- [7] P. I. Dee and C. W. Gilbert, "The disintegration of Boron into three α -particles," *Proceedings of the Royal Society of London, Series A: Mathematical and Physical Sciences*, vol. 154, pp. 279–296, 1936.
- [8] B. D. Anderson, M. R. Dwarakanath, J. S. Schweitze, and A. V. Nero, "A new determination of the partial widths of the 16.11 MeV state in ^{12}C ," *Nuclear Physics A*, vol. 233, pp. 1–15, 2018.
- [9] J. M. Davidson, H. Berg, M. Lowry, M. Dwarakanath, A. Sierk, and P. Batay-Csorba, "Low energy cross sections for ^{11}B ($p, 3\alpha$)," *Nuclear Physics A*, vol. 315, no. 1-2, pp. 253–268, 1979.
- [10] H. W. Becker, C. Rolfs, and H. P. Trautvetter, "Low-energy cross sections for ^{11}B ($p, 3\alpha$)," *Zeitschrift für Physik A Atomic Nuclei*, vol. 327, pp. 341–355, 1987.
- [11] W. M. Nevins and R. Swain, "The thermonuclear fusion rate coefficient for p - ^{11}B reactions," *Nuclear Fusion*, vol. 40, pp. 865–872, 2000.
- [12] V. S. Belyaev, A. P. Matafonov, V. I. Vinogradov et al., "Observation of neutronless fusion reactions in picosecond laser plasmas," *Physical Review*, vol. 72, Article ID 026406, 2005.
- [13] C. Labaune, C. Baccou, V. Yahia, C. Neuville, and J. Rafelski, "Laser-initiated primary and secondary nuclear reactions in Boron-Nitride," *Scientific Reports*, vol. 6, Article ID 21202, 2016.
- [14] F. Belloni, D. Margarone, A. Picciotto, F. Schillaci, and L. Giuffrida, "On the enhancement of p - ^{11}B fusion reaction rate in laser-driven plasma by $\alpha \rightarrow p$ collisional energy transfer," *Physics of Plasmas*, vol. 25, p. 2, Article ID 020701, 2018.
- [15] T. W. Jeong, P. K. Singh, C. Scullion et al., "CR-39 track detector for multi-MeV ion spectroscopy," *Scientific Reports*, vol. 7, pp. 2152–2158, 2017.
- [16] D. G. Hicks, "Charged-particle spectroscopy: A new window on inertial confinement fusion," Dissertations, Massachusetts Institute of Technology, Cambridge, MA, USA, 1999.
- [17] K. Taulbjerg and P. Sigmund, "Deduction of heavy-ion X-ray production cross sections from thick-target yields," *Physical Review A*, vol. 6, p. 1257, 1972.
- [18] M. Munch and H. O. Uldall Fynbo, "The partial widths of the 16.1 MeV $2+$ resonance in ^{12}C ," *The European Physical Journal A*, vol. 54, pp. 138–8, 2018.



Research Article

High-Sensitivity Thomson Spectrometry in Experiments of Laser-Driven Low-Rate Neutronless Fusion Reactions

M. Scisciò ¹, G. Di Giorgio,¹ P. L. Andreoli,¹ M. Cipriani,¹ G. Cristofari,¹ R. De Angelis,¹ M. Salvadori,¹ G. A. P. Cirrone,² L. Giuffrida,^{2,3} D. Margarone ^{2,3,4}, G. Milluzzo,² G. Petringa,² and F. Consoli ¹

¹ENEA Fusion and Technologies for Nuclear Safety and Security Department-C. R. Frascati, Via Enrico Fermi 45, 00044 Frascati, Italy

²Laboratori Nazionali del Sud, Istituto Nazionale di Fisica Nucleare (LNS-INFN), Catania 95125, Italy

³ELI Beamlines Facility, The Extreme Light Infrastructure ERIC, Dolni Brezany 252 41, Czech Republic

⁴Queen's University Belfast, School of Mathematics and Physics, Belfast BT7 1NN, UK

Correspondence should be addressed to M. Scisciò; massimiliano.sciscio@enea.it and F. Consoli; fabrizio.consoli@enea.it

Received 15 July 2022; Revised 1 October 2022; Accepted 14 December 2022; Published 13 January 2023

Academic Editor: Katarzyna Batani

Copyright © 2023 M. Scisciò et al. This is an open access article distributed under the Creative Commons Attribution License, which permits unrestricted use, distribution, and reproduction in any medium, provided the original work is properly cited.

The aneutronic $^{11}\text{B}(p, \alpha)2\alpha$ fusion reaction driven by the interaction of high-energy lasers with matter has become a popular topic of research, since it represents a potential long-term goal alternative to the most studied deuterium-tritium reaction. However, the detection of the typical ionic products, especially alpha particles, of this low-rate fusion reaction is a challenging issue, due to their low flux. One of the diagnostic devices that can be implemented in laser-driven proton-boron fusion experiments is a Thomson spectrometer (TS), which is capable of detecting and discriminating ions according to their mass-to-charge ratio (A/Z , where A is the mass number and Z is the atomic number of the ions). In this work, we report on the ultimate test of a TS, which was designed and developed at the ENEA Research Centre in Frascati, Italy, in the context of a $p + ^{11}\text{B}$ fusion experiment. Our device—designed to have high sensitivity and a robust shielding against electromagnetic pulses (EMPs)—was implemented at the PALS laser facility (~ 700 J in ~ 350 ps pulses) at a distance of 367 mm from the laser-plasma interaction point. We analyse here the measured signals obtained with our device, focusing on the assessment of their signal-to-background ratio. Despite the presence of strong EMPs and background radiation at such a short distance from the laser-irradiated target, the TS proved to be suitable for effectively detecting protons and heavier ions stemming from the plasma source.

1. Introduction

The nuclear reaction between deuterium and tritium nuclei (DT reaction) is a well-known candidate for future nuclear fusion power plants and has been extensively studied in the last decades [1]. The main advantages of exploiting DT reactions are the low energy required to initiate the fusion process and the high reaction cross-section at center-of-mass energies below 200 keV [2–5]. However, DT reactions require the use of radioactive fuel (tritium) and produce neutrons. These can be used for tritium breeding and in hybrid fusion-fission reactors [6, 7] but also have the drawback of having a low energy conversion efficiency and activating materials they

interact with. For these reasons, the neutronless $^{11}\text{B}(p, \alpha)2\alpha$ reaction [3–5, 8] has become a topic of research as an alternative to DT reactions for third-generation fusion reactors. The peak cross-section of this reaction is reached at about 600 keV center-of-mass energy [3]. This can be achieved in laboratory conditions with the interaction of high-power laser pulses and matter, which, in ad-hoc designed experiments, has been demonstrated to produce $p + ^{11}\text{B}$ reactions [3, 9–15]. These experiments exploit two main schemes: (i) irradiating specially designed targets (such as plastic targets doped with boron or silicon host targets enriched with hydrogen and boron [10, 12, 14, 15]) with energetic nano- and picosecond laser pulses in order to trigger $p + ^{11}\text{B}$ fusion reactions;

(ii) generating a laser-driven proton beam (typically using pico- and femtosecond laser pulses) that is directed onto a boron secondary target where the fusion reactions are initiated [3, 11, 16–18]. In these types of experiments, one of the main challenges is represented by the accurate characterization of the interaction conditions and, in particular, by the detection of the typical products of the $p+^{11}\text{B}$ fusion reactions, i.e., alpha particles with energies in the range of a few MeVs [3, 19]. Due to the low rate of the fusion reactions, the number of produced alpha particles is typically low, and the produced particle flux that can be collected by diagnostic devices is limited [16–19]. Moreover, laser-plasma interactions at high intensity produce a wide spectrum of ionizing electromagnetic (UV, X, and γ) [20] and particle radiation (electrons, ions) [21, 22] and electromagnetic pulses (EMPs) up to the MV/m order in the frequency range from radiofrequency to terahertz [23, 24]. These additional radiation types interact with the diagnostics and often generate a strong background “noise” that hinders the measurement of alpha particle spectra. Diagnostic devices placed at a close distance from the interaction point are often damaged by this radiation. Different types of diagnostic systems are commonly used for revealing energetic ions in laser-plasma experiments, such as time-of-flight diagnostics, solid-state nuclear track detectors (CR-39, PM355, etc.), and electric and/or magnetic spectrometers [25–27]. Among the latter category, Thomson spectrometers (TS) represent a well-known and popular solution, due to their combination of electric and magnetic fields [28, 29], which allows deflecting ion species with different mass-to-charge ratios (A/Z , where A is the mass number and Z is the atomic number) on different trajectories. The particles then impinge on a detector and draw different parabolic curves according to their A/Z value.

In recent years, intensive research and development has been carried out at the Fusion Physics department of ENEA related to diagnostic devices for $p+^{11}\text{B}$ fusion reaction experiments, in particular Thomson spectrometers. Prototypes of TS have been developed at the ENEA Research Center in Frascati with the intent to optimize them for the detection of alpha particles. These devices are designed to be placed inside the vacuum chamber at close distances to the interaction point, in order to maximize the number of collected particles, due to their large intercepted solid angle [30, 31]. Moreover, they feature compact dimensions, short-length bending dipoles (magnetic and electric) and ad-hoc shielding against EMPs. These characteristics allow to employ them close to the interaction point where the EMP intensity is maximum and is known to induce significant distortions to the TS signal [12]. One of these devices has been recently tested at the PHELIX laser facility at GSI (Germany) during an experiment where strong EMPs (in the multiple hundreds of kV/m order) were produced, proving an excellent capability to work in such harsh conditions at a distance from the laser-plasma source of $<1\text{ m}$ [32]. In this work, we report about a further test of this device: the experimental results were obtained during an experiment of laser-plasma-induced $p+^{11}\text{B}$ fusion reactions, performed at the PALS laser facility (350 ps laser pulses with an energy of about 700 J). In this experiment, our goal was to test the

TABLE 1: Key parameters of the Thomson spectrometer.

Internal (external) pinhole diameter	0.35 mm (2 mm)
Dipole length	25 mm
Dipole gap	5 mm
Magnetic field	0.405 T
Max. electric field	1.56 MV/m
Drift space	197 mm

performance of our diagnostic device in an environment of strong particle irradiation, EMP noise, and ionizing radiation: the typical harsh conditions of a $p+^{11}\text{B}$ fusion experiment. We aimed at efficiently separating and detecting protons and heavy ions, in particular those with $A/Z=2$, where alpha particles are included, by placing our device at a distance of less than 367 mm from the interaction point. In the following sections, we will focus on the evaluation of the measurements obtained for protons and $A/Z=2$ ions.

2. Materials and Methods

2.1. Thomson Spectrometer Parameters and Experimental Setup. The magnetic field of the deflecting dipole of our TS is $B = 0.405\text{ T}$ and the voltage applied to the electrodes can reach a maximum value of $\Delta V = 8\text{ kV}$ (resulting in a maximum electric field $E \approx 1.56\text{ MV/m}$). The length of the dipole section of the TS is $L = 25\text{ mm}$. The particles collected by the TS are typically revealed by imaging plates (IPs), placed on the support on the back side of the device after a drift space of $L_D = 197\text{ mm}$ between the deflecting dipole and the detector. The implementation of CR-39 detectors is also possible with the use of a specially designed frame that can be put in place of the IP support. Further details of the TS parameters are reported in Refs. [30, 31]. In Table 1, we summarize the most critical ones. In Figure 1(a), we show a schematic of the TS components. The black dashed line indicates the trajectory of the radiation that enters the device through the double pinhole assembly (a first pinhole with a diameter of 2 mm and a second one with a diameter of 0.35 mm) and generates the zeroth order signal on the IP: a x-ray pinhole image of the interaction. The red dashed line represents the trajectory of the ions, which are deflected along x by the magnetic field and along y by the electric field. The ions will then impinge on the detector, generating parabolic traces on the $x - y$ plane, according to equation (1)

$$y = \frac{Am_p A_E}{Zq_e A_B^2} x^2, \quad (1)$$

where Zq_e and Am_p are the charge and the mass of the considered ions, respectively; A_E and A_B are coefficients related to the electric and magnetic field distribution along the dipole of the TS, which also consider the effects of fringe fields (see refs. [30, 31] for further details).

We evaluated the quality of the retrieved signals from the traces for protons and $A/Z=2$ ions in terms of signal-to-background ratio (SBR). We discretized the x -axis of Figure 2, i.e., the horizontal axis on the IP image, in order to consider the actual resolution of the device. This is limited by the pinhole diameter as it is projected on the detector plane

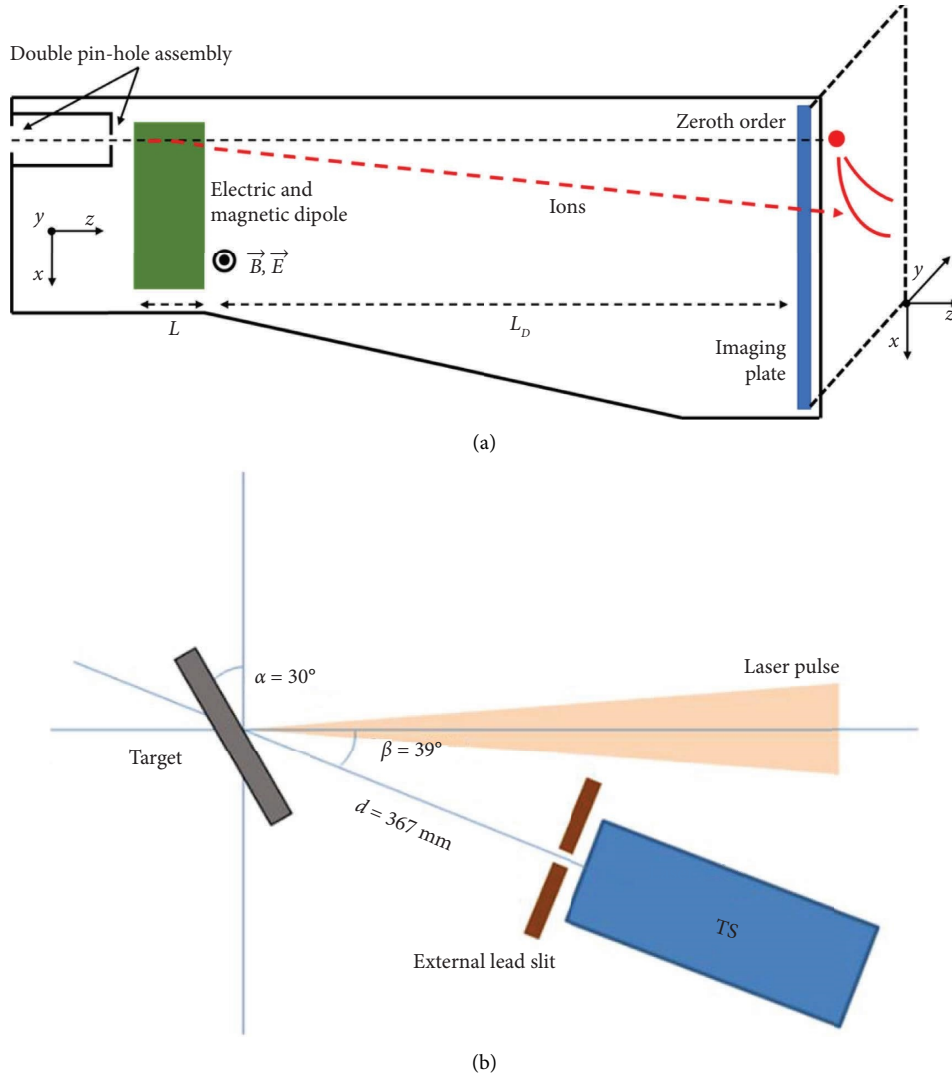


FIGURE 1: (a) Schematic of the TS components. (b) Schematic view of the experimental setup. The TS is positioned at a distance of 367 mm from the front side of the laser-irradiated target.

and can be evaluated by the thickness of the proton trace (it is inconvenient to evaluate it from the zeroth order in our case since the signal is oversaturated in that region). Hence, we graphically estimated that the pinhole image for protons is about 0.8 mm and for the other ions is about 0.6 mm. This gives the actual energy resolution of the TS for each specific trace. The retrieved signal is therefore divided into energy bins that correspond to subsets of pixels that have the same dimension as the pinhole image. According to the relation between horizontal position on the IP and energy of the particles, it is possible to calculate the average energy of each subset of pixels by considering its central position along the x coordinate [30]. It is calculated as follows:

$$x = \frac{A_B Z q_e}{\sqrt{2 A m_p E_i}} \quad (2)$$

where Zq_e , $A m_p$, and E_i are the charge, the mass, and the energy of the considered ions, respectively; A_B is the

coefficient related to the magnetic field of the TS (see equation (1) and reference [30] for further details). We indicate the discretized energy bins with their mean energy \bar{E}_i . We then evaluated the signal $S_{\bar{E}_i}$ within these bins by integrating the PSL values of the obtained subsets of pixels [30]. The values of the background signal $BG_{\bar{E}_i}$ were evaluated by integrating the PSL values taken from the region of the IP adjacent to the particle traces and this was performed for each position on the trace. So, the background is monitored and subtracted adaptively. We defined the signal-to-background ratio as $SBR_{\bar{E}_i} = S_{\bar{E}_i}/BG_{\bar{E}_i}$ for each energy bin. In Figure 4, we report, for the shot #56027, the obtained values of $S_{\bar{E}_i}$ and $BG_{\bar{E}_i}$ (protons and $A/Z=2$ particles in panels (a) and (b), respectively; for the latter case, we indicate \bar{E}_i in terms of MeV/nucleon, in order to have an equivalent scale for the different ion species that might contribute to the signal of the trace). In the plots of Figures 4(c) and 4(d) (protons and $A/Z=2$, respectively), the $SBR_{\bar{E}_i}$ is reported. These plots clearly indicate that the signal

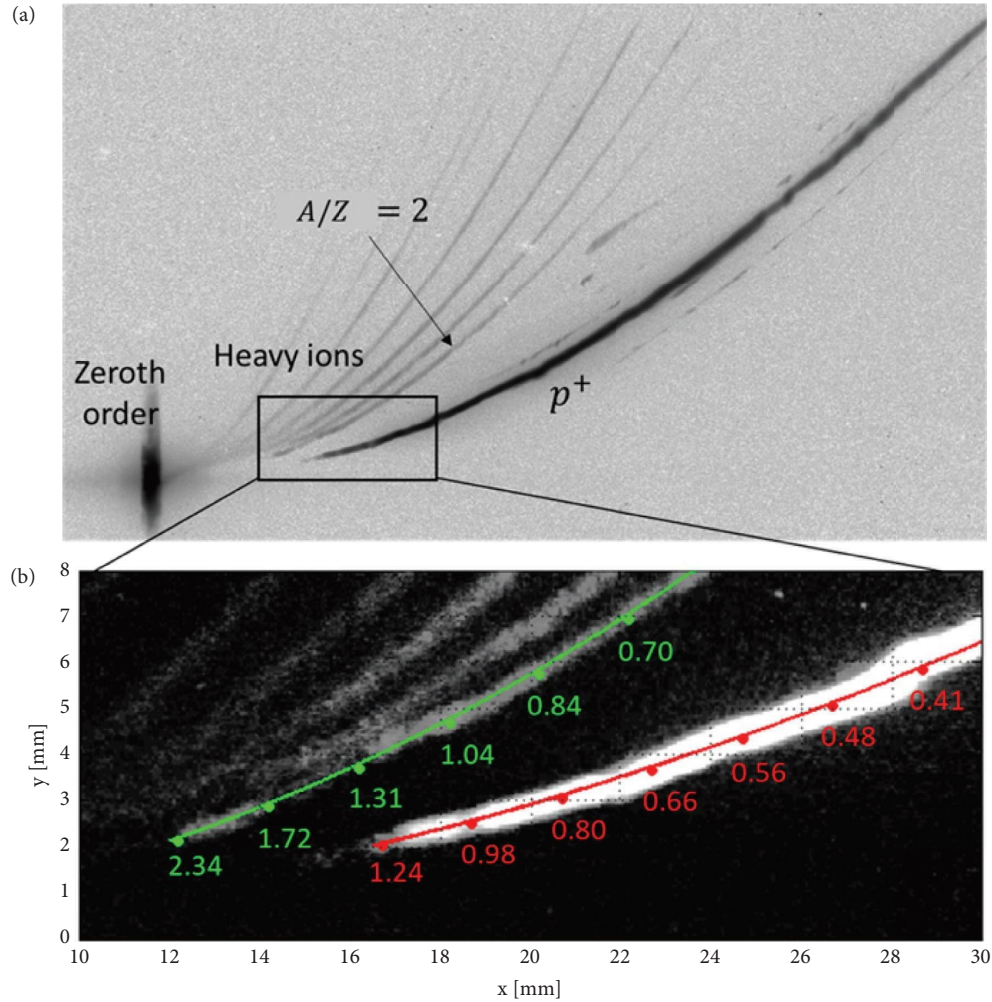


FIGURE 2: (a) IP scan of the shot #56027. (b) Zoomed frame of the retrieved parabolas for $A/Z = 1$ and $A/Z = 2$, in the region of the maximum energies. The coloured lines indicate the analytic curves and the numerical values of the associated energies (MeV) for protons (red) and alpha particles (green).

of retrieved traces exceeds the background noise across the entire analysed energy range, for both cases of $A/Z = 1$ and $A/Z = 2$. In case of protons, the signal exceeds the background by a factor ~ 100 in the range 0.1–0.7 MeV. At higher energies, $SBR_{\bar{E}_i} > 10$ for \bar{E}_i up to 1.1 MeV, i.e., in the spectral region where the collected particle charge diminishes (and, as a consequence, the values of the correspondent S_{E_i}). At the maximum energy of ~ 1.2 MeV, the $SBR_{\bar{E}_i}$ has still a value of about 4. For the $A/Z = 2$ trace (Figure 4(d)), which typically is harder to detect due to its weaker signal compared to the proton trace, we obtained $SBR_{\bar{E}_i} \geq 2$ for ion energies from 0.05 to 0.125 MeV/nucleon and $SBR_{\bar{E}_i} \geq 3$ from about 0.125 MeV/nucleon up to the maximum reached energy of ~ 0.55 MeV/nucleon.

A schematic drawing of the experimental setup used in the experiment at the PALS facility is reported in Figure 1(b). The laser pulses, with a wavelength $\lambda = 1315$ nm and a duration of ~ 350 ps, had an energy between 600 J and 700 J, depending on the case. They were focused down onto a solid target at an angle $\alpha = 30^\circ$ from the laser axis (see Figure 1(b)), yielding an intensity of $I \approx 10^{16}$ W/cm². The types of targets that were used varied

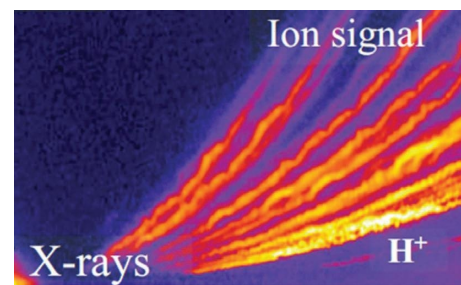


FIGURE 3: Signal retrieved from a TS implemented at the PALS facility during a $p+^{11}\text{B}$ fusion experiment with no special precautions regarding EMP shielding. Reprinted with permission from reference [12] copyright 2020 by the American Physical Society.

from shot to shot and will be indicated in the following sections. Our Thomson spectrometer was placed at an angle of $\beta = 39^\circ$ from the laser axis, in line of sight with the target surface irradiated by the laser. The distance between the TS and the target was $d = 367$ mm (measured from the target to the entrance pinhole of the TS). The maximum voltage applied to the

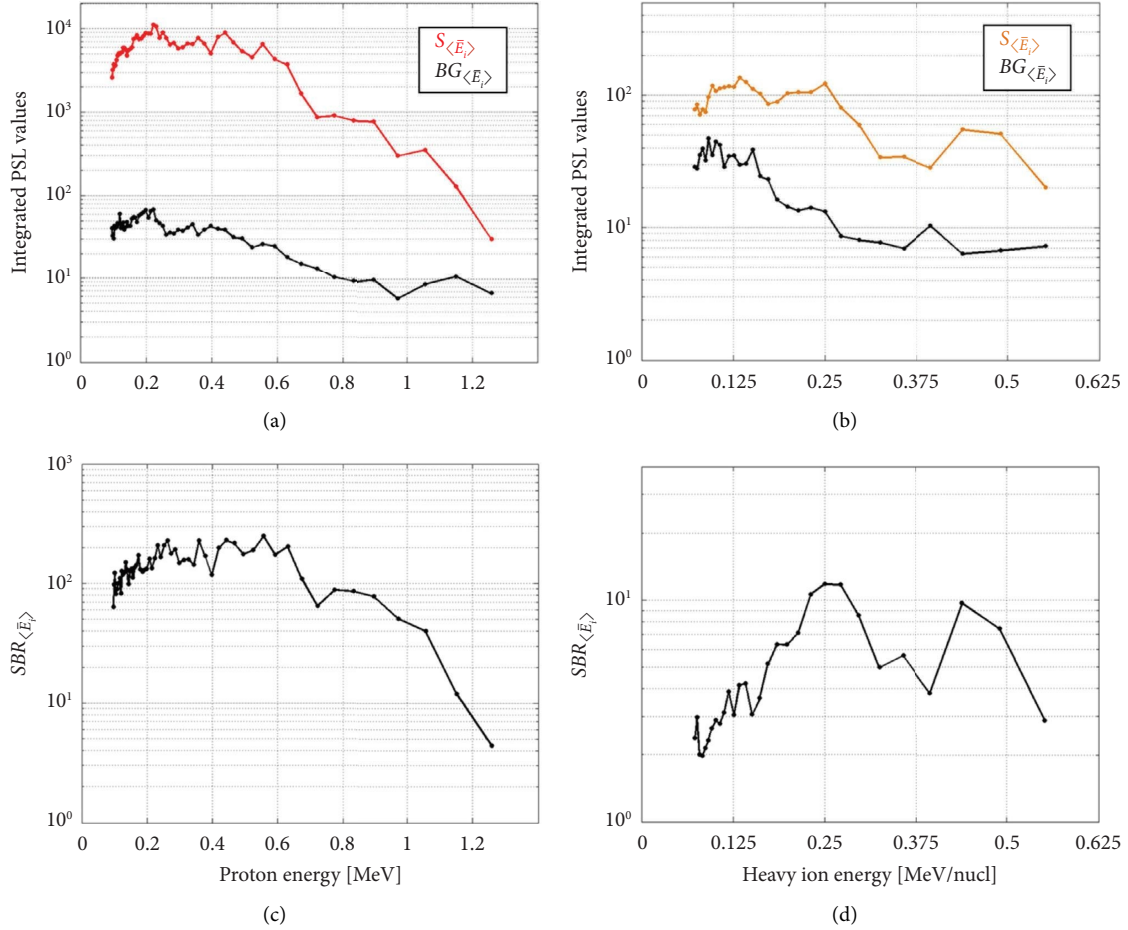


FIGURE 4: (a) Trace signal $S_{\langle \bar{E}_i \rangle}$ (red) and background signal $BG_{\langle \bar{E}_i \rangle}$ (black) obtained for the proton trace. (b) Trace signal $S_{\langle \bar{E}_i \rangle}$ (orange) and background signal $BG_{\langle \bar{E}_i \rangle}$ (black) obtained for the $A/Z=2$ trace. (c) Signal-to-background ratio $SBR_{\langle \bar{E}_i \rangle}$ obtained for the proton trace. (d) Signal-to-background ratio $SBR_{\bar{E}_i}$ obtained for the $A/Z=2$ trace. All plots refer to shot #56027.

electrodes of the TS was $\Delta V = 4$ kV (resulting in an electric field $E \approx 0.78$ MV/m). The nominal maximum voltage was not applied due to insufficient vacuum conditions. The deflected particles were detected by IPs of the type BAS-TR [33, 34]. In front of the TS, we placed an external lead slit (about 2 mm wide) as additional protection against incoming radiation.

2.2. Scanning of the Imaging Plate. The implemented IPs were of type BAS-TR, manufactured by Fujifilm. They were scanned after each shot with a Fujifilm IP Scanner BAS-1800II scanner (50 μm pixel size resolution, sensitivity $S=4000$, latitude $L=5$). This type of scanner produces 16 bit encoded images. In order to obtain the photo-stimulated luminescence (PSL) value of the pixels, which is necessary for the correct calibration of the signals/traces on the IP, we used the following formula [35]:

$$S_{\text{PSL}} = \left(\frac{R}{100}\right)^2 \times \left(\frac{4000}{S}\right) \times 10^{L(QL/G-0.5)}, \quad (3)$$

where R is the resolution (50 μm), S the sensitivity (4000), L the latitude (5), QL the encoded quantum level, and G the gradation (65335) of the original image. The IPs were scanned approximately 15 minutes after each shot. This time delay induces a

slight fading of the trace signal on the IP, which will be about 90% of the original value [36]. This effect is compensated by a correction factor that we included in the numerical script for the evaluation of the obtained particle spectra.

3. Results and Discussion

3.1. Assessment of the Thomson Spectrometer Sensitivity. We report in Figure 2(a) an IP scan as an example of what was typically retrieved from the performed shots. In this particular case (shot #56027), which we will analyse in detail in this section, the laser energy was 661 J, and the used target was made of a 10 μm thick plastic foil doped with ^{11}B . The traces drawn by the different ion species collected by the TS are clearly visible on the IP scan (no digital contrast enhancement was used in the image of Figure 2(a)). The parabolas are separated one from the other for all detected energies, i.e., the signals do not overlap even at the high-energy tail of the traces. Due to the large solid angle intercepted by the device, which was enabled by the short distance of 367 mm to the target (see Figure 1(b)), we obtained a significant high flux of ions (a delicate parameter, especially for the signals of heavy species), which was

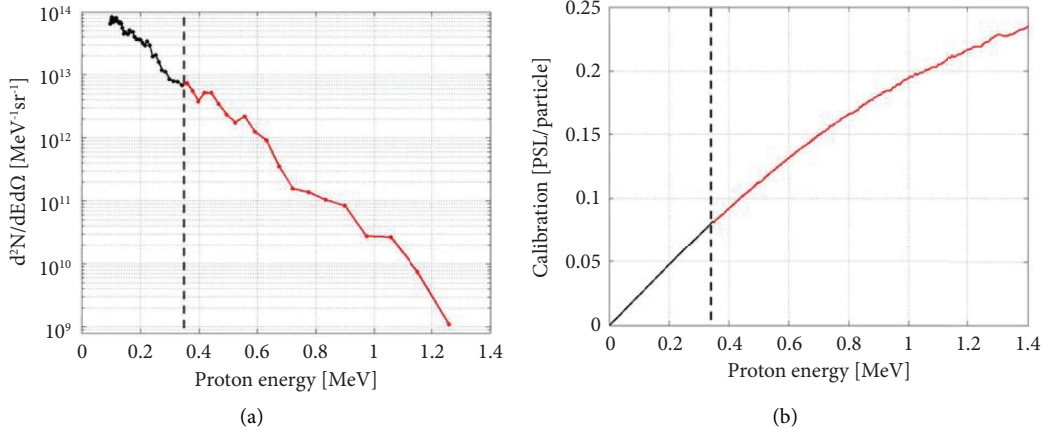


FIGURE 5: (a) Obtained proton spectrum for shot #56027. The number of particles at energies below 350 keV is evaluated using a linear response of the IP. (b) Calibration curve used for calculating the proton beam charge. The red part of the plot is from reference [33]. For the black part of the curve, for energies below 350 keV, a linear response of the IP is assumed.

revealed with accuracy by the high TS sensitivity. On the other hand, due to its proximity to the target, the TS is exposed to a strong flux of ionizing radiation and electrons generated by the laser-target interaction [20], which generally causes a background noise. This is somehow recognizable from the intense signal of the zeroth order, where the high X-yield directly impinges on the IP and leads to a saturated signal (even after multiple scans of the detector). However, the implementation of a thick external lead slit (which confers the elongated vertical shape of the zeroth order), the tailored double pinhole assembly for internal electron deflection and collection, and the thick metallic shielding case (shown in ref. [31] for further details) effectively protected the region of the IP where the ions were revealed. Our TS also proved to have remarkable robustness to significant EMP fields (typically, at the PALS facility, in the order of a fraction of MV/m at ~ 1 m distance from the target [24, 37]). The traces do not feature the typical oscillations that are caused by the presence of EMPs when no special precautions are taken. In refs. [12, 38], pictures of the very oscillating traces are shown for experiments on the same PALS facility. In particular, the results of reference [12], which we report here in Figure 3 for comparison, were obtained in an experiment of laser-driven $p+^{11}\text{B}$ fusion reactions using the same scheme as our experiment. Moreover, these results were achieved by placing the TS outside the chamber and at a distance of about 1.5–2 m from the interaction point. Hence, with EMPs intrinsically much lower (more than one order of magnitude) than those experienced by the TS that we implemented in our experiment. Near the $A/Z=1$ trace generated by protons, weaker traces are visible in the region of lower energies. These are possibly induced by a fraction of the low-energy particles of the beam that are deflected on a different trajectory by the fringe fields of the dipole and/or part of the deflected particles, which interact with the deflector edge and then reach the detector. In the zoomed frame of Figure 2 (panel (b)), we indicated with colored lines the analytic parabolas that correspond to the particles with $A/Z=1$ (protons) and $A/Z=2$ (here, we

used digital contrast enhancement for improving the image clarity for the reader). The numeric values on these lines indicate the particle energies in MeV that correspond to the different positions along the parabolas (for the $A/Z=2$ parabola, we considered here the energies of alpha particles).

The analysis of the $A/Z=2$ trace also allows estimating the minimum value of $p+^{11}\text{B}$ reactions that leads to a detectable quantity of alpha particles, in the case a TR type IP detector is used. In general, the signal level of the $A/Z=2$ trace can be written as follows:

$$S_{\bar{E}_i} = S_{\bar{E}_i, C^{6+}} + S_{\bar{E}_i, \alpha} \quad (4)$$

where $S_{\bar{E}_i, C^{6+}}$ and $S_{\bar{E}_i, \alpha}$ are the contributions of C^{6+} ions and alpha particles, respectively (note that, here, the energy values \bar{E}_i are in terms of MeV/nucleon). If we assume that—since the used target is made of plastic, which is a source of a large amount of fully ionized carbon ions—the signal level of the $A/Z=2$ trace is entirely given by C^{6+} ions, it can be considered a reference threshold for the detection of alphas. We can define a “minimum detectable contribution” of alphas $S_{\bar{E}_i, \alpha}^{\min}$ to the signal of the $A/Z=2$ trace, with respect to the contribution given by C^{6+} ions. For instance, assuming that the presence of alpha particles can be detected if the signal of the $A/Z=2$ trace has double intensity with respect to the reference case where only C^{6+} ions are present, the minimum detectable signal by alpha particles would be $S_{\bar{E}_i, \alpha}^{\min} = S_{\bar{E}_i, C^{6+}}$. In the following section of this study, where a quantitative analysis of the particle spectra is provided, we will use these definitions for estimating the minimum quantity of detectable alpha particles. Consequently, the minimum detectable gain of $p+^{11}\text{B}$ reactions—intended as the total energy of generated alpha particles with respect to the laser pulse energy—with the experimental parameters of the campaign at the PALS facility.

3.2. Spectra of Detected Ions with $A/Z=1$ and $A/Z=2$. It is worth stressing out that the signal related to the $A/Z=2$ parabola possibly contains the contributions of both alpha

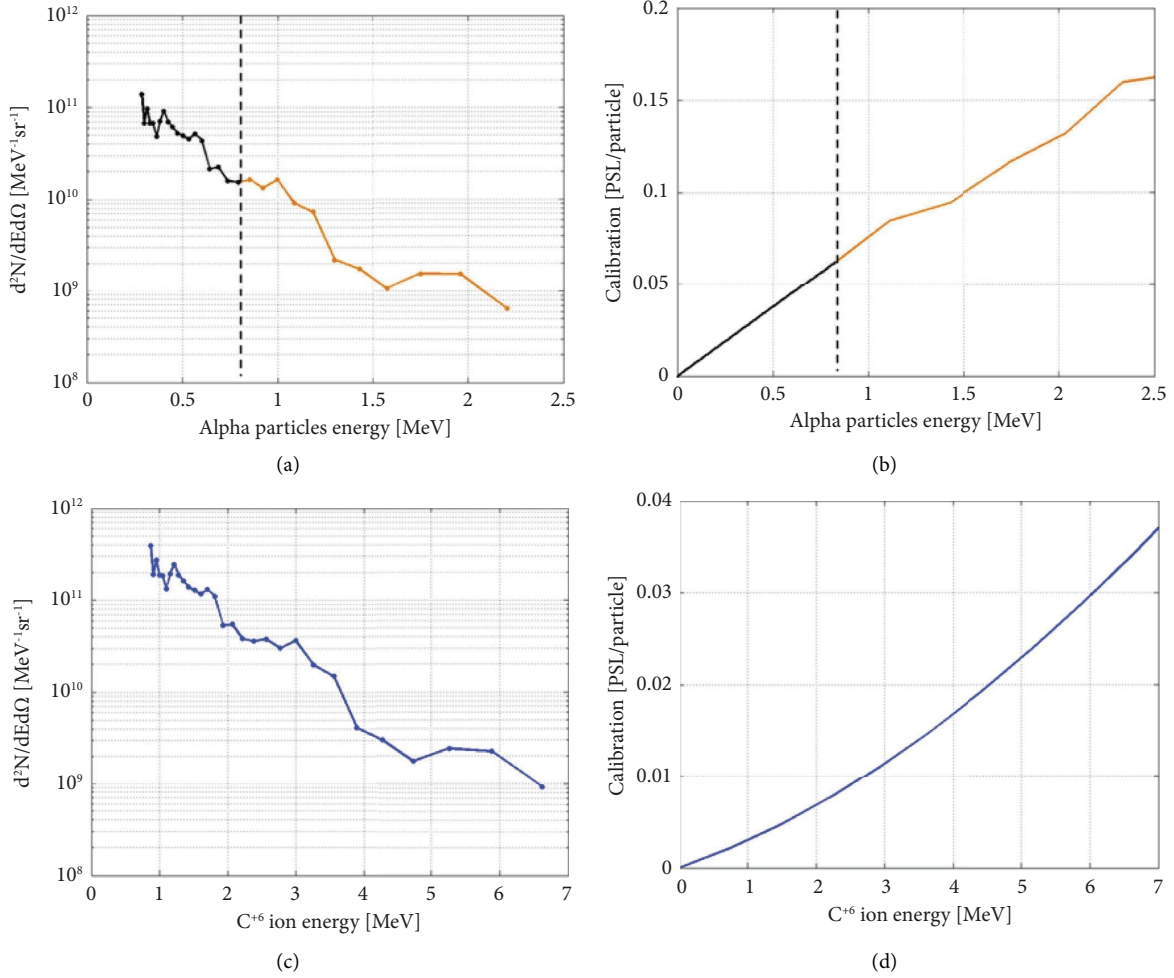


FIGURE 6: (a) Obtained spectrum for the $A/Z = 2$ trace of shot #56027 in the case where the entire contribution to the retrieved signal is due to alpha particles. The number of particles at energies below ~ 0.8 MeV is evaluated using a linear response of the IP. (b) Calibration curve used for calculating the alpha particle beam charge. The orange part of the plot is from ref. [41]. For the black part of the curve, with energies below 0.8 MeV, a linear response of the IP is assumed. (c) Obtained spectrum for the $A/Z = 2$ trace of shot #56027, in the case where the entire contribution to the retrieved signal is due to C^{6+} ions. (d) Calibration curve used for the number of C^{6+} ions obtained using the fitted calibration data in ref. [42].

particles and C^{6+} ions, besides possible O and N ions that can be present in the contaminants on the target surface. These cannot be distinguished with the use of an IP as a detector. The distinction of alpha particles from C^{6+} ions, for example, may require the implementation of alternative techniques, such as, in some cases, the use of CR39 detectors and/or differential filters [39, 40]. In this preliminary study, our main goal was to test the sensitivity of TS and its ability to obtain separate signals for protons and $A/Z = 2$ ions using IPs. For this reason, in the following section, we will analyse the spectra obtained from the $A/Z = 2$ trace considering both cases separately, i.e., under the hypothesis that the retrieved signal is entirely due to alpha-particles or alternatively entirely due to C^{6+} ions. The proton spectrum obtained from the $A/Z = 1$ trace is displayed in Figure 5(a). The retrieved maximum energy is of ~ 1.2 MeV, and the slope of the spectrum is exponentially decreasing, as is typical for laser-accelerated protons. This spectrum was obtained using the IP calibration curve that we report in Figure 5(b). For

energies > 350 keV, the calibration values are those reported in ref. [33] and are plotted in red. At lower energies, no calibration values for TR type IPs are available in literature, to the author's knowledge. Therefore, we assumed a linear response of the detector in the range 0–350 keV, as it is indicated by the black part of the curve of Figure 5(b) (left from the dashed line). The low-energy part of the spectrum, separated by the dashed line on Figure 5(a), is hence obtained using this linear calibration curve, down to a minimum proton energy of ~ 100 keV that our device was capable of detecting. To have a more precise spectrum estimation at $E < 350$ keV, we plan to perform suitable IP calibrations for proton expositions.

In Figures 6(a) and 6(c), we show the obtained spectra for the $A/Z = 2$ trace, assuming the two separate cases where the signal contribution on the IP comes either entirely from alpha particles (panel (a)) or entirely from C^{6+} ions (panel (c)). The alpha particle spectrum, obtained by using the calibration curve of Figure 6(b), has a cutoff energy of

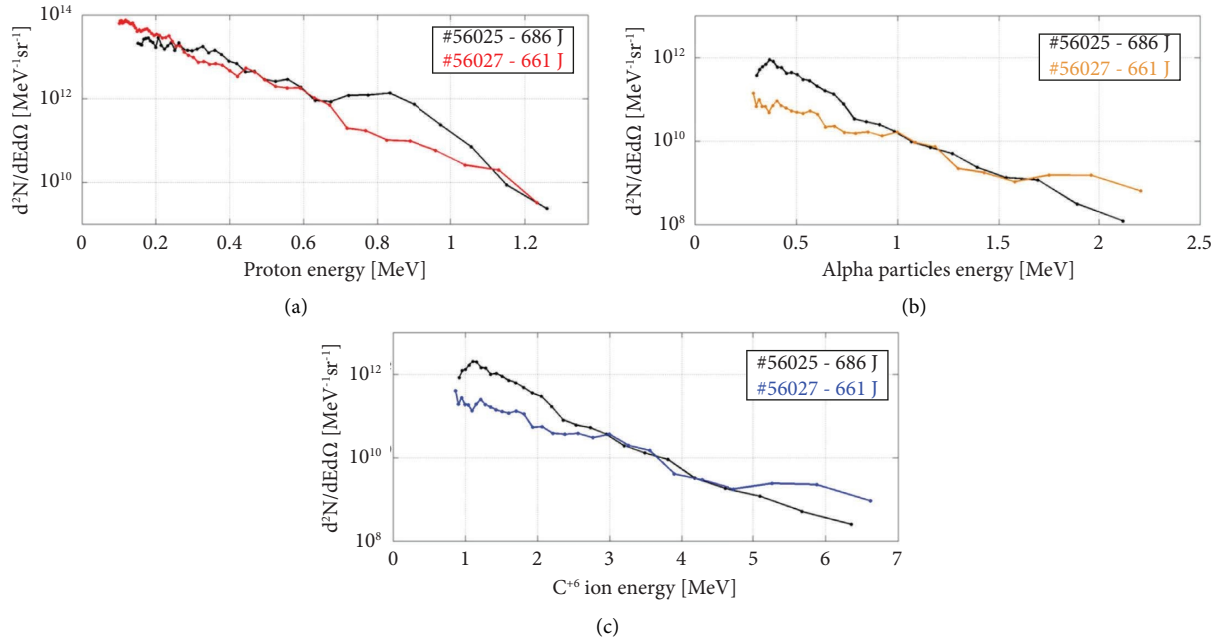


FIGURE 7: Spectra obtained for two typical shots (shot #56025 indicated by black curves and shot #56027 indicated by colored curves). (a) Proton traces. (b) $A/Z=2$ traces assuming that the signal is generated by α particles. (c) $A/Z=2$ traces assuming that the signal is generated by C^{6+} ions.

~ 2.2 MeV. This calibration is reported in reference [41] and similar to the case of protons does not provide calibration values for alpha particles below ~ 800 keV. For this reason, we again used a linear response here for evaluating the charge of the obtained alpha spectrum, as indicated by the black part of the plot (left of the dashed line). The case where the $A/Z=2$ signal is instead entirely generated by carbon ions is represented in Figure 6(c) and shows ions with a maximum energy of ~ 6.6 MeV. For this analysis, we used the calibration curve reported in panel (d), obtained by using the methodology reported in reference [42], where experimental data of TR IP calibrations for carbon ions are fitted with a polynomial curve. Calibration data for C^{6+} ions from ref. [42], are for an ion energy of ~ 12 MeV. Experimental calibration data for energies down to 3 MeV are also reported for C^{3+} ions, and since the stopping power of these accelerated ions is not influenced by their charge state, we assumed that the reported polynomial fit of ref. [42] extends to lower energies as well. For a more precise evaluation of the number of accelerated particles in both cases of alpha particles and carbon ions, a calibration of TR IPs at low energies is necessary and will be addressed in future studies. However, since the main goal of this work was to test the TS sensitivity in a proton-boron experiment and prove its capability of retrieving distinct signals for $A/Z=1$ and $A/Z=2$ traces, we believe that a preliminary evaluation of the beam charge, obtained with the linearized/fitted calibration curves of Figures 5(b), 6(b), and 6(d), serves well the purpose of our study.

From the spectra obtained from the $A/Z=2$ trace, it is also possible to quantitatively estimate the minimum contribution of alpha particles that is detectable with the used IP detector, given our experimental conditions. As discussed in the previous section, we can assume that the signal level of

the $A/Z=2$ trace is entirely given by C^{6+} ions and can therefore, be used as a reference background level, above which the signal of the alpha particles needs to be detected. A reasonable scenario is represented by the case where the contribution of alpha particles leads to a minimum threshold value of $S_{\bar{E}_i}$ that has double the intensity with respect to the case where only C^{6+} ions are present. Hence, the minimal contribution by alpha particles is equal to the reference one given by carbon ions, i.e., $S_{\bar{E}_i\alpha}^{\min} = S_{\bar{E}_i C^{6+}}$. This case is represented by the spectra reported in Figure 6, where we obtain calibrated spectra of alphas and carbon ions using the same signal retrieved from the IP. Indeed, the spectrum of Figure 6(a) represents the minimum quantity of detectable alpha particles in the case that we are considering. By integrating the curve of this spectrum, assuming an isotropic emission of the particles from the target within an emission cone of 70° degrees (half-angle), the total number of particles and the total energy of the particle beam E_α^T can be obtained. Note that the hypothesis of such an emission angle is due to the position of our TS from the target normal, i.e., 69° degrees. The total number of alpha particles, hence, is estimated to be $N_\alpha \approx 1.3 \cdot 10^{11}$. This value can be related to the number of C^{6+} ions obtaining $N_\alpha/N_{C^{6+}} \approx 1.3 \cdot 10^{11}/9.5 \cdot 10^{11} \approx 0.14$. This value represents an estimation of the minimum number of generated alpha particles per accelerated C^{6+} ion, which leads to a detectable signal of alpha particles. In terms of total energy of the alpha particles, we obtain $E_\alpha^T \approx 0.035$ J, which leads, with respect to the laser energy, to a minimum detectable gain of the $p+^{11}\text{B}$ reaction of $E_\alpha^T/E_{\text{laser}} \approx 5.3 \cdot 10^{-5}$.

In Figure 7, we report the comparison between the spectra obtained in two different typical shots, which were

evaluated with the methodology and the experimental setup that we discussed so far. For the $A/Z=2$ traces, we report both the cases of alpha and C^{6+} ions. Also, here, the quantity of protons and alphas (or C^{6+} ions) in the energy range that is not covered by the IP calibrations that are available in the literature, is evaluated using a linear response of the detector. We observe that these shots yield similar spectra, for both protons and $A/Z=2$ ions, in terms of maximum energy and estimated charge. For protons, the maximum energy is between 1.2 and 1.3 MeV for both shots. These results are consistent with the laser energy of the shots, which varies by less than 5% (it is 686 and 661 Joules for shots #56025 and #56027, respectively). This indicates that the TS is capable of providing reliable measurements of the laser-generated protons and ions. For the $A/Z=2$ traces, we find a similar behaviour in terms of energies that are similar for the analysed shots (cut-off energies between ~ 2.0 and ~ 2.2 MeV in case of alpha particles and ~ 6.4 and ~ 6.6 MeV in case of C^{6+} ions, for both shots).

4. Conclusions

We tested and analysed the performance of an advanced Thomson spectrometer in an experiment of high-intensity laser-plasma interactions devoted to the initiation of $p+^{11}\text{B}$ reactions. The conditions of operation of the device were significantly harsh, as is typical for this type of experiment: the effects of strong irradiation by X, gamma, and EMP radiations emitted from plasma were amplified by the very close proximity of the device to the target, i.e., only 367 mm. Despite the placement close to the interaction point, the TS demonstrated a remarkable robustness against these types of radiations and the associated background noise. This allowed for the retrieval of particle signals with a high signal-to-background ratio using TR-type IPs without the necessity of using additional filters. In particular, for the $A/Z=1$ trace, we obtained a SBR value of >100 for the energy range up to 0.7 MeV, >10 up to 1.1 MeV, and >4 for even higher proton energies. For the $A/Z=2$ trace, the SBR was ≥ 2 in the energy range 0.05–0.125 MeV/nucleon and ≥ 3 in the range 0.125–0.55 MeV/nucleon. This indicates that the shielding of the TS and the implementation of a double pinhole assembly protected the detector from the incoming X- and gamma-rays generated by the plasma and simultaneously allowed collecting a sufficiently high number of particles for a good-quality signal. Moreover, the traces did not exhibit the sinusoidal modulation that are typically induced (if no special precautions are taken) by the presence of EMPs in the RF spectrum, as it is reported in Ref. [12] where very similar laser-plasma interaction conditions were exploited but the TS device was placed outside the interaction chamber where the EMPs have significantly less intensity. This indicates that the shielding against this type of radiation provided good protection to our device despite the presence of EMP fields presumably in the order of magnitude of above 0.5 MV/m, as measured at the PALS facility [37]. Our setup allowed to cover a large solid angle, more than one order of magnitude higher with respect to previous other setups where the TS was placed 1.5–2 m far from target. This increases the actual sensitivity of the TS and can actually qualify it as an effective diagnostic tool of alpha products from low-rate nuclear fusion reactions with

unprecedented accuracy and SBR. In this preliminary campaign, we used TR IPs for a fast testing and an assessment of the TS features, especially the SBR, being these detectors very sensitive. The same TS is already equipped with a metallic frame for using CR39 detectors instead of IPs. This will be the main detector to use in the future for actual detection of alpha particles, due to its capability to discriminate incoming ions on the same trace, from the different track diameters left on the CR39 after etching. In this campaign, we evaluated the spectra of $A/Z=1$ and $A/Z=2$ traces for several shots. The maximum energy of protons varied in the range 1.2–1.3 MeV, and for the $A/Z=2$ trace, considering the case fully stripped of alpha particles, we obtained maximum energies of 2.0–2.2 MeV (6.4–6.6 MeV in the case of C^{6+} ions). The quantitative analysis of the measured spectra of shot #56027 allowed us to estimate the minimum threshold of generated alpha particles that leads to a signal that is detectable above the background signal, generated by the C^{6+} ions, given the conditions of our experiment. Assuming that the presence of alpha particles is detectable if the signal of the $A/Z=2$ trace is increased by a factor of two compared to the case where only C^{6+} ions are present, we obtained ~ 0.14 generated alpha particles per accelerated C^{6+} ion as the minimum value. In terms of total alpha particle energy with respect to the laser energy, we obtained a minimum value of $\sim 5.3 \cdot 10^{-5}$. It is worth mentioning that these threshold values can be significantly lowered by implementing filtering techniques that aim at reducing the quantity of detected C^{6+} ions in the energy ranges of alpha particles generated from laser-driven $p+^{11}\text{B}$ reactions [39, 40]. The results regarding the quantity of collected particles were obtained by using the linear response curves of the IPs for the energy ranges that are not covered by the calibration studies present in literature. Generally speaking, the calibration of IPs for low energy ions is still missing in literature, and we aim at addressing it in future works to extend the capability of our TS to provide full energy range calibrated spectra. In conclusion, we have successfully tested our TS in a $p+^{11}\text{B}$ reaction experiment with high energy laser, in a scheme and in experimental conditions that, so far, demonstrated the maximum number of alpha yield. The results of these tests clearly show that this diagnostic can be efficiently used for high-sensitivity detection, discrimination, and spectrometry of alpha particles produced in experiments of $p+^{11}\text{B}$ nuclear fusion reactions in environments with high-background values caused by high-energy and high-intensity laser pulses.

Data Availability

The experimental data used to support the findings of this study are available from the corresponding author upon reasonable request.

Conflicts of Interest

The authors declare that they have no conflicts of interest.

Acknowledgments

This work has been carried out within the framework of the EUROfusion Consortium, funded by the European Union

via the Euratom Research and Training Programme (Grant Agreement no. 101052200—EUROfusion). This research was partially funded by the Ministry of Education, Youth and Sports of the Czech Republic by the project “Advanced Research Using High Intensity Laser Produced Photons and Particles” (CZ.02.1.01/0.0/0.0/16_019/0000789).

References








- [1] J. Freiberger, *Plasma Physics and Fusion Energy*, Cambridge University Press, Cambridge, UK, 2007.
- [2] S. Atzeni and J. Meyer-ter-Vehn, *The Physics of Inertial Fusion: Beam Plasma Interaction, Hydrodynamics, Hot Dense Matter*, Oxford University Press, Oxford, UK, 2009.
- [3] C. Baccou, S. Depierreux, V. Yahia et al., “New scheme to produce aneutronic fusion reactions by laser-accelerated ions,” *Laser and Particle Beams*, vol. 33, no. 1, pp. 117–122, 2015.
- [4] H. W. Becker, C. Rolfs, and H. P. Trautvetter, “Low-energy cross sections for $^{11}\text{B}(p, \alpha)$,” *Zeitschrift für Physik A Atomic Nuclei*, vol. 327, no. 3, pp. 341–355, 1987.
- [5] W. Nevins and R. Swain, “The thermonuclear fusion rate coefficient for p-11B reactions,” *Nuclear Fusion*, vol. 40, no. 4, pp. 865–872, 2000.
- [6] J. E. Brandenburg, “The hybrid fusion-fission reactor as the solution to the energy crisis,” *Journal of Space Exploration*, vol. 3, 2014.
- [7] J. P. Freidberg and A. C. Kadak, “Fusion–fission hybrids revisited,” *Nature Physics*, vol. 5, no. 6, pp. 370–372, 2009.
- [8] G. L. Kulcinski and J. F. Santarius, “Advanced fuels under debate,” *Nature*, vol. 396, no. 6713, pp. 724–725, 1998.
- [9] S. Kimura, A. Anzalone, and A. Bonasera, “Comment on “Observation of neutronless fusion reactions in picosecond laser plasmas”,” *Physical Review A*, vol. 79, no. 3, Article ID 038401, 2009.
- [10] V. S. Belyaev, A. P. Matafonov, V. I. Vinogradov et al., “Observation of neutronless fusion reactions in picosecond laser plasmas,” *Physical Review A*, vol. 72, no. 2, Article ID 026406, 2005.
- [11] C. Labaune, C. Baccou, S. Depierreux et al., “Fusion reactions initiated by laser-accelerated particle beams in a laser-produced plasma,” *Nature Communications*, vol. 4, no. 1, p. 2506, 2013.
- [12] L. Giuffrida, F. Belloni, D. Margarone et al., “High-current stream of energetic α particles from laser-driven proton-boron fusion,” *Physical Review A*, vol. 101, no. 1, Article ID 013204, 2020.
- [13] A. Bonasera, A. Caruso, C. Strangio et al., “Measuring the astrophysical s-factor in plasmas,” in *Proceedings of the 4th Fission And Properties Of Neutron-Rich Nuclei*, pp. 503–507, Sanibel Island, FL, USA, November 2008.
- [14] A. Picciotto, D. Margarone, A. Velyhan et al., “Boron-proton nuclear-fusion enhancement induced in boron-doped silicon targets by low-contrast pulsed laser,” *Physical Review X*, vol. 4, no. 3, Article ID 031030, 2014.
- [15] D. Margarone, A. Picciotto, A. Velyhan et al., “Advanced scheme for high-yield laser driven nuclear reactions,” *Plasma Physics and Controlled Fusion*, vol. 57, no. 1, Article ID 014030, 2014.
- [16] D. Giulietti, P. L. Andreoli, D. Batani et al., “Laser-plasma energetic particle production for aneutronic nuclear fusion experiments,” *Nuclear Instruments and Methods in Physics Research Section B: Beam Interactions with Materials and Atoms*, vol. 402, pp. 373–375, 2017.
- [17] F. Ingenito, P. L. Andreoli, D. Batani et al., “Directional track selection technique in CR39 SSNTD for lowyield reaction experiments,” *EPJ Web of Conferences*, vol. 167, Article ID 05006, 2018.
- [18] M. Cipriani, F. Consoli, P. L. Andreoli et al., “Spectral characterization by CVD diamond detectors of energetic protons from high-repetition rate laser for aneutronic nuclear fusion experiments,” *Journal of Instrumentation*, vol. 14, no. 1, Article ID C01027, 2019.
- [19] F. Consoli, R. De Angelis, P. L. Andreoli et al., “Diagnostic methodologies of laser-initiated $^{11}\text{B}(p, \alpha)^{2}\alpha$ fusion reactions,” *Frontiers in Physics*, vol. 8, Article ID 561492, 2020.
- [20] W. L. Kruer, *The Physics of Laser Plasma Interactions*, Westview Press, Boulder, CO, USA, 2003.
- [21] A. Macchi, M. Borghesi, and M. Passoni, “Ion acceleration by superintense laser-plasma interaction,” *Reviews of Modern Physics*, vol. 85, no. 2, p. 751, 2013.
- [22] D. Umstadter, “Relativistic laser–plasma interactions,” *Journal of Physics D: Applied Physics*, vol. 36, no. 8, R165 pages, 2003.
- [23] F. Consoli, P. L. Andreoli, M. Cipriani et al., “Sources and space-time distribution of the electromagnetic pulses in experiments on inertial confinement fusion and laser-plasma acceleration,” *Philosophical Transactions of the Royal Society A: Mathematical, Physical & Engineering Sciences*, vol. 379, no. 2189, Article ID 20200022, 2020.
- [24] F. Consoli, V. T. Tikhonchuk, M. Bardon et al., “Laser produced electromagnetic pulses: generation, detection and mitigation,” *High Power Laser Science and Engineering*, vol. 8, p. e22, 2020.
- [25] P. R. Bolton, M. Borghesi, C. Brenner et al., “Instrumentation for diagnostics and control of laser-accelerated proton (ion) beams,” *Physica Medica*, vol. 30, no. 3, pp. 255–270, 2014.
- [26] R. Cassou and E. Benton, “Properties and applications of CR-39 polymeric nuclear track detector,” *Nuclear Track Detection*, vol. 2, no. 3, pp. 173–179, 1978.
- [27] G. Muenzenberg, “Development of mass spectrometers from Thomson and Aston to present,” *International Journal of Mass Spectrometry*, vol. 349–350, pp. 9–18, 2013.
- [28] J. J. Thomson, “Rays of positive electricity,” *Proceedings of the Royal Society A*, vol. 89, p. 607, 1913.
- [29] J. N. Olsen, G. W. Kuswa, and E. D. Jones, “Ion-expansion energy spectra correlated to laser plasma parameters,” *Journal of Applied Physics*, vol. 44, pp. 2275–2283, 1973.
- [30] F. Consoli, R. D. Angelis, A. Bonasera et al., “Study on a compact and adaptable Thomson Spectrometer for laser-initiated $^{11}\text{B}(p, \alpha)^{8}\text{Be}$ reactions and low-medium energy particle detection,” *Journal of Instrumentation*, vol. 11, no. 05, Article ID C05010, 2016.
- [31] G. D. Giorgio, F. Consoli, R. D. Angelis et al., “Development of advanced Thomson spectrometers for nuclear fusion experiments initiated by laser,” *Journal of Instrumentation*, vol. 15, no. 10, Article ID C10013, 2020.
- [32] M. Scisciò, F. Consoli, M. Salvadori et al., “High sensitivity Thomson spectrometry: analysis of measurements in high power picosecond laser experiments,” *Journal of Instrumentation*, vol. 17, no. 01, Article ID C01055, 2022.
- [33] T. Bonnet, M. Comet, D. Denis-Petit et al., “Response functions of Fuji imaging plates to monoenergetic protons in the energy range 0.6–3.2 MeV,” *Review of Scientific Instruments*, vol. 84, no. 1, Article ID 013508, 2013.
- [34] G. Boutoux, D. Batani, F. Burgy et al., “Validation of modelled imaging plates sensitivity to 1–100 keV x-rays and spatial resolution characterisation for diagnostics for the “PETawatt

- Aquitaine Laser”,” *Review of Scientific Instruments*, vol. 87, no. 4, Article ID 043108, 2016.
- [35] S. Singh, T. Slavicek, R. Hodak, R. Versaci, P. Pridal, and D. Kumar, “Absolute calibration of imaging plate detectors for electron kinetic energies between 150 keV and 1.75 MeV,” *Review of Scientific Instruments*, vol. 88, no. 7, Article ID 075105, 2017.
- [36] A. L. Meadowcroft, C. D. Bentley, and E. N. Stott, “Evaluation of the sensitivity and fading characteristics of an image plate system for x-ray diagnostics,” *Review of Scientific Instruments*, vol. 79, no. 11, Article ID 113102, 2008.
- [37] P. Raczka, J. Cikhardt, M. Pfeifer et al., “Measurement of strong electromagnetic pulses generated from solid targets at sub-ns kJ-class PALS laser facility,” *Plasma Physics and Controlled Fusion*, vol. 63, no. 8, Article ID 085015, 2021.
- [38] F. Grepl, J. Krasa, A. Velyhan et al., “Distortion of Thomson parabolic-like proton patterns due to electromagnetic interference,” *Applied Sciences*, vol. 11, no. 10, p. 4484, 2021.
- [39] A. Alejo, S. Kar, H. Ahmed et al., “Characterisation of deuterium spectra from laser driven multi-species sources by employing differentially filtered image plate detectors in Thomson spectrometers,” *Review of Scientific Instruments*, vol. 85, no. 9, Article ID 093303, 2014.
- [40] M. Salvadori, “Methodologies for the univocal discrimination of α particles produced by the $^{11}\text{B}(p,\alpha)2\alpha$ fusion reactions,” *Laser and Particle Beams*, 2020.
- [41] C. G. Freeman, G. Fiksel, C. Stoeckl et al., “Calibration of a Thomson parabola ion spectrometer and Fujifilm imaging plate detectors for protons, deuterons, and alpha particles,” *Review of Scientific Instruments*, vol. 82, no. 7, Article ID 073301, 2011.
- [42] D. Doria, S. Kar, H. Ahmed et al., “Calibration of BAS-TR image plate response to high energy (3-300 MeV) carbon ions,” *Review of Scientific Instruments*, vol. 86, no. 12, Article ID 123302, 2015.



Research Article

Path to Increasing p-B11 Reactivity via ps and ns Lasers

Thomas A. Mehlhorn ^{1,2}, **Lance Labun** ³, **Bjorn Manuel Hegelich** ³,
Daniele Margarone ^{4,5}, **Ming Feng Gu** ⁶, **Dimitri Batani** ^{2,7}, **E. Michael Campbell**,⁸
and **S. X. Hu** ⁹

¹Mehlhorn Engineering Consulting Services, Beaverton 97003, OR, USA

²HB11 Energy Holdings Pty, 11 Wyndora Ave, Freshwater 2096, NSW, Australia

³Department of Physics, University of Texas, Austin 78712, TX, USA

⁴Centre for Plasma Physics, Queen's University of Belfast, Belfast BT7 1NN, UK

⁵ELI Beamlines Facility, The Extreme Light Infrastructure ERIC, Dolni Brezany 252 41, Czech Republic

⁶Prism Computational Sciences, Madison, Wisconsin, USA

⁷University of Bordeaux, CNRS, CEA, CELIA (Centre Lasers Intenses et Applications), Talence F-33405, France

⁸MCM Consulting, San Diego 97127, CA, USA

⁹Laboratory for Laser Energetics, University of Rochester, Rochester 14623, New York, USA

Correspondence should be addressed to Thomas A. Mehlhorn; tamehlhorn97@gmail.com

Received 29 June 2022; Revised 4 August 2022; Accepted 9 December 2022; Published 24 December 2022

Academic Editor: Bhuvanesh Ramakrishna

Copyright © 2022 Thomas A. Mehlhorn et al. This is an open access article distributed under the Creative Commons Attribution License, which permits unrestricted use, distribution, and reproduction in any medium, provided the original work is properly cited.

The Lawson criterion for proton-boron ($p\text{-}^{11}\text{B}$) thermonuclear fusion is substantially higher than that for deuterium-tritium (DT) because the fusion cross section is lower and peaks at higher ion energies. The Maxwellian averaged $p\text{-}^{11}\text{B}$ reactivity peaks at several hundred keV, where bremsstrahlung radiation emission may dominate over fusion reactions if electrons and ions are in thermal equilibrium and the losses are unrestricted. Nonequilibrium burn has often been suggested to realize the benefits of this aneutronic reaction, but the predominance of elastic scattering over fusion reactivity makes this difficult to achieve. The development of ultrashort pulse lasers (USPL) has opened new possibilities for initiating nonequilibrium thermonuclear burns and significant numbers of $p\text{-}^{11}\text{B}$ alpha particles have been reported from several experiments. We present an analysis that shows that these significant alpha yields are the result of beam fusion reactions that do not scale to net energy gain. We further find that the yields can be explained by experimental parameters and recently updated cross sections such that a postulated avalanche mechanism is not required. We use this analysis to understand the underlying physics of USPL-driven nonequilibrium fusion reactions and whether they can be used to initiate fusion burns. We conclude by outlining a path to increasing the $p\text{-}^{11}\text{B}$ reactivity towards the goal of achieving ignition and describing the design principles that we will use to develop a computational point design.

1. Introduction

Fusion is the dominant energy source in the universe and occurs within the cores of gravitationally confined stars. Thermonuclear weapons are a demonstration of a single-shot, uncontrolled thermonuclear fusion device on Earth. The multidecadal international research program to design and construct a controlled thermonuclear reactor that achieves scientific breakeven (fusion energy out equal to energy invested in the fuel) is a testament to the difficulty of

creating the conditions for fusion burn and plasma gain (fusion energy/input energy to the plasma > 1) in a laboratory device. Recent success in nearly achieving scientific breakeven (fusion energy/incident laser energy) at the National Ignition Facility (NIF) [1], recording multisecond fusion burns in JET [2], demonstrating 20 Tesla magnet operation by CFS [3], and expectations of even higher performance in ITER [4], all using D-T fuel, have stimulated a resurgence of interest in fusion as an environmentally friendly energy source in the fight to control climate change.

This, in turn, has led to an unprecedented influx of venture capital to a growing number of companies that are pursuing a wide variety of approaches to reaching and exceeding scientific breakeven on the way to an economical and environmentally attractive fusion power plant. The science and engineering challenges of moving from a successful demonstration of scientific breakeven to such a fusion power plant are formidable. For example, for ICF, the excitement surrounding the achievement of significant yield on shot N210808 (August 8, 2021) is tempered by the fact that the 1.35 MJ of fusion yield obtained with an X-ray-driven capsule in a hohlraum began with 300 MJ stored in the capacitor banks which energized the flashlamps that pumped the Nd:glass NIF laser. The capsule in the hohlraum absorbed about 225 kJ of x-rays producing a capsule gain of ~ 6 . While several implosions since August have produced capsule gains greater than 1, no yields greater than 1 MJ have been obtained to date. Further, the laser shot rate (one/day), target fabrication rate (few/week or month), and many other missing factors (e.g., target injection and tritium breeding) need to be demonstrated or significantly increased to realize a practical power plant.

The U.S. Department of Energy (DOE) has begun to hold a series of Inertial Fusion Energy (IFE) workshops [5] to explore the range of options for driving the target (direct or indirect (X-ray) drive by lasers, pulsed power, or heavy ions) and to collect a list of basic research needs for developing the technologies and science required by an IFE reactor. The DOE has been chartering studies and funding fusion research for decades, primarily focused on magnetic fusion systems (tokamaks), with no clear timeline of developed metrics to achieve fusion power. However, the significantly increased private funding investment is motivating serious discussions with the government to establish exciting new legislation that would create private-public partnerships (PPPs) [6] to pursue the development and commercialization of fusion power plants. Such partnerships and legislation could significantly accelerate the timeline as compared to government-only projects. Further, following the successful partnership between NASA and multiple commercial spacecraft companies, a fusion PPP program should provide a parallel, competitive development path for fusion reactors.

HB11 Energy Pty LTD is a startup company for the purpose of developing an IFE power plant based on the proton-boron-11 ($p\text{-}^{11}\text{B}$) reaction. There are several articles that describe the HB11 roadmap [7] for translating their original patents [8] into a fusion power plant. The baseline approach calls for igniting a nonthermal H-B reaction through laser ion acceleration of protons toward a ^{11}B -rich fuel, confining the burning plasma in a laser-generated magnetic confinement system, further increasing the yield through an avalanche reaction, and generating electricity by direct capture of the energetic fusion alpha particles. The patents are based on a series of theoretical papers that have been published over many years and have been awaiting experimental testing. The development of ultrashort pulse lasers (USPL) has opened new possibilities for initiating nonequilibrium thermonuclear burn, and significant numbers of $p\text{-}^{11}\text{B}$ alpha particles have been reported from several

experiments that cite Prof. Hora's HB11 references. In subsequent sections, we report on our analysis of these experiments and what they inform us about the roadmap approach to developing a reactor for the $p\text{-}^{11}\text{B}$ reaction.

Proton-boron fusion is attractive because the reaction is aneutronic, produces limited radioactive waste, uses a stable, abundant, and nonradioactive fuel that avoids the engineering challenges of breeding, and has the possibility of higher energy conversion efficiency than a thermal cycle. However, it is well known that the Lawson criterion for $p\text{-}^{11}\text{B}$ is substantially higher than that for D-T because the fusion cross section is lower and peaks at higher ion energies. Therefore, the $p\text{-}^{11}\text{B}$ reactivity for Maxwellian ion distributions peaks at significantly higher temperatures than for DT. Further, if the plasma electrons are in equilibrium with the ions, there are concerns that bremsstrahlung radiation losses, given the relatively high charge state of boron ($Z=5$), may dominate over fusion reactions across the parameter space, making net energy gain impossible. A recent article [9] presents the framework of a generalized Lawson criteria to allow comparison between various fusion fuel cycles and fusion devices across the range of magnetic, inertial, and magnetized concepts. Their analysis of the $p\text{-}^{11}\text{B}$ burn using the standard fusion cross section and radiation rates concludes that ignition is not possible unless the electron temperature is lower than the ion temperature by a factor of 3–5. However, another recent paper [10] reports finding higher reactivity ($\sim 30\%$) using an updated cross section [11], as well as accounting for the kinetic effects of reaction products on the proton spectrum via a Fokker-Planck model. The authors conclude that ignition may be theoretically possible in the magnetic confinement device that they considered.

2. Neutron Yields from Laser-Driven Experiments with Deuterium Targets

The invention of the techniques of chirped pulsed amplification by Strickland and Moreau [12] greatly expanded the intensity horizon for laser-target experiments and was recognized with the 2018 Nobel Prize in Physics. High intensity short pulse lasers also opened new alternatives to the standard hot spot ignition approach to ICF. For example, in 1994, Tabak and colleagues proposed [13] to use ultra-powerful lasers to create a focused beam of hot electrons to locally heat and ignite a portion of a dense ball of DT that is precompressed by temporally shaped nanosecond laser beams to assemble the fuel in a high-density isochoric (constant density) state. This so-called "fast ignition" scheme separates the implosion of the fuel from the ignition process and thereby relaxes some of the constraints on implosion symmetry and the generation of mix. However, the efficiency of the generation and transport of hot electrons to the imploded fuel is complicated by the strong electrostatic fields that are generated (c.f. [14]). Early experiments on the world's first petawatt laser at LLNL showed high-energy proton generation that has also motivated proton-driven fast ignition [15]. Experiments have also shown the ability to focus the proton beam by shaping the target, and the

isochoric heating of targets by the protons has also been demonstrated. Research is underway to explore both fast ignition concepts. As previously mentioned, HB11 proposes to use USPLs to accelerate protons and initiate a non-equilibrium burn of the boron fuel, which requires detailed knowledge of which elements of the laser-target interaction have the greatest impact on fusion reactivity.

Analysis of neutron yields from experiments with USPL-irradiated deuterium targets can give valuable insight into the laser-target interaction physics because they have been widely performed and neutron activation and time-of-flight (TOF) are standard diagnostics at most laser facilities. Further, neutrons are not attenuated by the target material, nor are they influenced by electromagnetic fields. Therefore, they clearly reflect the fusion processes within the target. For example, in 1998 Norreys et al. [16] irradiated cryogenically cooled deuterated targets at up to 10^{19} W/cm² and measured the resultant neutron fluxes to gain insight into the laser plasma interaction process leading to deuteron acceleration. Their analysis showed that the neutron production was consistent with inflight D-D beam fusion reactions created by fast deuterons that are accelerated by the strong laser-generated fields, rather than thermonuclear fusion from a heated fuel region. Specifically, Norrey's paper shows a neutron TOF peak at 2.45 MeV for a laser intensity of 9×10^{17} W/cm², but shows a much broader peak extending to higher neutron energies at 5×10^{18} W/cm², which is consistent with deuteron acceleration to higher kinetic energies.

The first important insight that we get from these early experiments is that, at these intensities, the laser-target interaction physics requires the incorporation of kinetic particle interactions with the plasma that go beyond a single fluid model. That is, the hot electrons and accelerated fast ions are not in equilibrium with the background plasma, and these fast particles penetrate through the background fluid and lose energy and scatter primarily through Coulomb interactions, as described by a Fokker-Planck model. The fact that these fast particles have extended ranges accounts for the lack of localized plasma heating to thermonuclear temperatures. It also precludes the generation of strong shocks, which require a localized region of high-pressure region (piston) and a lack of preheating beyond the shock interface. This means that a single fluid, or even a two-fluid model, such as that of Lalouis et al. [17], cannot accurately capture the essential physics of this interaction.

As described by Krása et al. [18], other researchers have performed a variety of experiments to measure fast ion fluxes and D-D neutron production from laser-target interactions at fs, ps, and sub-ns pulse durations on several different laser systems. Interestingly, Figure 6 from his paper (reproduced above as Figure 1) shows that the measured neutron yields are consistent with the total laser beam energy across three orders of magnitude in laser pulse duration, except for the N98 data point [16], which is unique in that it had a cryogenic deuterium target, as will be discussed in more detail at the end of Section 4. This suggests that the

integrated number of neutrons produced via beam-fusion reactions is relatively insensitive to the details of the interaction physics, which are a complicated function of laser intensity, wavelength, and contrast ratio (ratio of the prepulse to the main pulse of the laser). For this set of experiments, the fast ion spectrum within the target is almost certainly different for lasers with different pulse durations and thereby different focal intensities, as was seen in the Norreys paper. This insensitivity in total yield may be attributed to the fact that beam fusion reactions appear to be dominant and the number of inflight reactions is a convolution of the reaction cross section over the ion stopping power, as described in equation (1). This means that for targets that are thicker than an ion range, the inflight nuclear reactions will occur from the highest ion energy down to energies where the cross section becomes negligible.

$$Y(E_0) = \int_0^{E_0} \sigma(E) \left(\frac{dE}{dx} \right)^{-1} dE. \quad (1)$$

Equation (1): Thick target inflight reaction yield for an incident particle with an initial ion energy E_0

As will be discussed in more detail in Section 5, as laser intensity increases, so does the hot electron temperature and corresponding fast ion energy. This means that as the laser intensity increases, the fast ions are sampling higher energy portions of the nuclear cross sections. Figure 2 shows the fusion cross sections for D-T, D-D, and p-B11 as a function of center-of-mass (COM) ion energy. Standard approaches to thermonuclear fusion, such as ICF and magnetic fusion energy (MFE), are focused on the reactivity of Maxwellian-averaged thermal distributions of ions, meaning that they are primarily focused on the accuracy of the low-energy portion of the cross section. Beam fusion reactions sample the cross sections downwards from the highest energy as the ions lose energy through inelastic collisions with electrons. This means that the accuracy of nuclear reaction yields, as calculated by equation (1), is sensitive to the high-energy portion of the cross sections, which may not be as thoroughly studied. Further, often fusion cross sections are presented as fits to analytic functions over specified energy regimes. For example, Table IV in Bosch and Hale [19] lists the parameters for the cross section fit for DD reactions in the energy range 0.5–5000 keV, which is more than adequate for computing thermal-averaged fusion reactivities. Beyond this range, it is important to look for experimental data points, for example in the EXFOR Experimental Nuclear Reaction Database [19]. There is limited data above for D-D fusion cross sections above a few MeV, so there is greater uncertainty in this region. Regardless, the data shows a decrease in cross section at higher deuteron energies, which helps explain the relative insensitivity of D-D neutron yield with laser intensity (peak deuteron energy), because all deuterons with energies above a few MeV generate their maximum yield as they slow down through the 100–1500 keV region, making their integrated reaction yield roughly constant.

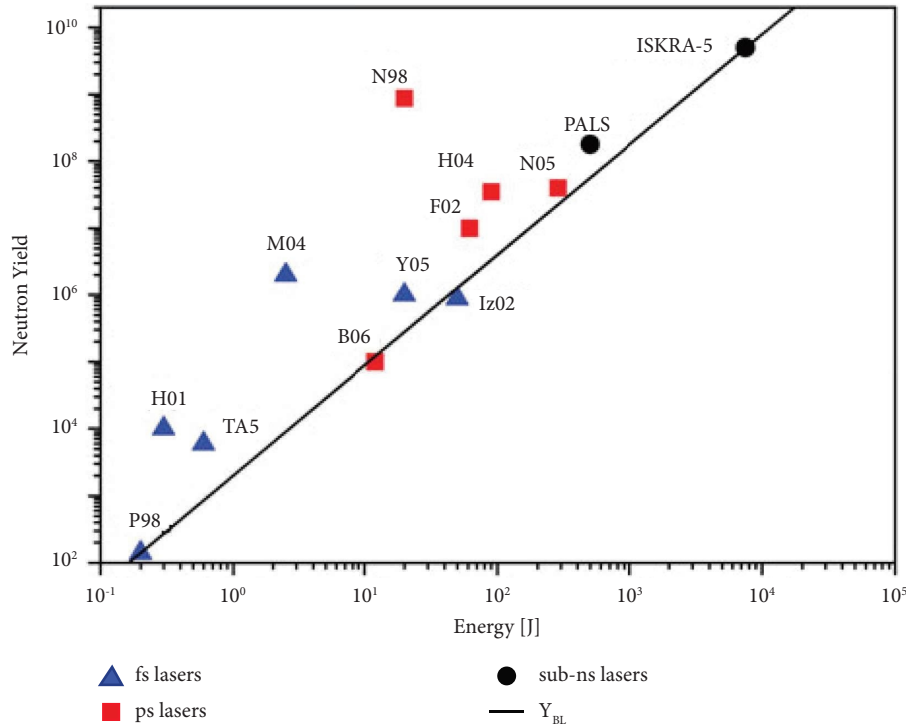


FIGURE 1: Neutron yield as a function of laser energy for fs, ps, and sub-ns lasers (Krasa Figure 6).

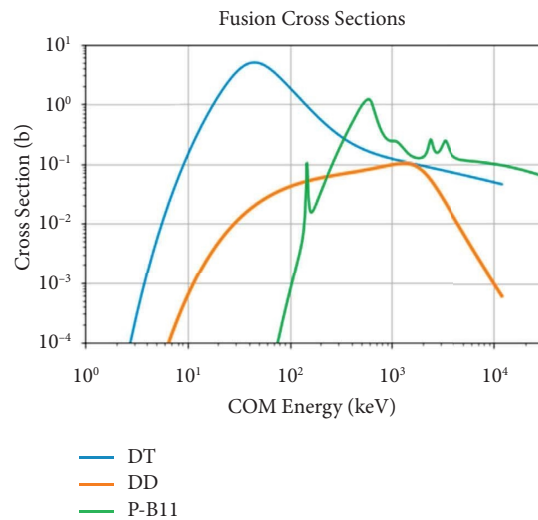


FIGURE 2: Nuclear fusion cross sections as a function of COM energy.

3. Alpha Yields from Laser-Driven Experiments with Boron Targets

One of the datasets in Figure 1 is from experiments reported in 2004–2006 by Belyaev and collaborators in Russia [20]. They reported measuring a considerable neutron yield of 5×10^4 per pulse from the irradiation of the surface of a solid deuterated target by a picosecond laser plasma at an intensity of $3 \times 10^{17} \text{ W/cm}^2$. In 2006, they also reported on the deleterious effects of laser prepulse on neutron production and

the importance of maintaining a good contrast ratio. In 2005, Belyaev used the same “Neodymium” laser facility to irradiate targets containing ^{11}B and reported on the first observation of alpha particles that escape the target from the neutron-less p- ^{11}B fusion reactions at peak intensities of $2 \times 10^{18} \text{ W/cm}^2$ [21]. Their reported yield was $10^3 \alpha/\text{pulse}$ (meaning per shot). However, their α particle diagnostics were less mature than the neutron diagnostics that were used in the deuterium experiments, and they are inherently more difficult to field due to the shortness of their range and the

dependence on CR-39 track detectors as a primary measurement tool. Kimura et al. revisited the analysis techniques and reported that the total yield was underestimated by at least a factor of 100, making the true yield 10^5 per pulse [22].

Since 2005, there have been a series of laser-driven p- ^{11}B experiments at several different facilities (Labaune et al. [23, 24], Picciotto et al. [25], Margarone et al. [26], Baccou et al. [27], Tayyab et al. [28], Giuffrida et al. [29], Margarone et al. [30], Bonvalet et al. [31], TPW [32], Margarone et al. [33]) and the measured alpha particle yields have shown an impressive increase, as seen in Figure 3. A common goal of these experiments has been to maximize the generation of high-energy protons via laser-driven charged particle acceleration (CPA) and to interact these protons with boron-containing targets to generate alpha particles via the p- ^{11}B reaction. Some of these experiments were performed in an “in-target” geometry, where the laser directly irradiates a solid target, and the accelerated protons interact with the bulk material. This is the geometry that Belyaev used in his initial experiments. Direct irradiation of monolithic in-targets allows the laser and fast electron energy to be deposited within the target material, and analysis of the interaction needs to account for the temperature dependence of the proton stopping power as it is transported in the medium. Many other of these experiments were performed in a “pitcher-catcher” geometry where the protons are generated from a laser-irradiated thin foil (the pitcher) and collide with a second target (catcher), thereby undergoing beam fusion reactions. In this case, the catcher target is normally an unheated solid, except for the Labaune experiment, where a ns laser was used to heat the catcher.

Given that there are relatively few of these experiments, it is remarkable that they represent such a wide variety of laser parameters, target geometries, and target compositions, as seen in Table 1. We see that experiments have been done at a variety of wavelengths, with laser energies varying from 15 J to 1.4 kJ, laser pulse widths of 25 fs to 300 ps, and focused intensities “ I ” from 3×10^{16} to 2×10^{21} . The experiments on the Ti:Sa laser system at the Laser Plasma Division, RRCAT, India [28] had the shortest 25 fs pulse width and focal intensities of 1×10^{20} . This ensemble of experiments also encompasses a broad range of laser prepulse or contrast ratios. Specifically, only the Labaune, Tayyab, and Hegelich experiments had low prepulse (high contrast ratio). The others had more significant prepulse energies that created plasma blowoff prior to the peak intensity and could modify the interaction physics. In Figure 3, the left-hand scale indicates the absolute particle flux (particles/sr), while the right-hand scale is normalized to the laser energy delivered on target (particles/sr/J). In subsequent sections, we will try to explain the underlying physics that governs the trends in the data, especially the normalized alpha yield per joule of laser energy, which reflects the relative energy gain of the fusion process. This rapid increase in alpha-particle flux from CPA-driven experiments over the past 17 years has been quite impressive, and the apparent ease of generating substantial yields has led to speculation that energy production from nonequilibrium aneutronic fusion is on the horizon. What does this data tell us about energy gain?

The p- ^{11}B reaction has a Q-value of 8.76 MeV, and this energy is partitioned between three alpha particles. From a target physics perspective, it is interesting to note that p- ^{11}B has roughly half the Q-value of D-T, but because 80% of the D-T energy is carried by a 14.1 MeV neutron, the alpha particle only has 3.5 MeV. This means that the target heating via alpha deposition is 2.5 times larger for p- ^{11}B than for DT, which will be an important consideration when calculating fusion reactivity. The p- ^{11}B Q-value can be used to calculate that 1 kJ of fusion energy is equivalent to 2.15×10^{15} alpha particles. Therefore, we can define scientific breakeven, which we define as fusion energy out equal to laser energy in, to be 2.15×10^{12} alphas/J. This means that the maximum normalized yield for this suite of experiments is at most 10^{-4} of scientific breakeven. As we shall discuss in more detail, despite the seductively large numbers of alpha particles seen in these USPL-driven experiments, the best yields are consistently associated with a proton acceleration efficiency of $\sim 10\%$ coupled with an inflight reaction probability of 10^{-3} to 10^{-4} . In the following sections, we will perform a deeper analysis of these experiments to discover what physical mechanisms produce the highest gains and how they might be harnessed to realize significant fusion gains in future target designs.

4. Comparison of Alpha Particles and DD Neutrons from Laser-Driven Experiments

Another way to view the data from Figure 3 and Table 1 is to plot the alpha particle yields as a function of laser energy on the same DD neutron yield plot of Figure 1. In fact, Figure 3 of Reference [34] and Figure 4 of Reference [35] show the Krassa data with faint p-B11 data points sketched onto the plot. A key point of the discussion in these papers is the nonthermal nature of the reactions in both cases, and there is mention that it is surprising that the proton-boron data lies above the neutron yield line and that this might indicate that there is some missing physics in USPL-driven experiments that increases the proton-boron fusion reactivity. Figure 4 shows the alpha particle yield from Figure 3 mapped onto the Krassa neutron yield seen in Figure 1. The ovals for the Belyaev and TPW data denote the range of yields from different experimental configurations. The results for PALS and LFEX extend beyond the limits of the original plot, emphasizing the higher yields for p-B 11 than for D-D for these laser-driven experiments.

Our analysis shows that the inflight reactivity of protons on ^{11}B is higher than that of deuterons on deuterium, such that the yields should be higher; it is important not to confuse these D-D reactions with the higher values expected for D-T fusion. This can be seen in Figure 5, which shows the thick target yields for protons on boron and deuterons on CD_2 as a function of initial projectile energy, as calculated by equation (1) using appropriate ion stopping powers and fusion cross sections. This analysis shows that these results can be explained by the higher cross section for protons on boron, as well as the greater ion acceleration efficiency of protons as compared to deuterons. The omnipresence of hydrogen in materials, coupled with their 1:1 charge-to-mass ratio as compared to 1:2 for deuterons, makes them

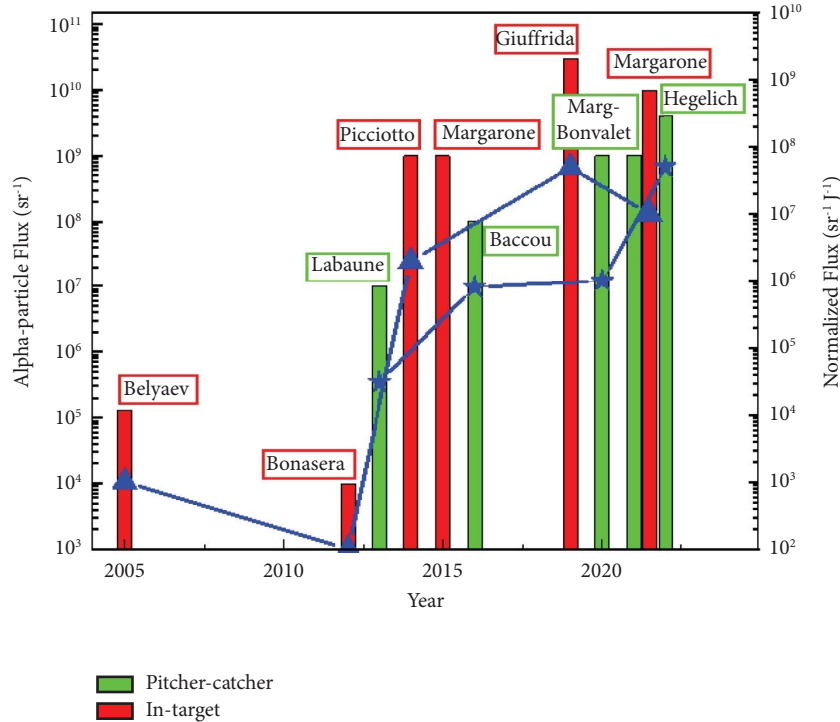


FIGURE 3: Maximum alpha particle yield by year for various lasers for both pitcher-catcher and in-target irradiation geometries. This is an updated version of Figure 1 in ref [33] that includes data from the Texas PW experiment. Data bars correspond to the left axis. Blue curves refer to the right axis: triangles denote in-target geometry; stars denote pitcher-catcher geometry.

TABLE 1: Summary of facility and laser parameters for p-B11 experiments since 2005.

	Year	Laser	Where	λ (μ)	Energy (J)	I (W/cm^2)	τ (ps)	Type	Alphas #/sr
Hegelich	2022	TPW	Texas	1	80	$2E+21$	0.14	Pitch-catch	$4.e+9$
Margarone	2022	LFEX	ILE	1.05	1400	$3E+19$	2	Intarget	$1.2e+10$
Bonvalet	2020	LFEX	ILE	1.05	1400	$3E+19$	2.7	Pitch-catch	$1e+9$
Giuffrida	2020	PALS	Prague	1.315	600	$3E+16$	300	Intarget	$3e+10$
Tayyab	2019	150 TW Ti:Sa	India	0.8	2.5	$1E+20$	0.025	Pitch-catch	$\sim 1.4e6$
Baccou	2015	ELFIE	LULI	1.056	12	$1E+19$	0.35	Pitch-catch	$1e+8$
Margarone	2014	PALS	Prague	1.315	500	$3E+16$	300	Intarget	$1e+9$
Picciotto	2014	PALS	Prague	1.315	600	$3E+16$	300	Intarget	$1e+9$
Labaune	2013	Pico2000	LULI	0.53	20	$6E+18$	1	Pitch-catch	$1e+7$
Belyaev	2005	Neodim TW	Russia	1	15	$2E+18$	1.5	Intarget	$1.3e+5$

more plentiful and easier to accelerate within a Child-Langmuir framework [36].

As mentioned previously, we note that the N98 neutron data point of Norreys et al. [16] lies significantly above most of the other data points, as has been discussed in [34]. As previously discussed, the neutron TOF data for this experiment shows that the D-D fusion reactions are not primarily thermonuclear and are instead due to inflight reactions by deuterons accelerated to MeV energies by nonlinear ponderomotive forces. We reiterate that this is consistent with the creation of both kinetic fast electrons and accelerated fast ions, which are kinetic in nature. These fast particles distribute the coupled laser energy in a nonlocal manner, and the fast ions undergo inflight fusion reactions that sample the peak fusion cross sections in the MeV energy regime. The fact that the N98 experiment achieved

significantly higher neutron yields than the N05 results can be explained by the fact that it used a frozen, cryogenic deuterium target that was able to accelerate significantly more deuterons than a CD_2 target (P. Norreys, email communication, Nov 28, 2020), where significant laser energy is parasitically expended in the ionization and acceleration of carbon ions and adsorbed hydrogen (protons).

5. USPL Intensities Create Fast Electrons and Ions

The development of chirped pulse amplification in 1985 enabled the generation of high intensity laser beams by USPLs, which in turn have opened new frontiers in high field physics and many different modalities of charged particle acceleration by laser-generated fields. It is useful to

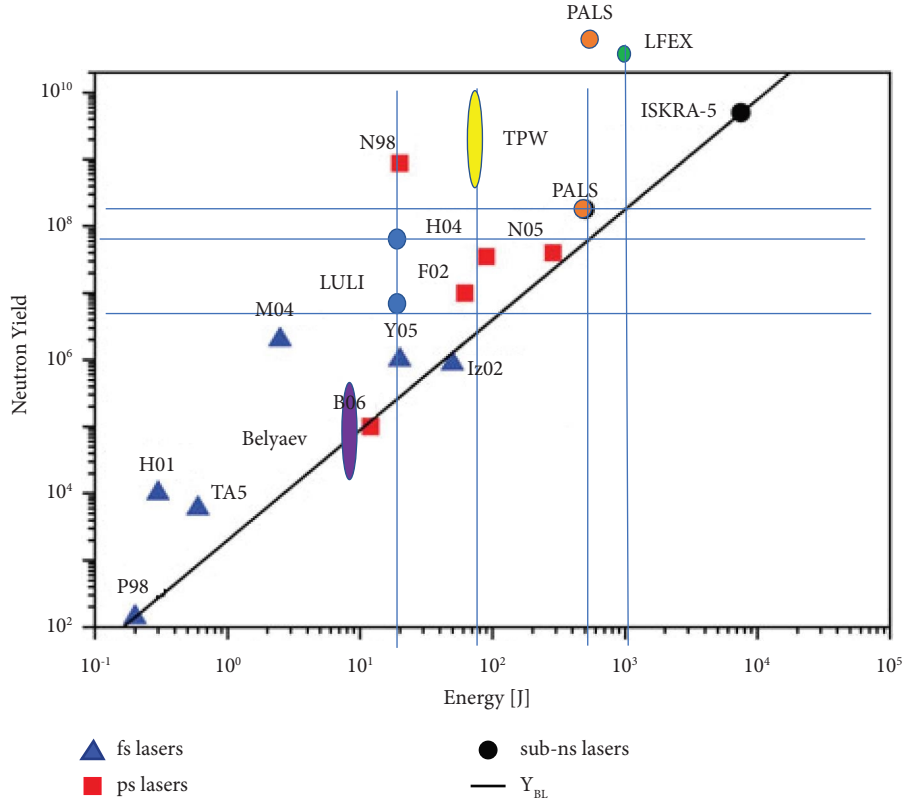


FIGURE 4: Comparison of p-B11 alpha particle and DD neutron yields as a function of laser energy.

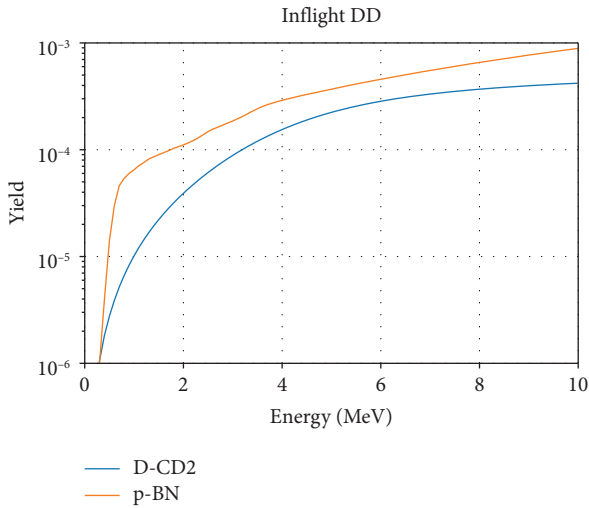


FIGURE 5: Thick target yield as a function of ion energy for protons on boron and deuterons on CD₂.

understand some of the fundamental physics associated with short pulse laser interactions with matter (cf Gibbon [37]) to gain insight into present and future p-¹¹B experiments, as well as to speculate how they might be used in future gain producing targets. For example, the generation of high charge states of carbon via multiphoton and tunneling ionization can be understood via the following appearance intensity:

$$I_{\text{app}} \cong 4 \times 10^9 \left(\frac{E_{\text{ion}}}{\text{eV}} \right)^4 Z^{-2} (\text{W cm}^{-2}). \quad (2)$$

Equation (2): Appearance intensity for ions due to multiphoton and tunneling ionization.

Table 2.1 of Ref [37] lists the ionization energies for H, C⁴⁺, and N⁵⁺ as 13.61, 64.5, and 97.9 eV, respectively, with a corresponding appearance intensity of 1.4×10^{14} , 4.3×10^{15} , and 1.5×10^{16} W/cm². Referring to Table 1, we see that all the proton-boron experiments exceed these appearance intensities, meaning that high charge states of carbon, nitrogen, and any other similar atoms will be highly ionized and competing with protons to be accelerated. In fact, the ionization energies for B⁵⁺, C⁶⁺, and N⁷⁺ are roughly 340 eV, 490 eV, and 667 eV corresponding to an appearance intensity of 2.14×10^{18} , 6.4×10^{18} , and 1.62×10^{19} W/cm², which means that the most recent experiments on ELFIE, LFEF, and TWP are at intensities that can fully strip atoms up through nitrogen. To maximize proton-boron reactions, we want to maximize the laser energy coupling to the protons, so avoiding energy-sapping higher Z ions is required. To begin with, the number of protons that are accelerated is proportional to the total laser energy, and the proton spectrum is characterized by the normalized vector potential a_0 as given below, which is a measure of the nonlinear force. I_{18} is the laser focal intensity in units of 10^{18} W/cm² and λ_L is the laser wavelength:

$$a_0 = 0.855\lambda_L (\mu\text{m})\sqrt{I_{18}(\text{Wcm}^{-2})}. \quad (3)$$

Equation (3) shows the normalized vector potential.

Table 2 lists the wavelength and maximum intensity of the experiments in Table 1 by laser system, as well as a_0 and the hot electron temperature T_h as estimated by Wilks et al. [38] (equation 5.86 in [37]). The final column in the approximate maximum reported proton energy. We see that all experiments have been performed at relativistic intensities of 10^{18} W/cm² for 1 micron light and above, except for the long pulse experiments on the PALS laser. Collisionless heating by a laser generates bi-Maxwellian proton distributions, the details of which depend on factors such as the peak laser intensity, contrast, and total energy. For example, preliminary data from Shot 13279 on the Texas PW is seen in Figure 6. The 0.6 PW focal intensity of the TPW shots is the highest of any experiment thus far and generated protons with energies of up to 68 MeV. The data for this shot has been represented as follows [32]:

$$\frac{dN}{dE} \approx A_{\text{soft}}e^{-(E/T_{\text{soft}})} + A_{\text{hard}}e^{-(E/T_{\text{hard}})}. \quad (4)$$

Equation (4) shows the Bi-Maxwellian proton distribution function.

Where $A_{\text{soft}} = 5.67 \times 10^9$, $T_{\text{soft}} = 1.19$ MeV, $A_{\text{hard}} = 2.09 \times 10^7$, and $T_{\text{hard}} = 27.5$ MeV. The hard portion of the spectrum comes from the initial interaction of the high-intensity beam with the solid target, while the soft portion of the spectrum comes from the interaction with the evolving blowoff plasma. The larger the laser energy, the more expanding plasma that will be created and the more ions in the “soft” spectrum, although their peak KE increases with laser energy. Using a plasma mirror, TPW delivers about 80 J of energy to the target. Integrating the proton distribution for this shot yields a conversion efficiency from laser to proton energy of $\sim 7\%$. Reference [31] shows a somewhat softer spectrum for experiments on LFEX (~ 30 – 35 MeV), which is consistent with the focal intensity being lower. The higher peak proton number is also consistent with the great laser energy (~ 1.3 kJ). The conversion efficiency for LFEX is also estimated to be $< 10\%$. Also, no plasma mirror was used at LFEX, and the intrinsic laser contrast is only $\sim 10^{-9}$ [39], two factors which imply the creation of a larger, expanding “preplasma” due to the laser prepulse.

The PALS experiments have been performed at 3×10^{16} W/cm², corresponding to $a_0 \sim 0.2$, meaning that the nonlinear forces are small (although the authors argue that probably self-focusing was increasing the effective laser intensity by up to a factor of 10). In this case, the acceleration mechanism is probably due primarily to interactions with the blowoff plasma. The significant number of protons up to ~ 1.5 MeV is consistent with the 500–600 J of laser energy at this low focal intensity. The three PALS experiments listed in Table 1 report approximately consistent proton numbers.

TABLE 2: Normalized vector potential and hot electron scaling by laser system.

Laser	λ (μ)	I_{18}	a_0	T_h (Wilks) (keV)	EP (MeV)
TPW	1	600	20.9	10.2	68
LFEX	1.05	30	4.9	2.05	30–35
Pico200	0.53	6	1.1	0.25	5–6
Neodim	1	2	1.2	0.29	?
PALS	1.315	0.03	0.2	0.01	1.5

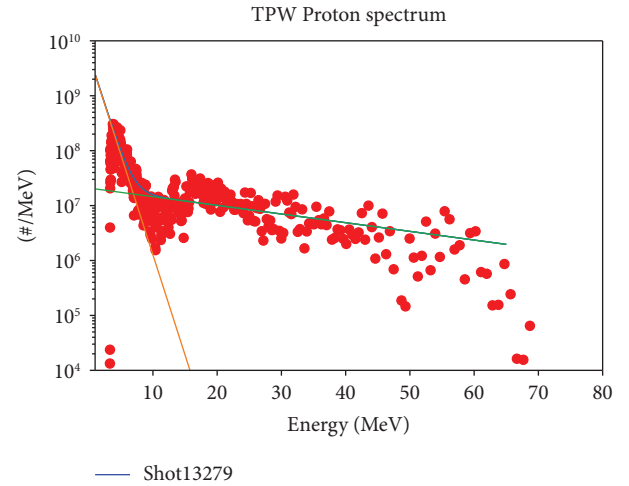


FIGURE 6: TPW data shot 13279, intensity 1.8×10^{21} W/cm², 108 J in 144 fs, 50% energy focal radius of 4.1 μ and strehl of 0.7.

6. Nuclear Cross Sections and Ion Stopping Powers

As seen in equation (1), the two elements that determine the reaction probability of an individual proton are the nuclear cross section and the proton stopping power. The alpha particle yield for the experiments in Table 1 is calculated using the p-¹¹B cross section. As noted above, Sikora and Weller (SW) have reported a higher p-¹¹B in the few MeV energy range that results in an approximately 30% increase in reactivity, as published by Putvinski. Figure 7 shows the Sikora and Weller (SW) data compared to the older EXFOR data. We note that the SW data only extends to a proton energy 3.5 MeV so for our calculations at higher proton energies, we used EXFOR data [40] to extend the cross section to 20 MeV and added an estimated point at 100 MeV. The figure also shows the evaluation of the Nevins cross section fit, which is often used for computing the fusion reactivity of thermal plasmas. We note that the Nevin fit is also only valid up to 3.5 MeV, which is sufficient for evaluating thermal reactivity, but significantly overestimates the cross section above about 5 MeV and gives erroneous results when used to calculate the yields for experiments on LFEX and TPW that exceed this energy, as we shall see in the next section. The green data points are EXFOR data for the ¹¹B(p, n)¹¹C endothermic nuclear reaction (-2.765 MeV). Counting the 20.364 min half-life of the ¹¹C decay via positron emission gives data on the

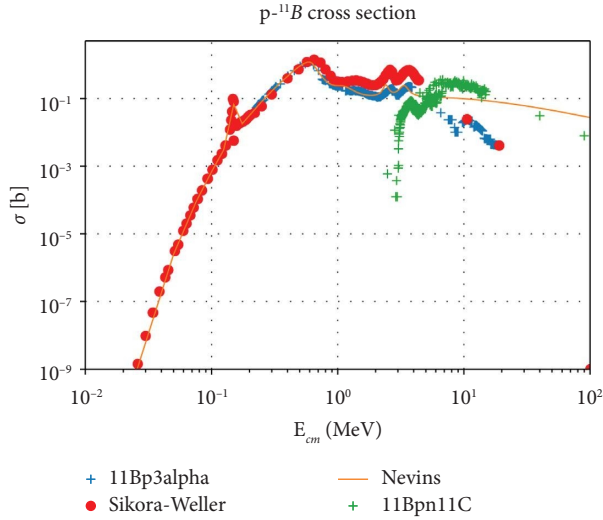


FIGURE 7: Sikora–Weller p-B11 cross section (red) compared to EXFOR data (blue) & Nevins fit; the green curve is the $^{11}\text{Bpn}^{11}\text{C}$ reaction.

integrated number of inflight proton reactions, which supplement alpha particle track counting of the $^{11}\text{B}(p, 2\alpha)^4\text{He}$ fusion reaction.

Proton stopping power is the other important factor in calculating the in-flight fusion reaction yield. Figure 8 shows the stopping power and range of protons in boron at normal density, as calculated by the enhanced RPA-LDA (eRPA-LDA) model of Gu et al. [41], and as a function of plasma temperature. We see that as the plasma electrons become hotter, their stopping power decreases for energies below the so-called Bethe regime, where dE/dx is proportional to $1/E$. Lower stopping power results in a longer ion range, which in turn results in higher inflight reactivity. The ranges are given in units of density thickness (g/cm^2) for normal density boron ($2.34 \text{ g}/\text{cc}$). Similar results would be obtained for lower-density boron foams or expanding plasmas, except for minor modifications due to changes in the ionization state. The results corroborate the calculations in Giuffrida et al. [29] which report that the alpha particle yield is increased by $\sim 10\times$ if the target is heated to 1 keV. Heating the catcher plasma with a ns laser to increase the proton range and fusion alpha yield was also the rationale behind the experiments performed by Labaune et al. at LULI.

The eRPA-LDA model can also accurately calculate the proton stopping power and range in plasmas of increasing density, where electron degeneracy becomes important. In Figure 9 we see that proton stopping power decreases and range increases as the plasma becomes increasingly dense and degenerate. Degeneracy affects the stopping of all ions in the plasma, including the fusion alphas, and has been proposed to create “chain reaction fusion” [42], which is related to the concept of avalanche which has been recently proposed to increase p-B11 yields [43]. Electron degeneracy effects are important when the plasma temperature is less than the Fermi temperature, which is given by the following equation:

$$E_F = \frac{\pi^2 \hbar^2}{2m_e} \left(\frac{3n_e}{\pi} \right)^{2/3}. \quad (5)$$

Equation (5): Fermi energy as a function of electron density n_e .

We find that the Fermi energy is of the order of 10 eV at solid density, 250 eV at 100x solid density, 1.2 keV at 1000x, and 250 keV at $10^5\times$. The eRPA-LDA model can self-consistently calculate stopping power in both dense and hot material, and we have plans to incorporate this model into hydrodynamic and hybrid burn codes.

A detailed analysis of the necessary conditions to achieve chain reaction fusion or avalanche is beyond the scope of this paper, but we plan to use our eRPA-LDA stopping power model to explore this regime of fusion burn space in the near future.

7. Thick Target Yields and Convolutions over Experimental Proton Spectra

We now use the cross sections and stopping powers of the previous section to evaluate the thick target yields for the $p-^{11}\text{B}$ and the $^{11}\text{B}(p,n)^{11}\text{C}$ nuclear reactions for protons with energies of up to 100 MeV in BN at cold, ambient conditions, as seen in Figure 10. Our calculations show that using the Nevins fit rather than our extended SW cross section points to calculate the thick target yield leads to almost 10x errors at 100 MeV proton energies. Although contributions to the thick target yield using the SW cross sections become negligible (few millibarns) above energies of about 20 MeV, it would be useful to have more high-energy data points to ensure the accuracy of the integrations. As long as the target is more than a range thick, the higher-energy protons eventually slow down through the peak of the cross section and create the peak number of alphas, however, at a diminishing efficiency of alpha production per proton energy. We note that the range of a 1 MeV proton is about 12 microns, at 40 MeV it is $\sim 1 \text{ cm}$, and at 100 MeV it is 4.4 cm, so high energy protons can penetrate some thin targets without interacting. Further, because the average range of a $p-^{11}\text{B}$ alpha particle is ~ 15 microns, many of the alphas will not escape a thick target and register on CR-39 track film, as previously mentioned. We see that the thick target yield for ^{11}C has a similar magnitude and energy dependence to the $p-^{11}\text{B}$ yield, so coincidence counting of the positron emission can provide a valuable cross-check to CR-39 track counting. For the experiments performed at PALS and LULI, the higher SW cross section in the few MeV range results in higher thick target yields, which can help explain why the experimental results are said to be higher than anticipated.

We can now convolve the reaction integral with the bi-Maxwellian proton spectrum to calculate the total alpha particle and ^{11}C yield for comparison with the experimental results for TPW shot 13279, as seen in Table 3. The values in this table do not yet include a final normalization due to the solid angle, and the absolute magnitude should be about a factor of 100 higher. The first row lists the integrated total proton number in the bi-Maxwellian as well as the hard and

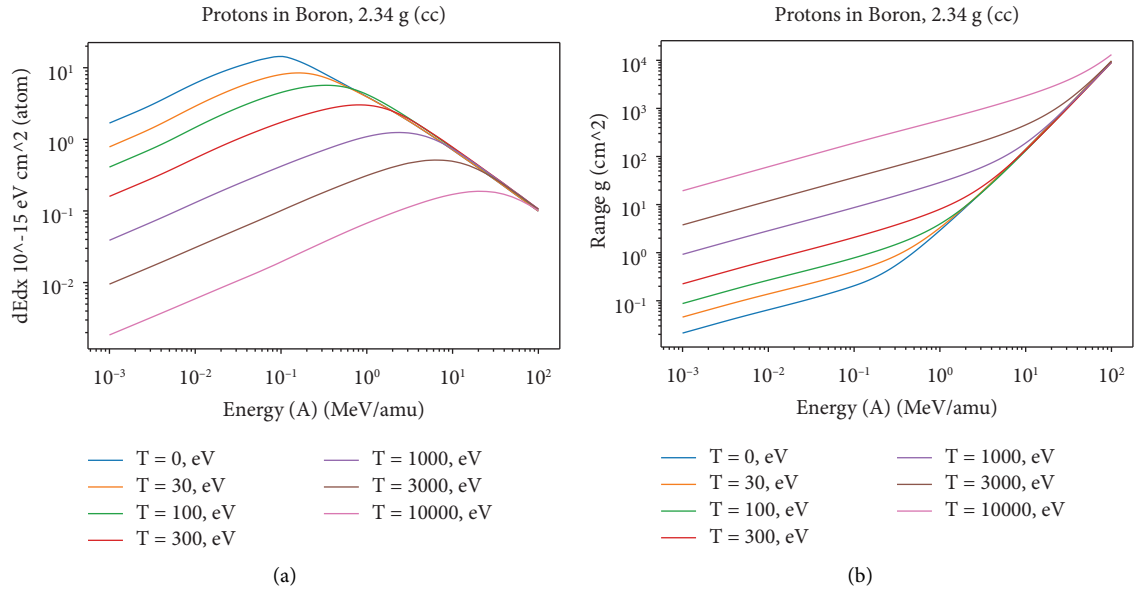


FIGURE 8: Proton stopping power and range in boron using the eRPA-LDA model for varying electron temperature.

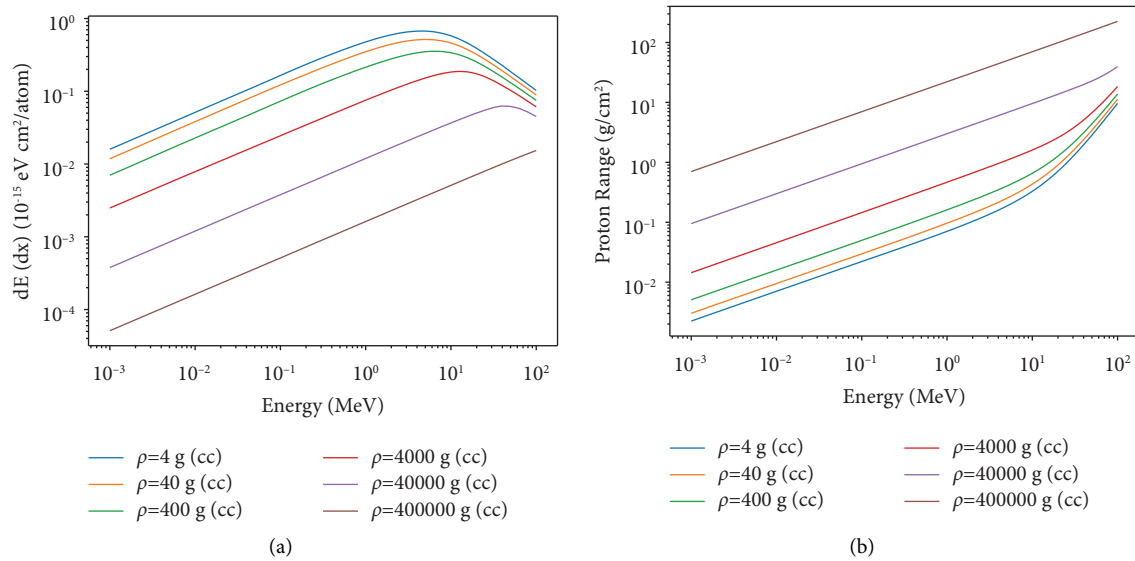


FIGURE 9: Proton stopping power and range in boron using the eRPA-LDA model for varying plasma density.

soft contributions. We see that there are roughly 10x more protons in the soft than in the hard part of the spectrum. The next row lists the total proton energy as well as its spectral components, showing that the hard spectrum contains more energy than the soft. The third row lists the total number of $p-^{11}\text{B}$ reactions (multiplied by 3 for alpha numbers) as well as the spectral contributions. It is interesting to note that there is almost a 50:50 split in the hard-to-soft production for this shot. The final row lists the total number of ^{11}C producing reactions, which we see is of the same order of magnitude as the alpha particle production.

8. Beam Fusion Reactions

The results from TPW shot 13279 can be compared with those of the other experiments listed in Table 1, which span a broad space of intensity and laser energy, in an attempt to uncover the underlying physics that are common to all of them, namely, that the alpha particles are being produced by in-flight beam target interactions. As previously noted, laser-target interactions at these intensities generate both fast electrons and ions that kinetically stream through the target material. While the fast ions are relatively efficient at

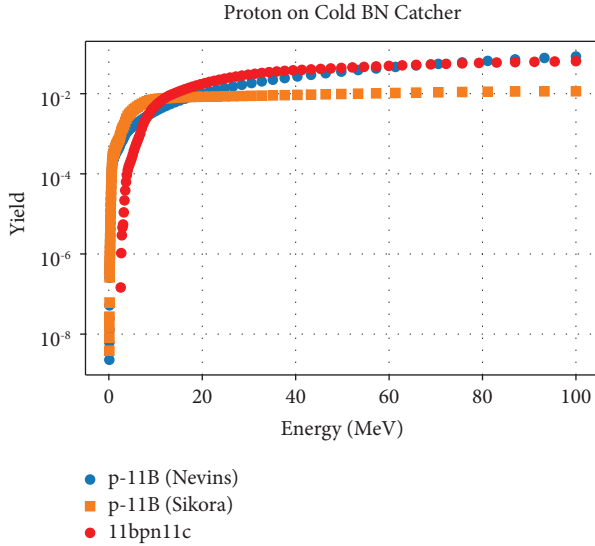


FIGURE 10: Thick target yield for protons on BN catcher.

TABLE 3: Integrated proton number, energy, and nuclear reactions for TPW #13279.

	Total	Hard	Soft
Proton #	$7.30E+09$	$5.50E+08$	$6.75E+09$
Proton energy (J)	$3.72E-03$	$2.43E-03$	$1.29E-03$
pB11 reactions	$1.70E+06$	$8.51E+05$	$8.38E+05$
C11 reactions	$2.50E+06$		

producing inflight fusion reactions, the interaction does not produce the localized energy concentration required to drive a fusion burn wave in normal density material, such as described in the fluid models of Chu and Lalouis [44, 45]. Further, it is well known that beam fusion reactions do not scale to net energy gain, as can be seen in the following simple analysis. The mean free path (mfp) to a p-¹¹B fusion event in boron with a density of 2.1 g/cm³ is given by the following equation:

$$\text{mfp}_{\text{fusion}} = \Sigma(E)^{-1} = \frac{1}{N_{\text{boron}} \sigma_{pb11}(E)} \sim 6.1 \text{ (cm)}. \quad (6)$$

Equation (6): Proton mean free path to fusion even in normal density boron.

We see that using the optimistic peak cross section of 1.4 barns, the mean free path to a p-boron fusion reaction is about 6 cm. This means that a proton with energy $E \geq 660$ keV must travel on average through 6 cm of pure boron at normal density for the probability of a fusion reaction to be 100%. However, the electronic stopping power of a proton in boron is such that the range R_p for a 1 MeV proton is about 12 μm and the stopping time is ~ 1.8 ps. Therefore, back-of-the-envelope probability of fusion before slowing down is given by the following equation:

$$\frac{R_p}{\text{mpf}} = \frac{0.012 \text{ cm}}{6 \text{ cm}} = 2 * 10^{-3}. \quad (7)$$

Equation (7) shows the ratio of proton range to fusion mean free path.

This is an overestimate of the probability because the peak cross section is a relatively narrow resonance and the cross section is negligible below about 100 keV, as seen above. Using the proton stopping power shown above, we find that the range of a 1 MeV proton in BN at ambient density (2.34 g/cc) and temperature is 3.2 mg/cm², which is $\sim 13.7 \mu$ and the corresponding thick target yield for p-B11 reactions is 6.6×10^{-5} . Given that the exothermic “Q-value” of the p-B11 reaction is 8.76 MeV, the gain of any one fusion reaction is of order 10, so a significant net gain requires many fusion reactions to be caused by a single proton—either through a “fusion flame” detonation process or by an avalanche or chain reaction fusion mechanism. This will be the topic of the next section that discusses the target gain requirements for a practical fusion power plant.

9. Target Gain Requirements for a Fusion Power Plant

The National Academy of Engineering has identified “providing energy from fusion” as one of the 14 top grand challenges of engineering [46]. Achieving scientific breakeven has been a multidecadal quest that has engaged the international research community. The NIF results have shown that the computational tools, target design principles, and driver and target fabrication that have been developed for ICF have put us on the path towards fusion energy. However, as startup companies, such as HB11 energy, attempt to fast track the development of a fusion power plant, it is important to keep in mind the target gain requirements that can be identified through a fundamental engineering power balance.

Figure 11 shows a simple power loop for a laser-driven IFE powerplant that HB11 has been using to develop the initial HB11 Energy techno-economic model. A key feature of fusion, especially IFE, is that the system functions as a power amplifier and not as a power source. That is, the fusion power available for conversion into electricity is proportional to the power on target multiplied by the target gain, G . In turn the power delivered to the target is the product of the laser power and the laser efficiency, η . The electrical power is determined by the generator conversion efficiency ϵ , and the power available to the grid is the generated power minus the power for the laser.

The following relations are useful in evaluating the key parameters of this model. The recirculating power fraction is given by $f = 1/\epsilon\eta G$. This analysis neglects the multiplication factor that can be present with D-T breeding blankets. Engineering breakeven is defined as $f = 1$, where the powerplant produces just enough power to operate. A recirculating power fraction $f = 0.25$ has been suggested as a starting point for nuclear fusion, and $f \leq 0.1$ is typical of nuclear fission reactors. The minimum target gain for operating at a given recirculating power fraction is given by $G = 1/\epsilon\eta f$. This relation leads to the simple rule of thumb, $\eta G \geq 10$, for a practical power plant. For a thermal power conversion system with ϵ of 36–40%, $\eta G = 10$ corresponds to a recirculating power fraction of $\sim 25\%$, while a value of 20 drops that fraction to about 10%, which is desirable for achieving the lowest cost of

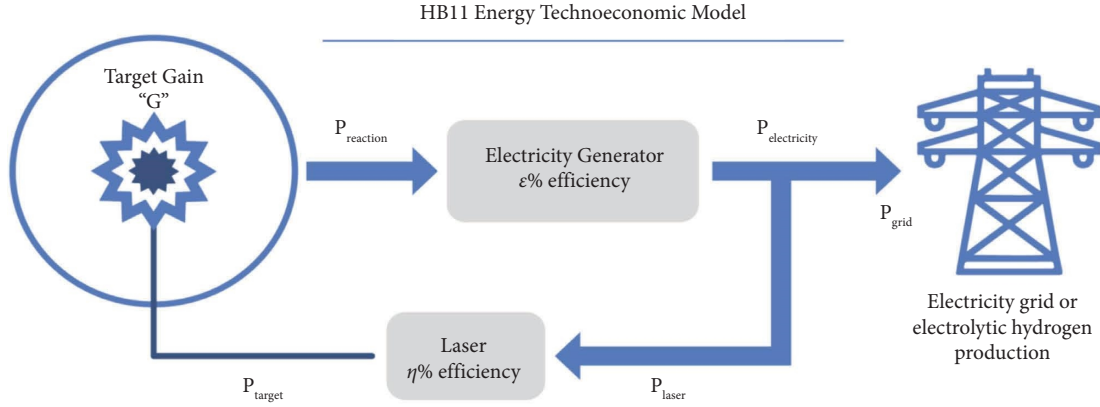
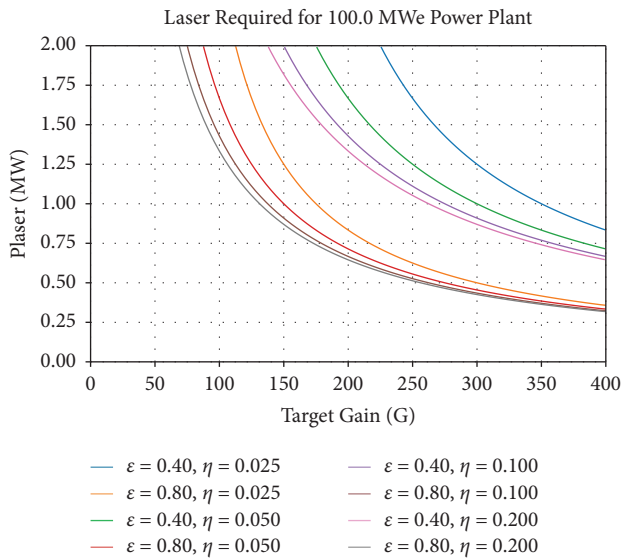


FIGURE 11: Power loop for laser-driven IFE.

FIGURE 12: Required laser power vs G laser efficiency from 2.5–20% and power conversion efficiency from $\epsilon = 40\%$ to 80%.

electricity (COE) for the plant. For a 10% laser efficiency, this means achieving a target gain of at least 100 to 200 to achieve energy production at today's prices (\$100–\$300/MWh), which is the topic of the final sections of this paper.

Two other relations that are useful in our preliminary technoeconomic analysis of an IFE powerplant are (1) $P_{\text{grid}}/P_{\text{laser}} = \epsilon G - 1/\eta$, which is the ratio of the grid and average laser powers and (2) $P_{\text{laser}} = P_{\text{grid}}/(\epsilon G - 1/\eta)$, which gives the required laser power to supply P_{grid} for given gain, conversion efficiency, and laser efficiency. The repetition rate needed to determine average laser power is likely to be 5–10 Hz, which has been the basis for most DT IFE system designs. Figure 12 shows the curves of P_{laser} as a function of target gain G to deliver 100 MWe to the grid for two different electrical conversion efficiencies (40 and 80%) and for laser efficiencies η of 2.5, 5, 10, and 20%. The 40% number is typical of an optimized thermal system. The 80% value is what might be possible if the fusion alpha particles can be directly converted to electrical power, the details of which are beyond the scope of this paper.

There are a couple of qualitative trends that can be seen in this data. First, the required laser power for a fixed power plant output is significantly lower if direct energy conversion efficiencies can be realized. Second, the impact of increased laser efficiency is diminished as the target gain increases. Finally, target gains of 200 are sufficient for practical power production at the higher conversion efficiency, while thermal conversion efficiencies will likely require even higher gains. While these gains are theoretically possible in target simulations, it is important to note that the best NIF shot has achieved $G \sim 0.75$ at a delivered laser energy of ~ 1.8 MJ to an x-ray-driven DT target. The capsule gain, however, was close to 6. Achieving fusion ignition for DT has been hard, and the path to a practical power plant is still a work in progress. In the following section, we will use what we have learned about USPL-driven aneutronic fusion reactions to outline a procedure for identifying regions in the burn space where $p\text{-}^{11}\text{B}$ has sufficient gain to enable power production.

10. Roadmap to Increasing p-B11 Reactivity and Developing Target Point Design

We have seen that USPL irradiation of boron targets has produced significant alpha yields, but that the beam fusion basis of these aneutronic fusion reactions does not scale to ignition, much less the required gains of 200 required for practical power production. (Please note that some of the material in this section has been directly reused from the authors' unpublished white paper for the DOE Inertial Fusion Energy Basic Research Needs Workshop [5, 48]) Further, we find that the target parameters outlined in the HB11 roadmap paper [7], namely 30 kJ of USPL energy in a $\sim 100 \mu$ diameter spot in 1 ps, which translates to $\sim 10^{20}$ W/cm² do not make sense in the light of what we have learned from the experiments listed in this paper. In particular, the LFEX and TPW experiments at 10^{19} to 10^{21} W/cm² clearly show that the laser target interactions generate ions with energies of 10–100 MeV that are kinetic and interpenetrate the target, rather than concentrating the energy in a thin region and generating strong detonation shocks.

As seen in equation (8), thermonuclear fusion power density and reactivity scale with the square of the ion

density, so conventional ICF schemes require significant compression to minimize the energy required for igniting the fuel. In this equation $u = |v_p - v_b|$ and Y is the fusion yield, which is 8.68 MeV for pB^{11} .

$$P_{\text{fus}} = n_p n_b \langle \sigma v \rangle Y, \quad (8)$$

$$\langle \sigma v \rangle = \iint f_p(v_p) f_b(v_b) \sigma(u) d^3 v_p d^3 v_b.$$

Equation (8) shows the fusion power density and fusion reactivity for arbitrary proton and boron distribution functions.

The USPL-driven p-B11 experiments reported thus far have all used uncompressed targets. We propose to investigate the possibility of achieving ignition and gain via a hybrid approach to p-B11 fusion that combines thermonuclear burn elements of fast ignition ICF with inflight fusion reactions by CPA laser-accelerated protons. The mainline approaches to ICF, supported by the NNSA, are pursuing hot spot ignition, which requires that the compression be accomplished while avoiding the growth of hydrodynamic instabilities that create a mix that precludes the generation of a sufficiently robust fusion spark. Traditional fast ignition decouples the implosion from the generation of the initiating spark, thereby relaxing some of the requirements on implosion symmetry. We see that the isochoric scaling published by Clark and Tabak in 2007 [47] is a good starting point for studying the implosion of proton-boron fuel at high densities. The requirements for the deposition of CPA laser-generated fast electron energy to achieve ignition in DT have been widely studied and published. Ions, notably protons and perhaps carbon, have also been proposed as an alternative ignition trigger because of their superior transport and focusing properties. We propose to develop a parallel set of criteria for the fast ignition of compressed p- ^{11}B fuel and then study options for igniting the fuel by a combination of proton energy deposition and inflight thermonuclear reactions. This will extend the successful ‘‘pitcher-catcher’’ concept described above to targets at significantly higher densities and regimes of density and temperature where proton ranges can be extended by both electron heating and degeneracy effects.

We have begun to develop an updated generalized Lawson criteria analysis for p-B11 that incorporates the new cross-section data as well as any other effects that indicate that it could be a viable fusion fuel cycle [48]. Figure 13 displays a preliminary result from our analysis of the Maxwellian-averaged reactivity of D-T and p-B11 (using the latest SW cross section), as well as the reactivity of high-energy beam protons. A recently published, paper on aneutronic fusion [49] references a 1973 report from LLNL [50] that contains a relevant discussion of the physics of p-B11 fusion. They developed a computer code (FOKN) that follows the energy distributions of nuclear reactants and products under the assumption of an infinite medium. They discuss various strategies for nonsteady operation including control of radiation and driving a strong detonation shock wave through extremely compressed fuel. We see that it will be necessary to pursue a modern revisit of this type of kinetic burn model for p- ^{11}B using hybrid codes, such as Voss’

Chicago code [51]. Hybrid kinetic-fluid simulations will play a key role in the further development of this updated generalized Lawson criteria analysis by accounting for the fusion reactivity of the thermal and beam components of the proton distribution function that properly accounts for elastic and inelastic processes as a function of fuel isotopic composition, density, and temperature, as well as accounting for the impact of kinetic energy exchange between the plasma distribution functions on the fusion reactivity.

Our study of proton-boron fast ignition ICF driven by short pulse lasers will use the latest cross sections as well as a hybrid kinetic-fluid approach to calculating the implosion, burn, and expansion physics of an IFE target. As noted by Putvinski, the peak of the cross section is at proton energies of about 1 MeV to a few MeV. This important energy region can be directly populated by USPL-generated protons and can be supplemented via up-scattering (‘‘lift’’) by collisions of plasma protons with fast alpha particles. We propose to study what we term a ‘‘hybrid burn’’ scenario where protons generated by CPA laser acceleration add an energetic population to the proton distribution function as well as providing additional fast alpha particles that will both heat the fuel and provide additional up-scattering events. This will require the development of a kinetic algorithm for tracking the proton distribution function across the broad energy range encompassed by the bulk thermonuclear component from below and the slowing-down beam-fusion component from above. We will quantify the possibility of ignition and burning in these fast ignition-like configurations, accounting for the power balance between heating, thermonuclear and inflight fusion reactions, charged particle deposition, Bremsstrahlung, thermal conduction, and hydrodynamic expansion via isochoric models and rad-hydro simulations. We will use models that include the effects of density and temperature on the interaction of charged particles in the plasma, including both slowing down and up scattering terms. We will also identify H : B isotopic ratios that maximize fusion yield and minimize Bremsstrahlung production, as well as designs that include radiation trapping layers to reduce losses (cf [52]). Wurzel and Hsu [9] analyze bremsstrahlung power loss as a function of ionic species concentration, but do not discuss the possibilities of radiation trapping layers. Since radiation loss is a dominant factor in determining the ignition threshold, identifying ways to limit these losses will be a top priority. Our goal is to identify whether there is a region where the hybrid burn concept can take advantage of the higher p-B11 reactivity in the ≥ 200 keV energy regime associated with the Sikora-Weller cross section, leading to ignition and gain when considering energy exchange processes between all plasma species.

It will be important to accurately model the time dependence of all processes in this pulsed ICF scenario, especially the slowing-down and interaction times of energetic species, to arrive at a self-consistent design. Further, the CPA laser interaction time scale must be consistent with the hydrodynamic time history. The fast ignition laser pulse must deliver the necessary energy and proton flux to the target prior to the expansion of the imploded fuel. As

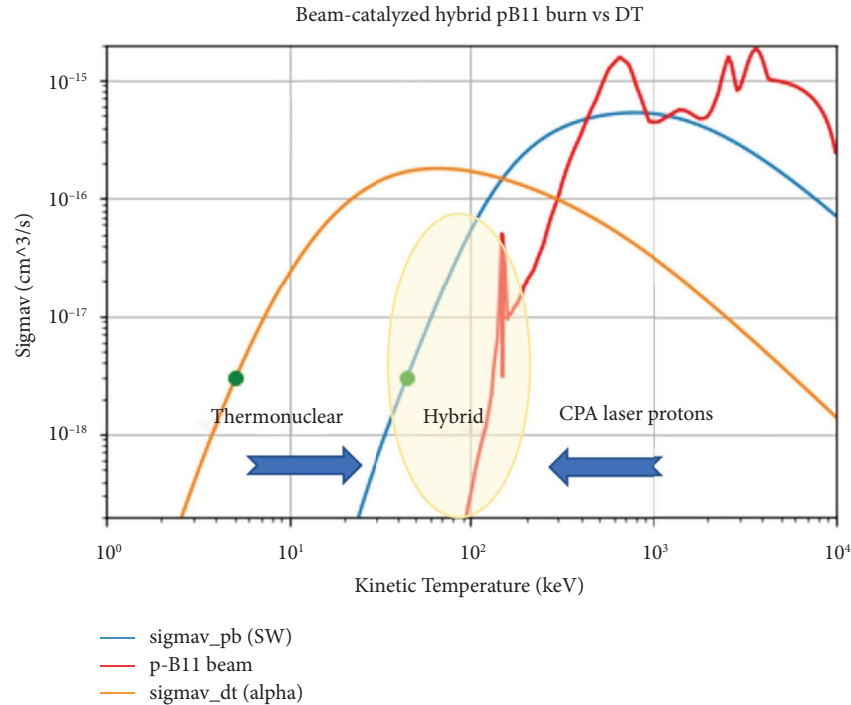


FIGURE 13: Fusion reactivity for thermonuclear DT and PB as well as beam-driven PB.

previously noted, laser acceleration generally generates bi-Maxwellian proton distributions, depending on the laser intensity. The size of the target, the total laser energy, and the laser pulse duration will set the laser intensity, which in turn will set the peak proton energy and associated distribution function. The hydrodynamic and laser acceleration calculations will need to be iterated until the range of the laser-generated protons is an appropriate match to the target ρr and the resulting fusion reactions give a sufficient burn-up fraction prior to hydrodynamic disassembly.

While we can begin to study the p-B11 burn physics through 0-D energetic models, detailed designs will require 1-D, 2-D, and eventually 3-D simulations. Pursuing these simulations will require that we first build the necessary computational capabilities for rigorous p-B11 studies, including an accurate EOS table, opacity, stopping power, and fusion reactivity models of pB-fuel from first-principles calculations and implementing them into rad-hydro codes, similar to what has been done for DT-ICF fusion studies [53–56]. Further, the hybrid burn model will require further development using Chicago or LSP to provide the kinetic simulation tools required to track the proton distribution function and its interaction with other energetic particle species. LSP or OSIRIS can also be used to model various laser acceleration scenarios for providing the energetic proton ignitor beam. We can then use these capabilities to examine design concepts for p-B11 targets and derive scaling laws for hybrid burning. To make sure that these simulations are well grounded in scientifically accurate plasma and nuclear physics, we will also propose to perform validation experiments on the Omega Facility (Omega-EP + Omega-60). Such experiments will be able to combine compression and

proton acceleration to study hybrid burning for the most promising target designs.

Data Availability

The data supporting these results are contained in other published journal articles. The article is not based on any personally held datasets. 2. We have included Ref 49, which cites an unpublished white paper from a LLNL website that includes some of the text contained in this article. This white paper was an internal working document for the US DOE fusion program planning community, but we have included this disclaimer to avoid any confusion. Please note that this is the first time that this text has been formally submitted for publication.

Conflicts of Interest

TAM, LL, BMH, and DB have received financial support from HB11 Energy PTY, LTD, including payment of article processing charges (APCs). TAM and EMC are Scientific Advisors and DB is the Lead Scientist to HB11 Energy PTY, LTD.

Acknowledgments

TAM, LL, BMH, and DB acknowledge financial support from HB11 Energy PTY, LTD. DM was supported by the Ministry of Education, Youth, and Sports of the Czech Republic through the project “Advanced Research Using High-Intensity Laser-Produced Photons and Particles” (CZ.02.1.010.00.016_0190000789). The authors would like to thank Igor Golovkin and Prism Computational Sciences for providing the results of ion stopping power calculations

using a newly developed model supported by the U.S. Department of Energy, Office of Science, Fusion Energy Sciences (FES) under Award Number DE-SC0022112.

References









- [1] A. B. Zylstra, O. A. Hurricane, D. A. Callahan et al., “Burning plasma achieved in inertial fusion,” *Nature*, vol. 601, no. 7894, pp. 542–548, 2022.
- [2] E. Gibney, *Nuclear-Fusion Reactor Smashes Energy Record*, Nature [News], Berlin, Germany, 2022.
- [3] D. L. Chandler, *MIT-Designed Project Achieves Major advance toward Fusion Energy*, MIT Energy Initiative, Cambridge, MA USA, 2022.
- [4] B. Bigot, “Progress toward ITER’s first plasma,” *Nuclear Fusion*, vol. 59, no. 11, Article ID 112001, 2019.
- [5] events bizzabo, “Basic Research Needs Workshop on Inertial Fusion Energy,” 2022, <https://events.bizzabo.com/IFEBRN2022/home>.
- [6] USDOE, *Department of Energy Announces First Round of FY 2021 Public-Private Partnership Awards to Advance Fusion Energy*, USDOE, Washington, DC USA, 2021.
- [7] H. Hora, S. Eliezer, G. Kirchhoff et al., “Road map to clean energy using laser beam ignition of boron-hydrogen fusion,” *Laser and Particle Beams*, vol. 35, no. 4, pp. 730–740, 2017.
- [8] H. Hora, “Method for Generating Electrical Energy by Laser-Based Nuclear Fusion and Laser Reactor,” United States Patent US20170125129A1, 2017.
- [9] S. E. Wurzel and S. C. Hsu, “Progress toward fusion energy breakeven and gain as measured against the Lawson criterion,” *Physics of Plasmas*, vol. 29, no. 6, Article ID 062103, 2022/06/01 2022.
- [10] S. V. Putvinski, D. D. Ryutov, and P. N. Yushmanov, “Fusion reactivity of the pB11 plasma revisited,” *Nuclear Fusion*, vol. 59, no. 7, Article ID 076018, 2019.
- [11] M. H. Sikora and H. R. Weller, “A New Evaluation of the $\alpha\alpha$ Reaction Rates,” *Journal of Fusion Energy*, vol. 35, no. 3, pp. 538–543, 2016.
- [12] D. Strickland and G. Mourou, “Compression of amplified chirped optical pulses,” *Optics Communications*, vol. 56, no. 3, pp. 219–221, 1985.
- [13] M. Tabak, J. Hammer, M. E. Glinsky et al., “Ignition and high gain with ultrapowerful lasers,” *Physics of Plasmas*, vol. 1, no. 5, pp. 1626–1634, 1994/05/01 1994.
- [14] R. R. Freeman, D. Batani, S. Baton, M. Key, and R. Stephens, “The generation and transport of large currents in dense materials: the physics of electron transport relative to fast ignition,” *Fusion Science and Technology*, vol. 49, no. 3, pp. 297–315, 2006.
- [15] M. Roth, T. E. Cowan, M. H. Key et al., “Fast ignition by intense laser-accelerated proton beams,” *Physical Review Letters*, vol. 86, no. 3, pp. 436–439, 2001.
- [16] P. A. Norreys, A. P. Fewes, F. N. Beg et al., “Neutron production from picosecond laser irradiation of deuterated targets at intensities of,” *Plasma Physics and Controlled Fusion*, vol. 40, no. 2, pp. 175–182, 1998/02/01 1998.
- [17] P. Lalouis, H. Hora, and S. Moustazis, “Optimized boron fusion with magnetic trapping by laser driven plasma block initiation at nonlinear forced driven ultrahigh acceleration,” *Laser and Particle Beams*, vol. 32, no. 3, pp. 409–411, 2014.
- [18] J. Krása, D. Klir, A. Velyhan et al., “Observation of repetitive bursts in emission of fast ions and neutrons in sub-nanosecond laser-solid experiments,” *Laser and Particle Beams*, vol. 31, no. 3, pp. 395–401, 2013.
- [19] H. S. Bosch and G. M. Hale, “Improved formulas for fusion cross-sections and thermal reactivities,” *Nuclear Fusion*, vol. 32, no. 4, pp. 611–631, 1992.
- [20] V. S. Belyaev, V. I. Vinogradov, A. S. Kurilov et al., “Neutron production in a picosecond laser plasma at a radiation intensity of $3 \times 10^{17} \text{ W/cm}^2$,” *Journal of Experimental and Theoretical Physics*, vol. 98, no. 6, pp. 1133–1137, 2004.
- [21] V. S. Belyaev, A. P. Matafonov, V. I. Vinogradov et al., “Observation of neutronless fusion reactions in picosecond laser plasmas,” *Physical Review A*, vol. 72, no. 2, Article ID 026406, 2005.
- [22] S. Kimura, A. Anzalone, and A. Bonasera, “Comment on ‘Observation of neutronless fusion reactions in picosecond laser plasmas,’” *Physical Review A*, vol. 79, no. 3, Article ID 038401, 2009.
- [23] C. Labaune, C. Baccou, S. Depierreux et al., “Fusion reactions initiated by laser-accelerated particle beams in a laser-produced plasma,” *Nature Communications*, vol. 4, no. 1, p. 2506, 2013.
- [24] C. Labaune, C. Baccou, V. Yahia, C. Neuville, and J. Rafelski, “Laser-initiated primary and secondary nuclear reactions in Boron-Nitride,” *Scientific Reports*, vol. 6, no. 1, Article ID 21202, 2016.
- [25] A. Picciotto, D. Margarone, A. Velyhan et al., “Boron-proton nuclear-fusion enhancement induced in boron-doped silicon targets by low-contrast pulsed laser,” *Physical Review X*, vol. 4, no. 3, Article ID 031030, 2014.
- [26] D. Margarone, A. Picciotto, A. Velyhan et al., “Advanced scheme for high-yield laser driven nuclear reactions,” *Plasma Physics and Controlled Fusion*, vol. 57, no. 1, Article ID 014030, 2014.
- [27] C. Baccou, S. Depierreux, V. Yahia et al., “New scheme to produce aneutronic fusion reactions by laser-accelerated ions,” *Laser and Particle Beams*, vol. 33, no. 1, pp. 117–122, 2015.
- [28] M. Tayyab, S. Bagchi, A. Moorti, and J. A. Chakera, “Experimental investigation on nuclear reactions using a laser-accelerated proton and deuteron beam,” *Plasma Physics and Controlled Fusion*, vol. 61, no. 11, Article ID 115007, 2019.
- [29] L. Giuffrida, F. Belloni, D. Margarone et al., “High-current stream of energetic alpha particles from laser-driven proton-boron fusion,” *Physical Review A*, vol. 101, no. 1, Article ID 013204, 2020.
- [30] D. Margarone, A. Morace, J. Bonvalet et al., “Generation of α -particle beams with a multi-kJ, peta-watt class laser system,” *Frontiers in Physics*, vol. 8, no. 343, (in English), 2020.
- [31] J. Bonvalet, P. Nicolai, D. Raffestin et al., “Energetic α -particle sources produced through proton-boron reactions by high-energy high-intensity laser beams,” *Physical Review A*, vol. 103, no. 5, Article ID 053202, 2021.
- [32] B. M. Hegelich, L. Labun, O. Z. Labun, E. McCary, and T. Mehlhorn, “Photon and neutron production as in-situ diagnostics of proton-boron fusion,” *Lasers and Particle Beams*, 2022.
- [33] D. Margarone, J. Bonvalet, L. Giuffrida et al., “In-target proton–boron nuclear fusion using a PW-class laser,” *Applied Sciences*, vol. 12, no. 3, p. 1444, 2022.
- [34] H. Hora, S. Eliezer, G. H. Miley, J. Wang, Y. Xu, and N. Nissim, “Extreme laser pulses for non-thermal fusion ignition of hydrogen–boron for clean and low-cost energy,” *Laser and Particle Beams*, vol. 36, no. 3, pp. 335–340, 2018.
- [35] H. Hora, G. H. Miley, S. Eliezer, and N. Nissim, “Pressure of picosecond CPA laser pulses substitute ultrahigh thermal

- pressures to ignite fusion,” *High Energy Density Physics*, vol. 35, Article ID 100739, 2020.
- [36] G. M. Petrov, D. P. Higginson, J. Davis et al., “Generation of energetic (>15 MeV) neutron beams from proton- and deuteron-driven nuclear reactions using short pulse lasers,” *Plasma Physics and Controlled Fusion*, vol. 55, no. 10, Article ID 105009, 2013.
- [37] P. Gibbon, *Short Pulse Laser Interactions with Matter* Imperial College Press, Covent Garden, London, UK, 2005.
- [38] S. C. Wilks, W. L. Kruer, M. Tabak, and A. B. Langdon, “Absorption of ultra-intense laser pulses,” *Physical Review Letters*, vol. 69, no. 9, pp. 1383–1386, 1992.
- [39] Y. Arikawa, S. Kojima, A. Morace et al., “Ultrahigh-contrast kilojoule-class petawatt LFEX laser using a plasmamirror,” *Applied Optics*, vol. 55, no. 25, pp. 6850–6857, 2016.
- [40] V. Zerkov and B. Pritychenko, “The experimental nuclear reaction data (EXFOR): extended computer database and Web retrieval system,” *Nuclear Instruments and Methods in Physics Research Section A: Accelerators, Spectrometers, Detectors and Associated Equipment*, vol. 888, pp. 31–43, 2018.
- [41] M. F. Gu, T. A. Mehlhorn, and I. Golovkin, “Electronic stopping power of ions in cold targets and warm plasmas,” in *Proceedings of the 2022 IEEE International Conference on Plasma Science (ICOPS)*, Seattle, WA, USA, May 2022.
- [42] M. Gryziński, “Fusion chain reaction—chain reaction with charged particles,” *Physical Review*, vol. 111, no. 3, pp. 900–905, 1958.
- [43] F. Belloni, “On a fusion chain reaction via suprathermal ions in high-density H–11B plasma,” *Plasma Physics and Controlled Fusion*, vol. 63, no. 5, Article ID 055020, 2021.
- [44] M. S. Chu, “Thermonuclear reaction waves at high densities,” *Physics of Fluids*, vol. 15, no. 3, pp. 413–422, 1972/03/01 1972.
- [45] P. Lalouis and H. Hora, “First direct electron and ion fluid computation of high electrostatic fields in dense inhomogeneous plasmas with subsequent nonlinear laser interaction,” *Laser and Particle Beams*, vol. 1, no. 3, pp. 283–304, 1983.
- [46] E. National Academies of Sciences, “NAE Grand Challenges for Engineering,” Global Grand Challenges Summit, London, UK, 2019, <http://www.engineeringchallenges.org/challenges.aspx>.
- [47] D. S. Clark and M. Tabak, “A self-similar isochoric implosion for fast ignition,” *Nuclear Fusion*, vol. 47, no. 9, pp. 1147–1156, 2007/08/22 2007.
- [48] T. A. Mehlhorn, S. X. Hu, and E. M. Campbell, “p-B11 ignition via ps & ns lasers: burn physics, target design, & experimental validation,” University of Rochester Laboratory For Laser Energetics, Rochester, NY USA, 2022, <https://lasers.llnl.gov/content/assets/docs/nif-workshops/ife-workshop-2021/white-papers/mehlhorn-LLE-IFE-workshop-2022.pdf> DOE Inertial Fusion Energy Basic Research Needs Workshop 2022.
- [49] M. L. Shmatov, “Igniting a microexplosion by a micro-explosion and some other controlled thermonuclear fusion scenarios with neutronless reactions,” *Physics-Uspekhi*, vol. 62, no. 1, pp. 70–81, 2019.
- [50] T. Weaver, G. Zimmerman, and L. Wood, “Exotic CTR Fuels: Non-Thermal Effects and Laser Fusion Applications,” Lawrence Livermore National Laboratory, Livermore, CA, USA, UCRL-74938, 1973.
- [51] D. R. Welch, N. Bennett, T. C. Genoni, C. Thoma, and D. V. Rose, “Fast hybrid particle-in-cell technique for pulsed-power accelerators,” *Physical Review Accelerators and Beams*, vol. 23, no. 11, Article ID 110401, 2020.
- [52] E. L. Dewald, J. E. Pino, R. E. Tipton et al., “Pushed single shell implosions for mix and radiation trapping studies using high-Z layers on National Ignition Facility,” *Physics of Plasmas*, vol. 26, no. 7, Article ID 072705, 2019.
- [53] S. X. Hu, B. Militzer, V. N. Goncharov, and S. Skupsky, “Strong coupling and degeneracy effects in inertial confinement fusion implosions,” *Physical Review Letters*, vol. 104, no. 23, Article ID 235003, 2010.
- [54] S. X. Hu, B. Militzer, V. N. Goncharov, and S. Skupsky, “First-principles equation-of-state table of deuterium for inertial confinement fusion applications,” *Physical Review B*, vol. 84, no. 22, Article ID 224109, 2011.
- [55] Y. H. Ding, A. J. White, S. X. Hu, O. Certik, and L. A. Collins, “Ab initio studies on the stopping power of warm dense matter with time-dependent orbital-free density functional theory,” *Physical Review Letters*, vol. 121, no. 14, Article ID 145001, 2018.
- [56] T. A. Mehlhorn, “A finite material temperature model for ion energy deposition in ion-driven inertial confinement fusion targets,” *Journal of Applied Physics*, vol. 52, no. 11, pp. 6522–6532, 1981.



Research Article

Investigation of Proton Beam-Driven Fusion Reactions Generated by an Ultra-Short Petawatt-Scale Laser Pulse

Marius S. Schollmeier ¹, Vahe Shirvanyan,¹ Christie Capper,¹ Sven Steinke ¹,
Adam Higginson ², Reed Hollinger ², John T. Morrison,² Ryan Nedbailo ²,
Huanyu Song ², Shoujun Wang ², Jorge J. Rocca ^{2,3} and Georg Korn¹

¹Marvel Fusion GmbH, Munich 80339, Germany

²Electrical and Computer Engineering Department, Colorado State University, Fort Collins, Colorado 80523, USA

³Physics Department, Colorado State University, Fort Collins, Colorado 80523, USA

Correspondence should be addressed to Marius S. Schollmeier; marius.schollmeier@marvelfusion.com

Received 13 June 2022; Revised 25 August 2022; Accepted 6 September 2022; Published 13 October 2022

Academic Editor: Dimitri Batani

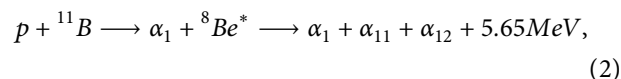
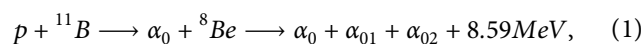
Copyright © 2022 Marius S. Schollmeier et al. This is an open access article distributed under the Creative Commons Attribution License, which permits unrestricted use, distribution, and reproduction in any medium, provided the original work is properly cited.

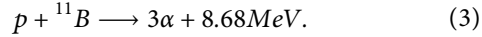
We present results from a pitcher-catcher experiment utilizing a proton beam generated with nanostructured targets at a petawatt-class, short-pulse laser facility to induce proton-boron fusion reactions in a secondary target. A 45-fs laser pulse with either 400 nm wavelength and 7 J energy, or 800 nm and 14 J, and an intensity of up to 5×10^{21} W/cm² was used to irradiate either thin foil targets or near-solid density, nanostructured targets made of boron nitride (BN) nanotubes. In particular, for 800 nm wavelength irradiation, a BN nanotube target created a proton beam with about five times higher maximum energy and about ten times more protons than a foil target. This proton beam was used to irradiate a thick plate made of boron nitride placed in close proximity to trigger $^{11}\text{B}(p, \alpha) 2\alpha$ fusion reactions. A suite of diagnostics consisting of Thomson parabola ion spectrometers, postshot nuclear activation measurements, neutron time-of-flight detectors, and differentially filtered solid-state nuclear track detectors were used to measure both the primary proton spectrum and the fusion products. From the primary proton spectrum, we calculated (p, n) and (α , n) reactions in the catcher and compare with our measurements. The nuclear activation results agree quantitatively and neutron signals agree qualitatively with the calculations, giving confidence that primary particle distributions can be obtained from such measurements. These results provide new insights for measuring the ion distributions inside of proton-boron fusion targets.

1. Introduction

An emerging new scheme for a nuclear fusion microreactor that utilizes an ultra-intense laser pulse irradiating a fuel target consisting of a mixture of protons, borons, and potentially other additional fuels has been published recently by Ruhl and Korn [1]. In this concept, an ultrahigh-contrast, short-wavelength, short-pulse laser is used to irradiate a periodic arrangement of solid density nanowires with well-controlled diameter and pitch with an ensemble near-critical density. The nanowire array is made of boron and hydrogen in a 1:1 ratio. This target configuration allows for laser propagation into the bulk and continuous laser energy

depletion. Upon propagation, the laser ionizes the nanowires fully, accelerates the released electrons to MeV energies, and expels them from the high-intensity region. The remaining positively charged ions of the nanowires undergo a Coulomb explosion, which accelerates the lighter protons to few-MeV energies. Upon colliding with the slower boron ions, pB-fusion reactions can be triggered that each generates three alpha particles via the reactions [2]:





Further details of the reactor concept are outlined in Reference [1]. An experimental realization of this integrated fusion reactor concept poses unique challenges in many aspects, such as, for example, fulfilling the laser driver requirements, in target manufacturing, and to accurately diagnose the laser-target interaction under the demanding conditions inside the reactor. Most investigations about laser-driven proton-boron fusion have measured the escaping alpha particles [2–11] to infer fusion efficiencies. However, alpha particle detection in such experiments is challenging due to the fact that the target also emits other ions such as protons and borons, with identical or similar energies and charge-to-mass ratios as the alpha particles, leading to overlapping signals in detectors. Being charged particles, the alphas are subject to electromagnetic fields that may surround the target, which can further complicate the analysis of the primary emission since the fields may accelerate or deflect the alphas [5, 9]. Hence, additional diagnostic methodologies are needed to increase confidence in data interpretation. For example, measuring neutrons or activation products from secondary reactions is complementary to alpha particle detection and can lead to a better understanding of the physical processes occurring inside a fusion reactor.

The reactor design discussed above requires ordered nanowire arrays with very high aspect ratios made of boron and hydrogen. For our study, few-nm-diameter, unordered boron nitride (BN) nanowire nanotube (BNNT) targets that were developed by BNNT materials, LLC, were combined in a pitcher-catcher configuration [2–4, 8, 10, 11] to experimentally measure the proton source decoupled from the fusion reaction. This combination enables the characterization and optimization of the proton beams and the dependence on laser and target parameters in pitcher-only experiments. Knowing the incoming proton beam parameters, secondary reactions such as those in Equations (1)–(3), but also neutron- or photon-generating reactions in a catcher target can be measured and compared to calculations using tabulated cross-sectional values [12]. We include measured data from neutron time-of-flight, postshot nuclear activation, Thomson parabola ion spectrometer, and CR39 solid-state nuclear track detectors in our analysis. Nuclear activation results agree quantitatively and neutron signals qualitatively with the calculations, which ensure a reliable measurement of the primary particle distributions by this method. However, our analysis additionally highlights potential issues with such measurements if alpha particles are to be inferred.

2. Materials and Methods

The experiments were performed at the Advanced Laser for Extreme Photonics (ALEPH) at Colorado State University, Fort Collins, CO, USA [13]. ALEPH is a 0.85 PW, 45 fs Ti:Sapphire laser system operating at 800 nm wavelength. After compression, the pulse is converted to its second harmonic (400 nm) before it is directed to the target chamber. Five

dichroic mirrors with >99.5 transmission at 800 nm are used to efficiently remove unconverted light yielding a contrast of $>10^{12}$ up to ~ 5 ps before the main pulse [14]. A dual-coated $f/2$ off-axis parabolic mirror is used to focus the laser pulse to a focal spot of about $1.5\ \mu\text{m}$ full-width-at-half-maximum (FWHM). After second harmonic generation (SHG), the laser delivered 7 J on target, reaching a peak intensity of 5×10^{21} W/cm². We have also performed experiments at the fundamental wavelength, bypassing the SHG crystal and dichroic mirrors. Here, the laser delivered 14.3 J on target. The temporal contrast was lower than for the SHG pulse due to an ASE prepulse of nanosecond duration with $\sim 10^{-8}$ intensity contrast. The stronger prepulse may result in reduced coupling to the nanostructured targets. However, the about twofold higher laser energy offsets the reduced coupling and leads to an overall higher proton yield as will be shown below.

2.1. Targets. For each measurement series, up to 30 shots were performed for statistics and to ensure the results are reproducible. The data were then averaged in postprocessing to yield single-shot results. We compared the efficiency of proton beam generation from 1.2- μm -thick Mylar foils (400 nm pulse), 7- μm aluminum foils (800 nm; thicker foil to reduce preheat of the rear side during the prepulse), and BN nanotube targets (both wavelengths). BN nanotubes have a similar tubular structure as carbon nanotubes in which carbon atoms are replaced entirely by boron and nitrogen atoms, arranged in a hexagonal lattice. The individual tubes are between 2 nm and 8 nm in diameter and can be several tens of microns long. The BN nanotubes formed a dense, unordered matrix (bucky paper sheets), wherein the tubes are randomly oriented and overlap to form thicker (several microns) clumps with voids in-between them. While the individual BN nanotubes have a near-solid density (~ 2 g/cm³), the average density of the BN nanotube targets was 0.55 g/cm.

Figure 1(a) shows a sketch of the target chamber with the relevant diagnostics. The targets were continuous sheets of either thin foils or BN nanotubes. The sheets were sandwiched between two aluminum plates: one thicker plate to hold the samples on one side to which a 400- μm thin plate was bolted with 32 M2 screws to apply even pressure on the BN nanotube samples. An array of 3-mm-diameter holes in the plates spaced 8 mm apart in a 5×6 hole pattern enabled a shot series of up to 30 shots within one vent cycle. The inset in the bottom left corner shows a photograph of the target frame. The targets were mounted at the center of the chamber and irradiated by the s-polarized laser pulse at normal incidence. Figure 1(b) shows the pitcher-catcher configuration, where a 30- μm -thick BNNT target was irradiated by the 14.3 J, 800 nm pulse at normal incidence. A 1.5-mm (1/16 in.)-thick, commercially available BN ceramic plate in 400 μm distance was used as a catcher. The plate consists of 95% BN and about 5% B₂O₃. The natural boron used consists of 80% ¹¹B and 20% ¹⁰B. A gap between the two targets was formed by using a second 400- μm plate identical to the one used on the BN nanotube target frame in direct

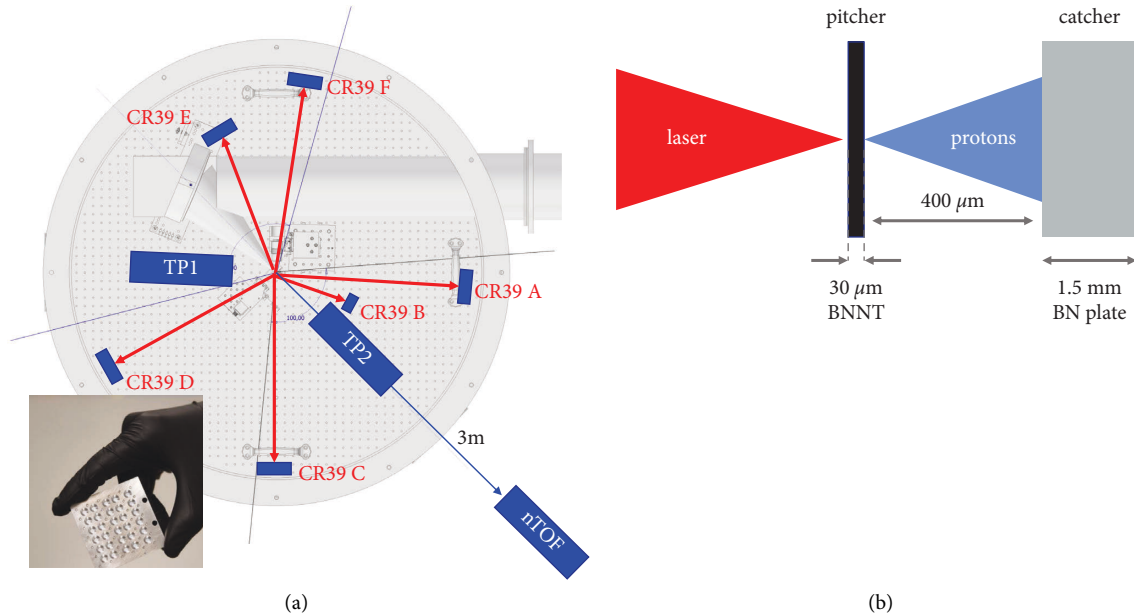


FIGURE 1: Experiment layout and target configuration. (a) shows a sketch of the target chamber with the relevant diagnostics. The laser pulse is focused by an $f/2$ off-axis parabolic mirror to an intensity of $\sim 5 \times 10^{21}$ W/cm² onto a target at the center of the chamber. Thomson parabola (TP) ion spectrometers are used to diagnose the generated proton beam. A filtered CR39 solid-state nuclear track detector is used to corroborate the TP measurements. A neutron time-of-flight (nTOF) detector is placed in about 3 m distance along the target normal direction. The inset in the lower-left corner shows a photograph of the target holder. (b) shows a sketch of the pitcher-catcher configuration. The laser pulse irradiates a 30- μ m boron nitride nanotube target to create a proton beam (pitcher). The protons then irradiate a secondary boron nitride target (catcher) in 400 μ m distance to trigger nuclear reactions.

contact with the pitcher and catcher plates. For each of the 30 targets, the hole in the plate resembled a cylindrical cavity with 3 mm diameter and 400 μ m length. This configuration allowed us to place the catcher as close as possible to the source without interrupting the TNSA mechanism [15], but close enough to benefit from potential preheat by hot electrons or x-rays that lead to the generation of a hot, dense plasma in front of the catcher and potentially enhances the pB-fusion yield [3].

2.2. Diagnostics. Two identical, compact Thomson parabola (TP) ion spectrometers are used to diagnose the accelerated ions. The TPs are custom-made by the facility with a design similar to Carroll et al. [16]. The TPs were equipped with either Fuji MS or TR image plate to detect the parabolic ion traces. The image plates were scanned 20 min after the last shot on the target frame with a pixel size of 50 μ m. The image plate data were converted to proton numbers using the calibration by Bonnet et al. [17]. Since the image plate digitizations were performed using a different scanner from the one used in [17], a 2×2 cm² piece of filtered CR39 (Mi.am Srl, Piacenza, Italy) was placed next to the TP entrance at position “B” to corroborate the TP measurements and verify the calibration. Six different Al filters with 2, 15, 30, 45, 60, and 75 μ m thicknesses were put in front of the CR39 to obtain information about the proton (and ion) energies hitting the CR39. The CR39 were etched for 30 minutes in 6.5 M NaOH solution at 70°C to reveal the ion tracks (“pits”). The pit diameter depends on not only the ion

stopping power but also on the etch time. Longer etching is preferred for an increased accuracy of the track analysis (e.g., [18]). However, the ion flux for the thinnest filter was already close to saturation for most BN nanotube targets; therefore, the etch time had to be kept to a minimum. After etching, the images were digitized using a Keyence VHX-7000 digital microscope equipped with a 12.2 megapixel VHX-7100 image acquisition unit. The microscope resolution was determined with a high-resolution microscopy USAF test chart (Edmund Optics) to be 2400 lp/mm, which is sufficient to detect the ~ 0.5 - μ m-diameter proton pits. After digitization, the pits were registered using a custom MATLAB routine.

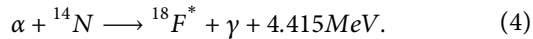
To measure neutrons from (p, n) or (α, n) fusion reactions in either target, an EJ-228 plastic scintillator-photomultiplier tube (PMT; Hamamatsu H2431-50) time-of-flight detector was placed in 3 m distance from the target location along the laser axis. The detector was enclosed in a housing made of 5-cm-thick lead bricks to reduce the high-energy photon signal reaching the PMT. The detector was calibrated previously [14, 19]. However, due to the strong photon signal generated during the experiments with 800 nm wavelength, the PMT bias voltage had to be reduced significantly to avoid saturation of the trace, which negated the calibration.

2.3. Nuclear Reactions Creating Neutrons and/or Positron Emitters. In addition to the on-shot diagnostics, two Scionix Holland 51B51/2M-E1 gamma spectrometers equipped with a 51-mm-diameter, 51-mm-long NaI (Tl) scintillator,

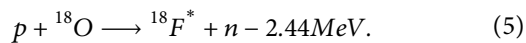
coupled to a CAEN DT5725S digitizer, were used to measure the activation of the target remnants after the shots. An integration time of 5 minutes was chosen to provide sufficient counts at later times. This setup enabled us to measure the gamma spectrum of the samples vs. time, not just the activation [2], to verify that the measured signal is from positron emitters and not from other decay channels such as, for example, excited nuclei from Bremsstrahlung photoexcitation.

In the pitcher-catcher experiment, the accelerated protons can create a multitude of nuclear reactions [2, 4]. Table 1 lists some of the possible (p, x) and (α, x) reactions that create a neutron or a positron emitter as reaction products. Some of the reactions have a negative Q value of a few MeV, meaning the incident projectile needs to overcome a threshold energy to trigger the reaction. The second column in the table lists approximate values of the reaction cross section near the peaks for a quick judgment of the likelihood of the reaction. The analysis discussed below uses the tabulated values that were obtained with the Java-based nuclear information software (JANIS) [12] across multiple databases. The third column lists the half-life of the generated positron emitters. The most probable activation product is $^{11}\text{C}^*$ with a half-life of about 20 minutes. For early times, the activation may have a contribution of $^{13}\text{N}^*$, and for late times, the measurements may detect the presence of $^{18}\text{F}^*$ that has a half-life of about 2 hours.

The $^{18}\text{F}^*$ isotope was used in [2] to infer the presence of alpha particles in a BN catcher via the reaction



However, there are two potential issues with this inference. One issue is the rather low cross-sectional value of only 5 mb. This low value ruled out this alpha particle detection path in an earlier work looking at nuclear reaction diagnostics for magnetic fusion devices [20]. The other issue is that $^{18}\text{F}^*$ can also be produced when the target contains oxygen impurities via



The stable ^{18}O isotope has an abundance of about 0.2% in natural oxygen. The $^{18}\text{O}(p, n)^{18}\text{F}$ reaction has a high cross section of ~ 500 mb at 5 MeV [21, 22]. Since this reaction is triggered by the primary protons and not by alphas, if $^{18}\text{F}^*$ is detected in the experiment a precise knowledge of the oxygen contamination and the incoming proton spectrum are required to infer the relative contributions of proton and alpha particles to the $^{18}\text{F}^*$ generation.

3. Results and Discussion

3.1. Proton Spectra for 2ω Irradiation, Pitcher-Only. Starting with 2ω irradiation, Figure 2 compares proton spectra measured with TP1 and TP2 for a 1.2- μm -thick Mylar foil compared to a BN nanotube target. The BN nanotube target was 110 μm thick and had an average density of 0.55 g/cm^3 , which is 2–3 times lower than solid

density. The plots show the proton spectra for a single shot, normalized to 1 J of laser energy.

Figures 2(a) and 2(b) show the Mylar foil proton spectra at the front (laser irradiated) and back side, respectively. The spectra look nearly identical, confirming the high contrast of the laser pulse that leads to TNSA proton acceleration on both sides of the target [23]. The maximum proton energies are 4–5 MeV. The spectral shape can be described by

$$\frac{dN}{dE} = \frac{N_0}{E} \exp\left(\frac{-E}{k_B T_e}\right), \quad (6)$$

where N_0 and $k_B T_e$ are the fit parameters (orange lines). Except for Figure 2(c), $N_0 \approx 10^8$ and $k_B T_e \approx 0.1$ MeV. Using the filtered CR39 plates (positions A thru F), we confirm that the proton emission is strongly peaked in the target normal directions, as expected.

Figures 2(c) and 2(d) show the proton spectra for the 110- μm -thick BN nanotube target. Of striking difference is the front side proton spectrum, which reaches almost 10 MeV. Here, $N_0 \approx 10^7$ and $k_B T_e \approx 0.5$ MeV. The rear side spectrum is similar to the Mylar foil, even though the BN nanotube is 100 times thicker than the Mylar foil. The filtered CR39s measured about 100 times more particles along the target normal directions, as well as significant particle counts in all the measured off-normal directions. We interpret these findings as due to enhanced, volumetric absorption of the laser pulse compared to surface absorption for the foil target due to both the nanostructured surface and the overall reduced density.

3.2. Proton Spectra for 2ω vs. 1ω Irradiation, Pitcher-Only. After verifying that BN nanotubes lead to hotter proton spectra at high-contrast, 400-nm irradiation, we repeated a similar measurement using the fundamental wavelength and with higher laser energy. Figure 3(a) shows a direct comparison of Mylar foil and BN nanotube target backside proton spectra for 2ω irradiation, and Figure 3(b) the same for 1ω , for 30- μm BNTs, and for a 7- μm Al foil. The spectra were measured by integrating over 10 shots (2ω , 20 shots for 1ω) for reproducibility. The plots show the processed proton spectra for a single shot, normalized to 1 J of laser energy.

The 2ω spectra are very similar for both the foil and the BN nanotube targets, despite the BN nanotube target being 100 times thicker. Compared to 2ω irradiation, the 1ω spectra exhibit about 100 times more protons at 1 MeV. Additionally, the BN nanotube target accelerated protons up to 20 MeV energy, about five times higher than the Al foil target. This finding supports the hypothesis that thinner BN nanotube targets outperform comparable foil targets as a proton source. The hundredfold higher particle numbers were not expected; as a result, the TP traces for the 1ω shots are saturated over large parts of the parabolic traces. The saturated parts were removed from the analysis and the spectrum was analyzed near the high and low energy ends of the trace where the dispersion in the TP was large enough to reduce the particle flux below saturation (low energies) or the particle numbers were low enough (high energies).

TABLE 1: Nuclear reactions creating neutrons and/or positron emitters in boron, nitrogen, and oxygen.

Reaction	Max. cross section (mb)	Half-life (min.)
Boron:		
$\alpha + {}^{10}\text{B} \rightarrow {}^{13}\text{N}^* + n + 1.06 \text{ MeV}$	100	9.97
$p + {}^{10}\text{B} \rightarrow {}^{11}\text{C}^* + \gamma + 8.69 \text{ MeV}$	$\sim \mu\text{b}$	20.4
$\alpha + {}^{11}\text{B} \rightarrow {}^{14}\text{N} + n + 0.158 \text{ MeV}$	100	Stable
$p + {}^{11}\text{B} \rightarrow {}^{11}\text{C}^* + n - 2.765 \text{ MeV}$	400	20.4
$p + {}^{11}\text{B} \rightarrow 3\alpha + 8.6 \text{ MeV}$	1200	Stable
Nitrogen:		
$\alpha + {}^{14}\text{N} \rightarrow {}^{18}\text{F}^* + \gamma + 4.415 \text{ MeV}$	5	109.8
$p + {}^{14}\text{N} \rightarrow {}^{14}\text{O}^* + n - 5.93 \text{ MeV}$	100	70 s
$p + {}^{14}\text{N} \rightarrow {}^{11}\text{C}^* + \alpha - 2.92 \text{ MeV}$	200	20.4
$\alpha + {}^{14}\text{N} \rightarrow {}^{17}\text{F}^* + n - 4.73 \text{ MeV}$	50	64.3 s
Oxygen:		
$p + {}^{16}\text{O} \rightarrow {}^{13}\text{N}^* + \alpha - 5.22 \text{ MeV}$	150	9.97
$p + {}^{18}\text{O} \rightarrow {}^{18}\text{F}^* + n - 2.44 \text{ MeV}$	500	109.8

The primary alpha-generating fusion reaction is listed for comparison (see Equations (1)–(3)). The reactions are used in the analysis to infer primary proton and alpha yields. The cross-sectional values quoted are approximate values near the peaks for a quick judgment; the analysis uses the tabulated values. The half-life of the created positron emitters is given in minutes, unless otherwise quoted.

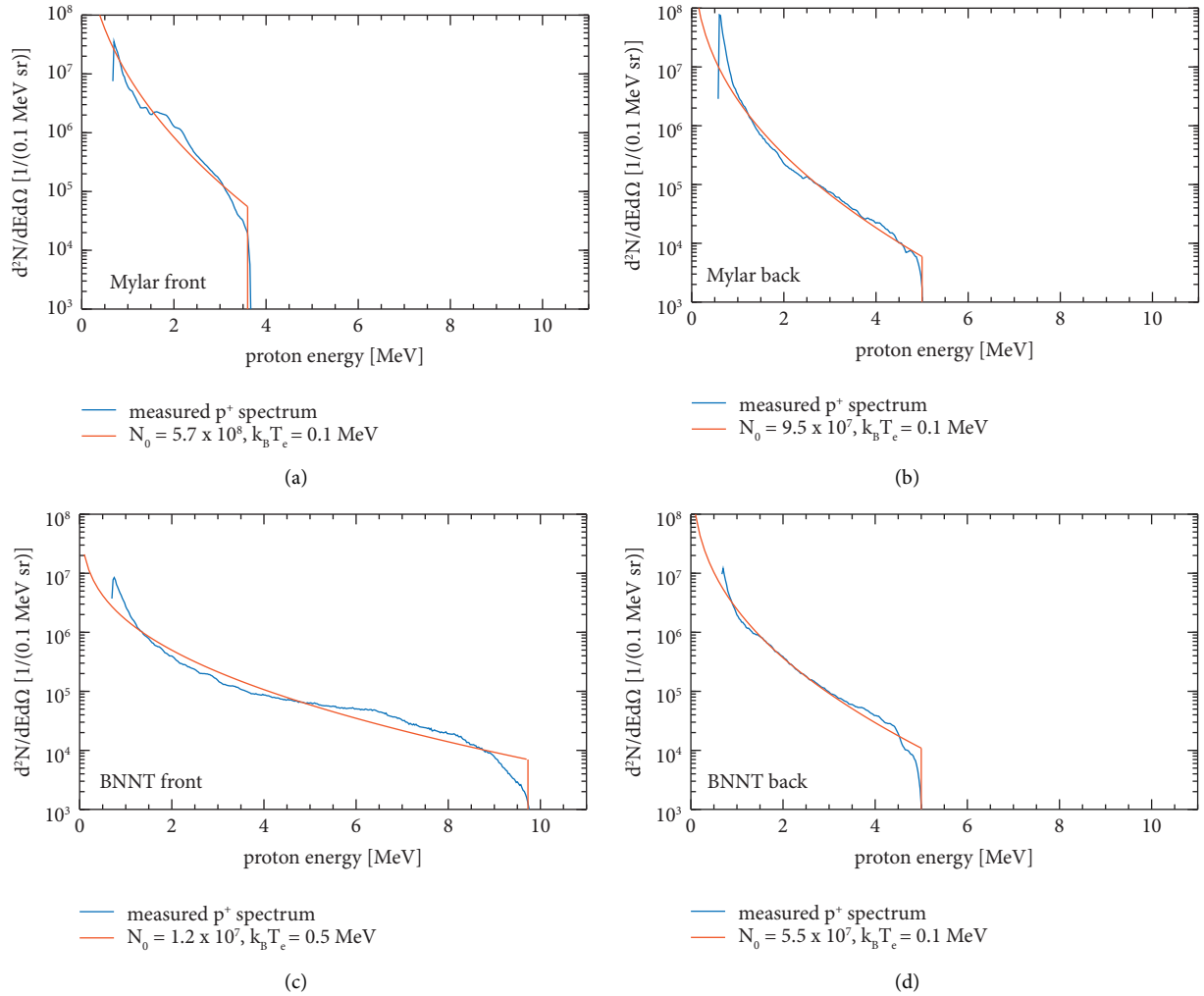


FIGURE 2: Proton spectra for 2ω irradiation, Mylar foil vs. BN nanotube target. The proton spectra from front (a) and back side (b) of the 1.2- μm Mylar foil are nearly identical indicating TNSA on both sides of the target. The 100- μm -thick BN nanotube target results in more than double the maximum energy on the front side (c) and still ~ 5 MeV from the rear side (d), suggesting that the laser is absorbed more efficiently due to the nanostructure of the BN nanotubes.

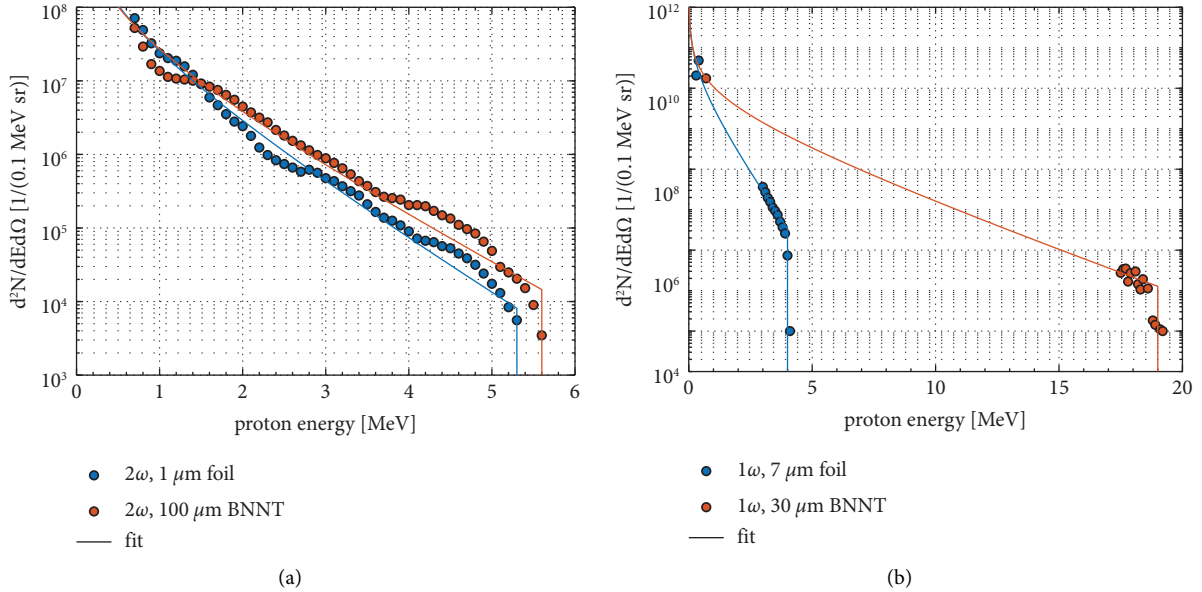


FIGURE 3: Rear-side TP ion spectra (TNSA protons) show 10^4 times more particles for 1ω vs. 2ω irradiation. The data show single-shot spectra, per 1 J of laser energy, by dividing the multishot integrated measurement by the number of shots and laser energy. (a) The 2ω spectra are very similar for both the Mylar foil and the BN nanotube target, despite the BN nanotube target being 100 times thicker. (b) The 1ω spectra exhibit about 100 times more protons at 1 MeV. Additionally, the BN nanotube target accelerated protons up to 20 MeV energy, about five times higher than the Al foil target.

After plotting the extracted particle numbers from the TP traces, we fitted spectra using Equation (6) to determine the particle yields and slope.

For the $7\text{-}\mu\text{m}$ Al foil irradiated at 1ω , we compared the particle flux detected with CR39 #B and the TP trace. The particle count in this CR39 detector reached about 5×10^8 protons/sr/J/shot behind the $75\text{-}\mu\text{m}$ Al filter, corresponding to protons with energies above 1.6 MeV. This filter thickness ensures that only protons were detected in the CR39. Alpha particles need ~ 12 MeV and carbon or B, N ions need > 60 MeV to penetrate the filter. The pit diameters behind this filter are all about 500 nm, in line with the expected proton pit diameters for our etch conditions. Integrating the TP spectrum for energies above 1.6 MeV results in a proton count of 3×10^8 protons/sr/J/shot, giving confidence in our TP calibration. For comparison, the BN nanotube created about ten times more protons.

We did not field an imaging proton spectrometer such as, for example, a stack of radiochromic films [24, 25] to measure the full beam size or divergence angle. However, typically TNSA beams exhibit a cone angle of up to $\pm 15^\circ$ [24–28] for the lower energies, which contribute the most to the particle numbers. Assuming this value as an estimate for the proton beam divergence for both target types results in 4×10^9 protons per shot for the Al foil and 4×10^{10} protons for the BN nanotube target. These yields are similar to the results from [28], who compared proton beam from thin foils to foam-coated thin foils. There, the foam-coating resulted in enhanced laser absorption and about four times higher proton yield than uncoated foils. Our results indicate that BN nanotube targets could yield even better absorption and more protons, potentially due to the nanostructures

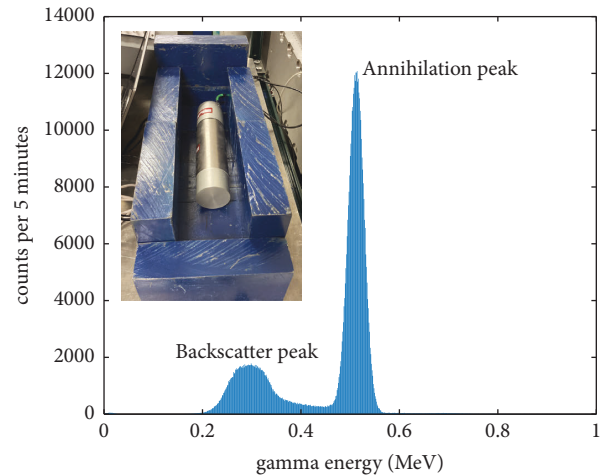


FIGURE 4: Postshot gamma spectroscopy of the pitcher-catcher shots. A strong peak at 511 keV is measured, verifying the existence of positron emitters (in contrast to, e.g., excited nuclei from photoexcitation). The second peak at about 250 keV is from backscattered 511 keV primary photons in the lead shielding nearby. The photograph in the inset shows one of the detectors inside of the lead housing with the top removed.

spanning the entire material. Even higher proton energies are expected from thinner BN nanotube targets [29, 30], but this was beyond the scope of this investigation.

3.3. Pitcher-Catcher Experiment at 1ω Irradiation. After having determined that BN nanotube targets irradiated at 1ω created the proton source with the highest particle numbers and energies, a pitcher-catcher experiment was performed

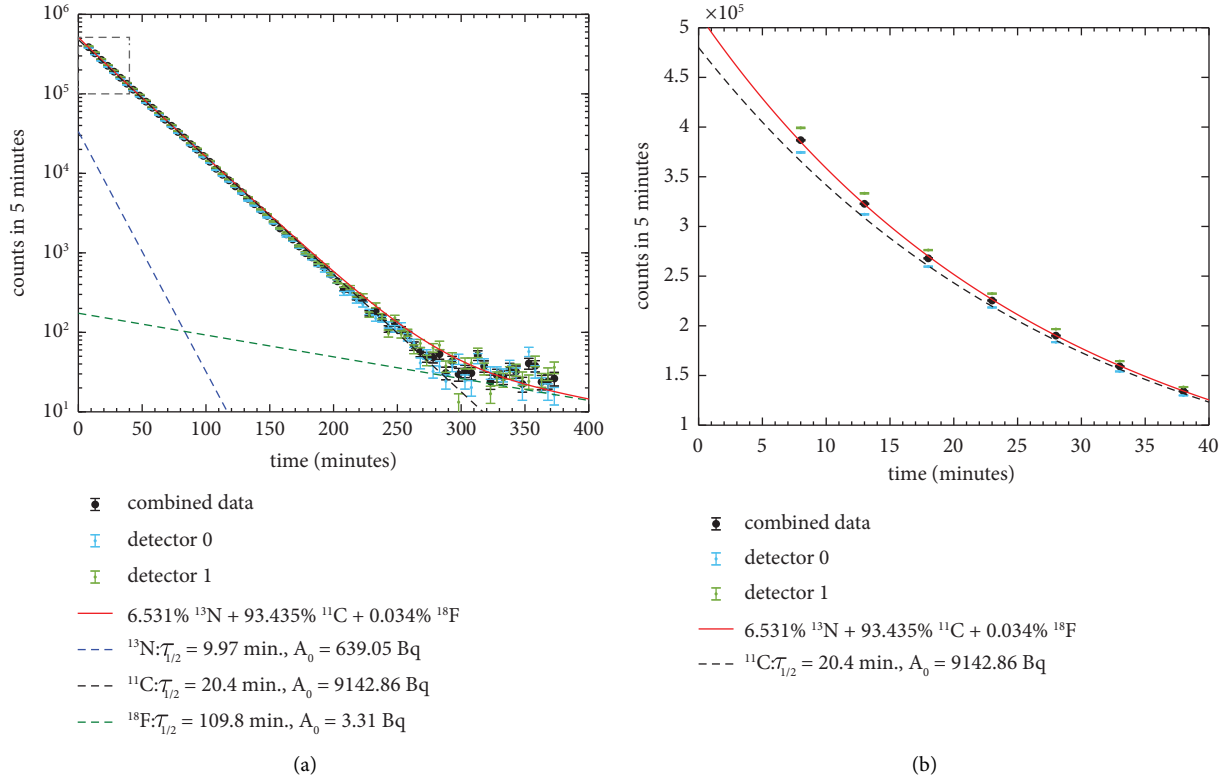


FIGURE 5: Pitcher-catcher nuclear activation measurements. (a) Each black data point shows the background-corrected counts as an average of the two spectrometer counts (shown in light-blue and light-green). Time zero corresponds to the time of the last laser shot on the targets. The dashed lines are the result of fitting the decays of ^{13}N , ^{11}C , and ^{18}F to the data. Note the logarithmic ordinate. Details are given in the figure legend and the text. (b) is a zoomed view of the data at early times, on a linear scale, to better visualize that the $\sim 6.5\%$ contribution of ^{13}N is needed to match the measurements.

where the proton beam was directed at a BN plate as described in Figure 1(b). The most striking results were that we measured significant nuclear activation during the postshot gamma spectroscopy, as well as a neutron time-of-flight signal, both of which are clear evidence for nuclear reactions.

3.4. Nuclear Activation. An example measurement is shown in Figure 4. The gamma spectrum is dominated by the 511 keV electron-positron annihilation peak, verifying the existence of positron emitters (in contrast to, e.g., excited nuclei from Bremsstrahlung photoexcitation). The second peak at about 250 keV is from backscattered 511 keV primary photons in the lead shielding nearby. The decay of the 511 keV peak was monitored in 5-minute integration intervals until it reached background levels. Prior to the measurements, the background counts were determined using the same integration time. Two gamma spectrometers on either side of the target frame were used in ~ 1 cm distance to monitor an almost 4π solid angle. The detection efficiency of the NaI scintillator for 511 keV photons was estimated as 35% [20].

The activation results for the pitcher-catcher shots are plotted in Figure 5. The pitcher-only shots performed earlier did not produce any measurable activation above the background. Therefore, we can assume that the majority of the measured activation is from the BN catcher plate and not

TABLE 2: Activation results for the pitcher-catcher shots after 30-shot integration.

Isotope	^{11}C	^{13}N	^{18}F
Half-life (min)	20.4	9.94	109.8
Decay constant (min^{-1})	0.034	0.0697	0.0063
Relative contribution (%)	93.435	6.531	0.034
Activity A at $t=0$ (Bq)	9143	639	3.3
Number of nuclei N_2	1.6×10^7	5.5×10^5	3.2×10^4
N_2 per shot per J	37,000	1300	75

Each column lists physical and fit parameters for the three discussed nuclei. N_2 is the calculated number of nuclei based on the measured activity A . The last row is the same number, normalized per shot per 1 J of energy.

the primary source target. As discussed above and shown in Table 1, the most likely isotopes to be created are ^{11}C , ^{13}N , and ^{18}F . The three decays were fitted to the measured data to obtain the partial contributions of each nuclide. The decay curves can be extrapolated to t_0 when the last laser shot occurred to get the activity A right after the shots. The total activity A_{total} was 11.5 kBq after 30 shots. From the activity and the decay constant $\lambda = \ln(2)/\tau$, where τ is the half-life, the number of activated nuclei can be easily calculated as $N = A/\lambda$.

The fit results are summarized in Table 2 and plotted with the dashed lines in Figure 5. The most abundant isotope is ^{11}C , which is from protons fusing with ^{11}B to create the ^{11}C isotope and a neutron.

TABLE 3: Reaction product yields per primary projectile in BN and expected yields for the BN nanotube 1ω spectrum.

Reaction product	3α	^{11}C	^{13}N	^{18}F		
Reaction	$^{11}\text{B}(p, \alpha)2\alpha$	$^{11}\text{B}(p, n)^{11}\text{C}$	$^{10}\text{B}(\alpha, n)^{13}\text{N}$	$^{16}\text{O}(p, \alpha)^{13}\text{N}$	$^{14}\text{N}(\alpha, \gamma)^{18}\text{F}$	$^{18}\text{O}(p, n)^{18}\text{F}$
Q value (MeV)	8.59	-2.76	1.06	-5.22	4.415	-2.44
Threshold energy (MeV)	0	3.017	0	5.547	0	2.575
Target ion density (cm^{-3})	2×10^{22}	2×10^{22}	5×10^{21}	1.5×10^{21}	2.5×10^{22}	3×10^{18}
Expected N_2 per J	6×10^6	66,000	0.5	800	1	80
Measured N_2 per J (Table 2)	n/a	37,000	1300	1300	75	75

The ion densities are calculated assuming the BN plate (density of 2.1 g/cm^3) contains $\sim 95\%$ BN and $\sim 5\%$ oxygen contamination. The natural boron consists of $80\% ^{11}\text{B}$ and $20\% ^{10}\text{B}$. Of the natural oxygen, the ^{18}O isotope is about 0.2% abundant. N_2 is given per shot per J of laser energy.

It is worthwhile to compare our results to earlier measurements by Labaune et al. [2]. In [2], the laser energy was about 10 J. Up to 500 Bq of nuclear activation was detected. Our laser delivered 14.3 J and created ~ 400 Bq per shot, which is similarly efficient but does not require a secondary laser pulse to boost the activation levels. Unlike [2], we see a clear contribution of ^{13}N to the measurements as shown in the zoomed view in Figure 5(b). At late times, ^{18}F appears with an activity of 3 Bq, about the same activity as measured in [2]. However, the relative contributions of the three different isotopes are very different. In [2], the ^{18}F isotope had a relative abundance of 0.6% , whereas our measurements yield an about 20x lower contribution. Reference [2] interpreted the ^{18}F creation to be originated by alpha particles and a proof-of-concept that secondary reactions are possible. If that is true, the alpha particles should also create ^{13}N isotopes. The measurements in [2] showed hints of ^{13}N creation but were not conclusive.

Our measurements show a clear evidence for ^{13}N isotopes, as well as ^{18}F . In the following, we calculate the expected number of isotopes assuming beam-target fusion reactions and using the 1ω BN nanotube target spectrum from Figure 3 as input. The number of reaction products N_2 depends on the number of incoming projectiles $N_{\text{projectile}}$, target ion density n_{target} , cross section σ , and projectile range R :

$$N_2 = N_{\text{projectile}} n_{\text{target}} \sigma R. \quad (7)$$

The projectile range R depends on the incoming projectile energy E_0 and the ion-stopping power dE/dx . As the projectile slows down in the material, its energy is reduced and correspondingly the cross section changes. Therefore, the product σR in Equation (7) is replaced by an integral over the cross section and stopping power to calculate N_2 [5]:

$$N_2 = N_{\text{projectile}} n_{\text{target}} \int_0^{E_0} \sigma(E) \left(\frac{dE}{dx} \right)^{-1} dE. \quad (8)$$

The stopping power was taken from the SRIM software package [31], and the cross-sectional data were obtained via the Janis database [12]. Taking the proton-boron fusion reaction $^{11}\text{B}(p, \alpha)2\alpha$ as an example, with the analytic cross section from [32], an incoming proton energy of $E_0 = 1 \text{ MeV}$, and noting that this reaction creates three alpha particles per proton, we calculate a yield of 3.9×10^{-5} alpha particles per proton. The slight discrepancy to the efficiency obtained in [5] results from the different density of the BN plate used in our work.

Next, we integrate Equation (8) over the 1ω BN nanotube proton spectrum to calculate the total number of activated nuclei. Here, the energy intervals for integration are between the threshold energy of the reaction (for negative Q values, zero elsewhere) and the 19 MeV maximum energy.

The results are summarized in Table 3. The first column shows the calculated alpha particle yield, which is 6×10^6 per shot per J. The second column shows that the calculated ^{11}C yield matches the measured one fairly closely. The difference could be due to the assumption of $\pm 15^\circ$ cone angle, which overestimates the proton yield for higher energies. Additionally, the catcher target featured some shallow ablation craters after the shot, which may have reduced the target activation due to some missing material.

The third column compares the calculated and measured ^{13}N generation. In pure BN, ^{13}N can be generated by alpha particles [2], but since our target had significant oxygen contamination, there is also a very probable proton-induced reaction channel. Assuming that all alpha particles generated by the primary $p\text{-}^{11}\text{B}$ reaction (column 1) have energies between 1 and 5 MeV and are all stopped in the BN, the most optimistic calculation results in less than one ^{13}N nucleus being created per J. However, our measurement indicates that about 1300 nuclei/J are created. The calculated ^{13}N yield per alpha particle is $\sim 8 \times 10^{-8}$. If we attribute all the measured ^{13}N nuclei as being created by alpha particles, this results in $\sim 2 \times 10^{10}$ alpha particles per shot per J. Performing the same estimate for the ^{18}F yield (using a constant $\sigma = 5 \text{ mb}$ due to the lack of detailed cross-sectional data) results in a ^{18}F yield per alpha particle of 1.8×10^{-7} , translating into $\sim 4 \times 10^8$ alphas per shot per J. The two calculated alpha yields are inconsistent with each other by a factor of 50. The estimate from ^{13}N is also within a factor of two of the measured proton yield, which appears too high given the low fusion probability due to beam-target interaction.

Performing the ^{13}N calculation under the assumption of the proton-oxygen reaction results in a similar number as the measured one. The same comparison holds true for ^{18}F generation.

Therefore, we conclude that for our pitcher-catcher experiment, the majority of the measured radioactive isotopes are the result of protons interacting with ^{11}B or oxygen contamination. However, some discrepancies still prevail between the calculated and measured data. In particular, the calculated ^{11}C number is higher while the calculated ^{13}N is lower than measured, leaving room for potentially higher alpha numbers than calculated here.

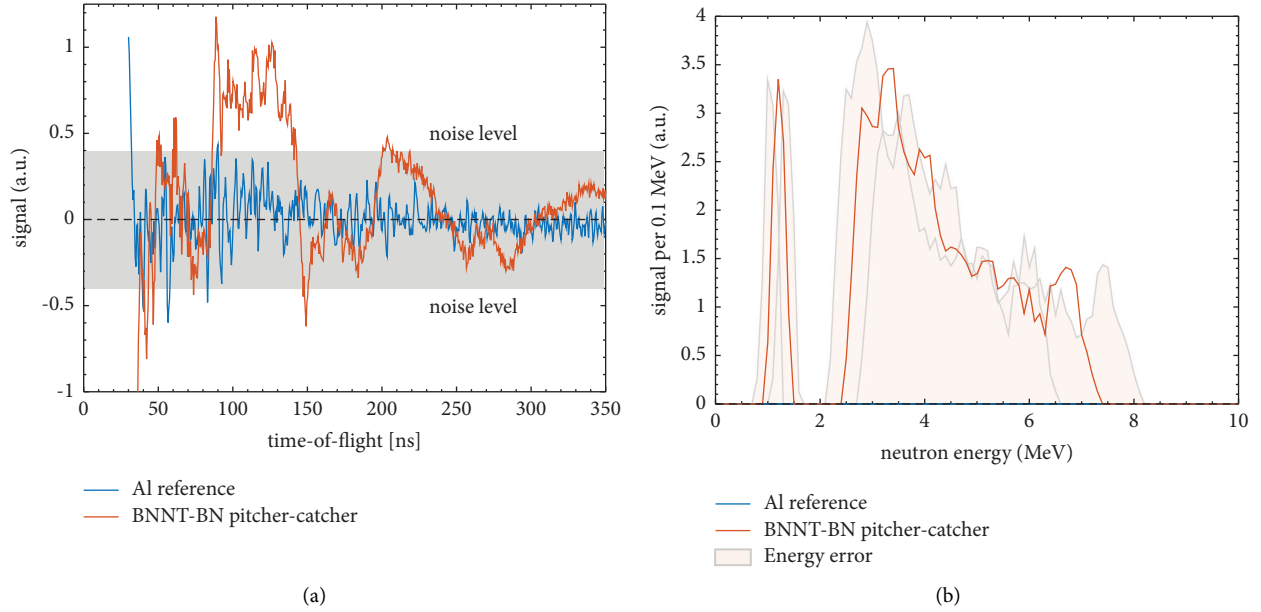


FIGURE 6: Neutron time-of-flight data and spectra, from an average of 30 shots. (a) shows the background-corrected traces for the pitcher-catcher experiment vs. a pitcher-only aluminum target. The pitcher-catcher trace shows a signal at around 100 ns that is above the noise level. (b) shows the same data, converted to neutron kinetic energy. The first peak corresponds to $\sim 2\text{--}7$ MeV energy, and a potential second peak is at ~ 1.3 MeV energy. It is at present not clear whether this second peak is an artifact due to the noise; we have planned to investigate this in the future. The uncertainty in the detector distance leads to an error of the calculated energies, visualized by the shaded areas.

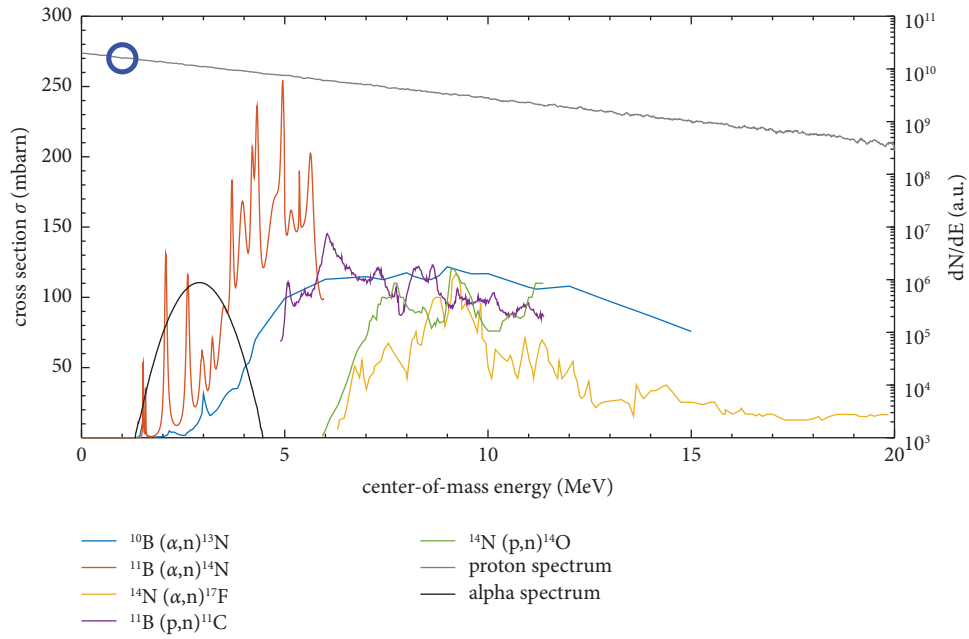
3.5. Neutron Spectra. The data of the previous section show that the majority of the activation is from $^{11}\text{B}(p, n)^{11}\text{C}$, which creates a neutron with each created ^{11}C nucleus. For 14 J laser energy, this should create about $10^6\text{--}10^7$ neutrons per laser shot. This neutron yield is detectable at ALEPH as shown in earlier works [14, 19]. Figure 6(a) shows the neutron time-of-flight trace for the pitcher-catcher shots compared to shots using an Al pitcher only. The traces were averaged for 30 shots. The initial high-energy photon flash was very intense in all of the shots and created a temporary saturation of the traces followed by an exponential decay. Nonetheless, we have observed modulations of the traces during the decay of the scintillator for our pitcher-catcher shots with BN nanotube targets that were not present when the Al targets were used. To find out whether these modulations correspond to neutrons, and for a better comparison between the reference and pitcher-catcher shots, a multi-exponential function with constant offset was fitted to the decay curves and subtracted from the data to reveal a neutron signal. The fast rise time of the photon flash indicates the arrival time of the laser pulse on target, which was correspondingly used to calculate the neutron time-of-flight. Even with background subtraction, the data exhibit high-frequency noise and a poor signal-to-noise ratio due to the presence of a strong electromagnetic pulse. Using the noise amplitude of the Al data, for which we do not expect to measure any neutrons, we defined a baseline noise level of ± 0.35 V (marked by the shaded area in Figure 6(a)). The amplitude of the pitcher-catcher signal at delay times between approximately 100 to 150 ns is significantly stronger than this noise level, suggesting it may be from neutrons.

To generate a neutron spectrum, we disregard data that fall within the noise level by setting these values to zero. The

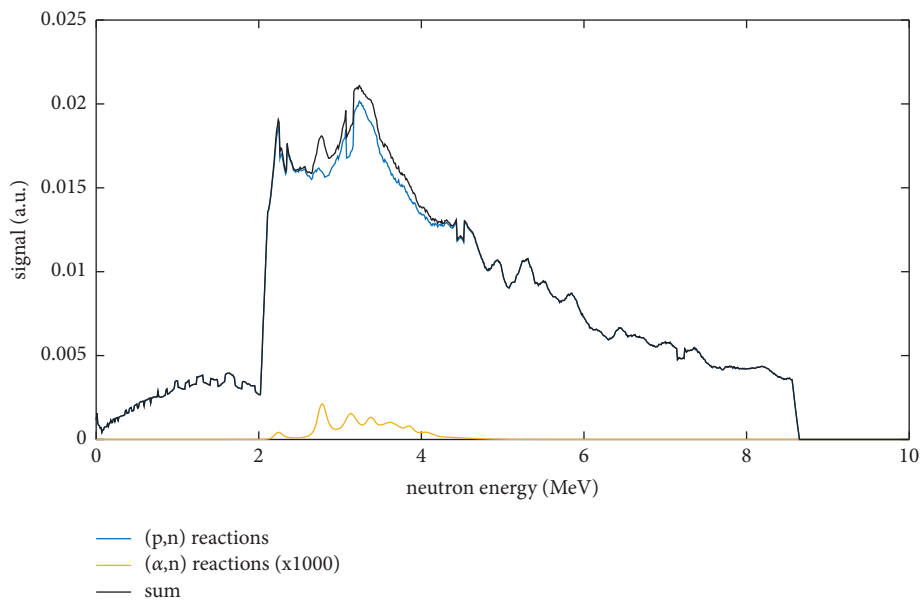
time-of-flight data were converted to neutron kinetic energies and then sorted into a histogram with 0.1 MeV step size. We assume a constant detector response for the conversion from TOF into the spectrum. Since we had to change the bias voltage of the PMT to a level beyond our calibration, we cannot convert the PMT response to a neutron flux. In addition to that, the neutron signal occurred during the decay of the scintillator due to the strong gamma flash. The instrument response vs. neutron flux in this operating mode is not known. Therefore, the spectrum is given in “signal-per-0.1-MeV” units, which will only allow for qualitative but not for quantitative comparisons to our calculations.

The resulting spectrum corresponds to neutrons between 2 and 7 MeV, with an error of ± 0.5 MeV due to uncertainties in the detector distance. The spectrum decays toward higher neutron energy. The irregular shape of the spectrum is partly due to the high-frequency noise mentioned above and partly due to the low neutron statistics (for $\sim 10^6$ neutrons emitted into 4π , about 10 neutrons per shot are hitting the detector). We also observe a single peak at about 1.3 MeV from the signal at ~ 200 ns that is above the noise level. It is at present not clear whether this is an artifact due to the noise; we have planned to investigate this in the future.

To aid in the interpretation of the neutron data, we modeled an expected neutron spectrum using the 1ω BN nanotube proton spectrum as an input, together with the cross sections for (p, n) and (α, n) reactions from Table 1. The neutron spectra were generated using a custom Monte Carlo code to generate an exponentially decaying population of 10^6 protons that resembled the measured spectrum, times a multiplicative factor to account for the actual number of protons. A second, Gaussian spectrum that is centered at



(a)



(b)

FIGURE 7: Continued.

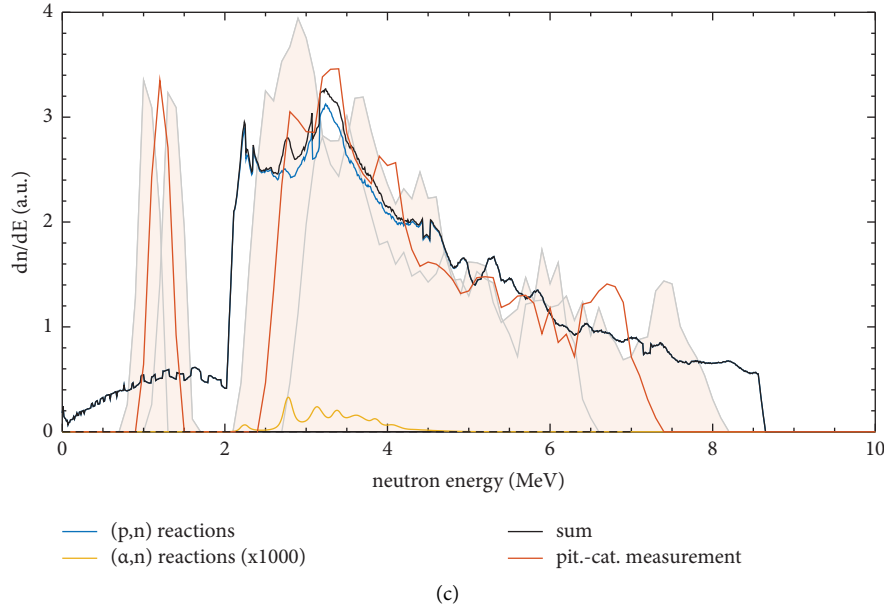


FIGURE 7: Calculated vs. measured neutron spectra. (a) The cross-sectional data for neutron-producing reactions in BN show that multiple reaction channels for (p, n) and (α, n) exist with relatively high cross sections. The grey and black curves are plots of the p and α distributions used to generate the artificial neutron spectra shown in (b). Note that the alpha-generated neutron spectrum was multiplied by a factor of 1000 for visualization purposes; otherwise, its contribution to the total spectrum would not be visible. The comparison between the calculated and measured spectra shown in (c) shows that it is plausible that the measured neutrons originate from (p, n) reactions, showing its diagnostic potential. An (α, n) contribution to the measurement would fall into the same energy range. A potential (α, n) contribution cannot be resolved with the current measurement sensitivity.

3 MeV with a FWHM of 1 MeV was used to simulate an assumed population of 10^6 alpha particles, again times a multiplicative factor to correct for the actual number. For each population, the energy-dependent probability of creating a neutron was calculated via interpolation of the cross-sectional data tables. The neutron energy was determined by the nuclear reaction kinematics for binary collisions where the neutron is generated in the forward direction. The resulting neutron population was then converted to a histogram to generate the spectrum. The total number of neutrons was weighted by the primary particle numbers to calculate the relative neutron yields from protons and alpha particles. Figure 7(a) shows plots of the initial particle distributions (grey and black lines), plus the cross sections of the neutron-producing reactions. The alpha particle yield was assumed to be dominated by the number of 1 MeV protons, indicated by the blue circle.

Figure 7(b) shows the calculated neutron spectrum and its relative contributions from protons and alpha particles. Note that the alpha spectrum had to be multiplied by 1000 to become visible. This plot shows that the expected neutron energies from both kinds of projectiles overlap in their energies, and that for beam-target interactions as assumed here the neutron yield from protons far outweighs the neutron yields from alphas. Due to the interplay between the threshold energy to trigger the reaction and its cross sections, the spectrum is dominated by the $^{14}\text{N}(p, n)^{14}\text{O}$ reaction for energies below 2 MeV. Above that, the neutron spectrum is dominated by $^{11}\text{B}(p, n)^{11}\text{C}$ reactions. The proton-neutron spectrum decays toward higher energies due to the exponential proton spectrum.

Since we assume a Gaussian alpha particle spectrum centered at 3 MeV, the resulting alpha-neutron spectrum is shifted to about 4 MeV due to the reaction kinematics. The alpha-neutron energies are roughly centered in-between the proton-neutron energies. Overall, the neutron spectrum is dominated by (p, n) reactions in our experiments.

Figure 7(c) qualitatively compares the calculated neutron spectrum to the measured nTOF spectrum. The measured energies and slope are fairly well reproduced; however, the measured spectrum appears to fall into a narrower energy range. This may be due to an insufficient background correction of the measured data for reasons mentioned above, as well as due to the low particle statistics that result in near single events at the scintillator.

4. Summary and Conclusions

The measurements and results discussed in this study demonstrate that BN nanotube targets are a significantly more efficient proton source than regular foils, potentially better than previously published nanostructured targets [7, 28]. This warrants further investigations into their use as efficient proton sources for applications.

The strongest proton beams were created by irradiating a BN nanotube target with a 1ω pulse resulting in a yield of 6×10^8 protons/sr/J/shot. Assuming a cone angle of $\pm 15^\circ$ [24–28], this results in 4×10^{10} protons/J/shot. When this proton beam was directed to a BN catcher target, it created nuclear activation with more than 10 kBq, as well as a measurable neutron signal. Our analysis showed that the

nuclear activation was mainly due to $^{11}\text{B}(p, n)^{11}\text{C}$ reactions, with small contributions from ^{13}N and ^{18}F . Using tabulated nuclear reaction cross-sectional values and the input proton spectrum measured without the catcher, we were able to reproduce the quantity of activated nuclei within a factor of two. Through these calculations, we infer a theoretically calculated alpha particle yield due to proton-boron beam-target interaction of $6 \times 10^6/\text{J}$. This is comparable to similar pitcher-catcher experiments published in [3], but without an additional heating laser.

Comparing our nuclear activation measurements with calculations of the expected yields due to the incoming proton spectrum, we show that the ^{13}N and ^{18}F nuclei created in our BN sample are most likely due to protons activating oxygen contamination inside the bulk material and less likely due to alpha particles creating secondary reactions. In fact, attributing all of the measured ^{13}N nuclei to being generated by alpha particles via $^{10}\text{B}(\alpha, n)^{13}\text{N}$, and ^{18}F nuclei via $^{14}\text{N}(\alpha, \gamma)^{18}\text{F}$ as suggested in [2] would, in our case, result in alpha yields that are not only inconsistent with each other but also within a factor of two of the measured primary proton yield, which appears too high given the expected low yields of beam-target fusion reactions. However, more careful examination shows that our calculated ^{11}C count due to proton reactions is higher than measured while the calculated ^{13}N count due to proton reactions is lower than measured, which could be explained by a higher alpha contribution than expected due to pure beam-target fusion. Future investigations with improved diagnostics and better-controlled catcher plates might reveal higher alpha yields than those calculated here.

Both the activation measurements and corresponding calculations show that it should be possible to design a catcher material composition that triggers selected multiple nuclear reactions that can be used to infer the primary particle energy distributions with sufficient accuracy. In a similar vein, we show that, while neutron spectroscopy in BN targets may not be used as a diagnostic tool for alpha particles when fast protons are present, the close resemblance of the measured and calculated data for protons demonstrates its high potential as a diagnostic for the proton distribution. Such nuclear diagnostics will become relevant for diagnosing the particle distributions inside integrated fusion devices, such as, for example, the emerging, laser-driven, and mixed-fuel microreactor concept [1].

Data Availability

The data used to support the findings of this study can be obtained from the corresponding author upon reasonable request.

Conflicts of Interest

MS, VS, CC, SvS, and GK are or were employed at Marvel Fusion GmbH.

Acknowledgments

The authors would like to thank Juliana Metzler and Marco Tosca for their help with CR39 analysis and Hartmut Ruhl

for fruitful discussions about laser-driven particle acceleration and proton-boron fusion. J. J. Rocca acknowledges the support of a DOD Vannevar Bush Faculty Fellowship, ONR award N000142012842. The experiments were performed at the ALEPH laser facility at Colorado State University supported by LaserNetUS under grant US DE-SC0019076 from the U.S. Department of Energy. This work was funded by Marvel Fusion GmbH.

References




- [1] H. Ruhl and G. Korn, "A non-thermal laser-driven mixed fuel nuclear fusion reactor concept," 2022, <https://arxiv.org/abs/2204.00269>.
- [2] C. Labaune, C. Baccou, V. Yahia, C. Neuville, and J. Rafelski, "Laser-initiated primary and secondary nuclear reactions in Boron-Nitride," *Scientific Reports*, vol. 6, no. 1, Article ID 21202, 2016.
- [3] C. Labaune, C. Baccou, S. Depierreux et al., "Fusion reactions initiated by laser-accelerated particle beams in a laser-produced plasma," *Nature Communications*, vol. 4, no. 1, p. 2506, 2013.
- [4] J. Bonvalet, P. Nicolai, D. Raffestin et al., "Energetic α -particle sources produced through proton-boron reactions by high-energy high-intensity laser beams," *Physical Review E - Statistical Physics, Plasmas, Fluids, and Related Interdisciplinary Topics*, vol. 103, no. 5, Article ID 053202, 2021.
- [5] L. Giuffrida, F. Belloni, D. Margarone et al., "High-current stream of energetic alpha particles from laser-driven proton-boron fusion," *Physical Review E - Statistical Physics, Plasmas, Fluids, and Related Interdisciplinary Topics*, vol. 101, no. 1, Article ID 013204, 2020.
- [6] D. Margarone, J. Bonvalet, L. Giuffrida et al., "In-target proton-boron nuclear fusion Using a PW-class laser," *Applied sciences*, vol. 12, no. 3, 2022.
- [7] D. Margarone, O. Klimo, I. J. Kim et al., "Laser-driven proton acceleration enhancement by nanostructured foils," *Physical Review Letters*, vol. 109, no. 23, Article ID 234801, 2012.
- [8] D. Margarone, A. Morace, J. Bonvalet et al., "Generation of α -particle beams With a multi-kJ, peta-watt class laser system," *Frontiers in Physics*, vol. 8, 2020.
- [9] A. Picciotto, D. Margarone, A. Velyhan et al., "Boron-proton nuclear-fusion enhancement Induced in boron-doped silicon Targets by low-contrast pulsed laser," *Physical Review X*, vol. 4, no. 3, 2014.
- [10] M. Tayyab, S. Bagchi, A. Moorti, and J. A. Chakera, "Experimental investigation on nuclear reactions using a laser-accelerated proton and deuteron beam," *Plasma Physics and Controlled Fusion*, vol. 61, no. 11, 2019.
- [11] C. Baccou, S. Depierreux, V. Yahia et al., "New scheme to produce aneutronic fusion reactions by laser-accelerated ions," *Laser and Particle Beams*, vol. 33, no. 1, pp. 117–122, 2015.
- [12] N. Soppera, M. Bossant, and E. Dupont, "JANIS 4: an improved version of the NEA java-based nuclear data information system," *Nuclear Data Sheets*, vol. 120, pp. 294–296, 2014.
- [13] Y. Wang, S. Wang, A. Rockwood et al., "085 PW laser operation at 33 Hz and high-contrast ultrahigh-intensity $\lambda = 400$ nm second-harmonic beamline," *Optics Letters*, vol. 42, no. 19, pp. 3828–3831, 2017.
- [14] A. Curtis, R. Hollinger, C. Calvi et al., "Ion acceleration and D-D fusion neutron generation in relativistically transparent

- deuterated nanowire arrays,” *Physical Review Research*, vol. 3, no. 4, Article ID 043181, 2021.
- [15] E. Brambrink, T. Schlegel, G. Malka et al., “Direct evidence of strongly inhomogeneous energy deposition in target heating with laser-produced ion beams,” *Physical Review*, vol. 75, no. 6, Article ID 065401, 2007.
- [16] D. C. Carroll, P. Brummitt, D. Neely et al., “A modified Thomson parabola spectrometer for high resolution multi-MeV ion measurements-application to laser-driven ion acceleration,” *Nuclear Instruments and Methods in Physics Research Section A*, vol. 620, no. 1, pp. 23–27, 2010.
- [17] T. Bonnet, M. Comet, D. Denis-Petit et al., “Response functions of imaging plates to photons, electrons and 4He particles,” *Review of Scientific Instruments*, vol. 84, no. 10, Article ID 103510, 2013.
- [18] C. Baccou, V. Yahia, S. Depierreux et al., “CR-39 track detector calibration for H, He, and C ions from 0.1-0.5 MeV up to 5 MeV for laser-induced nuclear fusion product identification,” *Review of Scientific Instruments*, vol. 86, no. 8, Article ID 083307, 2015.
- [19] A. Curtis, C. Calvi, J. Tinsley et al., “Micro-scale fusion in dense relativistic nanowire array plasmas,” *Nature Communications*, vol. 9, no. 1, p. 1077, 2018.
- [20] F. E. Cecil, S. S. Medley, E. B. Nieschmidt, and S. J. Zweben, “Nuclear reaction diagnostics of fast confined and escaping alpha particles,” *Review of Scientific Instruments*, vol. 57, no. 8, pp. 1777–1779, 1986.
- [21] S. Takács, F. Tarkanyi, A. Hermanne, and R. Paviotti de Corcuera, “Validation and upgrading of the recommended cross section data of charged particle reactions used for production of PET radioisotopes,” *Nuclear Instruments and Methods in Physics Research Section B*, vol. 211, no. 2, pp. 169–189, 2003.
- [22] E. Hess, S. Takacs, B. Scholten, F. Tarkanyi, H. H. Coenen, and S. M. Qaim, “Excitation function of the $^{18}\text{O}(p, n)^{18}\text{F}$ nuclear reaction from threshold up to 30 MeV,” *Radiochimica Acta*, vol. 89, no. 6, pp. 357–362, 2001.
- [23] T. Ceccotti, A. Levy, H. Popescu et al., “Proton acceleration with high-intensity ultrahigh-contrast laser pulses,” *Physical Review Letters*, vol. 99, no. 18, Article ID 185002, 2007.
- [24] F. Nurnberg, M. Schollmeier, E. Brambrink et al., “Radiochromic film imaging spectroscopy of laser-accelerated proton beams,” *Review of Scientific Instruments*, vol. 80, no. 3, Article ID 033301, 2009.
- [25] M. Schollmeier, M. Geissel, A. B. Sefkow, and K. A. Flippo, “Improved spectral data unfolding for radiochromic film imaging spectroscopy of laser-accelerated proton beams,” *Review of Scientific Instruments*, vol. 85, no. 4, Article ID 043305, 2014.
- [26] S. Steinke, J. Bin, J. Park et al., “Acceleration of high charge ion beams with achromatic divergence by petawatt laser pulses,” *Physical Review Accelerators and Beams*, vol. 23, no. 2, Article ID 021302, 2020.
- [27] M. Afshari, J. Hornung, A. Kleinschmidt, P. Neumayer, D. Bertini, and V. Bagnoud, “Proton acceleration via the TNSA mechanism using a smoothed laser focus,” *AIP Advances*, vol. 10, no. 3, Article ID 035023, 2020.
- [28] I. Prencipe, J. Metzkes-Ng, A. Pazzaglia et al., “Efficient laser-driven proton and bremsstrahlung generation from cluster-assembled foam targets,” *New Journal of Physics*, vol. 23, no. 9, Article ID 093015, 2021.
- [29] J. Fuchs, P. Antici, E. d’Humieres et al., “Laser-driven proton scaling laws and new paths towards energy increase,” *Nature Physics*, vol. 2, no. 1, pp. 48–54, 2005.
- [30] J. Schreiber, P. R. Bolton, and K. Parodi, “Invited Review Article: “Hands-on” laser-driven ion acceleration: a primer for laser-driven source development and potential applications,” *Review of Scientific Instruments*, vol. 87, no. 7, Article ID 071101, 2016.
- [31] J. F. Ziegler, J. P. Biersack, and M. D. Ziegler, “SRIM, the Stopping and Range of Ions in Matter,” *Nuclear Instruments and Methods in Physics Research Section B*, vol. 268, 2008.
- [32] W. M. Nevins and R. Swain, “The thermonuclear fusion rate coefficient for p-11B reactions,” *Nuclear Fusion*, vol. 40, no. 4, pp. 865–872, 2000.



Research Article

Alpha-Particle Generation from H-¹¹B Fusion Initiated by Laser-Accelerated Boron Ions

Defeng Kong ¹, Shirui Xu,¹ Yinren Shou,¹ Ying Gao,¹ Zhusong Mei,¹ Zhuo Pan,¹ Zhipeng Liu,¹ Zhengxuan Cao,¹ Yulan Liang,¹ Ziyang Peng,¹ Pengjie Wang,¹ Di Luo,^{2,3} Yang Li,^{2,3} Zhi Li,^{2,3} Huasheng Xie,^{2,3} Guoqiang Zhang,⁴ Wen Luo,⁵ Jiarui Zhao ¹, Shiyong Chen,¹ Yixing Geng,¹ Yanying Zhao,¹ Jianming Xue,¹ Xueqing Yan,^{1,6,7} and Wenjun Ma ^{1,6,7}

¹State Key Laboratory of Nuclear Physics and Technology, and Key Laboratory of HEDP of the Ministry of Education, CAPT, Peking University, Beijing 100871, China

²Hebei Key Laboratory of Compact Fusion, Langfang 065001, China

³ENN Science and Technology Development Co., Ltd., Langfang 065001, China

⁴Shanghai Institute of Applied Physics, Chinese Academy of Sciences, Shanghai 201800, China

⁵School of Nuclear Science and Technology, University of South China, Hengyang 421001, China

⁶Beijing Laser Acceleration Innovation Center, Huairou, Beijing 101400, China

⁷Institute of Guangdong Laser Plasma Technology, Baiyun, Guangzhou 510540, China

Correspondence should be addressed to Jiarui Zhao; jrzhao@pku.edu.cn and Wenjun Ma; wenjun.ma@pku.edu.cn

Received 11 April 2022; Accepted 28 June 2022; Published 26 September 2022

Academic Editor: Fabio Belloni

Copyright © 2022 Defeng Kong et al. This is an open access article distributed under the Creative Commons Attribution License, which permits unrestricted use, distribution, and reproduction in any medium, provided the original work is properly cited.

Here, we report the generation of MeV alpha-particles from H-¹¹B fusion initiated by laser-accelerated boron ions. Boron ions with maximum energy of 6 MeV and fluence of 10⁹/MeV/sr@5 MeV were generated from 60 nm-thick self-supporting boron nanofoils irradiated by 1 J femtosecond pulses at an intensity of 10¹⁹ W/cm². By bombarding secondary hydrogenous targets with the boron ions, 3 × 10⁵/sr alpha-particles from H-¹¹B fusion were registered, which is consistent with the theoretical yield calculated from the measured boron energy spectra. Our results demonstrated an alternative way toward ultrashort MeV alpha-particle sources employing compact femtosecond lasers. The ion acceleration and product measurement scheme are referential for the studies on the ion stopping power and cross section of the H-¹¹B reaction in solid or plasma.

1. Introduction

Nuclear fusion between proton (H) and boron (¹¹B), ${}^1_1\text{H} + {}^{11}_5\text{B} \rightarrow 3\alpha + 8.68 \text{ MeV}$, is a widely concerned reaction [1–7] due to its appealing potential in fusion energy harness [8–10]. Unlike the D-D reaction and the D-⁶Li/D-T cycle [11], the H-¹¹B reaction releases alpha-particles instead of neutrons, which offers clean energy without neutron radiation hazards. More importantly, ¹¹B is stable and abundant on Earth, which sheds off the fuel problem in D-T fusion. With the rapid development of high-power lasers, laser fusion based on the H-¹¹B reaction attracts more and more

attention. However, self-sustained H-¹¹B fusion under equilibrium conditions is highly challenging due to the insurmountable radiation loss problem at elevated temperatures. Many explorations on the H-¹¹B reaction have been ongoing, such as driving the fusion out of thermal equilibrium by using ultrashort lasers [12–14] to reduce the radiation loss or revisiting the fusion reactivity [15–17] in the plasma environment.

In addition to the potential for clean fusion energy, the alpha-particle generation from the H-¹¹B reaction could be a valuable source for medical and industrial applications [18–20]. The cross section for the H-¹¹B reaction is very

large, e.g., 1.2 barn [21] at 620 keV (center-of-mass energy), and one reaction can release 1 MeV and two of 4 MeV alpha-particles [15, 22] in a simplified view. With high-energy reactants, the yield and the kinetic energies of the alpha-particles could be prominent, depending on the reaction channels. The alpha-particle generation from laser-driven H-¹¹B reaction was firstly reported in 2005 with a yield of 10³/sr/shot [23] using a boron-rich polyethylene target irradiated by a picosecond laser. In subsequent experiments, the yields have been continuously increased to 10⁶ α/sr/shot and 10⁹ α/sr/shot [12, 24] in the so-called “pitcher-catcher” scheme, where energetic protons are produced from a μm-thick target through target normal sheath acceleration (TNSA) and bombard a secondary boron target.

Besides the boron-rich polyethylene targets, “sandwich” targets (SiH/B/Si) and thick boron-nitride (BN) targets were irradiated with kilojoule-scale sub-ns lasers, producing 10⁹ and 10¹⁰ /sr/shot alpha-particles, respectively [25–27]. It was found that, in spite of the difference in the driving lasers, the observed yield of the alpha-particles had a similar scaling law of about 10⁵–10⁶ α/sr/.

Up to now, all the reported alpha-particle generation was driven by low-repetition rate, high-energy, long-pulse lasers. Operating one-shot typically takes an hour or more, which severely limits potential applications. Routes that employ femtosecond lasers as the drivers are noteworthy to study, which can operate at a much higher repetition rate. Besides the high-repetition rate, another advantage of femtosecond lasers is that their intensities are much higher than long-pulse lasers for the given pulse energy. The 100s TW or PW femtosecond lasers can deliver intensities of 10¹⁸–10²² W/cm² on the targets. Laser-ion acceleration at such high intensity can produce copious MeV ions from nonequilibrium laser-plasma interaction, matching the cross section’s apex nicely.

Moreover, all the reported studies of laser-ion-initiated H-¹¹B fusion utilize protons to bombard boron targets [12, 23–28]. If the opposite scheme, i.e., initiating H-¹¹B fusion with energetic boron ions, is adopted, the generated alpha-particles would be more directional due to the higher mass of boron atoms [29]. The yield may also be enhanced as studies show that the energy conversion efficiencies from laser energy to heavy ions are higher than that of protons in favorable acceleration regimes [30, 31]. Furthermore, this scheme can be employed to investigate the stopping power of boron ions inside solid or plasma targets, which is very important for future H-¹¹B nuclear reactors [29, 32, 33]. However, the alpha-particle generation by bombarding hydrogenous solid or plasma targets with laser-accelerated boron ions has not been realized yet. The main reason is the shortage of energetic laser-accelerated boron ions. In the widely adopted TNSA regime, the targets are μm-thick solid foils [34]. Ions with the highest charge-to-mass ratio, i.e., protons, favorably gain energy from the sheath field. The acceleration of heavy ions is drastically suppressed. With the development of laser and target-fabrication technology, ultrathin targets with nm-scale thickness were allowed to be used in the experiments, indicating the prominent efficiency for heavy ion acceleration. The variation of the laser and

target parameters leads to different regimes such as radiation pressure acceleration (RPA) [35, 36], relativistic induced transparency (RIT) [37–39], breakout afterburner acceleration (BOA) [40, 41], or hybrid acceleration [31, 42]. So far, energetic heavy ions such as C⁶⁺, Al¹³⁺, and Au⁵¹⁺ have been produced with maximum energy up to 1.2 GeV [31, 39, 43].

In this work, we report the first H-¹¹B fusion and alpha-particle generation results by bombarding hydrogenous targets with laser-accelerated boron ions. The MeV-level boron ions were accelerated from 60 nm-thick boron targets under the irradiation of high-contrast femtosecond laser pulses. The alpha-particles from H-¹¹B fusion were measured by CR39 ion track detectors. The fusion reactions happening inside the hydrogenous targets are discussed considering the ion-nuclear collision, and the theoretical yield is calculated based on the measured ¹¹B spectra, which is consistent with our experimental results.

2. Experimental Setup

2.1. Laser Parameters. The experiment was performed on a 200 TW CLAPA Ti: sapphire laser system at Peking University [44]. The experimental layout is shown in Figure 1(a). An s-polarized laser pulse was normally focused on the 60 nm-thick boron nanofoils with the spot size of 8.4 × 9.2 μm (full width at half maximum) by an f/3 off-axis-parabolic mirror. The central wavelength and duration of the laser pulse were 800 nm and 30 fs, respectively. A cross-polarized wave system and a single plasma mirror system were employed to improve the laser contrast ratio up to 10⁹@ 40 ps and prevent the damage of targets from prepulses. The on-target laser energy was 1 J, corresponding to a peak intensity of 1 × 10¹⁹ W/cm². A 5 μm-thick plastic (C₁₀H₈O₄) foil with the proton density of 4 × 10²²/cm³ was located 0.5 mm behind the targets at the laser axis as the “catcher” for H-¹¹B reactions.

2.2. Boron Nanofoil Target. The boron nanofoils are prepared by the RF-magnetron sputtering deposition using the natural boron. The atomic ratio of ¹⁰B and ¹¹B is 1 : 4. The details of the target-fabrication method will be reported elsewhere. To optimize the ion acceleration, we used 60 nm-thick self-supporting B foils, the thinnest that could be fabricated at that time, as the targets in the experimental campaign. Figure 1(b) depicts the top-view morphology of a 60 nm-thick self-supporting boron nanofoils on a target hole with a diameter of 0.5 mm. The chemical composition of the targets is characterized by an energy dispersive spectrometer in a scanning electron microscope (Figure 1(c)). Due to the oxidation of the targets in the air, the atomic ratio of B : O is 1.1 : 1. Besides, the Si atoms are from the silicon wafer as a target substrate during the fabrication. The C atoms come from the contaminated layer of nanofoils. The density of the foils, measured by the weighting method, is about 0.95 g/cm³. If the target is fully ionized, the electron density would be $n = 160n_c$ and here the critical density would be $n_c = m_e \omega^2 / (4\pi e^2) = 1.7 \times 10^{21} \text{ cm}^{-3}$.

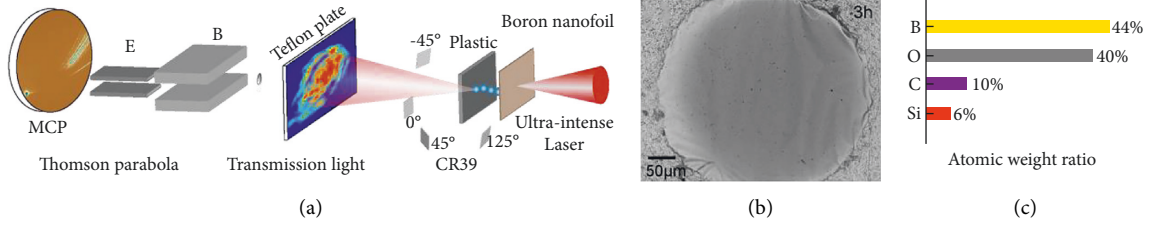


FIGURE 1: (a) Experimental setup. The laser pulses irradiate a boron nanofoil with a normal incidence. A $5\ \mu\text{m}$ -thick plastic foil was located $0.5\ \text{mm}$ behind the boron nanofoil to initiate the $\text{H-}^{11}\text{B}$ fusion. The CR39, TPS, and Teflon plate were placed around the target to measure the alpha-particles and boron ions and collect the transmitted light, respectively, (b) the top-view morphology of self-supporting nanofoils three hours after preparation, and (c) the atomic weight ratio of the boron nanofoil.

2.3. Diagnostics. The energy spectra of the ions were measured by a Thomson parabola spectrometer (TPS) with a microchannel plate (MCP) equipped with a phosphor screen positioned $0.78\ \text{m}$ away from the targets in the normal direction of the targets. The collimated ions with different energy and charge-to-mass ratio (CMR) were deflected by the electromagnetic fields and hit on the MCP with parabola traces. Ion signal multiplied by the MCP was converted to optical signals captured by a 16-bit EMCCD camera. For a good resolution of the traces, a tiny collimating aperture was employed. The corresponding acceptance angle is only $4.2 \times 10^{-8}\ \text{sr}$, which allows the recognition of single-ion events on the MCP [43, 45]. A Teflon plate with a through-hole was placed behind the target to collect the transmitted light, which can be used as a diagnostic for the laser-plasma interaction.

The alpha-particles generated from $\text{H-}^{11}\text{B}$ fusion were detected by CR39 ion track detectors at angles of -45° , 0° , 45° , and 125° . Here, 0° is the laser-axis direction. The distance between CR39 and the targets was $130\ \text{mm}$. The CR39 sheets were wrapped in $10\ \mu\text{m}$ -thick aluminium foils to block low-energy ions. According to the Monte Carlo simulation results from SRIM [46], the minimum energy required to penetrate $10\ \mu\text{m}$ aluminium for proton, alpha-particle, boron, carbon, and oxygen ions is $0.8\ \text{MeV}$, $2.9\ \text{MeV}$, $9.5\ \text{MeV}$, $12\ \text{MeV}$, and $16.5\ \text{MeV}$, respectively. In our experiments, all the carbon and oxygen ions were blocked by the Al foils (see below), and only protons and alpha-particles with energy above $0.8\ \text{MeV}$ and $2.9\ \text{MeV}$ could go through and result in visible traces in CR39 after etching.

3. Result

3.1. Energy Spectra of Borons and Other Ions. The absolute energy spectra of boron ions can be obtained from our TPS. Figure 2(a) shows a raw image recorded by the TPS after the shooting (without the secondary plastic foil). More than ten spectral lines from boron, carbon, oxygen ions, and protons can be identified. The parabolic traces of ^{11}B ions are marked with different lines. The boron ions with high charge states ($^{11}\text{B}^{3+}$, $^{11}\text{B}^{4+}$, $^{11}\text{B}^{5+}$) can be clearly identified. Different from protons and carbon ions, the traces of boron ions are composed of cluster signals with similar shapes and clear boundaries. Due to the small acceptance angle of the TPS, the boron ions are sparsely distributed on the parabolic

traces, and a distinct cluster signal is the response of a single boron ion hitting in MCP, indicating a “single-ion” event. By summing up the counts for distinct clusters as the function of ion energy, we can obtain the response of a single boron ion [43]. Based on the single-ion response data, the absolute energy spectra of $^{11}\text{B}^{5+}$, $^{11}\text{B}^{4+}$, and $^{11}\text{B}^{3+}$ ions have been derived in Figure 2(b). The vertical error bars come from deviations of the single-ion response, and horizontal error bars reflect the width of the energy bins, which was adopted to $0.2\ \text{MeV}$ to obtain smooth spectra curves. We can find that the maximum energy of $^{11}\text{B}^{3+}$, $^{11}\text{B}^{4+}$, and $^{11}\text{B}^{5+}$ is $2.7\ \text{MeV}$, $4.2\ \text{MeV}$, and $5.8\ \text{MeV}$, respectively. The corresponding ion temperature is $0.25\ \text{MeV}$, $0.25\ \text{MeV}$, and $0.47\ \text{MeV}$, respectively. The typical fluence is 10^8 – $10^{10}/\text{MeV}/\text{sr}$, depending on the energy. For instance, the fluence of $^{11}\text{B}^{5+}$ is $10^9/\text{MeV}/\text{sr}$ at $5\ \text{MeV}$. The spectra of proton, carbon, and oxygen ions from this shot are given in Figure 2(c).

3.2. Alpha-Particle Measurement. The CR39 sheets used for alpha-particle measurement were etched in $6\ \text{mol/L}$ NaOH solution at 98°C for 2 hours to reveal the ion tracks. Figure 3(a) displays the CR39 images with a solid angle of $3.3 \times 10^{-5}\ \text{sr}$ at the angle of 0° and 125° after three shots in a row. A control CR39 sheet that was not put inside the chamber was also etched with the same procedure, whose surface morphology is shown in Figure 3(a) as well.

According to Figures 2(b) and 2(c), the maximum energy of laser-accelerated boron, carbon, and oxygen ions is $6\ \text{MeV}$, $7\ \text{MeV}$, and $8\ \text{MeV}$, respectively. Therefore, those ions were completely blocked by the Al foils. The tracks of protons and alpha-particles can be easily distinguished from each other based on their sizes. We referred to the calibration of protons and alpha-particles from Zhang et al.’s works under the same etch condition [47], shown as the lines in Figure 3(b). Therefore, the dense grey dots with diameters of 4 – $6\ \mu\text{m}$ represent the protons, while the alpha-particles are larger black pits with diameters of 20 – $30\ \mu\text{m}$, as shown in Figure 3(a). According to the proton’s spectrum from TPS and considering their energy loss in the plastic and Al foil, the proton tracks in the CR39s can be estimated as $9 \times 10^9/\text{sr}$ at the 0° . So, about 10^5 protons can be observed in the CR39 image within a solid angle of $3.3 \times 10^{-5}\ \text{sr}$, consistent with the high number density of grey dots. We can find 31 alpha-particle tracks at the 0° direction and only 7 at 125° . The

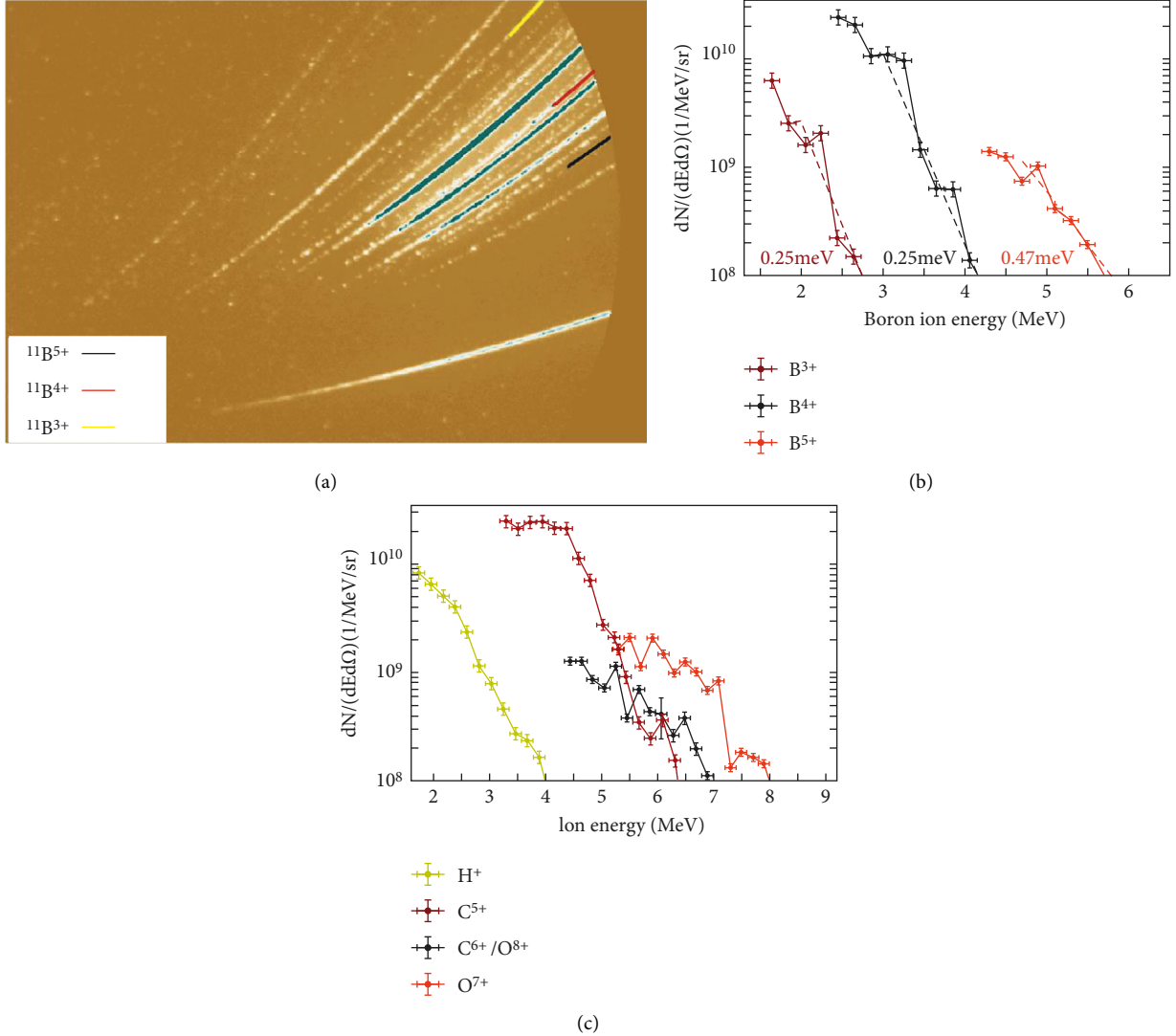


FIGURE 2: (a) Raw TPS data from a 60 nm-thick boron nanofoil. The parabolic traces of $^{11}\text{B}^{3+}$, $^{11}\text{B}^{4+}$, and $^{11}\text{B}^{5+}$ ions have been marked with different lines, (b) ion spectra of $^{11}\text{B}^{3+}$, $^{11}\text{B}^{4+}$, and $^{11}\text{B}^{5+}$, and (c) ion spectra of proton, carbon, and oxygen ions.

energy of the alpha-particles can be roughly estimated from the size of the tracks. The brown circles in Figure 3(b) show some representative alpha-particles from 0° direction. The energy range of alpha-particles is 3–5 MeV, which is consistent with the kinetic energy obtained from the fusion reactions. By counting the number of the alpha-particles, we can get the averaged angular distribution of alpha-particle flux per shot as can be seen in Figure 3(c). Due to the off-line measurement of CR39 and the limited beamtime, we did not perform more shots and, unfortunately, cannot give the shot-to-shot fluctuations. Generally speaking, the angular distribution shows a directional feature in the forward direction due to the momentum of the boron ions. The peak yield is $3 \pm 0.2 \times 10^5/\text{sr}/\text{J}$ and the experimental uncertainty comes from the statistical error of tracks on CR39. It should be noted that the given values in Figure 3(c) are conservative as only alpha-particles with energies above 2.9 MeV can be detected after the shielding of the Al foils.

4. Discussion

We can theoretically calculate the yield of the alpha-particles from the measured boron spectra and compare it with that from the CR39 measurement. The number of boron-induced fusion reactions N_f can be estimated using the differential equation describing the ion-nuclear collisional process in the target nucleus [48] with a thickness of D represented as

$$dN_f = \int n\sigma(E)v_b(x)dt dN_b = n \int_0^D \sigma(E)dx \frac{dN_b}{dE^*} dE^*, \quad (1)$$

where $n = 4 \times 10^{22}/\text{cm}^3$ is the proton density of the target nucleus, $\sigma(E)$ is the nuclear cross section, and v_b, N_b are the velocity and number of incident ions, respectively. dN_f is the number of reactions driven by the boron ions impinging on the target with kinetic energy between E^* and $E^* + dE^*$. dN_b/dE^* represents the energy spectrum of the incident boron ions, as reported in Figure 2(b). The thickness D of

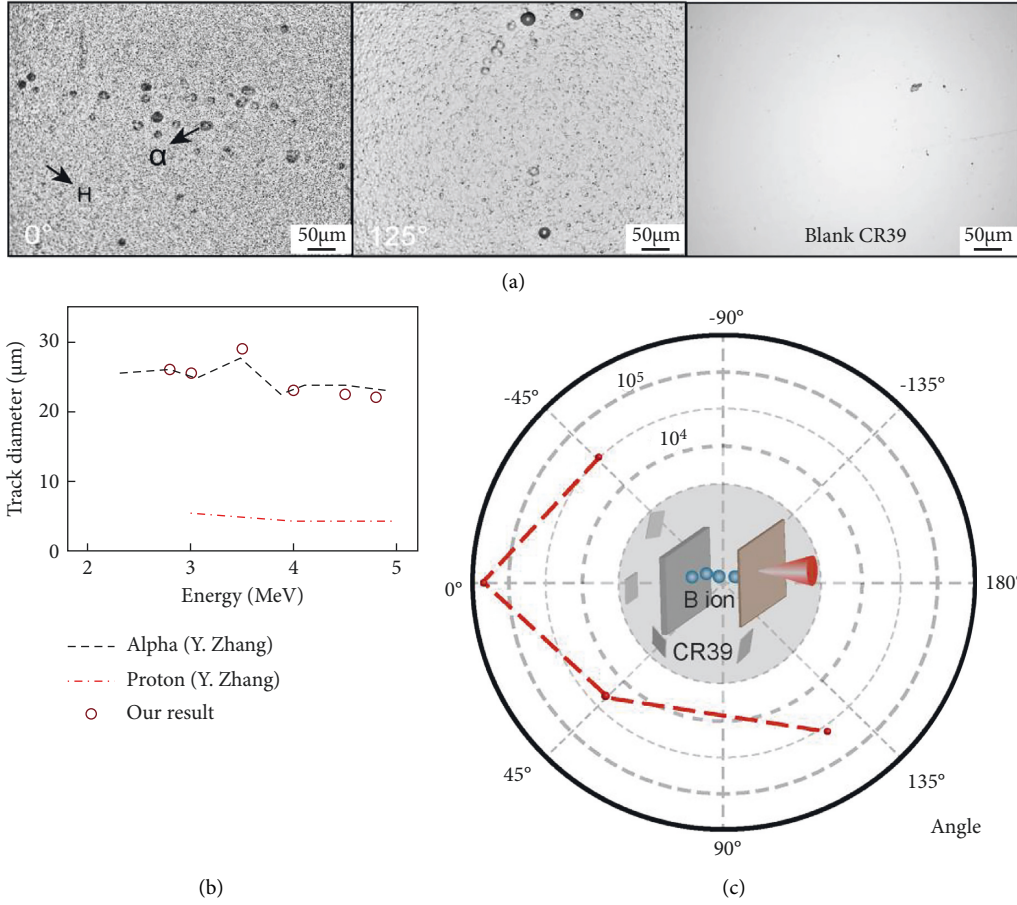


FIGURE 3: Alpha-particle generation from H-¹¹B fusion measured by CR39. (a) Raw images of CR39 sheets, (b) calibrated track diameters versus the energy of protons and alpha-particles [47] and representative alpha-particles of our result, and (c) the angular dependence of alpha-particle flux. The inset shows the experimental layout of the pitcher-catcher scheme.

5 μm is close to the projected range $R_{E=5.8\text{MeV}} = 7.8\mu\text{m}$ for boron ions with the maximum energy of 5.8 MeV. Although some high-energy boron ions can pass through the second target, the number is small, an order of magnitude lower than that of the 4 MeV-boron ions as shown in Figure 2(b). Moreover, their kinetic energy has degraded to below 2 MeV, corresponding to a pretty low fusion reactivity. Therefore, we believe that most boron ions are exhausted and stopped in the target nucleus for simplicity. Equation (1) can be further expressed in terms of the energy E of boron ions,

$$dN_f = n \int_0^{E^*} \frac{\sigma(E)}{dE/dx} dE \frac{dN_b}{dE^*} dE^* = n \int_0^{E^*} \frac{\sigma(E)}{S(E)} dE \frac{dN_b}{dE^*} dE^*, \quad (2)$$

where $S(E) = -dE/dx$ represents the stopping power of the target nucleus against incident boron ions. By integrating the energy E , the number of all alpha-particles generated from H-¹¹B fusion can be expressed as

$$N_\alpha = 3N_f = 3n \int_0^{E_0} \left(\int_0^{E^*} \frac{\sigma(E)}{S(E)} dE \right) \frac{dN_b}{dE^*} dE^*. \quad (3)$$

Figure 4 depicts the curves of $\sigma(E)$, $S(E)$, and dN_b/dE^* as the function of boron-ion energy. The $S(E)$ in plastic

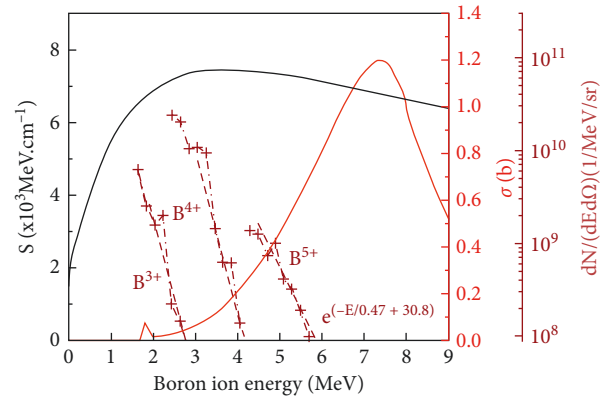


FIGURE 4: Blackline: the stopping power $S(E)$ of boron ions. Redline: the cross section $\sigma(E)$ of H-¹¹B fusion as a function of boron-ion energy in the lab. Brown lines: the energy spectra dN_b/dE^* of $^{11}\text{B}^{5+}$, $^{11}\text{B}^{4+}$, and $^{11}\text{B}^{3+}$. The dashed lines are the exponential fitting of energy spectra.

($\text{C}_{10}\text{H}_8\text{O}_4$) is simulated with SRIM [46], including the electronic and nuclear energy loss based on the cold target. The $\sigma(E)$ of H-¹¹B fusion is expressed according to Nevins and Swain's results [21, 49] and polynomially fitted as given

TABLE 1: Curve fitting functions of $\sigma(E)$, $S(E)$, and dN_b/dE^* and the number of alpha-particles N_α .

Ions	$^{11}\text{B}^{5+}$	$^{11}\text{B}^{4+}$	$^{11}\text{B}^{3+}$	Total
dN_b/dE^*	$e^{(-E/0.47+30.8)}$	$e^{(-E/0.25+34.3)}$	$e^{(-E/0.25+29.2)}$	—
$\sigma(E)$	$0.0004934 E^5 - 0.0132 E^4 + 0.1155 E^3 - 0.3694 E^2 + 0.4366 E - 0.115$	—	—	—
$S(E)$	$0.0006076 E^5 - 0.02117 E^4 + 0.2801 E^3 - 1.767 E^2 + 5.194 E + 1.748$	—	—	—
N_α	1.04×10^5	5.58×10^4	3.78×10^2	1.6×10^5
Ratio	64.9%	34.8%	0.3%	100%

[†]The units of the parameters match the axes in Figure 4.

in Table 1. The dN_b/dE^* of $^{11}\text{B}^{5+}$, $^{11}\text{B}^{4+}$, and $^{11}\text{B}^{3+}$ are also exponentially fitted in Table 1 according to Figure 2(b). The low-energy boron ions that were not measured by the TPS are also included by extrapolation down to 1 MeV. Table 1 gives the theoretical yield of alpha-particle from $^{11}\text{B}^{5+}$, $^{11}\text{B}^{4+}$, and $^{11}\text{B}^{3+}$ ions. One can find that the contribution from $^{11}\text{B}^{5+}$ and $^{11}\text{B}^{4+}$ is 64.9% and 34.8%, respectively. The energy of contribution from $^{11}\text{B}^{4+}$ cannot be ignored even though their energy is lower than that of $^{11}\text{B}^{5+}$. The total yield of alpha-particles is $N_\alpha \approx 1.6 \times 10^5/\text{sr}$, which matches the experimental measurement from CR39 very well. Besides the $^{11}\text{B}(p, \alpha)2\alpha$, other channels such as $^{12}\text{C}(p, \alpha)$ and $^{16}\text{O}(p, \alpha)$ can also contribute to the alpha-particle generation. However, the cross section of these reactions is two to three orders of magnitude lower at the relevant energy [50]. Based on the measured energy spectra, the estimated total alpha-particle yield from the accelerated C, O, and H is about $10^3/\text{sr}$, two orders of magnitude lower than the observation.

The theoretical and measured alpha-particle yield of $10^5\alpha/\text{sr}/\text{shot}$ with 1 J femtosecond laser pulses reaches a similar level to the case of proton-induced laser-driven fusion [12, 24, 25]. It should be noted that the reaction condition is still far from the apex of the cross section at 7.4 MeV ($\sigma = 1.2$ barn) (see Figure 4). Further enhancement of the energy of B ions would lead to a higher yield and better collimation of the alpha-particles. Our simulation shows that the yield can be increased from 1.04×10^5 to $1.89 \times 10^6\alpha/\text{sr}/\text{shot}$ if the maximum $^{11}\text{B}^{5+}$ energy and the temperature can be enhanced to 13 MeV and 1.3 MeV, respectively (total $^{11}\text{B}^{5+}$ ion number keeps the same), which is very promising at higher laser intensities. Alternatively, further optimizing the thickness of the targets would also lead to higher ion energy and more H- ^{11}B reactions. Our 60 nm-thick B targets are slightly thicker than the optimum thickness of 10 nm in the RPA regime, according to $l \sim \lambda a_0 n_c / n_e$. Here, $a_0 = 2.2$ is the normalized laser field. In these targets, TNSA probably is the primary acceleration mechanism. Further reducing the thicknesses of the targets would enable us to utilize more favorable acceleration regimes such as RPA or RIT.

5. Conclusion

In summary, we report the generation of $3 \pm 0.2 \times 10^5/\text{sr}/\text{J}$ alpha-particles initiated by boron ions driven by a compact femtosecond laser for the first time. The yield is in good agreement with the theoretical calculation based on the measured ^{11}B spectra, the stopping power of the boron ions in solid targets, and the reported cross section of H- ^{11}B fusion. Our results demonstrate an alternative way toward

ultrashort MeV alpha-particle sources with compact femtosecond lasers. The ion acceleration and product measurement scheme can provide a referential method for future studies on the stopping power of boron ions and the corresponding nuclear cross section of H- ^{11}B fusion in plasma by heating the ‘‘catcher’’ target into plasma. With higher laser intensities or thinner nanofoils in the future, the energies and the number of boron ions would further increase. The resulting higher-yield and directional alpha-particles at high-repetition rate could be promising for medical studies and industrial applications.

Data Availability

The data used to support the findings of this study are available from the corresponding author upon request.

Conflicts of Interest

The authors declare that they have no conflicts of interest.

Acknowledgments

This work was supported by the following projects: NSFC Innovation Group Project (grant number 11921006) and National Grand Instrument Project (grant number 2019YFF01014402).

References

- [1] D. C. Moreau, ‘‘Potentiality of the proton-boron fuel for controlled thermonuclear fusion,’’ *Nuclear Fusion*, vol. 17, no. 1, pp. 13–20, 1977.
- [2] J. M. Martínez-Val, S. Eliezer, M. Piera, and G. Velarde, ‘‘Fusion burning waves in proton-boron-11 plasmas,’’ *Physics Letters A*, vol. 216, no. 1–5, pp. 142–152, 1996.
- [3] H. Hora, G. H. Miley, M. Ghoranneviss, B. Malekynia, and N. Azizi, ‘‘Laser-optical path to nuclear energy without radioactivity: fusion of hydrogen-boron by nonlinear force driven plasma blocks,’’ *Optics Communications*, vol. 282, no. 20, pp. 4124–4126, 2009.
- [4] S. Eliezer and J. M. Martínez-Val, ‘‘Proton-boron-11 fusion reactions induced by heat-detonation burning waves,’’ *Laser and Particle Beams*, vol. 16, no. 4, pp. 581–598, 2009.
- [5] I. Last, S. Ron, and J. Jortner, ‘‘Aneutronic H+B11 nuclear fusion driven by Coulomb explosion of hydrogen nanodroplets,’’ *Physical Review A*, vol. 83, no. 4, 2011.
- [6] P. Lalouis, H. Hora, and S. Moustazis, ‘‘Optimized boron fusion with magnetic trapping by laser driven plasma block initiation at nonlinear forced driven ultrahigh acceleration,’’ *Laser and Particle Beams*, vol. 32, no. 3, pp. 409–411, 2014.

- [7] H. Hora, G. Korn, L. Giuffrida et al., G. H. Miley, S. Moustazis, and G. Mourou, Fusion energy using avalanche increased boron reactions for block-ignition by ultrahigh power picosecond laser pulses-ERRATUM,” *Laser and Particle Beams*, vol. 33, no. 4, p. 773, 2015.
- [8] N. Rostoker, M. W. Binderbauer, and H. J. Monkhorst, “Colliding beam fusion reactor,” *Science*, vol. 278, no. 5342, pp. 1419–1422, 1997.
- [9] N. Rostoker, M. W. Binderbauer, and H. J. Monkhorst, “Colliding beam fusion reactor,” in *Proceedings of the 12th International Conference on High-Power Particle Beams. BEAMS’98. Proceedings (Cat.No. 98EX103)*, pp. 195–202, Haifa, Israel, 1998.
- [10] H. Hora, G. H. Miley, M. Ghoranneviss, B. Malekynia, N. Azizic, and X.-T. He, “Fusion energy without radioactivity: laser ignition of solid hydrogen-boron (11) fuel,” *Energy & Environmental Science*, vol. 3, no. 4, pp. 478–485, 2010.
- [11] O. Hurricane, D. A. Callahan, D. T. Casey et al., J. D. Salmonson, P. T. Springer, and R. Tommasini, Fuel gain exceeding unity in an inertially confined fusion implosion,” *Nature*, vol. 506, no. 7488, pp. 343–348, 2014.
- [12] C. Labaune and C. Baccou, S. Depierreux, C. Goyon, G. Loisel, V. Yahia, and J. Rafelski, Fusion reactions initiated by laser-accelerated particle beams in a laser-produced plasma,” *Nature Communications*, vol. 4, no. 1, p. 2506, 2013.
- [13] C. Baccou, S. Depierreux, V. Yahia et al., “New scheme to produce aneutronic fusion reactions by laser-accelerated ions,” *Laser and Particle Beams*, vol. 33, no. 1, pp. 117–122, 2015.
- [14] H. Hora, S. Eliezer, G. H. Miley, J. Wang, Y. Xu, and N. Nissim, “Extreme laser pulses for non-thermal fusion ignition of hydrogen-boron for clean and low-cost energy,” *Laser and Particle Beams*, vol. 36, no. 3, pp. 335–340, 2018.
- [15] S. Stave, M. W. Ahmed, R. H. France et al., “Understanding the $^{11}\text{B}(p, \alpha)\alpha$ reaction at the 0.675 MeV resonance,” *Physics Letters B*, vol. 696, no. 1-2, pp. 26–29, 2011.
- [16] M. H. Sikora and H. R. Weller, “A new evaluation of the $^{11}\text{B}(p, \alpha)\alpha$ reaction rates,” *Journal of Fusion Energy*, vol. 35, no. 3, pp. 538–543, 2016.
- [17] S. V. Putvinski, D. D. Ryutov, and P. N. Yushmanov, “Fusion reactivity of the pB^{11} plasma revisited,” *Nuclear Fusion*, vol. 59, no. 7, 2019.
- [18] D.-K. Yoon, J.-Y. Jung, and T. S. Suh, “Application of proton boron fusion reaction to radiation therapy: a Monte Carlo simulation study,” *Applied Physics Letters*, vol. 105, no. 22, 2014.
- [19] L. Giuffrida, D. Margarone, G. A. P. Cirrone, A. Picciotto, G. Cuttone, and G. Korn, “Prompt gamma ray diagnostics and enhanced hadron-therapy using neutron-free nuclear reactions,” *AIP Advances*, vol. 6, no. 10, 2016.
- [20] G. A. P. Cirrone, L. Manti, D. Margarone et al., “First experimental proof of Proton Boron Capture Therapy (PBCT) to enhance protontherapy effectiveness,” *Scientific Reports*, vol. 8, no. 1, p. 1141, 2018.
- [21] W. M. Nevins and R. Swain, “The thermonuclear fusion rate coefficient for $\text{p-}^{11}\text{B}$ reactions,” *Nuclear Fusion*, vol. 40, no. 4, pp. 865–872, 2000.
- [22] C. Labaune, C. Baccou, V. Yahia, C. Neuville, and J. Rafelski, “Laser-initiated primary and secondary nuclear reactions in Boron-Nitride,” *Scientific Reports*, vol. 6, no. 1, Article ID 21202, 2016.
- [23] V. S. Belyaev, A. P. Matafonov, V. I. Vinogradov et al., “Observation of neutronless fusion reactions in picosecond laser plasmas,” *Physical Review E: Statistical, Nonlinear, and Soft Matter Physics*, vol. 72, Article ID 026406, 2005.
- [24] J. Bonvalet, P. Nicolai, D. Raffestin et al., “Energetic α -particle sources produced through proton-boron reactions by high-energy high-intensity laser beams,” *Physical Review*, vol. 103, no. 5-1, Article ID 053202, 2021.
- [25] A. Picciotto, D. Margarone, A. Velyhan et al., “Boron-proton nuclear-fusion enhancement induced in boron-doped silicon targets by low-contrast pulsed laser,” *Physical Review X*, vol. 4, no. 3, 2014.
- [26] D. Margarone, A. Picciotto, A. Velyhan et al., “Advanced scheme for high-yield laser driven nuclear reactions,” *Plasma Physics and Controlled Fusion*, vol. 57, no. 1, 2015.
- [27] L. Giuffrida, F. Belloni, D. Margarone et al., “High-current stream of energetic alpha particles from laser-driven proton-boron fusion,” *Physical Review E-Statistical Physics, Plasmas, Fluids, and Related Interdisciplinary Topics*, vol. 101, no. 1-1, Article ID 013204, 2020.
- [28] S. Kimura, A. Anzalone, and A. Bonasera, “Comment on “Observation of neutronless fusion reactions in picosecond laser plasmas,”” *Physical Review E-Statistical, Nonlinear and Soft Matter Physics*, vol. 79, no. 3 Pt 2, Article ID 038401, 2009.
- [29] A. F. Lifschitz, R. Farengo, and N. R. Arista, “Ionization, stopping, and thermalization of hydrogen and boron beams injected in fusion plasmas,” *Physics of Plasmas*, vol. 7, no. 7, pp. 3036–3041, 2000.
- [30] B. M. Hegelich, D. Jung, B. J. Albright et al., “Experimental demonstration of particle energy, conversion efficiency and spectral shape required for ion-based fast ignition,” *Nuclear Fusion*, vol. 51, no. 8, 2011.
- [31] W. J. Ma, I. J. Kim, J. Q. Yu et al., “Laser acceleration of highly energetic carbon ions using a double-layer target composed of slightly underdense plasma and ultrathin foil,” *Physical Review Letters*, vol. 122, no. 1, Article ID 014803, 2019.
- [32] R. L. Singleton, “Charged particle stopping power effects on ignition: some results from an exact calculation,” *Physics of Plasmas*, vol. 15, no. 5, Article ID 056302, 2008.
- [33] C. Deutsch and G. Maynard, “Ion stopping in dense plasmas: a basic physics approach,” *Matter and Radiation at Extremes*, vol. 1, no. 6, pp. 277–307, 2016.
- [34] S. C. Wilks, A. B. Langdon, T. E. Cowan et al., “Energetic proton generation in ultra-intense laser-solid interactions,” *Physics of Plasmas*, vol. 8, no. 2, pp. 542–549, 2001.
- [35] T. Esirkepov, M. Borghesi, S. V. Bulanov, G. Mourou, and T. Tajima, “Highly efficient relativistic-ion generation in the laser-piston regime,” *Physical Review Letters*, vol. 92, no. 17, Article ID 175003, 2004.
- [36] X. Q. Yan, C. Lin, Z. M. Sheng et al., “Generating high-current monoenergetic proton beams by a circularly polarized laser pulse in the phase-stable acceleration regime,” *Physical Review Letters*, vol. 100, no. 13, Article ID 135003, 2008.
- [37] A. Henig, D. Kiefer, K. Markey et al., “Enhanced laser-driven ion acceleration in the relativistic transparency regime,” *Physical Review Letters*, vol. 103, no. 4, Article ID 045002, 2009.
- [38] B. M. Hegelich, I. Pomerantz, L. Yin et al., “Laser-driven ion acceleration from relativistically transparent nanotargets,” *New Journal of Physics*, vol. 15, no. 8, Article ID 085015, 2013.
- [39] S. Palaniyappan, C. Huang, D. C. Gautier et al., “Efficient quasi-monoenergetic ion beams from laser-driven relativistic plasmas,” *Nature Communications*, vol. 6, no. 1, Article ID 10170, 2015.
- [40] L. Yin, B. J. Albright, B. M. Hegelich, and J. C. Fernández, “GeV laser ion acceleration from ultrathin targets: the laser

- break-out afterburner,” *Laser and Particle Beams*, vol. 24, no. 2, pp. 291–298, 2006.
- [41] L. Yin, B. J. Albright, K. J. Bowers, D. Jung, J. C. Fernández, and B. M. Hegelich, “Three-dimensional dynamics of breakout afterburner ion acceleration using high-contrast short-pulse laser and nanoscale targets,” *Physical Review Letters*, vol. 107, no. 4, Article ID 045003, 2011.
- [42] A. Higginson, R. J. Gray, M. King et al., “Near-100 MeV protons via a laser-driven transparency-enhanced hybrid acceleration scheme,” *Nature Communications*, vol. 9, no. 1, p. 724, 2018.
- [43] P. Wang, Z. Gong, S. G. Lee et al., “Super-heavy ions acceleration driven by ultrashort laser pulses at ultrahigh intensity,” *Physical Review X*, vol. 11, no. 2, 2021.
- [44] Y.-X. Geng, Q. Liao, Y.-R. Shou et al., “Generating proton beams exceeding 10 MeV using high contrast 60 TW laser,” *Chinese Physics Letters*, vol. 35, no. 9, 2018.
- [45] M. Nishiuchi, N. P. Dover, M. Hata et al., “Dynamics of laser-driven heavy-ion acceleration clarified by ion charge states,” *Physical Review Research*, vol. 2, no. 3, 2020.
- [46] J. F. Ziegler, M. D. Ziegler, and J. P. Biersack, “SRIM—the stopping and range of ions in matter,” *Nuclear Instruments and Methods in Physics Research Section B: Beam Interactions with Materials and Atoms*, vol. 268, no. 11–12, pp. 1818–1823, 2010.
- [47] Y. Zhang, H.-W. Wang, Y.-G. Ma et al., “Energy calibration of a CR-39 nuclear-track detector irradiated by charged particles,” *Nuclear Science and Techniques*, vol. 30, no. 6, 2019.
- [48] K. S. Krane, *Introductory Nuclear Physics*, John Wiley & Sons, Hoboken, NJ, USA, 1991.
- [49] H. Becker, C. Rolfs, and H. Trautvetter, “Low-energy cross sections for $^{11}\text{B}(p, 3\alpha)$,” *Zeitschrift für Physik A Atomic Nuclei*, vol. 327, no. 3, pp. 341–355, 1987.
- [50] A. Whitehead and J. Foster, “Activation cross sections for $\text{C}^{12}(p, pn)\text{C}^{11}$, $\text{O}^{16}(p, \alpha)\text{N}^{13}$, and $\text{F}^{19}(p, pn)\text{F}^{18}$,” *Canadian Journal of Physics*, vol. 36, no. 10, pp. 1276–1285, 1958.



Research Article

Laser-Driven Proton-Boron Fusions: Influences of the Boron State

Xiaochuan Ning ¹, Tianyi Liang ¹, Dong Wu ², Shujun Liu ¹, Yangchun Liu ¹,
Tianxing Hu ¹, Zhengmao Sheng ¹, Jieru Ren,³ Bowen Jiang,⁴ Yongtao Zhao ³,
Dieter H. H. Hoffmann ³ and X.T. He¹

¹Institute for Fusion Theory and Simulation, Department of Physics, Zhejiang University, Hangzhou 310027, China

²Key Laboratory for Laser Plasmas and School of Physics and Astronomy, and Collaborative Innovation Center of IFSA (CICIFSA), Shanghai Jiao Tong University, Shanghai 200240, China

³MOE Key Laboratory for Nonequilibrium Synthesis and Modulation of Condensed Matter, School of Physics, Xi'an Jiaotong University, Xi'an 710049, China

⁴Technische Universität Darmstadt Institut für Kernphysik, Schloßgartenstraße, Darmstadt 64289, Germany

Correspondence should be addressed to Dong Wu; dwu.phys@sjtu.edu.cn

Received 25 June 2022; Revised 24 August 2022; Accepted 3 September 2022; Published 26 September 2022

Academic Editor: Dimitri Batani

Copyright © 2022 Xiaochuan Ning et al. This is an open access article distributed under the Creative Commons Attribution License, which permits unrestricted use, distribution, and reproduction in any medium, provided the original work is properly cited.

The proton-boron ($p^{11}\text{B}$) reaction is regarded as the holy grail of advanced fusion fuels, where the primary reaction produces 3 energetic α particles. However, due to the high nuclear bounding energy and bremsstrahlung energy losses, energy gain from the $p^{11}\text{B}$ fusion is hard to achieve in thermal fusion conditions. Owing to advances in intense laser technology, the $p^{11}\text{B}$ fusion has drawn renewed attention by using an intense laser-accelerated proton beam to impact a boron-11 target. As one of the most influential works in this field, Labaune et al. first experimentally found that states of boron (solid or plasma) play an important role in the yield of α particles. This exciting experimental finding rouses an attempt to measure the nuclear fusion cross section in a plasma environment. However, up to now, there is still no quantitative explanation. Based on large-scale, fully kinetic computer simulations, the inner physical mechanism of yield increment is uncovered, and a quantitative explanation is given. Our results indicate the yield increment is attributed to the reduced energy loss of the protons under the synergetic influences of degeneracy effects and collective electromagnetic effects. Our work may serve as a reference for not only analyzing or improving further experiments of the $p^{11}\text{B}$ fusion but also investigating other beam-plasma systems, such as ion-driven inertial confinement fusions.

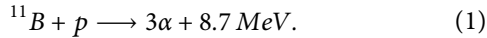
1. Introduction

Progress in fusion experiments has been continuously made towards the final goal of contributing to the world's energy supply. Both the magnetic confinement fusion (MCF) experiments and the inertial confinement fusion (ICF) experiments have achieved significant milestones in recent years. The Experimental Advanced Superconducting Tokamak (EAST) at Hefei has made a world record for realizing a 101-second H-mode discharge [1], and the most advanced ICF experiments at the Livermore National Ignition Facility (NIF) have obtained a 1.35-MJ fusion energy output recently, which

is about 70% of the laser input energy [2]. Despite the great achievements, there remains a long way to go to solve the energy crisis. For the magnetic confinement approach, adequate plasma confinement time and qualified materials for the first wall of the reactor, which can bear the tough conditions, are still two main issues to be addressed. As for the inertial confinement approach, in the case of the NIF, though it obtains 1.35-MJ energy, it starts with more than 400 MJ of total stored energy. From this perspective, the ratio of the total output energy to the total input energy is quite low and far from the envisioned goal of achieving a gain of 10. Moreover, 14-MeV neutrons produced by deuterium-tritium (D-T)

fusion also raise some concerns about induced radioactivity, and it is still a challenging problem to efficiently convert neutron energy into useful electricity.

While we are convinced that nuclear fusion is the world energy source of the future, it is obvious that even if, from now on, all fusion scenarios based on the ITER technology or similar technology proceed on schedule, fusion will not contribute significantly to eliminating the problems associated with climate change in a short time. Having said that, we believe that it makes sense to investigate fusion scenarios that use fusion fuel that is not radioactive and is available in abundant quantities. The holy grail of advanced fusion fuels, therefore, is considered to be the $p + {}^{11}\text{B}$ reaction, where the primary reaction produces 3 energetic α particles.



Only secondary reactions produce neutrons and induce radioactivity. Although the peak fusion cross section is comparable to the D-T fusion, due to the much higher nuclear bounding energy and bremsstrahlung energy losses, energy gain from the $p + {}^{11}\text{B}$ fusion is hard to achieve in thermal fusion conditions.

Owing to advances in laser technology [3, 4], it has become easier to obtain high-intensity ion beams [5, 6] and explore warm-dense-matter physics [7, 8] or high-energy-density physics [9, 10], and the $p + {}^{11}\text{B}$ fusion has also drawn renewed attention [11–13]. The proposal of using intense laser beams or intense laser-accelerated proton beams to impact a boron target so as to generate the $p + {}^{11}\text{B}$ fusion is becoming increasingly attractive. Based on this method, a number of groups [14–20] have performed a series of experiments on the $p + {}^{11}\text{B}$ fusion reaction and measured the yields of α particles. Meanwhile, significant progress has also continuously been made in this field. The record yield of α particles has increased from $10^5/\text{sr}$ in 2005 [14, 21] to $10^{10}/\text{sr}$ in 2020 [18]. However, there still remain unclear physical mechanisms in the interaction of a proton beam and a boron target, which strongly depends on the intensity of the proton beam as well as the conditions of the boron target, including temperature, density, ingredients, and so on, and potentially has a large influence on the possibility of the $p + {}^{11}\text{B}$ fusion reaction and the α -particle yield. Labaune et al. [15] first experimentally found that states of boron (solid or plasma) play an important role in the yield of α particles produced by the $p + {}^{11}\text{B}$ fusion reaction. In their experiments, compared with boron solid, a boron plasma ablated by a nanosecond laser can produce many more (nearly two orders of magnitude more) α particles under the impact of a proton beam accelerated by a picosecond laser. As the inner physical mechanism of their experiments is still not clear, in order to figure out the issue, we have recently performed a set of simulations according to their experiments.

2. The Interaction between a Nanosecond Laser and a Boron Solid

To ascertain the specific state of the boron target after it is ablated, we have performed a one-dimensional radiation-

hydrodynamic simulation with the MULTI-1D code [22] on the interaction of a nanosecond laser pulse and a boron solid, which is the first step in the experiment of Labaune et al. The MULTI-1D code has been widely used by various authors [23–27]. Readers are suggested to refer to Ref. [22] for more detailed information. In our simulation, the grid size is $8 \mu\text{m}$ and the time step is 0.02 ns. To be consistent with the experiments, the laser duration time is 1.5 ns with a $0.53 \mu\text{m}$ wavelength and an intensity of $6 \times 10^{14} \text{ W cm}^{-2}$. The initial mass density of the boron solid is set to 2.34 g cm^{-3} . The simulation results of the mass density distributions and the temperature distributions of the boron target at different moments are displayed in Figures 1(a) and 1(c). For the purpose of further analysis, we have extracted the data at $t = 1.2 \text{ ns}$, as shown in Figures 1(b) and 1(d). A low-density boron plasma is widely formed in the region away from the boron solid, whereas, on the surface of the boron solid, there actually exists a high-density boron plasma that is driven by shocks. To the best of our knowledge, this high-density boron plasma was not considered seriously in previous studies. It can also be seen in Figures 1(b) and 1(d) that the surface high-density boron plasma is about 5 times denser than the boron solid, its range is about tens of microns, and its temperature is about 10 eV. Under this condition, the ionization degree of the boron target is about two [28]. To quantitatively evaluate the impact of degeneracy effects, we can define the degeneracy degree of plasma electrons as $\theta = k_B T_e / E_F$, where $k_B T_e$ is the thermal energy and $E_F = (3\pi^2 n_e)^{2/3} \hbar^2 / (2m_e)$ is the Fermi energy. Here, n_e is the density of plasma electrons, \hbar is the reduced Planck's constant and m_e is the electron mass. By using the above parameters of the boron target, we can obtain.

$$\theta = \frac{k_B T_e}{E_F} = 0.23 < 1. \quad (2)$$

This indicates that after the laser ablated the boron solid, degeneracy effects indeed should be taken into account.

3. The Interaction Between a Proton Beam and a Boron Target under the Different States

Next, we further performed another set of simulations with the LAPINS code [29–33] on the $p + {}^{11}\text{B}$ fusion by injecting proton beams into a boron solid and a boron plasma, respectively. To make the simulations more credible and closer to the real experimental situation, modules of collisional effects [30], degeneracy effects [31] and nuclear reactions [32] are contained in the LAPINS code. Detailed information on these modules can be found in the relevant references. Moreover, to deal with the self-generated electromagnetic fields of the beam-target system, collective electromagnetic effects are also considered in the LAPINS code. As a hybrid PIC code, the LAPINS code treats plasma ions and the injected beam particles by using the traditional PIC method, while plasma electrons are treated as a fluid, of which the current density is solved by applying Ampere's law as follows [34]:

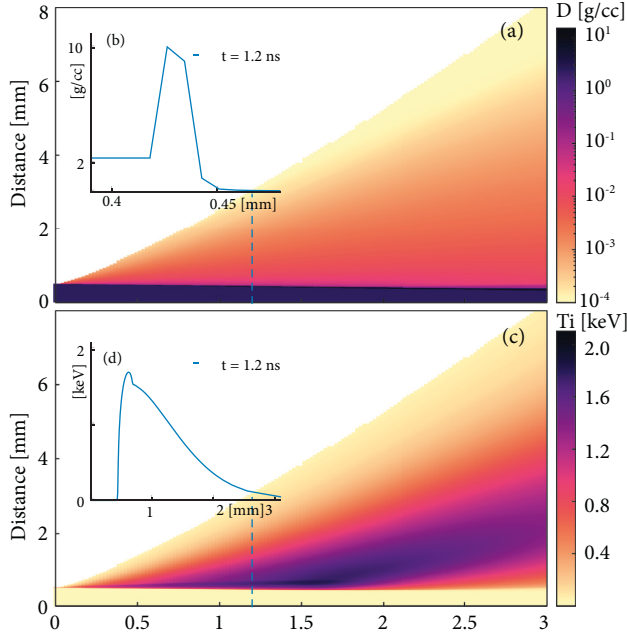


FIGURE 1: Evolution of the mass density distribution in (a) and the temperature distribution in (c) of boron ions with time. (b) and (d) correspond to the mass density distribution and the temperature distribution at $t = 1.2$ ns, respectively.

$$J_e = \frac{1}{2\pi} \nabla \times B - \frac{1}{2\pi} \frac{\partial E}{\partial t} - J_b - J_i, \quad (3)$$

where B is the magnetic field, E is the electric field, J_b is the beam current density and J_i is the plasma ion current density. Applying the continuity equation $\nabla \cdot J + \partial \rho / \partial t = 0$, where $J = J_b + J_e + J_i$ is the total current density, and ρ is the charge density, we can see that the Poisson's equation $\nabla \cdot E = 2\pi\rho$ is rigorously satisfied, which indicates the charge separation electric field is naturally contained in the LAPINS code.

When a charged particle beam is injected into a target, target electrons will quickly respond to the electromagnetic fields generated by the beam and neutralize the beam's charge and current. The fields generated by the beam-target system depend on not only the quality of the beam but also the target's ability to cancel the beam charge and current [34]. A widely used model to calculate the electric field is the basic Ohm's law [34–38], $E = \eta J_e$, where η is the resistivity, which is obtained by averaging over all binary collisions at each time step for each simulation cell in a natural manner. The LAPINS code applies to a more general form as follows:

$$E = \eta J_e - v_e \times B - \frac{1}{en_e} \nabla p_e, \quad (4)$$

where v_e is the flow velocity of plasma electrons, p_e is the plasma electron thermal pressure, n_e is the plasma electron density, and e is the elementary charge. The magnetic field is finally derived from Faraday's law, $\partial B / \partial t = -\nabla \times E$. As only a part of Maxwell's equations needs to be solved, this method is of high speed and particularly useful for large-scale simulations.

As mentioned above, degeneracy effects and collective electromagnetic effects are important in our cases. To evaluate the influences of these two effects on the $p^{11}\text{B}$ fusion, we have performed four simulations. With the module of collective electromagnetic effects on/off, a proton beam interacts with a boron solid/plasma. These simulations are based on a two-dimensional Z–Y Cartesian geometry. The grid size is $0.1 \mu\text{m} \times 0.2 \mu\text{m}$, and the time step is 1.6 fs. To make the proton beam possess a wide energy spectrum similar to the experimental result obtained by Labaune et al., we set both the kinetic energy and the temperature of the proton beam to 1 MeV. The duration time of the proton beam is 1 ps. The parameters of the boron targets are extracted from the results of the MULTI-1D simulation in Section 2. The density of the boron solid and the boron plasma is 2.34 g/cm^3 and 11.4 g/cm^3 , respectively. The temperature of the boron solid is set to 0.0243 eV (room temperature), and the temperature of the boron plasma is set to 10 eV. The simulation results of the proton mass density distributions and the electric field distributions at $t = 1.3$ ps are displayed in Figure 2.

4. Results and Discussion

Comparing Figures 2a and 2b, we can see that for the boron solid, the proton beam can only penetrate to the surface, whereas for the boron plasma, it can penetrate to a longer distance. This difference can be explained as follows. The boron solid has a large resistivity, and the boron plasma, with abundant free electrons, has a much lower resistivity. Ohm's law (4) reveals the fact that the large difference in resistivity will lead to a significant difference in the electric field generation. As shown in Figure. 2c and 2d, the maximum value of the electric field in the boron solid is more than 100 times stronger than that in the boron plasma. Such a strong electric field in the boron solid will greatly prevent the beam from penetrating deeper into the target.

Imitating the experimental measurement method, we have recorded the energy spectra of α particles escaping from the left simulation boundary in the range of 0 to 6.5 MeV, which are plotted in Figure 3. Comparing the cases of the boron plasma without electromagnetic fields (5N-noEB) and the boron solid without electromagnetic fields (N-noEB), we find that when electromagnetic fields are not calculated in the simulations, there are about 40% more α particles produced by the $p^{11}\text{B}$ fusion reactions in the laser-ablated boron solid (boron plasma). This difference is attributed to degeneracy effects, which do not play a role in the solid boron target but become non-negligible after laser ablation, as mentioned above. A theoretical explanation can be given here. For degenerate electrons, their velocity distribution is governed by the Fermi-Dirac (FD) statistics as follows:

$$f_{FD}(v_e) = \frac{2m_e^3}{(2\pi\hbar)^3 n_e} \frac{1}{\exp[\beta(E_e - \mu)] + 1}, \quad (5)$$

where m_e is the electron mass, $\beta = 1/k_B T_e$, E_e is the electron energy, and μ is the chemical potential. The dielectric function of degenerate electrons can be expressed as [39].

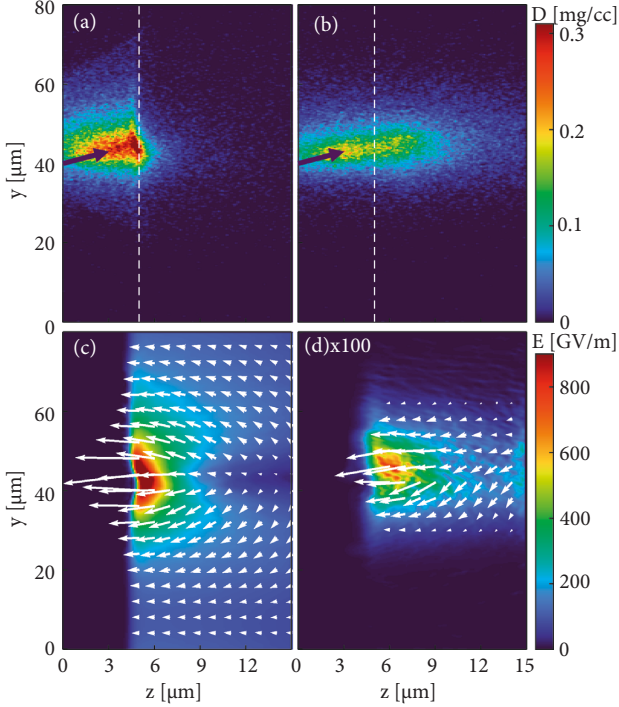


FIGURE 2: Mass density distributions of the proton beam and the electric field distributions at $t = 1.3$ ps for the boron solid in (a) and (c) and for the laser-ablated boron solid (boron plasma) in (b) and (d), respectively. The boron targets are located on the right side of the white dashed lines in (a) and (b). The black arrows in (a) and (b) indicate the incident direction of the proton beams, of which the angle is 45° to the z -axis. The white arrows in (c) and (d) are the directions of the electric fields. In (d), the white ‘ $\times 100$ ’ means the electric field is magnified by a factor of 100, which generally suggests the real electric field in (d) is at least 100 times weaker than that in (c).

$$\varepsilon(k, \omega) = 1 + \frac{1}{4\pi k_F a_0^2 z^3} [g(u+z) - g(u-z)]. \quad (6)$$

Here, a_0 is the Bohr radius, $k_F = m_e v_F \hbar = (3\pi^2 n_e)^{1/3}$, $u = \omega/kv_F$, $z = k/2k_F$, and

$$g(x) = \int_0^\infty \frac{y dy}{\exp(Dy^2 - \beta\mu) + 1} \ln\left(\frac{x+y}{x-y}\right), \quad (7)$$

where $D = E_F \beta$ is the degeneracy parameter. Finally, the stopping power of degenerate electrons can be obtained by the widely used dielectric formalism [40–43].

$$sp = \frac{dE}{dz} = \frac{2(Ze)^2}{\pi v^2} \int_0^\infty \frac{dk}{k} \int_0^{kv} d\omega \omega \text{Im} \left[\frac{-1}{\varepsilon(k, \omega)} \right]. \quad (8)$$

For the convenience of analysis, it is instructive to take advantage of the stopping power per unit density (SPPUD) to evaluate the influence of degeneracy effects

$$sp' = \frac{sp}{n_e}. \quad (9)$$

Figure 4 shows the numerical results of (9) for different electron densities. It can be seen that if the electron density is

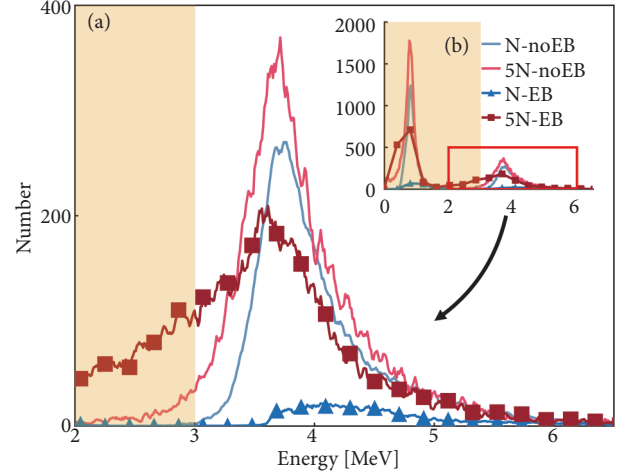


FIGURE 3: The energy spectra of α particles escaping from the left simulation boundary in the range of 0 MeV to 6.5 MeV: (1) the blue line (N-noEB), the boron solid without electromagnetic fields; (2) the red line (5N-noEB), the boron plasma without electromagnetic fields; (3) the blue triangle line (N-EB), the boron solid with electromagnetic fields; (4) the red square line (5N-EB), the boron plasma with electromagnetic fields. The yellow patch corresponds to where it cannot be measured in the experiments.

increased from $2.52 \times 10^{23} \text{ cm}^{-3}$ (density of the boron solid) to $1.26 \times 10^{24} \text{ cm}^{-3}$ (density of the boron plasma), SPPUD of the electrons is decreased. In our cases, the yield of α particles produced by the $p^{11}\text{B}$ fusion can be expressed as [18].

$$N_\alpha = \frac{3N_p n_e}{Z_i} \int_0^{E_0} \sigma(E) \left(\frac{dE}{dz} \right)^{-1} dE = \frac{3N_p}{Z_i} \int_0^{E_0} \frac{\sigma(E)}{sp'} dE, \quad (10)$$

where N_p is the number of protons, Z_i is the charge number of the boron ion, and $\sigma(E)$ is the cross section of the $p^{11}\text{B}$ fusion. (10) reveals the relation between the yield of α particles and the SPPUD of the electrons and implies that the proton beam propagating in the high-density boron plasma will have more chances to collide with boron nuclei, generate the $p^{11}\text{B}$ fusion and produce α particles, which is consistent with our simulation results about the gap between the cases of the boron solid without electromagnetic fields (5N-noEB) and the boron solid without electromagnetic fields (N-noEB) in Figure 3. Both the theory and the simulations indicate that degeneracy effects have an influence on the $p^{11}\text{B}$ fusion. Nonetheless, quantitatively speaking, they are not the primary factor that causes the significant difference in the yield of α particles in the experiments of Labaune et al. since, as shown in Figure 3, they can only increase the yield by about 40%.

It can be seen in Figure 3 that there is a large gap between the cases of the boron solid without electromagnetic fields (N-noEB) and the boron solid with electromagnetic fields (N-EB), which indicates that in terms of the boron solid, collective electromagnetic effects have a huge influence on the number of fusion reactions and the yield of α particles. As mentioned above and shown in Figure 2c, when the

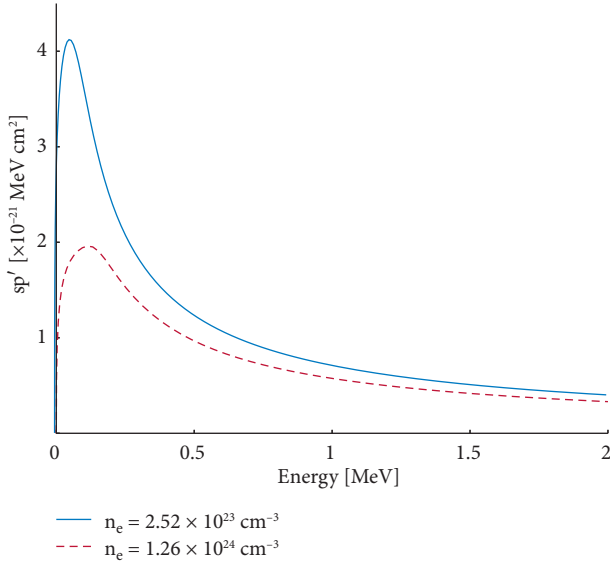


FIGURE 4: SPPUD as a function of the proton energy. For the blue solid line, the electron density is $n_e = 2.52 \times 10^{23} \text{ cm}^{-3}$, corresponding to the density of the boron solid, and for the red dotted line, the electron density is $n_e = 1.26 \times 10^{24} \text{ cm}^{-3}$, corresponding to the density of boron plasma.

proton beam is injected into the boron solid, a strong stopping electric field will be generated. On the one hand, it can greatly increase the energy loss of the proton beam and prevent the beam from penetrating. Recently, Ren et al. presented a piece of experimental evidence on the significantly enhanced energy loss of a laser-accelerated proton beam in the dense ionized matter [44], which is similar to the case we are describing. On the other hand, (10) shows that if the energy loss of the beam increases, the number of fusion reactions and the yield of α particles will decrease accordingly. For the boron plasma, the gap between the cases of the boron plasma without electromagnetic fields (5N-noEB) and the boron plasma with electromagnetic fields (5N-EB) is not that large because, compared with the boron solid, the boron plasma has a much lower resistivity and, according to Ohm's law Eq. (4), the generated electric field will also be smaller, as displayed in Figure 2c and 2d. Therefore, collective electromagnetic effects in the boron plasma are not as significant as in the boron solid. Collective electromagnetic effects described in this paper are a kind of nonlinear effects caused by a large number of injected ions. Previously commonly used single-particle theories and simulation models cannot be used here. Collective electromagnetic effects depend on many factors, such as the current density of the proton beam, the resistivity of the boron target, and the flow velocity of plasma electrons.

For the cases of the boron solid without electromagnetic fields (N-EB) and the boron plasma with electromagnetic fields (5N-EB), both degeneracy effects and collective electromagnetic effects are taken into account. The gap in the yields of α particles between these two cases is about a tenth of a second, which is in good agreement with the results at $dt = 1.2 \text{ ns}$ in the experiments of Labaune et al. As we have discussed above separately, the gap here originates from two

aspects: degeneracy effects and collective electromagnetic effects. They exert influences on the number of fusion reactions by changing the energy loss of the proton beam. To be specific, the more energy the proton beam losses during its transport in boron targets, the smaller the number of fusion reactions between protons and boron atomic nuclei will be. Readers may notice that the specific numbers of recorded α particles in our simulations are greater than those in the experiments. Actually, it is caused by the difference in the total number of injected protons between our simulations and their experiments. As shown in Eq. (10), the yield of α particles produced by the $p^{11}\text{B}$ fusion is proportional to the number of protons. If the total numbers of protons in our simulations is greater than that in the experiments, then there will be an equal multiple difference in the yields of α particles. In this work, we are concerned with the difference in the α -particle yields produced in different states of boron targets rather than the specific numbers. From this perspective, our simulations are indeed in good agreement with the experiments.

Eventually, it should be mentioned that while α particles produced by the $p^{11}\text{B}$ fusion are propagating in boron targets, they are simultaneously heated and being stopped by the background particles [45–47], which, as a matter of fact, will alter the initial energy spectrum of α particles. This indicates that degeneracy effects and collective electromagnetic effects influence not only the yield of α particles but also their energy spectrum or velocity distributions. Degeneracy effects can be considered to be isotropic if local fluctuations of the boron density and temperature are ignored, but it is not the case with collective electromagnetic effects. For the α particles moving forward (the opposite direction of the electric field), their energy loss will be increased, whereas for the α particles moving backward (the same direction as the electric field), they will be accelerated by the electric field and gain energy. Whether one tries to use the $p^{11}\text{B}$ fusion to obtain a net energy output to solve the energy crisis or view the $p^{11}\text{B}$ fusion as α -particle source, the influences of degeneracy effects and collective electromagnetic effects on the energy evolution of α particles could be a topic worthy of in-depth study in future work.

5. Conclusion

The influences of the boron state on the yield of α particles produced by the $p^{11}\text{B}$ fusion have been studied. It is found that compared with a boron solid, a boron plasma can produce much more α particles under the impact of a proton beam, which in this paper is proved to be attributed to degeneracy effects and collective electromagnetic effects. First, when a boron solid is ablated into a boron plasma by a nanosecond laser, degeneracy effects become non-negligible and can increase the yield of α particles by about 40%. Besides, a boron solid, as a poor conductor of electricity, has a large resistivity, while a boron plasma with abundant free electrons has a much lower resistivity. Ohm's law (4) indicates that such a transition from boron solid to a boron plasma will lead to a reduction in the generation of electromagnetic fields. Simulation results show that the

reduction of collective electromagnetic effects can significantly increase the yield of α particles by one to two orders of magnitude. Degeneracy effects and collective electromagnetic effects exert influences on the number of fusion reactions by changing the energy loss of the proton beam. To be specific, if the energy loss of the proton beam is decreased during its transporting in boron targets, the protons will have more chances to collide with boron nuclei, generate the $p^{11}\text{B}$ fusion, and produce α particles.

Our results are in good agreement with the experiments of Labaune et al., and we believe that for future experiments of the $p^{11}\text{B}$ fusion, a promising method to improve the yield of α particles is to heat and compress boron solid into a high-density plasma before injecting a proton beam, because in doing so, the energy loss of the proton beam will be reduced and, accordingly, more fusion reactions are expected to occur. Moreover, our findings may also be able to serve as a reference for investigating other beam-plasma systems, such as ion-driven inertial confinement fusions.

Data Availability

The data that support the findings of this study are available from the corresponding authors upon reasonable request.

Conflicts of Interest

The authors declare that there are no conflicts of interest.

Acknowledgments

This work was supported by the National Natural Science Foundation of China (Grant Nos. 12075204, 11875235 and 61627901), the Strategic Priority Research Program of Chinese Academy of Sciences (Grant no. XDA250050500) and Shanghai Municipal Science and Technology Key Project (No. 22JC1401500). Dong Wu thanks the sponsorship from Yangyang Development Fund. The authors thank Dr. Jinlong Jiao for his help in the radiation hydrodynamics simulations with the MULTI-1D code.

References

- [1] B. N. Wan, Y. F. Liang, X. Z. Gong et al., "The EAST team, and Collaborators. Overview of EAST experiments on the development of high-performance steady-state scenario," *Nuclear Fusion*, vol. 57, Article ID 102019, 2017.
- [2] D. Clery, "Laser-powered fusion effort near," *Science*, vol. 373, p. 841, 2021.
- [3] C. N. Danson, C. Haefner, J. Bromage et al., "Petawatt and exawatt class lasers worldwide," *High Power Laser Science and Engineering*, vol. 7, p. e54, 2019.
- [4] K. Burdonov, A. Fazzini, V. Lelasseux et al., "Characterization and performance of the apollon short-focal-area facility following its commissioning at 1 pw level," *Matter and Radiation at Extremes*, vol. 6, Article ID 064402, 2021.
- [5] E. L. Clark, K. Krushelnick, J. R. Davies et al., "Measurements of energetic proton transport through magnetized plasma from intense laser interactions with solids," *Physical Review Letters*, vol. 84, no. 4, pp. 670–673, 2000.
- [6] W. J. Ma, I. J. Kim, J. Q. Yu et al., "Laser acceleration of highly energetic carbon ions using a double-layer target composed of slightly underdense plasma and ultrathin foil," *Physical Review Letters*, vol. 122, no. 1, Article ID 014803, 2019.
- [7] Z. Chen, X. Na, C. B. Curry et al., "Observation of a highly conductive warm dense state of water with ultrafast pump-probe free-electron-laser measurements," *Matter and Radiation at Extremes*, vol. 6, no. 5, Article ID 054401, 2021.
- [8] R. Roycroft, P. A. Bradley, E. McCary et al., "Experiments and simulations of isochorically heated warm dense carbon foam at the Texas petawatt laser," *Matter and Radiation at Extremes*, vol. 6, no. 1, Article ID 014403, 2021.
- [9] N. A. Tahir, C. Deutsch, V. E. Fortov et al., "Proposal for the study of thermophysical properties of high-energy-density matter using current and future heavy-ion accelerator facilities at gsi darmstadt," *Physical Review Letters*, vol. 95, no. 3, Article ID 035001, 2005.
- [10] B. Y. Sharkov, D. H. H. Hoffmann, A. A. Golubev, and Y. T. Zhao, "High energy density physics with intense ion beams," *Matter and Radiation at Extremes*, vol. 1, no. 1, pp. 28–47, 2016.
- [11] H. Hora, G. H. Miley, N. Azizi, B. Malekynia, M. Ghoranneviss, and X. T. He, "Nonlinear force driven plasma blocks igniting solid density hydrogen boron: laser fusion energy without radioactivity," *Laser and Particle Beams*, vol. 27, no. 3, pp. 491–496, 2009.
- [12] H. Hora, G. H. Miley, M. Ghoranneviss, B. Malekynia, and N. Azizi, "Laser-optical path to nuclear energy without radioactivity: fusion of hydrogen-boron by nonlinear force driven plasma blocks," *Optics Communications*, vol. 282, no. 20, pp. 4124–4126, 2009.
- [13] H. Hora, G. H. Miley, M. Ghoranneviss, B. Malekynia, N. Azizi, and X. T. He, "Fusion energy without radioactivity: laser ignition of solid hydrogen-boron (11) fuel," *Energy Environ. Sci.* vol. 3, no. 4, pp. 479–486, 2010.
- [14] V. S. Belyaev, A. P. Matafonov, V. I. Vinogradov et al., "Observation of neutronless fusion reactions in picosecond laser plasmas," *Physical Review E - Statistical Physics, Plasmas, Fluids, and Related Interdisciplinary Topics*, vol. 72, no. 2, Article ID 026406, 2005.
- [15] C. Labaune, C. Baccou, S. Depierreux et al., "Fusion reactions initiated by laser-accelerated particle beams in a laser-produced plasma," *Nature Communications*, vol. 4, no. 1, p. 2506, 2013.
- [16] A. Picciotto, D. Margarone, A. Velyhan et al., "Boron-proton nuclear-fusion enhancement induced in boron-doped silicon targets by low-contrast pulsed laser," *Physical Review X*, vol. 4, no. 3, Article ID 031030, 2014.
- [17] C. Baccou, S. Depierreux, V. Yahia et al., "New scheme to produce aneutronic fusion reactions by laser-accelerated ions," *Laser and Particle Beams*, vol. 33, no. 1, pp. 117–122, 2015.
- [18] L. Giuffrida, F. Belloni, D. Margarone et al., "High-current stream of energetic alpha particles from laser-driven proton-boron fusion," *Physical Review E - Statistical Physics, Plasmas, Fluids, and Related Interdisciplinary Topics*, vol. 101, no. 1, 2020.
- [19] D. Margarone, A. Morace, J. Bonvalet et al., "Generation of α -particle beams with a multi-kj, peta-watt class laser system," *Frontiers in Physiology*, vol. 8, p. 343, 2020.
- [20] J. Bonvalet, P. Nicolai, D. Raffestin et al., "Energetic alpha-particle sources produced through proton-boron reactions by high-energy high-intensity laser beams," *Physical Review E -*

- Statistical Physics, Plasmas, Fluids, and Related Interdisciplinary Topics*, vol. 103, 2022.
- [21] S. Kimura, A. Anzalone, and A. Bonasera, "Comment on "observation of neutronless fusion reactions in picosecond laser plasmas," *Physical Review E - Statistical Physics, Plasmas, Fluids, and Related Interdisciplinary Topics*, vol. 79, no. 3, Article ID 038401, 2009.
- [22] R. Ramis, R. Schmalz, and J. Meyer-Ter-Vehn, "Multi — a computer code for one-dimensional multigroup radiation hydrodynamics," *Computer Physics Communications*, vol. 49, no. 3, pp. 475–505, 1988.
- [23] J. Jiao, B. Zhang, J. Yu et al., "Generating high-yield positrons and relativistic collisionless shocks by 10 pw laser," *Laser and Particle Beams*, vol. 35, no. 2, pp. 234–240, 2017.
- [24] M. Cipriani, S. Yu. Gus'kov, R. De Angelis et al., "Laser-supported hydrothermal wave in low-dense porous substance," *Laser and Particle Beams*, vol. 36, no. 1, pp. 121–128, 2018.
- [25] F. Y. Wu, R. Ramis, Z. H. Li et al., "Numerical simulation of the interaction between Z-pinch plasma and foam converter using code MULTI (#18353)," *Fusion Science and Technology*, vol. 72, no. 4, pp. 726–730, 2017.
- [26] B. Cui, Z. Fang, Z. Dai et al., "Nuclear diagnosis of the fuel areal density for direct-drive deuterium fuel implosion at the shenguang-ii upgrade laser facility," *Laser and Particle Beams*, vol. 36, no. 4, pp. 494–501, 2018.
- [27] G. Rigon, B. Albertazzi, T. Pikuz et al., "Micron-scale phenomena observed in a turbulent laser-produced plasma," *Nature Communications*, vol. 12, no. 1, pp. 2679–9, 2021.
- [28] T. A. Heltemes and G. A. Moses, "Badger v1. 0: a fortran equation of state library," *Computer Physics Communications*, vol. 183, no. 12, pp. 2629–2646, 2012.
- [29] D. Wu, W. Yu, S. Fritzsche, and X. T. He, "High-order implicit particle-in-cell method for plasma simulations at solid densities," *Physical Review E - Statistical Physics, Plasmas, Fluids, and Related Interdisciplinary Topics*, vol. 100, no. 1, Article ID 013207, 2019.
- [30] D. Wu, X. T. He, W. Yu, and S. Fritzsche, "Monte Carlo approach to calculate proton stopping in warm dense matter within particle-in-cell simulations," *Physical Review E - Statistical Physics, Plasmas, Fluids, and Related Interdisciplinary Topics*, vol. 95, no. 2, Article ID 023207, 2017.
- [31] D. Wu, W. Yu, S. Fritzsche, and X. T. He, "Particle-in-cell simulation method for macroscopic degenerate plasmas," *Physical Review E - Statistical Physics, Plasmas, Fluids, and Related Interdisciplinary Topics*, vol. 102, no. 3, p. 033312, 2020.
- [32] D. Wu, Z. M. Sheng, W. Yu, S. Fritzsche, and X. T. He, "A pairwise nuclear fusion algorithm for particle-in-cell simulations: weighted particles at relativistic energies," *AIP Advances*, vol. 11, no. 7, Article ID 075003, 2021.
- [33] D. Wu, W. Yu, Y. T. Zhao, D. H. H. Hoffmann, S. Fritzsche, and X. T. He, "Particle-in-cell simulation of transport and energy deposition of intense proton beams in solid-state materials," *Physical Review E - Statistical Physics, Plasmas, Fluids, and Related Interdisciplinary Topics*, vol. 100, no. 1, Article ID 013208, 2019.
- [34] H. Cai, X. Yan, P. Yao, and S. Zhu, "Hybrid fluid-particle modeling of shock-driven hydrodynamic instabilities in a plasma," *Matter and Radiation at Extremes*, vol. 6, Article ID 035901, 2021.
- [35] J. R. Davies, "Electric and magnetic field generation and target heating by laser-generated fast electrons," *Physical Review E - Statistical Physics, Plasmas, Fluids, and Related Interdisciplinary Topics*, vol. 68, no. 5, Article ID 056404, 2003.
- [36] A. R. Bell, J. R. Davies, and S. M. Guerin, "Magnetic field in short-pulse high-intensity laser-solid experiments," *Physical Review E - Statistical Physics, Plasmas, Fluids, and Related Interdisciplinary Topics*, vol. 58, no. 2, pp. 2471–2473, 1998.
- [37] J. R. Davies, J. S. Green, and P. A. Norreys, "Electron beam hollowing in laser–solid interactions," *Plasma Physics and Controlled Fusion*, vol. 48, no. 8, pp. 1181–1199, 2006.
- [38] A. P. L. Robinson, M. H. Key, and M. Tabak, "Focusing of relativistic electrons in dense plasma using a resistivity-gradient-generated magnetic switchyard," *Physical Review Letters*, vol. 108, no. 12, Article ID 125004, 2012.
- [39] P. Norreys, D. Batani, S. Baton et al., "Fast electron energy transport in solid density and compressed plasma," *Nuclear Fusion*, vol. 54, no. 5, Article ID 054004, 2014.
- [40] R. Néstor, "Arista and Werner Brandt. Dielectric response of quantum plasmas in thermal equilibrium," *Physical Review A*, vol. 29, pp. 1471–1480, 1984.
- [41] R. Néstor, "Arista and Werner Brandt. Energy loss and straggling of charged particles in plasmas of all degeneracies," *Physical Review A*, vol. 23, 1981.
- [42] M. D. Barriga-Carrasco, "Applying full conserving dielectric function to the energy loss straggling," *Laser and Particle Beams*, vol. 29, no. 1, pp. 81–86, 2011.
- [43] D. Casas, A. A. Andreev, M. Schnürer, M. D. Barriga-Carrasco, R. Morales, and L. González-Gallego, "Stopping power of a heterogeneous warm dense matter," *Laser and Particle Beams*, vol. 34, no. 2, pp. 306–314, 2016.
- [44] C. F. Clouser and N. R. Arista, "Stopping power of dense plasmas: the collisional method and limitations of the dielectric formalism," *Physical Review E - Statistical Physics, Plasmas, Fluids, and Related Interdisciplinary Topics*, vol. 97, no. 2, Article ID 023202, 2018.
- [45] J. Ren, Z. Deng, W. Qi et al., "Observation of a high degree of stopping for laser-accelerated intense proton beams in dense ionized matter," *Nature Communications*, vol. 11, no. 1, p. 5157, 2020.
- [46] P. S. Ray and H. Hora, "On thermalisation of energetic charged particles in fusion plasma with quantum electrodynamic considerations," *Zeitschrift für Naturforschung A*, vol. 32, no. 6, pp. 538–543, 1977.
- [47] B. Malekynia, M. Ghoranneviss, H. Hora, and G. H. Miley, "Collective alpha particle stopping for reduction of the threshold for laser fusion using nonlinear force driven plasma blocks," *Laser and Particle Beams*, vol. 27, no. 2, pp. 233–241, 2009.
- [48] B. Malekynia, H. Hora, N. Azizi et al., "Collective stopping power in laser driven fusion plasmas for block ignition," *Laser and Particle Beams*, vol. 28, no. 1, pp. 3–9, 2010.



Review Article

Multiplication Processes in High-Density H-¹¹B Fusion Fuel

Fabio Belloni 

School of Electrical Engineering and Telecommunications, Faculty of Engineering, UNSW Sydney, Kensington, Australia

Correspondence should be addressed to Fabio Belloni; f.belloni@unsw.edu.au

Received 7 February 2022; Accepted 24 March 2022; Published 6 July 2022

Academic Editor: Katarzyna Batani

Copyright © 2022 Fabio Belloni. This is an open access article distributed under the Creative Commons Attribution License, which permits unrestricted use, distribution, and reproduction in any medium, provided the original work is properly cited.

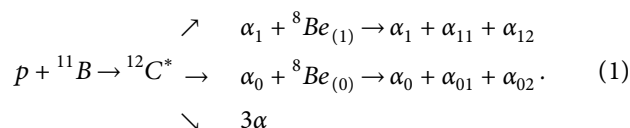
Proton-boron fusion would offer considerable advantages for the purpose of energy production as the reaction is aneutronic and does not involve radioactive species. Its exploitation, however, appears to be particularly challenging due to the low reactivity of the H-¹¹B fuel at temperatures up to 100 keV. Fusion chain-reaction concepts have been proposed as possible means to overcome this limitation. Relevant findings are reviewed in this article. Energy-amplification processes are also presented, which are of interest for beam-fusion experiments and fast ignition of H-¹¹B fuel. Directions for further work are outlined as well.

1. Introduction

The p-¹¹B fusion reaction produces 3 α -particles with a Q-value of about 8.7 MeV. A mixture of H and ¹¹B has been proposed as an advanced fusion fuel because of certain attractive features [1, 2]. With regard to the reactants, they are abundant in nature (implying that no breeding would be needed), stable (meaning that issues like those associated with the radioactivity of tritium in DT fusion would be avoided), and cheap. With regard to the fusion products, there are only charged particles so that all the reaction energy can be released to the fuel (it is also worth noticing the possibility of direct energy conversion into electricity, without passing through a thermodynamic cycle). More importantly, no neutron is generated, meaning no induced activation of the environment surrounding the fuel (actually, there is still a residual neutron production in the fuel through the (p,n) and (α ,n) side reactions on ¹¹B, though the rate is very low). Finally, as an inertial confinement fusion (ICF) fuel, the target would not need to be cryogenic.

A plot of the fusion cross section, σ_f , as a function of the centre of mass (CM) energy, E_{CM} , is shown in Figure 1(a). Resonances of major interest for H-¹¹B fusion are bounded by dashed lines: at 148 keV (with a width of just 5 keV) and 612 keV (with a width of 300 keV) [3]. At 612 keV, σ_f reaches its maximum value, 1.4 barn [6]. Below

approximately 3.5 MeV, the reaction proceeds through 3 channels [6, 7]: the low branching-ratio ¹²C direct breakup and the sequential decays via the first excited state or the ground state of ⁸Be, i.e.:



Summed over the reaction channels, the energy spectrum of the generated α -particles is a continuum; for an incoming proton with energy at the cross section maximum, it extends up to about 6.7 MeV in the laboratory. The spectrum is strongly peaked around 4 MeV. One can say that, on average, two α 's are emitted at 4 MeV, while one is emitted at 1 MeV [8]. The α 's angular distribution is isotropic in the CM system (nearly in the laboratory, because of the proton momentum).

In Figure 1(b), the reactivity, $\langle \sigma_f v \rangle$, is shown as a function of ion temperature for H-¹¹B fuel and, as a term of comparison, DT fuel [3, 4]. We recall that the thermonuclear specific reaction rate is given by $R \equiv n_X n_Y \langle \sigma_f v \rangle$, where n_X and n_Y are the number densities of the fusing species. The low reactivity represents a major drawback of H-¹¹B fuel: for

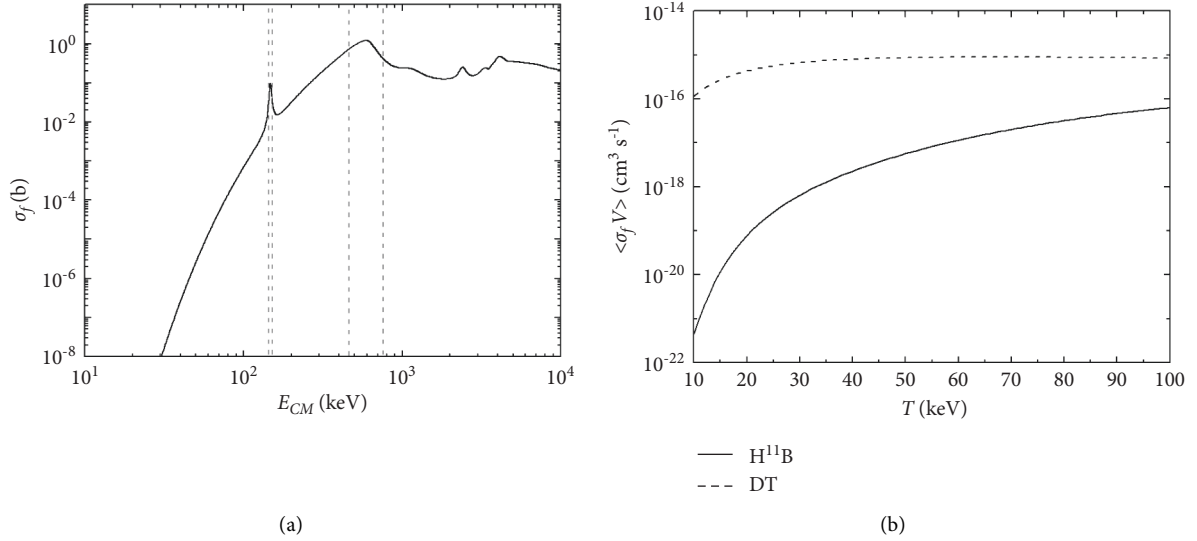


FIGURE 1: Fusion cross section and reactivity of H-¹¹B fuel. (a) Fusion cross section as a function of the CM energy, based on the analytic approximation of Nevins and Swain [3] below 3.5 MeV and, above, on TENDL evaluated data. Resonances of major interest for H-¹¹B fusion are bounded by dashed lines. (b) Reactivity as a function of ion temperature for H-¹¹B fuel and, as a term of comparison, DT fuel. Plots are based on the analytic approximations of Nevins and Swain [3] and Bosch and Hale [4], respectively. Republished from Belloni [5]. © IOP Publishing Ltd. 2021.

instance, at temperatures of the order of those currently achievable in magnetic and inertial confinement experiments (around 10 keV), the H-¹¹B reactivity is 5 orders of magnitude lower than the DT reactivity.

The first comprehensive assessment of the viability of H-¹¹B fuel for thermonuclear fusion was carried out by Moreau [9] at the Princeton Plasma Physics Laboratory, mid-seventies. A steady-state, two-temperature (T_e , T_i) analysis of the balance of the power fluxes was applied: namely, from the fusion products the heat goes entirely to the fuel ions, then from the ions to the electrons, finally into radiation. Note that this power flow scheme requires $T_i > T_e$. In the case $T_i = T_e$, the plasma was found to not ignite because of the predominance of radiation losses. We recall that the fusion power per unit volume, P_F , is given by the product RQ , where Q is the reaction Q -value; the specific power transfer from ions to electrons, $-dW_i/dt$, is proportional to $n_e^2(T_i - T_e)/T_e^{3/2}$, while the radiation power lost by bremsstrahlung, P_B , scales as $n_e^2 T_e^{1/2}$ and the synchrotron radiation power, P_S , as $n_e T_e B^2$, where B is the magnetic field. Confinement requires that $B^2 \propto (n_e T_e + n_i T_i)/\beta$, where β is the *beta ratio*, the main parameter for confinement efficiency (typically, $\beta \ll 1$ in tokamaks, though higher values are desirable for fusion power production). For ignition to occur, the curves $P_F = -dW_i/dt$ and $P_F = (P_B + P_S)(1 - \eta)$, where η is the recirculating power fraction, must intersect in the T_e - T_i plane.

For the case of magnetic confinement, upon realistic assumptions for the recirculating power and confinement conditions, this analysis showed that no ignition point could arise in the T_e - T_i plane when, in addition to bremsstrahlung, synchrotron radiation losses were also taken into account. The conclusion was that H-¹¹B fusion is unfeasible in

tokamaks. A chance, however, could come from inertial confinement, where only bremsstrahlung losses count. In this case, working at much higher densities, ignition points do exist in the T_e - T_i plane (Figure 2). For example, upon the hypothesis of a 70% fraction of fusion power to fuel ions, an ignition point exists for $T_e = 140$ keV and $T_i = 280$ keV, though these values are very high. At a fuel density of 10^{27} ion cm^{-3} (boron-to-proton concentration just lower than 10%), the Lawson criterion requires a minimum confinement time, τ_0 , of 16 ps. Then, igniting the smallest possible pellet, with radius r_0 times the speed of sound, would require a laser energy of 7 MJ. Such a figure is still challenging today, 40 years after Moreau's study. This explains why H-¹¹B fusion was put on hold, at least on the ground of experiment, and it took almost 30 years before having its first demonstration by lasers [10]. Moreover, the demonstration was achieved very far from the prescribed thermonuclear regime, indeed by exploiting an effect unknown at the time of Moreau's work, which is laser acceleration of ions.

This article is intended to give an overview of the nonthermal effects which can complement and supplement the thermonuclear burn of H-¹¹B fuel, through fusion events' multiplication or chain-like mechanisms. The following processes and concepts are reviewed:

- (a) Fusion chain progressing via intermediate nuclear reactions;
- (b) Suprathermal fusion chain, i.e., the chain sustained by suprathermal fuel ions elastically scattered by the fusion-born α 's; and
- (c) The *energy multiplication* (or *amplification*) factor in a beam-driven fusion scheme, which is relevant to proton fast ignition.

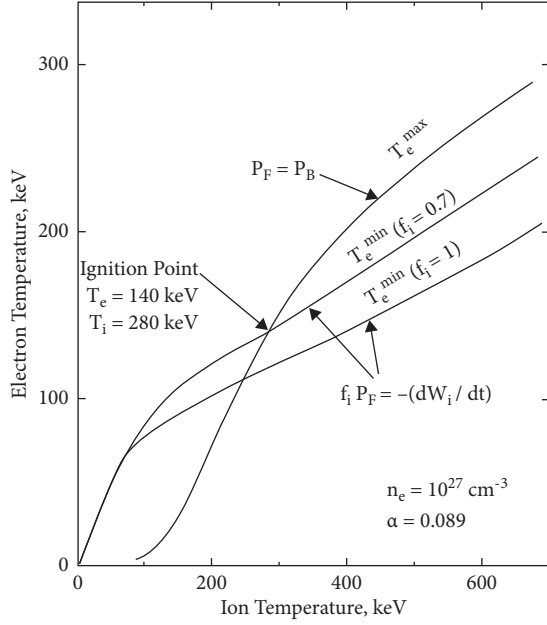
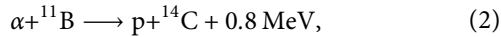


FIGURE 2: Ignition points in the T_e - T_i plane for high-density H- 11 B plasma. f_i is the fraction of fusion power to plasma ions; α is the boron-to-proton ion concentration. Reproduced from Moreau [9] with the permission of the publisher. © IAEA 1977.

2. Multiplication Processes

2.1. Fusion Chain via Intermediate Nuclear Reactions. The possibility of a fusion chain progressing via intermediate nuclear reactions in H-B targets has been presented in two works by Belyaev et al. [11, 12]. The basic chain relies on the fact that a fusion-born α -particle can in turn react with ^{11}B through the reaction:

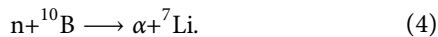


which generates a high-energy proton. This proton can in turn fuse with ^{11}B , possibly giving rise to a chain reaction. However, there is the competing reaction:



which acts as a sink of α 's and generates neutrons. The neutron- and proton-generating reactions have a comparable cross section.

To compensate for the loss of α -particles in the fuel due to the neutron channel, and to reabsorb the neutron inside the fuel, one should exploit neutron capture on ^{10}B , i.e.:



This means that natural boron should be used in the fuel, or ^{11}B should be adequately supplemented with ^{10}B .

Along all the reaction pathways in the chain, the authors find that the number of protons, α -particles, and neutrons in the fuel grows up as an avalanche over times of the order of $1 \mu\text{s}$, approximately; cfr. Figure 1 in ref. [12]. One has to remark, however, that this approach lies upon highly idealised assumptions, in particular,

- (i) maximum values of the reaction cross sections have been used,
- (ii) particles' energy losses have been neglected, and
- (iii) a too long confinement time is required, which is unrealistic for warm, solid-density fuel.

Shmatov [13] has finally shown that at least for temperatures up to 100 keV, only a tiny fraction of α -particles would be capable to react with ^{11}B because of their loss of energy in the fuel, thus preventing the development of the chain. On another note, if Belyaev et al.'s chain developed, fuel neutronicity would become considerably high, which would jeopardise the most appealing feature of H- ^{11}B fusion.

It is also worth mentioning that experiments have been done by Labaune et al. [14] at LULI, France, to test the possibility of inducing a chain reaction in natural-boron or boron-nitride targets under irradiation by laser-accelerated protons (generated from a thin foil). Targets were solid or conditioned in a plasma state by laser irradiation. The authors intended to exploit several nuclear reaction pathways, as detailed in Figure 3. Even in the absence of a self-sustaining chain, they hoped that secondary reactions could substantially increase the energy yield compared with a pure p- ^{11}B fusion scenario. While secondary reactions have successfully been induced and measured under such schemes, one has nevertheless to conclude that their rate is too low to induce any significant avalanche process or increase in the energy yield. For instance, in the case of a solid boron-nitride target, the overall number of the X(p, ^{11}C) reactions, with X = ^{11}B or ^{14}N (Figure 3(b)), was estimated at 10^6 per shot by means of ^{11}C decay measurements. This figure appears to be at least 1000 times smaller than the number of $^{11}\text{B}(\text{p}, 3\alpha)$ fusion reactions ($>10^9$ per shot).

2.2. Suprathermal Fusion Chain. The fact that three charged, massive, energetic particles are produced in the p- ^{11}B reaction suggests that the fusion yield could effectively be enhanced by the elastic scattering of fuel ions to energies corresponding to the highest values of σ_f . This particularly applies to protons because of their higher charge-to-mass ratio compared with ^{11}B ions. While thermalising, some of the protons in these showers can undergo fusion, eventually setting a chain reaction up. At high matter density, moreover, α 's tend to lose energy mostly to plasma ions rather than to electrons. This happens when the electrons' Fermi velocity (or their thermal velocity) becomes comparable to the α -particle velocity, while the ion thermal velocity remains substantially lower [15–17].

The suprathermal fusion chain in an infinite, homogeneous H- ^{11}B plasma can be effectively parameterised in terms of two multiplication (or reproduction) factors. An α -particle emitted at a certain energy $E_{\alpha,0}$ in a primary fusion event is characterised by the multiplication factor $k_\alpha(E_{\alpha,0})$, i.e., the average number of secondary α -particles generated via suprathermal processes during the slowing down of the

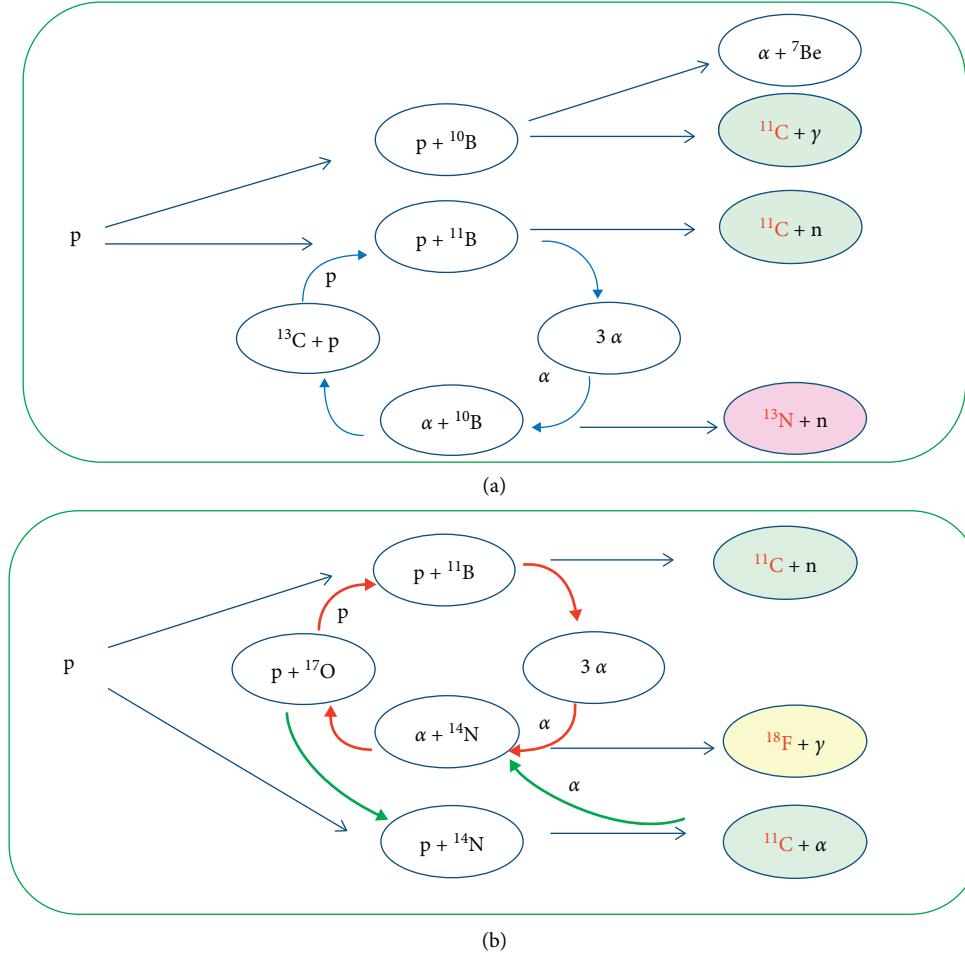


FIGURE 3: Scheme of the main primary and secondary nuclear reactions produced by the interaction between a laser-accelerated proton beam and (a) a natural boron target and (b) a boron-nitride target. Reproduced from Labaune et al. [14], under the terms of the Creative Commons CC BY License.

primary particle. Likewise, the multiplication factor can be expressed in terms of fusion events. Then, one defines k_{∞} as the average number of secondary fusion events per primary event. k_{∞} can be estimated through the integration of k_{α} over the α -emission spectrum, $\varphi(E_{\alpha,0})$ [5]:

$$k_{\infty} = \int k_{\alpha}(E_{\alpha,0})\varphi(E_{\alpha,0})dE_{\alpha,0}, \quad (5)$$

where $\int \varphi(E_{\alpha,0})dE_{\alpha,0} = 1$. Strictly speaking, the concept of k_{∞} is well grounded as long as the emitted α -particles have a comparable slowing-down time, and this quantity is in turn comparable to the (average) period between two consecutive generations of fusion events, τ_g . It is not difficult, then, to calculate the cumulative number of fusion events per unit volume at the time t , $n_f(t)$, in regime of multiplication, upon the thermonuclear specific rate R . Depending on the value of k_{∞} , one can distinguish three cases for the time evolution of n_f (hence, of the energy yield):

- (1) $k_{\infty} < 1 \Rightarrow n_f$ increases linearly with time, asymptotically to $Rt/(1 - k_{\infty})$, for $t \gg \tau_g$;
- (2) $k_{\infty} = 1 \Rightarrow n_f$ increases quadratically with time; in detail, $n_f(t) = R(t + t^2/2\tau_g)$; and

- (3) $k_{\infty} > 1 \Rightarrow n_f$ diverges exponentially, with the growth rate $\ln k_{\infty}/\tau_g$.

It goes without saying that the capability to achieve a chain reaction with multiplicity k_{∞} higher of or comparable to 1 would play a significant—if not indispensable—role in the possible exploitation of H-¹¹B fuel as an energy source.

The question is also how and how much a weak multiplication regime, namely when $k_{\infty} < 1$ (and especially $k_{\infty} \ll 1$), can enhance the pure thermonuclear burn. Using the full expression of $n_f(t)$, it is easy to calculate the ratio I of the suprathreshold-to-thermonuclear energy yield in the confinement time τ_c [5]; indeed, the total energy per unit volume is $n_f(\tau_c)Q$, the energy stemming from the sole thermonuclear burn is just $RQ\tau_c$, and the suprathreshold yield is given by the difference between the first two. I is shown in Figure (4) as a function of k_{∞} for several orders of magnitude of the parameter τ_c/τ_{α} , where $\tau_g \approx \tau_{\alpha}$ is assumed and τ_{α} is the thermalisation time of the α particle at its most probable emission energy. Note that in typical ICF conditions, the quantity τ_c/τ_{α} can reach the order of 10^3 . One can distinguish the following noticeable limits for I . For $\tau_c/\tau_{\alpha} \gg 1$ and $k_{\infty} \ll 1$, I scales as k_{∞} . On the contrary, when

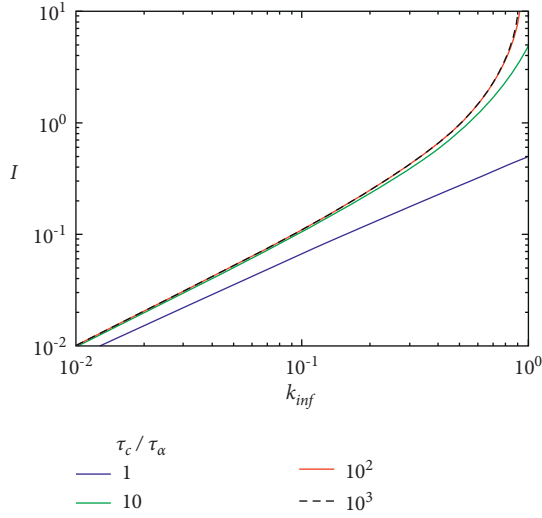


FIGURE 4: Suprathermal-to-thermonuclear energy ratio by the effect of a weak chain reaction. Republished from Belloni [5]. © IOP Publishing Ltd. 2021.

k_∞ approaches 1, I tends to $(1/2)\tau_c/\tau_\alpha$, which opens the possibility of very large increments in the energy output (consequently, high fusion gains). This means that k_∞ does not have to be necessarily larger than 1 to have a sizeable enhancement of the fusion yield.

The earliest studies were not encouraging, however. In the early 70s, Weaver et al. [18] estimated the increase in the H-¹¹B reaction rate due to nonthermal effects to vary between 5% and 15% in the density range of 10^{16} – 10^{26} cm⁻³ and in the temperature range of 150–350 keV. Subsequent calculations by Moreau [9, 19] returned multiplication factors of the order of 10^{-2} in a plasma with $100 \leq T_e \leq 300$ keV, cold ions, and Coulomb logarithm $\ln \Lambda = 5$. In both cases, however, important details have not been given; moreover, only the Coulomb interaction has been taken into account in the α -ion scattering in the case of Moreau, or poorly known nuclear data have been used for this purpose in the case of Weaver et al.

The recent study of Putvinski et al. [20] has substantially confirmed the findings of Weaver et al. [18]. The H-¹¹B reactivity has been calculated using a proton spectrum, which included *kinetic* effects at high energy: besides α -scattering, cooling on colder electrons ($T_e < T_i$) and depletion of the spectrum tail by the fusion burn. The proton spectrum was self-consistently calculated by solving the steady-state Fokker–Planck equation upon a simple burn model. For reference parameters $T_i = 300$ keV, $T_e = 150$ keV, $n_B/n_p = 0.15$, and $E_{\alpha,0} = 4$ MeV, the resulting reactivity showed a 10% increase compared with its purely Maxwellian form. Note that this treatment is formally independent of absolute densities as long as a fixed value is used for $\ln \Lambda$ (details are not given, however). Also in this case, the nuclear interaction does not appear to have been taken into account in the α -ion scattering.

Recently, a supposed experimental manifestation of the suprathermal chain reaction has been the subject of some controversies [21–26], which have finally been resolved in

favour of the impossibility to induce this effect in plasma conditions such as those achievable at the Prague Asterix Laser System (PALS), Czech Republic [27, 28]. A later study [5] has confirmed that in high-density, nondegenerate H-¹¹B plasma, k_∞ turns out to be of the order of 10^{-2} at most. The domain investigated is given by $10^{24} \leq n_e \leq 10^{28}$ cm⁻³, $T_i = 1$ keV, $\max[T_i, 5E_F(n_e)] \leq T_e \leq 100$ keV, where E_F is the Fermi energy; $E_F[\text{keV}] = 3.65 \times 10^{-18} (n_e[\text{cm}^{-3}])^{2/3}$. This represents a low- T_i regime, where the thermonuclear burn is very modest and is just used to seed the chain reaction; the hope was that the suprathermal chain could drive the plasma burn towards ignition, by increasing T_i quickly.

If T_i is sufficiently low, one can assume that, at least for the first few generations, the suprathermal showers elicited by the α particles do not interact with each other and do not significantly affect the background (thermal) Maxwell–Boltzmann distribution of plasma ions. In a scenario of this kind, each primary α -particle or fusion event can be treated independently through a simplified model compared with more sophisticated kinetic-theory approaches, which are indispensable at high reaction rates; see, e.g., refs. [29–31] for the case of DT fusion, and [20] for H-¹¹B fusion. The simplified approach of ref. [5], in particular, assesses whether the medium is *multiplicative* or not. Without entering details, the contribution to k_α of suprathermal H and ¹¹B ions ($k_{\alpha p}$ and $k_{\alpha B}$, respectively) is calculated separately, i.e.:

$$k_\alpha(E_{\alpha,0}) = k_{\alpha p}(E_{\alpha,0}) + k_{\alpha B}(E_{\alpha,0}). \quad (6)$$

Denoting by j the generic ion species and by $E_{j,0}$ its energy just after the scattering by an α particle, $k_{\alpha j}$ is related to the scattered ion spectrum, $dN_j/dE_{j,0}$, and the fusion probability of j , P_j , by the relation:

$$\frac{dk_{\alpha j}}{dE_{j,0}}(E_{j,0}; E_{\alpha,0}) = 3P_j(E_{j,0}) \frac{dN_j}{dE_{j,0}}(E_{j,0}; E_{\alpha,0}). \quad (7)$$

The spectrum $dN_j/dE_{j,0}$ in turn depends on the α -ion differential scattering cross section, $\sigma_{\alpha j}$, and the α -particle stopping power, dE_α/dx , according to the relation:

$$\frac{dN_j}{dE_{j,0}}(E_{j,0}; E_{\alpha,0}) = n_j \int_{(3/2)T_i}^{E_{\alpha,0}} \sigma_{\alpha j}(E_\alpha, E_{j,0}) \left(\frac{dE_\alpha}{dx}\right)^{-1} dE_\alpha. \quad (8)$$

P_j depends on σ_f and the stopping power of j , dE_j/dx , in a similar fashion:

$$P_{p(B)}(E_{p(B),0}) = n_{B(p)} \int_0^{E_{p(B),0}} \sigma_f(E_{CM}) \left(\frac{dE_{p(B)}}{dx}\right)^{-1} dE_{p(B)}. \quad (9)$$

From ref. [5], there are several points to remark and discuss. First of all, the contribution of suprathermal ¹¹B ions to k_α and k_∞ is of the order of 1% only. Nevertheless, the effect of the nuclear interaction in the α -¹¹B scattering should be counterchecked, in the light of the elastic cross section measurements at $E_\alpha < 5$ MeV performed by Spraker et al. [32]. In ref. [5], $\sigma_{\alpha B}$ is calculated as the Rutherford cross section only.

In the case of the scattered proton, the complete elastic cross section, accounting also for the nuclear interaction, must definitely be used in calculations. In Figure 5(a), $k_{\alpha p}$ is

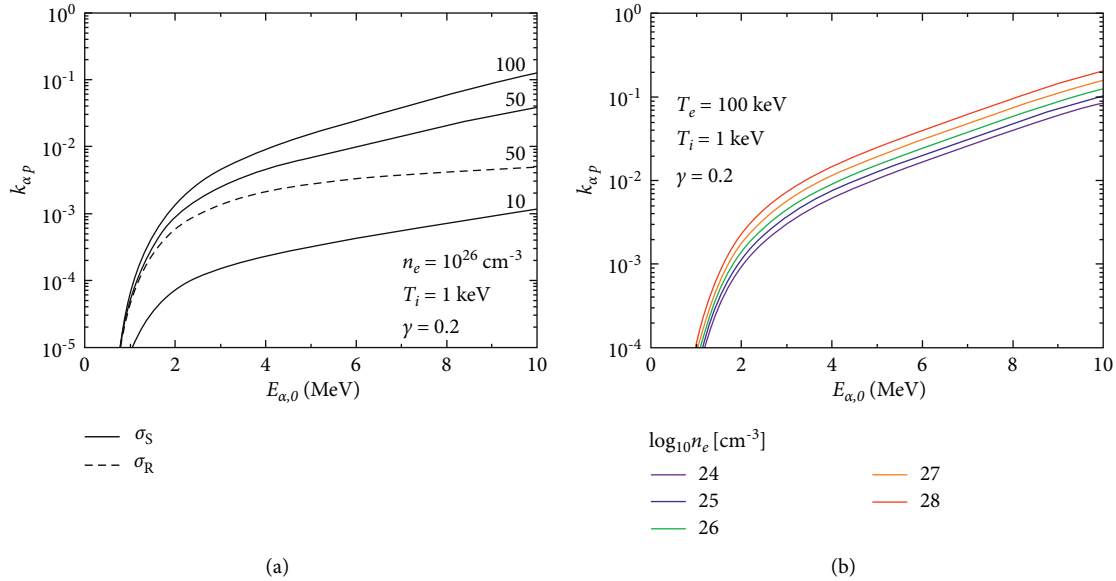


FIGURE 5: α -particle multiplication factor via suprathermal protons as a function of the initial α -energy, for different values of T_e at a fixed n_e (a), and of n_e at a fixed T_e (b). In (a), T_e values (in keV) are indicated next to the curves; σ_S is the complete α -p elastic scattering cross section, accounting also for the nuclear interaction. In (b), γ is the boron-to-proton ion concentration. Republished from Belloni [5]. © IOP Publishing Ltd. 2021.

plotted as a function of $E_{\alpha,0}$ for different values of T_e and $n_e = 10^{26} \text{ cm}^{-3}$. As a term of comparison, a curve based only on the Rutherford α -p scattering cross section, σ_R , is shown for $T_e = 50 \text{ keV}$. One can appreciate that for the most probable α -emission energy, 4 MeV, $k_{\alpha,p}$ is more than twice that found for a pure Coulomb scattering. At $E_{\alpha,0} = 10 \text{ MeV}$, the difference reaches a factor of 8.

A parametric analysis shows that $k_{\alpha,p}$ increases with both T_e and n_e , though it is much more sensitive to T_e . From Figure 5(b), one notes that $k_{\alpha,p}$ drops quickly below $E_{\alpha,0} \approx 2 \text{ MeV}$, while above 4 MeV, the shape of the curves is approximately linear in the semilog plot, meaning an exponential increase with $E_{\alpha,0}$ (up to at least 10 MeV). Even at the highest values of n_e and T_e considered (10^{28} cm^{-3} and 100 keV, respectively), $k_{\alpha,p}$ (hence, k_{∞}) remains significantly lower than 1; for instance, $k_{\alpha,p} = 0.2$ for $E_{\alpha,0} = 10 \text{ MeV}$, and $k_{\infty} \approx 0.01$ over the actual fusion spectrum. A fit of $k_{\alpha,p}$ -vs- $E_{\alpha,0}$ curves with an exponential function returns a common growth rate such that $k_{\alpha,p}$ increases by a factor of about 2.5 each time $E_{\alpha,0}$ increases by 2 MeV. At $n_e = 10^{28} \text{ cm}^{-3}$ and $T_e = 100 \text{ keV}$, one extrapolates $k_{\alpha,p} = 1$ for $E_{\alpha,0} \approx 13.6 \text{ MeV}$.

This means that if we could boost the energy of α 's—let us say—above 10 MeV, we could substantially increase the multiplication factor. How might this be achieved? In principle, two ways can be identified at present. One way is to use high-energy protons to trigger the fusion reaction, which can be referred to as a *kinematic boost*; α particles with energies up to 20 MeV have recently been generated by Bonvalet et al. [33] in a laser-driven pitcher-catcher experiment. Another way is to accelerate the fusion-born α 's; for instance, in the same laser-induced electric field which accelerates the protons in direct-target-irradiation experiments. Evidence of this effect has recently been reported by Giuffrida et al. [34]. With either of these means, it is not

obvious, however, how $E_{\alpha,0}$ could be kept so high for more than one generation. In the case of laser acceleration of the α particles, it is neither obvious how this effect, observed under irradiation of planar solid targets, could be reproduced on actual ICF targets.

It is also worth mentioning that the concept of a possible H- ^{11}B fusion reactor has been proposed (but in a low-density plasma, in this case) [35,36], which is based on α 's acceleration by the application of an external electric field to counterbalance the stopping power and induce an avalanche of reactions.

To summarise, values of k_{∞} very close to 1 are needed in an ICF scheme to enhance the suprathermal-to-thermonuclear energy yield by factors of up to 10^3 . Early computations by Weaver et al. [18] estimated the increase in the H- ^{11}B reaction rate due to suprathermal effects to vary only between 5% and 15% in the density range of 10^{16} – 10^{26} cm^{-3} ($n_e \approx n_i$) and temperature range of 150–350 keV ($T_e = T_i$). Subsequent calculations [9, 19] returned multiplication factors of the order of 10^{-2} in a plasma with $100 \leq T_e \leq 300 \text{ keV}$, $T_i = 0$, and $\ln \Lambda = 5$. Recently, Putvinski et al. [20] have substantially confirmed the findings of Weaver et al., whereas in the high-density, low- T_i domain $10^{24} \leq n_e \leq 10^{28} \text{ cm}^{-3}$, $T_e \leq 100 \text{ keV}$, and $T_i \sim 1 \text{ keV}$ (non-degenerate plasma), it has been found $k_{\infty} \sim 10^{-2}$ at most [5]. This latest work has also shown that particularly for the α -p scattering, the complete elastic cross section, which includes the nuclear interaction, is needed in calculations. Furthermore, k_{α} has been found to increase exponentially with the α -particle energy, at least in the range of 4–10 MeV, with a growth rate that is independent of n_e . This exponential growth could in principle be exploited in cases where the energy of the fusion-born α 's is boosted, e.g., kinematically [33] or electro-dynamically [34].

Finally, no experimental evidence of suprathermal multiplication has been achieved so far.

2.3. Energy Multiplication Factor in a Beam-Driven Fusion Scheme. Fast ignition may provide an option to ignite non-DT fuels inasmuch as it significantly relaxes implosion symmetry requirements (compared with central hot-spot ignition) and allows for nonspherical target configurations or fuel seeding [37]. Among the concepts for fast ignition, it has been proposed to use intense laser-accelerated proton beams [38]. In this approach, the energy deposited in the precompressed fuel by a proton beam generated outside the target bootstraps the fusion flame. Ideally, between 5 and 10% of the laser pulse energy is converted into kinetic energy of the beam as the result of the interaction of the pulse with a thin foil.

Here, we wish to emphasise that proton beam fast ignition is a particularly advantageous option for the case of H-¹¹B fuel. Indeed, while the protons transfer their energy to the plasma, additional heating is provided by in-flight fusion reactions. This is an exclusive effect of H-¹¹B fuel as it cannot obviously occur for other proposed fusion fuels under proton irradiation. On the quantitative ground, it is useful to make recourse to the so-called *energy multiplication factor*, a fundamental quantity in beam fusion. It is defined as the ratio of the fusion energy produced via in-flight reactions to the overall beam energy, i.e.:

$$F = \frac{P_p(E_0)Q}{E_0}, \quad (10)$$

where F is the energy multiplication factor, E_0 is the initial proton energy, Q is the fusion Q -value, and P_p is given by Equation (9) as long as it is sufficiently lower than 1. Denoting by E_b the beam energy, the overall energy deposited in the fuel, E_d , is then:

$$E_d = (1 + F)E_b. \quad (11)$$

An estimate of F is important to set the value of E_0 to be achieved in the laser acceleration of the protons.

A calculation of F vs E_0 for beam-driven H-¹¹B fusion has been carried out by Moreau [9]. This author considered protons injected into a ¹¹B plasma with warm electrons and cold ions. The results are shown in Figure 6 for several values of T_e . In all cases, there is a maximum at E_0 around 1 MeV; at high values of T_e , other two maxima appear just below 3 MeV and between 4 and 5 MeV, respectively. It is hard, however, to achieve a multiplication factor better than 30%. Anyway, Moreau's calculation should be redone with a more accurate fusion cross section (which was barely known at that time) and stopping power model (Sivukhin's model [39] was used).

Note that for a Maxwellian plasma, F is formally independent of density when the value of $\ln\Lambda$ is kept fixed. This comes from an implicit cancellation of the density in the product between n_b and $(dE_p/dx)^{-1}$ in Equation (9), with a residual density dependence holding through the expression of $\ln\Lambda$ in dE_p/dx [5]. This residual dependence is very weak, however. It is also worth noticing that in a fully degenerate

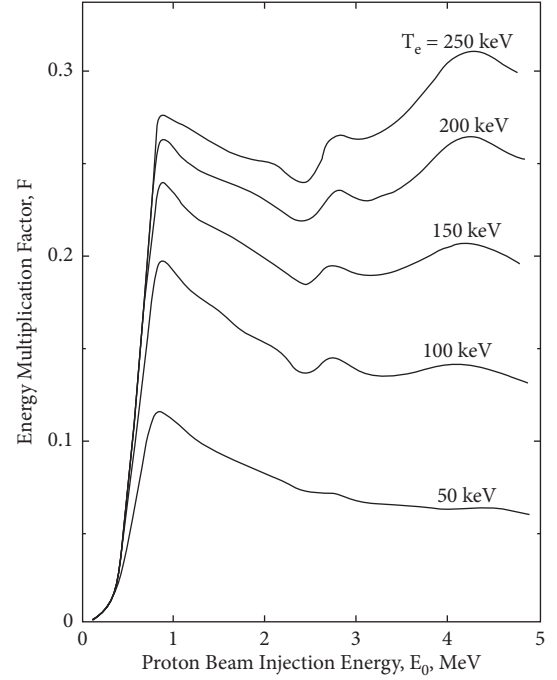


FIGURE 6: Energy multiplication factor vs proton injection energy for various electron temperatures. Protons are injected into a ¹¹B plasma with cold ions and warm electrons. The results are independent of plasma density when the value of $\ln\Lambda$ is fixed. Reproduced from Moreau [9] with the permission of the publisher. © IAEA 1977.

plasma, the electronic component of dE_p/dx would become independent of n_e and proportional to the proton velocity, under certain conditions. (In general, the stopping power of an ion in a fully degenerate plasma scales roughly linearly with n_e . However, when the velocity of the ion is much smaller than the Fermi velocity and the parameter $r_s = (me^2/\hbar^2)(3/4\pi n_e)^{1/3}$ —where m is the electron mass—is much smaller than 1, the stopping power becomes independent of n_e and proportional to the ion velocity. The condition $r_s \ll 1$ holds for $n_e \gg 10^{24} \text{cm}^{-3}$ [17, 40, 41]. As long as the ion-ion component of dE_p/dx can be neglected, P_p would then become truly proportional to n_b . This effect could boost P_p towards 1 even at low (possibly sub-MeV) values of E_0 , given the linear velocity dependence of the electronic stopping power. As a consequence, F could rise up significantly, well above unity.

Another aspect to emphasise is that the energy multiplication factor can be further increased if suprathermal chain reaction effects take place. It is easy to show that in this case, E_d is augmented by a term $S_l F E_b$ compared with Equation (11), where the factor S_l depends on the number of generations, l , and is essentially a partial summation of the geometric series with common ratio k_∞ , according to the relation:

$$S_l(k_\infty) + 1 = \sum_{i=0}^l k_\infty^i = \frac{1 - k_\infty^{l+1}}{1 - k_\infty}. \quad (12)$$

Explicitly,

$$E_d = (1 + F + S_l F) E_b, \quad (13)$$

where the energy multiplication factor can be redefined as follows:

$$F_{supr} \triangleq (1 + S_l) F. \quad (14)$$

Note that S_l converges to $k_\infty / (1 - k_\infty)$ when $k_\infty < 1$ and l is sufficiently large, while $S_l \rightarrow l$ when $k_\infty \rightarrow 1$. Now, if one was capable to keep the chain going for just two generations with k_∞ sufficiently close to 1, assuming $F=0.3$, Equation (13) would return $E_d \approx 2E_b$, which is quite a significant amplification. It is particularly relevant to this case what has been mentioned in the previous section, namely, that k_∞ could be made close to 1 by exploiting the kinematic boost of the proton beam.

3. Conclusions

Recent laser-based experiments [27, 28, 34, 42, 43], basic ICF physics considerations, and current advances in laser technology suggest that a possible scheme to burn H-¹¹B fuel is based on laser-driven proton fast ignition. By itself, this scheme will likely not be enough to achieve high gains. We are confident, however, that it can be complemented by suprathermal effects and strategies for the containment of bremsstrahlung losses in order to increase the fusion yield and relax ignition and burn requirements. In this article, we have reviewed and discussed nonthermal processes of interest, such as the progression of fusion chains via intermediate nuclear reactions, suprathermal multiplication, and beam energy amplification in proton fast ignition.

Fusion chain processes based on intermediate nuclear reactions do not show the potential to make a substantial contribution to ignition and burn of H-¹¹B fuel. Increasing suprathermal fusion's k_∞ above the order of 10^{-2} also appears problematic in present-day laser-driven plasma conditions; nevertheless, promising directions for further investigation can be drawn. In particular, the work of Belloni [5] should be extended to calculate suprathermal effects.

(i) at higher T_p , by adopting more refined kinetic approaches to the problem (e.g., steady-state spectral conditions, via the so-called Boltzmann–Fokker–Planck equation [44]);

(ii) in (partially) degenerate plasmas, a regime that is also of interest for bremsstrahlung reduction [17, 45].

After Moreau [9], the energy multiplication factor for a proton ignitor should be reassessed against the latest measurements of the fusion cross section [6]. The energy multiplication factor should account not only for the in-flight fusion reactions but also for possible suprathermal multiplication of the fusion products. Calculations should include realistic fuel compositions and degenerate plasma regimes.

Finally, on the experimental side, it is to remark that accurate calculations of nonthermal effects, including beam fusion, need reliable fusion cross section measurements well beyond 3 MeV.

Data Availability

This is a review article. Underlying data can be found in the references.

Conflicts of Interest

The author declares that there are no conflicts of interest regarding the publication of this study.

Acknowledgments

This article is based on the content of the talk given by the author at the 29th European Fusion Programme Workshop (EFPW 2021) and of his seminar in the context of the virtual topical series *HB11 Seminar*, organised by HB11 Energy Holdings Pty Ltd.

References

- [1] J. Dawson, “Advanced fusion reactors,” *Fusion*, Academic, vol. 1, New York, NY, USA, 1981.
- [2] H. Hora, S. Eliezer, G. J. Kirchoff et al., “Road map to clean energy using laser beam ignition of boron-hydrogen fusion,” *Laser and Particle Beams*, vol. 35, pp. 730–740, 2017.
- [3] W. M. Nevins and R. Swain, “The thermonuclear fusion rate coefficient for p-11B reactions,” *Nuclear Fusion*, vol. 40, no. 4, pp. 865–872, 2000.
- [4] H.-S. Bosch and G. M. Hale, “Improved formulas for fusion cross-sections and thermal reactivities,” *Nuclear Fusion*, vol. 32, no. 4, pp. 611–631, 1992.
- [5] F. Belloni, “On a fusion chain reaction via suprathermal ions in high-density H-¹¹B plasma,” *Plasma Physics and Controlled Fusion*, vol. 63, Article ID 055020, 2021.
- [6] M. H. Sikora and H. R. Weller, “A New Evaluation of the 11 B(p, α) $\alpha\alpha$ Reaction Rates,” *Journal of Fusion Energy*, vol. 35, no. 3, pp. 538–543, 2016.
- [7] H. W. Becker, C. Rolfs, and H. P. Trautvetter, “Low-energy cross sections for 11B(p, 3 α),” *Zeitschrift fuer Physik A Atomic Nuclei*, vol. 327, no. 3, pp. 341–355, 1987.
- [8] S. Stave, M. W. Ahmed, R. H. France III et al., “Understanding the 11B(p, α) $\alpha\alpha$ reaction at the 0.675 MeV resonance,” *Physics Letters B*, vol. 696, pp. 26–29, 2011.
- [9] D. C. Moreau, “Potentiality of the proton-boron fuel for controlled thermonuclear fusion,” *Nuclear Fusion*, vol. 17, no. 1, pp. 13–20, 1977.
- [10] V. S. Belyaev, A. P. Matafonov, V. I. Vinogradov et al., “Observation of neutronless fusion reactions in picosecond laser plasmas,” *Physical review. E, Statistical, nonlinear, and soft matter physics*, vol. 72, p. 026406, Article ID 026406, 2005.
- [11] V. S. Belyaev, V. P. Krainov, B. V. Zagreev, and A. P. Matafonov, “On the implementation of a chain nuclear reaction of thermonuclear fusion on the basis of the p+11B process,” *Physics of Atomic Nuclei*, vol. 78, no. 5, pp. 537–547, 2015.
- [12] V. S. Belyaev, V. P. Krainov, A. P. Matafonov, and B. V. Zagreev, “The new possibility of the fusion p + 11B chain reaction being induced by intense laser pulses,” *Laser Physics Letters*, vol. 12, Article ID 096001, 2015.
- [13] M. L. Shmatov, “Suppression of the chain nuclear fusion reaction based on the p+11B reaction because of the deceleration of alpha particles,” *Physics of Atomic Nuclei*, vol. 79, no. 5, pp. 666–670, 2016.

- [14] C. Labaune, C. Baccou, V. Yahia, C. Neuville, and J. Rafelski, "Laser-initiated primary and secondary nuclear reactions in Boron-Nitride," *Scientific Reports*, vol. 6, Article ID 21202, 2016.
- [15] M. Gryzinski, "Fusion chain reaction - chain reaction with charged particles," *Physical Review*, vol. 111, pp. 900–905, 1958.
- [16] B. Levush and S. Cuperman, "On the potentiality of the proton-boron fuel for inertially confined fusion," *Nuclear Fusion*, vol. 22, no. 11, pp. 1519–1525, 1982.
- [17] S. Son and N. J. Fisch, "Aneutronic fusion in a degenerate plasma," *Physics Letters A*, vol. 329, no. 1–2, pp. 76–82, 2004.
- [18] T. Weaver, G. Zimmerman, and L. Wood, *Exotic CTR Fuels: Nonthermal Effects and Laser Fusion Applications*, Preprint UCRL-74938, Lawrence Livermore Laboratory), Livermore, CA, USA, 1973.
- [19] D. C. Moreau, "Potentiality of the proton-boron fuel for controlled thermonuclear fusion," *Nuclear Fission*, vol. 17, 2011.
- [20] S. V. Putvinski, D. D. Ryutov, and P. N. Yushmanov, "Fusion reactivity of the pB^{11} plasma revisited," *Nuclear Fusion*, vol. 59, Article ID 076018, 2019.
- [21] H. Hora, P. Lalouis, L. Giuffrida et al., "Petawatt laser pulses for proton-boron high gain fusion with avalanche reactions excluding problems of nuclear radiation," *Proceedings of SPIE Optics*, 2015.
- [22] H. Hora, G. Korn, S. Eliezer et al., "Avalanche boron fusion by laser picosecond block ignition with magnetic trapping for clean and economic reactor," *High Power Laser Science Engineering*, vol. 4, Article ID e35, 2016.
- [23] S. Eliezer, H. Hora, G. Korn, N. Nissim, and J. M. Martinez Val, "Avalanche proton-boron fusion based on elastic nuclear collisions," *Physics of Plasmas*, vol. 23, Article ID 050704, 2016.
- [24] M. L. Shmatov, "Comment on 'Avalanche proton-boron fusion based on elastic nuclear collisions'," *Physics of Plasmas*, vol. 23, Article ID 050704, 2016.
- [25] S. Eliezer, H. Hora, G. Korn, N. Nissim, and J. M. Martinez Val, "Response to 'Comment on 'Avalanche proton-boron fusion based on elastic nuclear collisions,'" *Physics of Plasmas*, vol. 23, Article ID 094703, 2016.
- [26] F. Belloni, D. Margarone, A. Picciotto, F. Schillaci, and L. Giuffrida, "On the enhancement of $p-^{11}B$ fusion reaction rate in laser-driven plasma by $\alpha \rightarrow p$ collisional energy transfer," *Physics of Plasmas*, vol. 25, Article ID 020701, 2018.
- [27] A. Picciotto, D. Margarone, A. Velyhan et al., "Boron-proton nuclear-fusion enhancement induced in boron-doped silicon targets by low-contrast pulsed laser," *Physical Review X*, vol. 4, Article ID 031030, 2014.
- [28] D. Margarone, A. Velyhan, J. Krasa et al., "Advanced scheme for high-yield laser driven nuclear reactions," *Plasma Physics and Controlled Fusion*, vol. 57, Article ID 014030, 2015.
- [29] A. Peres and D. Shvarts, "Fusion chain reaction - a chain reaction with charged particles," *Nuclear Fusion*, vol. 15, no. 4, pp. 687–692, 1975.
- [30] Y. Afek, A. Dar, A. Peres, A. Ron, R. Shachar, and D. Shvarts, "The fusion of suprathermal ions in a dense plasma," *Journal of Physics D: Applied Physics*, vol. 11, no. 16, pp. 2171–2173, 1978.
- [31] A. Kumar, J. P. Ligou, and S. B. Nicli, "Nuclear scattering and suprathermal fusion," *Fusion Science and Technology*, vol. 12, pp. 476–487, 1986.
- [32] M. C. Spraker, M. W. Ahmed, M. A. Blackston et al., "The $^{11}B(p, \alpha)^{8}Be \rightarrow \alpha + \alpha$ and the $^{11}B(\alpha, \alpha)^{11}B$ reactions at energies below 5.4 MeV," *Journal of Fusion Energy*, vol. 31, no. 4, pp. 357–367, 2012.
- [33] J. Bonvalet, P. h. Nicolai, D. Raffestin et al., "Energetic α -particle sources produced through proton-boron reactions by high-energy high-intensity laser beams," *Physical Review E - Statistical Physics, Plasmas, Fluids, and Related Interdisciplinary Topics*, vol. 103, Article ID 053202, 2021.
- [34] L. Giuffrida, F. Belloni, D. Margarone et al., "High-current stream of energetic α particles from laser-driven proton-boron fusion," *Physical Review E - Statistical Physics, Plasmas, Fluids, and Related Interdisciplinary Topics*, vol. 101, Article ID 013204, 2020.
- [35] S. Eliezer and J. M. Martinez-Val, "A novel fusion reactor with chain reactions for proton-boron11," *Laser and Particle Beams*, vol. 38, no. 1, pp. 39–44, 2020.
- [36] S. Eliezer, Y. Schweitzer, N. Nissim, and J. M. Martinez-Val, "Mitigation of the stopping power effect on proton-boron11 nuclear fusion chain reactions," *Frontiers in Physics*, vol. 8, Article ID 573694, 2020.
- [37] S. Atzeni and J. Meyer-ter-Vehn, *The Physics of Inertial Fusion*, Oxford University Press, Oxford, UK, 2004.
- [38] M. Roth, T. E. Cowan, M. H. Key et al., "Fast ignition by intense laser-accelerated proton beams," *Physical Review Letters*, vol. 86, no. 3, pp. 436–439, 2001.
- [39] D. V. Sivukhin, "Coulomb Collisions in a Fully Ionized Plasma," *Reviews of Plasma Physics*, vol. 4, 1966.
- [40] E. Fermi and E. Teller, "The capture of negative mesotrons in matter," *Physical Review*, vol. 72, no. 5, pp. 399–408, 1947.
- [41] J. Lindhard, "On the properties of a gas of charged particles," *Dan. Mat. Fys. Medd.* vol. 28, no. 8, 1954.
- [42] C. Labaune, C. Baccou, S. Depierreux et al., "Fusion reactions initiated by laser-accelerated particle beams in a laser-produced plasma," *Nature Communications*, vol. 4, no. 1, p. 2506, 2013.
- [43] C. Baccou, S. Depierreux, V. Yahia et al., "New scheme to produce aneutronic fusion reactions by laser-accelerated ions," *Laser and Particle Beams*, vol. 33, no. 1, pp. 117–122, 2015.
- [44] K. Przybylski and J. Ligou, "Numerical analysis of the Boltzmann equation including fokker-planck terms," *Nuclear Science and Engineering*, vol. 81, no. 1, pp. 92–109, 1982.
- [45] S. Eliezer, P. T. León, J. M. Martinez-Val, and D. V. Fisher, "Radiation loss from inertially confined degenerate plasmas," *Laser and Particle Beams*, vol. 21, no. 4, pp. 599–607, 2003.



Research Article

Particles Detection System with CR-39 Based on Deep Learning

Gal Amit ^{1,2}, **Idan Mosseri**,³ **Ofir Even-Hen** ¹, **Nadav Schneider** ³, **Elad Fisher** ^{3,4},
Hanan Datz ¹, **Eliahu Cohen** ², and **Noaz Nissim** ⁵

¹Radiation Safety Department, Soreq Nuclear Research Center, Yavne, Israel

²Faculty of Engineering and the Institute of Nanotechnology and Advanced Materials, Bar Ilan University, Ramat Gan 5290002, Israel

³Technology Division, Soreq Nuclear Research Center, Yavne, Israel

⁴Maritime Policy & Strategy Research Center (HMS), Hatter Department of Marine Technologies, University of Haifa, Haifa 3498838, Israel

⁵Applied Physics Department, Soreq Nuclear Research Center, Yavne, Israel

Correspondence should be addressed to Gal Amit; galam@soreq.gov.il

Received 10 May 2022; Accepted 14 June 2022; Published 30 June 2022

Academic Editor: Dimitri Batani

Copyright © 2022 Gal Amit et al. This is an open access article distributed under the Creative Commons Attribution License, which permits unrestricted use, distribution, and reproduction in any medium, provided the original work is properly cited.

We present a novel method that we call FAINE, fast artificial intelligence neutron detection system. FAINE automatically classifies tracks of fast neutrons on CR-39 detectors using a deep learning model. This method was demonstrated using a LANDAUER Neutrak® fast neutron dosimetry system, which is installed in the External Dosimetry Laboratory (EDL) at Soreq Nuclear Research Center (SNRC). In modern fast neutron dosimetry systems, after the preliminary stages of etching and imaging of the CR-39 detectors, the third stage uses various types of computer vision systems combined with a manual revision to count the CR-39 tracks and then convert them to a dose in mSv units. Our method enhances these modern systems by introducing an innovative algorithm, which uses deep learning to classify all CR-39 tracks as either real neutron tracks or any other sign such as dirt, scratches, or even cleaning remainders. This new algorithm makes the third stage of manual CR-39 tracks revision superfluous and provides a completely repeatable and accurate way of measuring either neutrons flux or dose. The experimental results show a total accuracy rate of 96.7% for the true positive tracks and true negative tracks detected by our new algorithm against the current method, which uses computer vision followed by manual revision. This algorithm is now in the process of calibration for both alpha-particles detection and fast neutron spectrometry classification and is expected to be very useful in analyzing results of proton-boron11 fusion experiments. Being fully automatic, the new algorithm will enhance the quality assurance and effectiveness of external dosimetry, will lower the uncertainty for the reported dose measurements, and might also enable lowering the system's detection threshold.

1. Introduction

Much interest in the aneutronic fusion reaction of proton-boron11 (p-B11) has risen lately due to the unexpectedly large amount of reactions obtained in several high intensity laser experiments (see, e.g., [1, 2]).

As the physical processes involved in the production of such excess of reactions are not yet fully understood and may even involve nonlinear processes such as the avalanche process [3, 4], intensive research programs are ongoing in many academic institutes and private companies [5–7].

Moreover, a high flux of highly energetic particles such as protons, heavy ions, and the desired fusion product of alpha-particles accompany the harsh plasma environment that characterizes laser-initiated p-B11 fusion experiments, making the analysis of such experiments a nontrivial task. The most common diagnostics in such experiments are solid state nuclear track detectors such as CR-39 [8, 9]. Although the CR-39 are very reliable for the measurement of the absolute alpha-particle flux, the analysis of the CR-39 passive detector involves a long and tedious process which includes chemical etching, a smart image analysis, and a manual

revision, thus limiting the accuracy and efficiency of the data analysis. For this reason, it is highly desirable to develop automatic software tools to carry out analysis for a large number of nuclear track detectors, hence enhancing the overall outputs of future p-B11 experiments at various laser facilities. That is the main goal behind our current research, which uses deep learning to automate the classification of neutron tracks on CR-39 detectors.

For fast neutron dosimetry, a CR-39 detector is added to a standard TLD card dosimeter. The CR-39 detector is composed of an organic polymer whose chemical name is polyallyl diglycol carbonate (PADC) and its chemical formula is $C_{12}H_{18}O_7$. It is suitable for neutron personal monitoring due to its high sensitivity to protons hit [10], which has been recognized some decades ago as a basic requirement for a fruitful neutron personal monitoring [11].

CR-39 detectors hold some important advantages for serving as neutron dosimeters, among them are their low fast neutron energy threshold, their insensitivity to photon and beta irradiation, their high sensitivity over a wide range of neutron energies [12, 13], and the low influence of environmental effects [14] on its response as well as low signal fading. Although other neutron detecting technologies, such as the bubble detector [15], may have advantages in sensitivity, angle, and energy response dependence, the CR-39 detector still remains the most versatile, easy to carry along with a TLD card, and cheapest neutron dosimeter alternative.

Nevertheless, the main drawback of CR-39 as a fast neutrons dosimeter is its ability to accurately measure high flux neutron fields due to the tedious task of counting the neutron tracks. Other challenges for the CR-39 are distinguishing between different neutron energies and distinguishing between neutrons and alpha-particles.

2. Materials and Methods

The External Dosimetry Lab (EDL) at Soreq Nuclear Research Center (SNRC) provides dosimetry services to all radiation workers around the country, most of them are monitored monthly for X-rays and gamma and beta radiation and some of them for both thermal and fast neutrons.

Since late 70's [16] and until recently, SNRC fast neutron dosimetry system has been an in-house system. In 2018, a new personal neutron dosimetry system, LANDAUER Neutrak[®] system, has been adopted at SNRC [17]. This system is designed to measure CR-39 detectors using a Zeiss microscope, which is coupled to a CCD camera and to a robotic arm that feeds the microscope's moving tray with plastic holders one at a time, each holder having six CR-39 detectors. The CR-39 detector dimensions are 9×19 mm.

After the EDL receives the CR-39 detectors from the customers, the first stage is the etching stage. The detectors are inserted for 15 hours into an etching bath filled with NaOH heated to 74°C at a concentration of 5.5 mol/l in order to enlarge the tracks size. After etching is finished, the CR-39 detectors are thoroughly rinsed to remove all etching residues, to achieve optimal optical reading conditions.

Following the rinsing stage, the second stage is imaging the etched CR-39 detectors using the CCD camera. Ten images of different areas of the CR-39 detector are taken for the fast neutron counting. The images are then analyzed by Landauer's computer vision analysis software. Afterwards, the EDL staff either adds undetected tracks (false negatives) or deletes detected tracks (false positives) using Landauer's data review SW, according to a set of rules adopted by the scientific lab team.

We developed for the first time to our knowledge a method that detects fast neutron tracks on CR-39 detectors, which is based on deep learning, and we name it FAINE, Fast artificial intelligence neutron detection. FAINE uses an artificial neural network of type U-Net and its development consisted with three stages. The first stage is neutrons tracks manual tagging, the second stage is neural network architecture setup and training, and the last stage was evaluating the neural network performance on a test set of neutron track images over CR-39 detectors. These three stages are discussed in detail in the following subsections. The first and third stages were carried out using a designated SW written for the user interface (UI) of the deep learning model as shown in Figure 1.

2.1. Neutron Tracks Manual Tagging. The first stage was the tagging stage, where we picked 23 dosimeters consisting of 230 images and manually tagged all neutron tracks. Then, we used classical image processing algorithms to automatically detect all the objects in the images and match them to the tagged neutron tracks. Inside the 230 images, 23,567 objects were found and 2,615 of them were valid neutron tracks and 20,952 were not. The rules for deciding which signs are valid neutron tracks were taken from the EDL's work instruction for developing CR-39 detectors for evaluation of fast neutrons, which was adopted from Landauer's work instruction. This instruction relies on a worldwide knowledge and experience regarding the neutron tracks morphology. For instance, neutron tracks need to be between certain size limits, they need to have both inner bright circle and outer dark crown and they need to be clear and distinct from their surrounding background. Moreover, they also need to be evenly scattered across the detector area when accumulating large enough statistics. Of course, all the above rules for classifying neutron tracks are somewhat arbitrary, and so is the task of classifying them in every fast neutron dosimetry system. The main important directives to the EDL staff to follow for this classifying task were to obey the above rules and to be as repeatable as a human can be, so the deep learning algorithm described in the next step can learn the neutron tracks features as accurately as possible.

2.2. Neural Network Architecture Setup and Training. For the neutron tracks classification, we chose a state-of-the-art convolutional artificial neural network (ANN) of type U-Net, which was first introduced in 2015 [18] and was fine-tuned later [19]. This network's name is due to both its contracting (downsampling) and expansive (upsampling) paths, which give it the u-shaped architecture (Figure 2). The

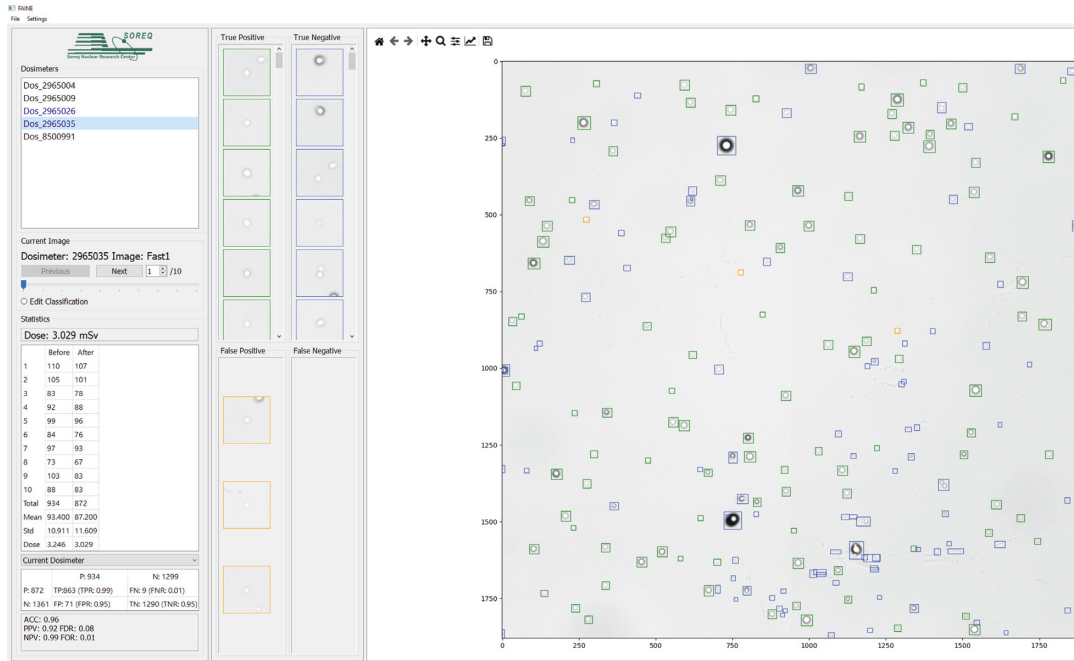


FIGURE 1: An example for the user interface of FAINE. At the large right pane is the 1st out of 10 fields of dosimeter number 2965035 as noted in the upper left pane. At the lower left pane, the statistics of this dosimeter are presented to the user, including predicted vs. real (input) neutron tracks, the confusion matrix, and the algorithm accuracy. In the middle pane, all detected signs are presented in zoom mode, so the user can examine them if needed.

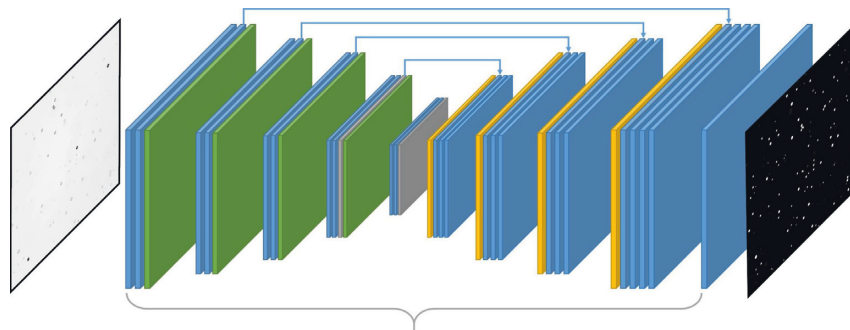


FIGURE 2: Basic schematics of the U-Net architecture. The model input is a raw image and its output is a segmented (masked) image of the neutron tracks. The U-Net consists of a contracting path and an expansive path (encoder-decoder). The contracting path follows the typical architecture of a convolutional network while the expansive path consists of an upsampling of the feature map followed by a 2×2 convolution (“upconvolution”) and two 3×3 convolutions, each followed by a rectified linear activation function (ReLU).

contracting path mainly serves as feature extraction for the net, while the expansive path is more for the localization of objects. U-Net architecture is commonly used for semantic segmentation tasks, e.g., processes of linking each pixel in an image to a class label, in our case either “track” or “nontrack.”

In order to feed the U-Net training stage with good quality images, we used dosimeter images that were taken under different lighting and environment conditions. We then manipulated the data with preprocessing techniques using some classical image processing algorithms such as canny edge detection, dilation, erosion, fill holes, and object detection. For the training stage, we used 80% of the total

23, 567 tagged signs that were created out of the 23 dosimeters, where each image containing such a sign is of resolution of 128×128 pixels.

2.3. *U-Net Performance Evaluation on Neutron Tracks.* After the training stage, we tested the U-Net classifier over the remaining 20% of the 23,567 tagged signs. The metric we used for evaluating the classifier’s performance is accuracy. Accuracy is defined as the number of correct predictions over the number of total predictions, so in terms of a binary classification model as in our case, we have the following definition:



FIGURE 3: An example of FAINE tagging signs inside a CR-39 image. Green squares indicate true positives, blue squares indicate true negatives, red squares indicate false positives, and orange squares indicate false negatives.

$$\text{accuracy} = \frac{TP + TN}{TP + TN + FP + FN}, \quad (1)$$

where TP stands for true positives and is defined as the number of correctly predicted neutron tracks (seen as the track signs inside the green squares in Figure 3), TN stands for true negatives and is defined as the number of correctly predicted signs that are not neutron tracks (seen as the track signs inside the blue squares in Figure 3), FP stands for false positives and is defined as the number of signs that are not neutron tracks, which were falsely predicted as neutron tracks (seen as the track signs inside the red squares in Figure 3), and FN stands for false negatives and is defined as the number of neutron tracks, which were falsely predicted as signs that are not neutron tracks (seen as the track signs inside the orange square in Figure 3).

3. Results and Discussion

As can be seen from Table 1, and using equation (1), when choosing the segmentation threshold to be 0.4, we get an accuracy of 96.7% on our test data.

This accuracy was achieved with respect to 4,509 different tagged signs. We can achieve different true positive

TABLE 1: Confusion matrix of our U-Net model. As can be seen from the definition of accuracy, the two important quantities that contribute to high accuracy are true positives (TP) and true negatives (TN).

Real	Predicted	
		Positives: 1,782
Positives: 1,697	TP: 1,665	FN: 32
Negatives: 2,812	FP: 117	TN: 2,695

Threshold: 0.4.

rate (TPR) to false positive rate (FPR) ratios by applying different classification thresholds over our models prediction. We chose to apply a classification threshold of 0.4 in order to gain a high enough TPR while still maintaining the false negative rates small enough. Of course, this choice of threshold is application-specific, and each model in any scientific field will eventually need to take this choice in order to apply a certain model.

The effectiveness of measuring fast neutron dosimeters at our EDL will dramatically improve, due to the automatic nature of our new tool, which will make the lab technician attendance redundant.

Another advantage of our new tool is the fast neutrons measurement uncertainty expected improvement. Since some of this uncertainty contribution come from the robustness uncertainty, our tool should slightly improve the overall measurement uncertainty by eliminating the worker A vs. worker B robustness term [17].

This measurement uncertainty improvement shall in turn lower the system's detection threshold. The fast neutrons detection threshold is defined in ISO 21909 : 2015 to be "the minimum measured dose equivalent, which is significantly higher (at the 95% confidence level) than the mean dose equivalent of a sample of nonirradiated detectors." Needless to note that the mean dose equivalent of unirradiated detectors measured by our new tool is supposed to be equal or lower than the one measured by the former method, since the former method used an overshoot dose assessment as a way to address the inherent computer vision problem to detect all fast neutron tracks.

4. Conclusions and Future Work

To conclude, we developed a novel algorithm that uses a deep learning U-Net model to accurately and repeatedly classify fast neutron tracks on CR-39 detectors with a high accuracy of 96.7%. This method can replace manual revision of track counting by an automatic repeatable process that will save a large amount of human time, especially as the number of CR-39 detectors to analyze gets higher in high neutron flux experiments.

It is worth mentioning that such deep learning methods are not limited to detection of massive particles, similar U-Net models can be also used for detection, imaging, and classification tasks with visible, X-ray and gamma photons (see, e.g., [20, 21]) which are now explored at SNRC as well.

In the near future, we plan to extend our U-Net model in order to gain new capabilities for differentiating between alpha-particles and protons and for fast neutrons and alpha-particles spectrometry using machine learning classification. For this extension of our model, we already started a process of its calibration for both alpha-particles detection and for fast neutron spectrometry classification, and we expect that our model will be very useful in analyzing results of proton-boron11 fusion experiments in the future.

Data Availability

The data used to support the findings of this study are available from the corresponding author upon request.

Conflicts of Interest

The authors declare that they have no conflicts of interest.

Authors' Contributions

Both Gal Amit and Idan Mosseri contributed equally to this research and should be considered as co-first authors.

Acknowledgments

This research was funded by the Israeli Ministry of Energy (grant number 01030961) and by the IAEC-UPBC PAZY Foundation (grant number 2472020).

References

- [1] S. Eliezer, H. Hora, J. M. Martinez Val, F. Belloni, and N. Nissim, "Editorial: non-local thermodynamic equilibrium (NLTE) hydrogen-boron fusion," *Frontiers in Physiology*, vol. 8, 2021.
- [2] D. Margarone, J. Bonvalet, L. Giuffrida et al., "In-target proton-boron nuclear fusion using a PW-class laser," *Applied Sciences*, vol. 12, no. 3, p. 1444, 2022.
- [3] S. Eliezer, H. Hora, G. Korn, N. Nissim, and J. M. Martinez Val, "Avalanche proton-boron fusion based on elastic nuclear collisions," *Physics of Plasmas*, vol. 23, no. 5, 2016.
- [4] F. Belloni, "On a fusion chain reaction via suprathermal ions in high-density H-¹¹B plasma," *Plasma Physics and Controlled Fusion*, vol. 63, no. 5, 2021.
- [5] H. Hora, S. Eliezer, G. Kirchhoff et al., "Road map to clean energy using laser beam ignition of boron-hydrogen fusion," *Laser and Particle Beams*, vol. 35, no. 4, pp. 730-740, 2017.
- [6] <https://marvelfusion.com/>.
- [7] <https://hb11.energy/>.
- [8] L. Tommasino, G. Zapparoli, P. Spiezia, R. V. Griffith, and G. Espinosa, "Different etching processes of damage track detectors for personnel neutron dosimetry," *Nuclear Tracks and Radiation Measurements*, vol. 8, pp. 335-339, 1982.
- [9] B. G. Cartwright, E. K. Shirk, and P. B. Price, "A nuclear-track-recording polymer of unique sensitivity and resolution," *Nuclear Instruments and Methods*, vol. 153, no. 2-3, pp. 457-460, Jul. 1978.
- [10] O. P. Massand, H. K. Kundu, M. P. Dhairyawan, and P. K. Marathe, "Studies with CR-39 solid state nuclear track detector for personnel neutron monitoring," *Bull. Radiat. Protect.* vol. 15, p. 27, 1992.
- [11] O. P. Massand, H. K. Kundu, P. K. Marathe, and S. J. Supe, *Development of Neutron Personnel Monitoring System Based on CR-39 Solid State Nuclear Track Detector*, Atomic Energy Commission, India, 1990.
- [12] E. Pitt, A. Scharmann, and R. Simmer, "Model calculations for the fast neutron response of a CR-39 detector covered with a radiator," *International Journal of Radiation Applications and Instrumentation - Part D: Nuclear Tracks and Radiation Measurements*, vol. 19, no. 1-4, pp. 517-520, 1991.
- [13] B. Morelli, E. Vilela, and E. Fantuzzi, "Dosimetric performance of the fast neutron dosimeter for ENEA personal dosimetry service," *Radiation Protection Dosimetry*, vol. 85, no. 1, pp. 105-108, 1999.
- [14] J. Charvat, "Neutron dosimetry based on chemical etching of proton tracks in CR-39," *Radiation Protection Dosimetry*, vol. 23, no. 1-4, pp. 171-174, 1988.
- [15] F. d'Errico, W. G. Alberts, and M. Matzke, "Advances in superheated drop (bubble) detector techniques," *Radiation Protection Dosimetry*, vol. 70, no. 1, pp. 103-108, 1997.
- [16] Y. Eisen, A. Eliaou, and Z. Karpinowitz, "A stable high voltage, high frequency power supply for electrochemical etching," *Nuclear Instruments and Methods*, vol. 174, no. 3, pp. 613-615, 1980.
- [17] G. Amit, O. Even-Hen, O. Awad, Y. Levi, L. Buchbinder, and H. Datz, "A performance study of a new personal neutron

- dosimetry system at SNRC,” *Radiation Protection Dosimetry*, vol. 189, no. 2, pp. 242–252, 2020.
- [18] J. Long, E. Shelhamer, and T. Darrell, “Fully convolutional networks for semantic segmentation,” 2014, <https://arxiv.org/abs/1411.4038>.
- [19] O. Ronneberger, P. Fischer, T. Brox, and U-Net, *Convolutional Networks for Biomedical Image Segmentation*, <https://arxiv.org/abs/1505.04597>, 2015.
- [20] T. Shimobaba, Y. Endo, T. Nishitsuji et al., “Computational ghost imaging using deep learning,” *Optics Communications*, vol. 413, pp. 147–151, 2018.
- [21] T. Bian, Y. Yi, J. Hu, Y. Zhang, Y. Wang, and L. Gao, “A residual-based deep learning approach for ghost imaging,” *Scientific Reports*, vol. 10, p. 12149, 2020.



Research Article

Analysis of the p-¹¹B Fusion Scenario with Compensation of the Transfer of Kinetic Energy of Protons and Alpha Particles to the Gas Medium by the Electric Field

Mikhail L. Shmatov 

Ioffe Institute, St. Petersburg 194021, Russia

Correspondence should be addressed to Mikhail L. Shmatov; m.shmatov@mail.ioffe.ru

Received 15 April 2022; Accepted 28 May 2022; Published 28 June 2022

Academic Editor: Dimitri Batani

Copyright © 2022 Mikhail L. Shmatov. This is an open access article distributed under the Creative Commons Attribution License, which permits unrestricted use, distribution, and reproduction in any medium, provided the original work is properly cited.

The energy balance of the p-¹¹B fusion scenario with compensation of the transfer of kinetic energy of protons and alpha particles to the gas medium by the electric field is considered. It is shown that such scenario cannot provide the use of p-¹¹B fusion reaction for power production due to the very low ratio of the energy release of the fusion reaction to the energy necessary for compensation. The upper boundary of this ratio is about 2×10^{-3} .

1. Introduction

The influence of chain reactions on the rate R_1 of p-¹¹B fusion reaction



is discussed since 1973 [1–12]. One of the chain reactions consists of the scattering of at least one of the three alpha particles, generated by reaction (1), on proton(s) with acceleration of the proton(s) to kinetic energies, corresponding to a relatively high cross-section σ_1 for reaction (1) and the subsequent participation of the accelerated proton(s) in this reaction [1, 4, 6–12]. According to [1], at the temperature of 150–350 keV and the density of 10^{16} – 10^{26} cm^{-3} , this chain reaction and other “nonthermal” effects result in an increase in R_1 on 5–15%. The type of particles with such densities was not mentioned [1], but this detail is not essential because in plasma under consideration, the densities of all particles are comparable [8]. According to [2–4, 7, 9, 10, 12], at least if special measures are taken, the increase in R_1 due to the chain reactions can be so high that it will provide the possibility of the use of reaction (1) for power production. The negative results of analysis of such assumptions from [2–4] are presented in [5, 6, 8, 11].

In 2020, Eliezer and Martinez-Val [9] and Eliezer et al. [10] proposed p-¹¹B fusion scenarios with the influence of electric and magnetic fields on protons and alpha particles in the gas medium. The main idea of the proposal is that during some time periods, time-dependent electric field should compensate approximately for the transfer of kinetic energy ε_p of a proton with $\varepsilon_p \approx \varepsilon_p^*$, where ε_p^* is ε_p corresponding to the largest value of σ_1 for the collision of proton with the nucleus of ¹¹B in the rest, to the medium and for transfer of the kinetic energy of the alpha particle to the medium [9, 10]. This compensation should increase the probability of participation of the protons in reaction (1) and that of “useful” acceleration of protons due to the scattering of alpha particles on them. The magnetic field should provide the realization of these scenarios in reactors with acceptable sizes [9, 10]. Below, it is shown that in the scenario proposed in [10], the ratio g of energy release of reaction (1) to the average value $\langle W_s \rangle$ of the energy spent for the initiation of one reaction (1) will be unacceptably low for power production.

2. The Upper Boundary of g

Eliezer et al. [10] analyzed the situations when reaction (1) occurs in gaseous $\text{H}_3{}^{11}\text{B}$ or other hydride of ¹¹B with a density of 10^{19} cm^{-3} or of the order of 10^{19} cm^{-3} and

temperature of about 1 eV or few eV. Ionization of this gas is supposed negligible [10]. Since a free molecule of H_3B does not exist and at the temperature above $700^\circ C$ all hydrides of boron dissociate into boron and hydrogen [13], we will estimate the lowest boundary W_s^l of $\langle W_s \rangle$ in gas medium consisting of atoms of ^{11}B with the density

$$n_{11B} \approx 2.5 \times 10^{18} \text{ cm}^{-3}, \quad (2)$$

and molecules of H_2 with the density

$$n_{H_2} \approx 3.75 \times 10^{18} \text{ cm}^{-3}. \quad (3)$$

At the conditions described in [10], the medium containing atoms of boron and molecules of hydrogen will also contain atoms of hydrogen and ions, but this is not essential for the analysis of the acceptability of attainable values of g for power production. The ratio n_{11B}/n_{H_2} corresponds to the ratio of the numbers of nuclei of ^{11}B and protons in the nonexistent free molecule of $H_3^{11}B$ discussed in [10]. The choice of n_{11B} corresponds to an example presented on page 5 of Reference [10] and is mainly important for an estimate of the typical proton path $l_{typ} = 1/(\sigma_1 n_{11B})$, corresponding to one reaction (1). The estimate of W_s^l presented below yields that this parameter is independent of n_{11B} .

In the situation under consideration, the change $d\varepsilon_p$ of ε_p on proton path dx is given approximately by

$$d\varepsilon_p \approx [eE - k_{H_2}^p(\varepsilon_p)n_{H_2} - k_B^p(\varepsilon_p)n_{11B}] dx, \quad (4)$$

where e is the proton charge, E is the strength of the electric field, and $k_{H_2}^p$ and k_B^p are the parameters describing the transfer of ε_p to molecules of hydrogen and atoms of boron, respectively. The parameter $k_{H_2}^p$ was calculated as

$$k_{H_2}^p = 2 A_H m_u S_{H_2}^p, \quad (5)$$

where A_H is the atomic mass of hydrogen, m_u is the atomic mass unit, and $S_{H_2}^p$ is the stopping power of molecular hydrogen for proton. The parameter k_B^p was calculated as

$$k_B^p \approx \frac{m_u}{2} (A_{Be} S_{Be}^p + A_C S_{Cam}^p), \quad (6)$$

where A_{Be} is the atomic mass of beryllium, S_{Be}^p is its stopping power for proton, A_C is the atomic mass of carbon, and S_{Cam}^p is the stopping power of amorphous carbon with the density of 2 g/cm^3 for proton. The values of $S_{H_2}^p$, S_{Be}^p , and S_{Cam}^p from [14] were used.

The parameter k_B^p was approximated by (6) due to the absence of data on the stopping power of boron for proton in [14]. This equation corresponds to the assumption that the product P of the stopping power of the medium, consisting of atoms or molecules of one chemical element with atomic number Z , on the atomic mass of this element depends on Z approximately linearly and, therefore,

$$P(Z) \approx [P(Z - \Delta Z) + P(Z + \Delta Z)]/2, \quad (7)$$

where ΔZ is a small natural number, for example, unity or two. In order to demonstrate that at least in some situations, the accuracy of (7) is rather high, let us compare

$P(Z = 6, \varepsilon_p = 600 \text{ keV}) \approx 3797 \text{ MeV cm}^2 \text{ g}^{-1}$ and $P(Z = 6, \varepsilon_p = 700 \text{ keV}) \approx 3440 \text{ MeV cm}^2 \text{ g}^{-1}$, calculated using S_{Cam}^p from [14], with the same parameters, calculated using (7) and $\Delta Z = 2$. Substituting S_{Be}^p and the stopping power of molecular oxygen for proton from [14] into (7), we obtain $P(Z = 6, \varepsilon_p = 600 \text{ keV}) \approx 3773 \text{ MeV cm}^2 \text{ g}^{-1}$ and $P(Z = 6, \varepsilon_p = 700 \text{ keV}) \approx 3424 \text{ MeV cm}^2 \text{ g}^{-1}$. Thus, in these cases, the relative accuracy of (7) is better than 1%. This allows us to assume that at $600 \text{ keV} \leq \varepsilon_p \leq 700 \text{ keV}$ (see below), the relative accuracy of (6) is of the order of 1% or even better.

According to [15], $\varepsilon_p^* \approx 646.2 \text{ keV}$ and

$$\sigma_1(\varepsilon_p = \varepsilon_p^*) \approx 1.196 \text{ b}. \quad (8)$$

Let us denote the value of E corresponding to the condition $d\varepsilon_p/dx = 0$, i.e., to the almost exact compensation of the transfer of kinetic energy of protons to the gas medium by the electric field, as E_0 . This value depends on ε_p ((4)). Equations (2)–(6) and (8) yield that at $\varepsilon_p = \varepsilon_p^*$, $l_{typ} \approx 3.34 \times 10^5 \text{ cm}$, $E_0 \approx 24.9 \text{ kV/cm}$, $eE_0 l_{typ} \approx [k_{H_2}^p(n_{H_2}/n_{11B}) + k_B^p]/\sigma_1 \approx 8.32 \text{ GeV}$, and $(8.7 \text{ MeV})/(eE_0 l_{typ}) \approx 1.046 \times 10^{-3}$.

At $\varepsilon_p \approx \varepsilon_p^*$, $k_{H_2}^p$ and k_B^p decrease with increasing ε_p ((5) and (6) and [10, 14]). This results, in particular, in the impossibility to provide a stable motion of proton with such kinetic energy at constant E [10]. The highest value of $1/(eE_0 l_{typ})$ corresponds to $\varepsilon_p \approx 657.6 \text{ keV}$, $E_0 \approx 24.6 \text{ kV/cm}$, $l_{typ} \approx 3.36 \times 10^5 \text{ cm}$, $eE_0 l_{typ} \approx 8.27 \text{ GeV}$, and $(8.7 \text{ MeV})/(eE_0 l_{typ}) \approx 1.052 \times 10^{-3}$. These values of $eE_0 l_{typ}$ and $(8.7 \text{ MeV})/(eE_0 l_{typ})$ can serve as W_s^l and the upper boundary of g , respectively. It should be emphasized that the real value of $\langle W_s \rangle$ can be much greater than $eE_0 l_{typ}$ due to acceleration of secondary charged particles, i.e., molecular ions of hydrogen, protons, ions of ^{11}B , and electrons created by the fast protons considered above and alpha particles, etc. [16–18]. At sufficiently high temperature, the acceleration of electrons and ions arising due to thermal ionization can also be important. The problem of the possibility of electric breakdown in the gas medium under consideration can probably be solved only experimentally. The presented estimate of W_s^l corresponds to the assumption that the magnetic field prevents the acceleration of electrons and relatively slow molecular ions of hydrogen, protons, and ions of ^{11}B by the electric field. However, the accuracy of this estimate is sufficient for the reliable qualitative conclusion about the unacceptability of the scenario proposed in [10] for power production: in any case, $\langle W_s \rangle$ will include $eE_0 l_{typ}$ and, therefore, g will be too low. The reason is that the efficiency of the use of any fusion reaction for power production will be determined, in particular, by the cost of electricity [19, 20]. According to [20], for the inertial fusion energy power plant with conversion of fusion energy into thermal energy and subsequent conversion of 30–35% of the latter into electricity, the cost of electricity will be acceptable

when the product of the target gain on the driver efficiency η_d exceeds ten. The target gain is the ratio of fusion energy release of one microexplosion to the energy delivered to the target for ignition of the microexplosion [20]. This parameter should exceed ten even if η_d is close to unity and is an analog of the parameter g . Thus, g of the order of 10^{-3} and less is not sufficient for power production involving conversion of fusion energy into thermal energy. Note that Weaver et al. [1] discussed briefly the potential feasibility of power production in the regime of subignition operation corresponding to $g < 1$. In any case, g of the order of 10^{-3} and less seems to be too low even for this regime.

Note also that in the scenario proposed in [10], the acceleration of alpha particles, if it is not suppressed by the magnetic field, will not provide the effective acceleration of protons and, therefore, will serve mainly as a process increasing $\langle W_s \rangle$. This can be shown using equations, similar to (4)–(6), and the data from [10, 11, 14, 21] for the analysis of the motion of alpha particles and the transfer of their kinetic energy to protons. The compensation of deceleration of protons in the gas medium consisting mainly of atoms of ^{11}B will also not provide sufficiently high values of g : at $n_{\text{H}_2} = 0$, the highest value of $1/(eE_0 l_{\text{typ}})$ corresponds to $\varepsilon_p \approx 656.6 \text{ keV}$, $eE_0 l_{\text{typ}} \approx 4.30 \text{ GeV}$, and $(8.7 \text{ MeV})/(eE_0 l_{\text{typ}}) \approx 2.024 \times 10^{-3}$.

3. Conclusion

The scenario proposed in [10] cannot be used for effective power production due to the very low attainable g , the upper boundary of which is about 10^{-3} . A decrease in $n_{\text{H}_2}/n_{^{11}\text{B}_2}$ down to zero can result only in an approximately two-fold increase in the upper boundary of g . The real value of g can be much less than its upper boundary.

Data Availability

The data used to support the findings of this study are included within the article.

Conflicts of Interest

The author declares that there are no conflicts of interest.

Acknowledgments

The author would like to thank the company HB11 Energy Pty Ltd. for the payment of APC for the publication of this manuscript.

References

- [1] T. Weaver, G. Zimmerman, and L. Wood, *Exotic CTR Fuels: Non-thermal Effects and Laser Fusion Applications*, Preprint UCRL-74938, Lawrence Livermore Laboratory, Livermore, CA, USA, 1973.
- [2] V. S. Belyaev, V. P. Krainov, B. V. Zagreev, and A. P. Matafonov, "On the implementation of a chain nuclear reaction of thermonuclear fusion on the basis of the $p + ^{11}\text{B}$ process," *Physics of Atomic Nuclei*, vol. 78, no. 5, pp. 537–547, 2015.
- [3] V. S. Belyaev, V. P. Krainov, A. P. Matafonov, and B. V. Zagreev, "The new possibility of the fusion $p + ^{11}\text{B}$ chain reaction being induced by intense laser pulses," *Laser Physics Letters*, vol. 12, no. 9, Article ID 096001, 2015.
- [4] S. Eliezer, H. Hora, G. Korn, N. Nissim, and J. M. Martinez Val, "Avalanche proton-boron fusion based on elastic nuclear collisions," *Physics of Plasmas*, vol. 23, no. 5, Article ID 050704, 2016.
- [5] M. L. Shmatov, "Suppression of the chain nuclear fusion reaction based on the $p + ^{11}\text{B}$ reaction because of the deceleration of alpha particles," *Physics of Atomic Nuclei*, vol. 79, no. 5, pp. 666–670, 2016.
- [6] M. L. Shmatov, "Comment on "Avalanche proton-boron fusion based on elastic nuclear collisions"," *Physics of Plasmas*, vol. 23, no. 9, Article ID 094703, 2016.
- [7] S. Eliezer, H. Hora, G. Korn, N. Nissim, and J. M. Martinez Val, "Response to "Comment on "Avalanche proton-boron fusion based on elastic nuclear collisions"," *Physics of Plasmas*, vol. 23, no. 9, Article ID 094704, 2016.
- [8] M. L. Shmatov, "Igniting a microexplosion by a micro-explosion and some other controlled thermonuclear fusion scenarios with neutronless reactions," *Physics–Uspekhi*, vol. 62, no. 1, pp. 70–81, 2019.
- [9] S. Eliezer and J. M. Martinez-Val, "A novel fusion reactor with chain reactions for proton-boron11," *Laser and Particle Beams*, vol. 38, no. 1, pp. 39–44, 2020.
- [10] S. Eliezer, Y. Schweitzer, N. Nissim, and J. M. Martinez Val, "Mitigation of the stopping power effect on proton-boron11 nuclear fusion chain reactions," *Frontiers in Physics*, vol. 8, Article ID 573694, 2020.
- [11] F. Belloni, "On a fusion chain reaction via suprathreshold ions in high-density $\text{H-}^{11}\text{B}$ plasma," *Plasma Physics and Controlled Fusion*, vol. 63, no. 5, Article ID 055020, 2021.
- [12] J. Gruenwald, "On fusion chain reactions in ^{11}B targets for laser driven aneutronic fusion," *Journal of Technological and Space Plasmas*, vol. 2, no. 1, pp. 104–108, 2021.
- [13] V. L. Vasilevskiy, *Borovodorody ["Hydrides of Boron"], in Bol'shaya Sovetskaya Encyclopedia [Big Soviet Encyclopedia, Sovetskaya Encyclopedia, Moscow, Russia, 1970.*
- [14] M. J. Berger, J. S. Coursey, M. A. Zuker, and J. Chang, "Stopping-power and range tables for electrons, protons and helium ions," 2009, <https://www.nist.gov/pml/data/star>.
- [15] W. M. Nevins and R. Swain, "The thermonuclear fusion rate coefficient for $p - ^{11}\text{B}$ reactions," *Nuclear Fusion*, vol. 40, no. 4, pp. 865–872, 2000.
- [16] L. Nagy and L. Végh, "Ionization of molecular hydrogen by proton impact. I. Single ionization," *Physical Review A*, vol. 46, no. 1, pp. 284–289, 1992.
- [17] L. Nagy and L. Végh, "Ionization of molecular hydrogen by proton impact. II. Two-electron processes," *Physical Review A*, vol. 46, no. 1, pp. 290–295, 1992.
- [18] Y. P. Raizer, *Fizika Gazovogo Razryada [Physics of Gas Discharge]*, Izd. Dom Intellect, Dolgoprudny, Russia, 2009.
- [19] E. Teller, "A future ICE (thermonuclear, that is!)," *IEEE Spectrum*, vol. 10, no. 1, pp. 60–64, 1973.
- [20] V. P. Smirnov, V. I. Subbotin, and B. Y. Sharkov, *Printsipial' Naya schema ITS ["Principal scheme of ICF"]*, in *Yadernyi Sintez S Inertsionnym Uderzhaniem [Nuclear Fusion with Inertial Confinement]*, Fizmatlit, Moscow, Russia, 2005.
- [21] L. D. Landau and E. M. Lifshitz, *Mechanics*, Pergamon Press, Oxford, UK, 1962.